UNIVERSITÀ DEGLI STUDI DI TRIESTE

XXXIV CICLO DEL DOTTORATO DI RICERCA IN FISICA

NON-EQUILIBRIUM RESPONSE OF QUANTUM MATERIALS TO RESONANT LOW-ENERGY ELECTRONIC PHOTO-EXCITATIONS

Settore scientifico-disciplinare: FIS/03

DOTTORANDA:
Angela Montanaro

COORDINATORE:
Prof. Francesco Longo

SUPERVISORE DI TESI:
Prof. Daniele Fausti

ANNO ACCADEMICO 2020/2021

ABSTRACT

The properties of quantum materials are determined by the delicate balance among many interacting degrees of freedom. The existence of several competing orders makes these systems highly susceptible to even small perturbations that can induce giant responses and eventually change the macroscopic state of the material. The microscopic understanding of the intricate interplay between electrons, ions and spins is thus the key to attain new material functionalities.

Pump-probe optical experiments are a powerful tool to study the non-equilibrium states of quantum materials, offering unique insight into the sub-picosecond dynamics of the energy redistribution among the coupled modes.

The aim of the first part of this thesis is to implement a three-pulse experiment in which, by combining a visible pump, a mid-infrared pump and a supercontinuum probe, the high- and low-energy degrees of freedom are simultaneously excited in the material and its transient optical response is probed over a broad energy range. The large frequency-tunability of the sources allows to selectively target specific excitations in matter and to dynamically study their coupling.

The high versatility of this setup makes it ideally suited to study a wide range of different materials. We will discuss the application to a cuprate superconductor, in which pulses with photon energy either above or below the superconducting d-wave gap are found to photo-excite an anisotropic quasiparticle distribution. We will then investigate the role of dd orbital excitations in determining the magnetic properties of TiOCl, a one-dimensional spin-Peierls compound at low temperatures. Finally, we will study the optical response of bulk black phosphorus, a layered van der Waals material in which the photo-excitation by suitable sub-gap pulses is found to possibly trigger a non-adiabatic modification of the screening environment.

In the second part of the thesis, we develop a covariance-based technique to study time-resolved electronic Raman scattering in cuprates. By probing the system with randomized pulses and implementing a single-shot frequency-resolved acquisition, we are able to unveil the spectral correlations imprinted in the pulses by the inelastic scattering from the pump-induced Cooper pair breaking. The momentum selectivity peculiar to Raman scattering, in combination with the sub-picosecond temporal resolution of the technique, allows to measure the correlation dynamics projected onto different regions of the Brillouin zone, thus enabling the isolation of the nodal and antinodal contributions. The observation of gap-size correlations in the pseudogap phase hints at the presence of a local pairing that survives even when the superconducting state is macroscopically melted.

CONTENTS

1

INTRODUCTION

1.1 INVITATION TO READ

In the perspective that consecrated "*the beautiful friendship*" between the fields of ultrafast spectroscopy and quantum materials [1], J. Orenstein illustrates a simple example that well captures the strength of time-resolved techniques for studying these systems.

Let us imagine dissolving a given amount of common sodium chloride in water. In this basic chemistry experiment, by measuring the ionic concentration as a function of temperature, the free energy difference between the crystalline and the dissociated phases can be inferred. However, these static measurements are inherently blind to the strength of the interaction between the ions in the solution, that can only be estimated by measuring the kinetics of the reaction $Na^{+}+Cl^{-} \rightarrow NaCl$.

This simple picture, so close to our daily experience, is surprisingly similar to what happens in much more exotic systems, like superconductors, where the role of the crystalline NaCl is played by the condensate and its co-existing quasiparticles replace the solvated ions. At equilibrium, the Cooper pairs constantly evaporate from the condensate and recombine, and these reverse processes occur at the same rate. In analogy with our example, only the study of the system in out-of-equilibrium conditions allows to measure the kinetics of the quasiparticle recombination and can hence contribute to investigate the glue that mediates the pairing.

In a more general framework, the possibility of revealing the sub-picosecond dynamics of impulsively excited states has revolutionized the study of **quantum materials**, where the simultaneous presence of electronic, magnetic, lattice and orbital excitations having comparable energy scales precludes the isolation of the different contributions at equilibrium [2]. By taking advantage of the different thermalization timescales peculiar to each degree of freedom, time-domain techniques offer the unique opportunity of disentangling the response to the different contributions and thus unveiling the leading interactions in the material.

The almost negligible energy difference between competing excitations makes these systems highly responsive to external perturbations that can tip this precarious energy balance in favour of one competitor. As a result, quantum materials are often on the verge of multiple phase transitions and the tuning of parameters such as chem-

ical doping, temperature and pressure gives rise to their complex phase diagrams.

In addition to detect the competing order, the interaction with ultrashort light pulses can also be used as a further knob to control the functional properties of matter on the sub-picosecond timescale. The photo-injection of a large number of excitations within a time-window which is much shorter than the characteristic relaxation times of the system, results in an anomalous energy redistribution among its relevant degrees of freedom. By strongly perturbing the coupling among electrons, ions and spins, it is then possible to drive the material into highly off-equilibrium metastable phases, often not adiabatically accessible otherwise [3, 4, 5].

While the most widely used approach consists in injecting high-energy photo-excitations (>1 eV), the idea of using mid-infrared ultrashort pulses is recently emerging as a more attractive option. Mid-infrared pulses do not directly inject hot carriers, but resonantly couple to the **low-lying energy states** in the system. Long-wavelength electromagnetic fields can hence trigger coherent and collective excitations that are unaffected by the thermodynamics of the material. Recent investigations in transition metal oxides have shown that the coherent coupling to other energy modes can induce insulator-metal phase transitions [6], melt the magnetic and orbital order [7, 8], and even trigger light-induced superconducting and ferroelectric states [9, 10, 11, 12].

A second relevant aspect in quantum materials is the role played by **fluctuations** that naturally emerge from the strong correlation effects. The presence of fluctuations, both classical and quantum, is an essential element to grasp many exotic phenomena in these materials [13]. In particular, phase fluctuations of the superconducting order parameter [14], along with the widely-reported observation of spin [15, 16] and lattice [17] fluctuations, have been proposed to concur in the onset of high-temperature superconductivity in copper oxides.

In this work, we approach the study of the non-equilibrium response of quantum materials from two perspectives. First, we investigate the effects of resonant low-energy photo-excitations by means of a newly-implemented spectroscopic tool, the **three-pulse spectroscopy**. We combine mid-infrared and visible tunable pulsed sources to excite, selectively and simultaneously, low- and high-energy degrees of freedom in matter and address in this way the interdependence of their dynamical coupling. Second, we employ a **noise-assisted covariance-based technique** that leverages on the evaluation of the spectral correlations within stochastic ultrashort pulses to measure nonlinear material responses. In going beyond the standard mean-value observables, this approach is ideally suited for probing materials in which fluctuations play an important role.

1.2 DETAILED SUMMARY

The thesis is divided into two main parts. In the first part, the broadband three-pulse spectroscopy is used to study the non-equilibrium response in two classes of materials: transition metal oxides ($Bi_2Sr_2Ca_{0.92}Y_{0.08}Cu_2O_{8+\delta}$ and TiOCl) and layered van der Waals semiconductors (black phosphorus). The second part is dedicated to the development of a stochastic approach to time-resolved electronic Raman scattering, exploiting the combination of a covariance-based detection and an input noisy source. I will discuss its application to a non-equilibrium study of the superconducting gap in $Bi_2Sr_2CaCu_2O_{8+\delta}$, a cuprate in which superconducting fluctuations survive tens of K above the critical temperature.

In **Chapter 2**, I present in detail the three-pulse technique that we have designed to simultaneously excite different degrees of freedom of materials, both in the visible and in the mid-infrared energy range. This unique configuration allows for the direct study and control of the coupling between low- and high-energy excitations in matter. The combination with a white-light supercontinuum probe further empowers the technique, enabling a full time-dependent reconstruction of the non-equilibrium dielectric function of the material over a broad energy range.

I present in **Chapter 3** the application of the technique to the study of non-thermal states in optimally-doped $Bi_2Sr_2Ca_{0.92}Y_{0.08}Cu_2O_{8+\delta}$ (Y-Bi2212), a representative of the cuprates family. The cuprates are unconventional superconductors in many ways. First of all, contrarily to the BCS systems, their high-frequency electrodynamics undergoes drastic changes when the superconducting (SC) phase is entered, suggesting a direct involvement of the high-energy excitations (having either orbital or charge-transfer character) in the pairing mechanism. Secondly, the SC gap has a d-wave symmetry, implying that, even in the limit $T \to 0$, thermal excitations dominate the response at the nodes, where the gap vanishes. The study of out-of-equilibrium states is thus pivotal to understand how the **k**-resolved electronic excitations control the d-wave gap. We used a time-dependent Drude-Lorentz model to study the visible transient reflectivity of Y-Bi2212 to photo-excitation both above and below the SC gap ($\sim$75 meV). We found that the dynamics is ruled by the transient modification of an interband excitation at 2 eV, whose spectral weight dynamics depends on the pump photon energy and marks the onset of the SC phase. Furthermore, the three-pulse technique revealed that the photon energy of the excitation may be a critical parameter to dynamically control the **k**-dependent distribution of the non-thermal quasiparticles.

In **Chapter 4**, I present a non-equilibrium study of the optical properties of TiOCl, a 1D antiferromagnet that undergoes a first-order phase transition to a dimerized spin-Peierls phase at low temperatures. The $3d^1$ configuration of the Ti ions sets the orbital degeneracy within the t_{2g} triplet, making TiOCl a good candidate for hosting an orbitally ordered phase. At equilibrium, the crystal field splitting completely

removes the d-orbital degeneracy and, consequently, the breaking of the inversion symmetry makes the dd transitions optically active. We leverage this aspect to study the transient transmissivity of TiOCl upon the resonant stimulation of two dd transitions: the d_{yz} (0.7 eV), that has lobes lying out-of-plane with respect to the antiferromagnetic 1D chain, and the $d_{x^2-y^2}$ (1.5 eV), that points towards the in-plane oxygen atoms and favours the superexchange channel. In the spin-Peierls phase, the simultaneous excitation of the two dd transitions via the three-pulse technique revealed that they undergo different de-excitation pathways, possibly indicating the presence of a magnon-orbiton coupling that is usually neglected in the formal description of the dimerized spin-Peierls phase at equilibrium.

I discuss in **Chapter 5** how the photo-excitation of bulk black phosphorus (BP) induces remarkably different optical responses depending on the photon energy of the pulses employed. BP is a recently exfoliated 2D material with strongly layer-dependent electronic properties. In the few-layer form, the band gap energy (E_g) is about 2 eV and the optical absorption is dominated by narrow exciton resonances with extremely large binding energies. With increasing thickness, the electron-hole Coulomb attraction gets significantly screened by the strong interlayer interactions, leading to a progressive redshift of the band gap (E_g = 0.3 eV in the bulk) and a flat absorption band above E_g. By tuning the photon energy of the pump excitation across the band gap in bulk BP, we found that, while above-gap pulses induce a broadband transparency due to phase space filling, below-gap pulses trigger an anomalous response which is peaked in correspondence of the single-layer exciton of the phosphorene monolayer. With the support of DFT calculations, our findings suggest that below-gap pulses may drive a non-adiabatic modification of the 3D screening through the coherent redistribution of the charge carriers.

I introduce in **Chapter 6** the fundamental concepts of standard electronic Raman scattering and the Raman tensor in cuprates. The great advantage of the technique is the possibility of isolating the response to the different Raman symmetries (and so different regions of the Brillouin zone) by properly selecting the polarization of the incident and the scattered beams. This led to one of the first spectroscopic evidences of the d-wave gap in cuprates, where the electronic scattering from Cooper pair-breaking can be directly probed.

In **Chapter 7**, I present the "Femtosecond Covariance Spectroscopy" (FCS), the stochastic approach we have developed to study nonlinear optical processes. The technique rejects the use of mean-value observables to extract information from the stroboscopic repetitions of the same experiment, and rather takes advantage of the uniqueness of each repetition to evaluate the spectral correlations encoded in each ultrashort pulse by the nonlinear process. We validate the method by studying stimulated Raman scattering in α-quartz. Finally, we discuss the implementation of a "time-resolved version" of FCS and focus on how, by disentangling the time- and frequency-resolution, it circumvents the uncertainty principle, that represents a

major limitation in standard time-resolved Raman experiments.

I present in **Chapter 8** the preliminary time-resolved FCS measurements on optimally-doped Bi2212. We observed a pump-induced covariance signal in the SC phase that indicates a non-null correlation on an energy scale consistent with the amplitude of the SC gap. This indicates that the covariance-based approach is sensitive to the inelastic scattering from the Cooper pairs, which imparts a frequency-mixing across the randomized pulses. While this correlation signal is suppressed in the normal phase, we observed that it endures in the pseudogap phase. This evidence poses puzzling new questions about the nature of the pseudogap phase and, in turn, about the possibility of a local pairing in cuprates even above the SC critical temperature.

REFERENCES

[1] Joseph Orenstein. Quantum materials. *Physics Today*, 65(9):44, 2012.

[2] Claudio Giannetti, Massimo Capone, Daniele Fausti, Michele Fabrizio, Fulvio Parmigiani, and Dragan Mihailovic. Ultrafast optical spectroscopy of strongly correlated materials and high-temperature superconductors: a non-equilibrium approach. *Advances in Physics*, 65(2):58–238, 2016.

[3] Andrea Cavalleri, Cs Tóth, Craig W Siders, JA Squier, F Ráksi, P Forget, and JC Kieffer. Femtosecond structural dynamics in VO_2 during an ultrafast solid-solid phase transition. *Physical review letters*, 87(23):237401, 2001.

[4] Daniele Fausti, Oleg V Misochko, and Paul HM van Loosdrecht. Ultrafast photoinduced structure phase transition in antimony single crystals. *Physical Review B*, 80(16):161207, 2009.

[5] S De Jong, R Kukreja, Christoph Trabant, N Pontius, CF Chang, T Kachel, Martin Beye, Florian Sorgenfrei, CH Back, B Bräuer, et al. Speed limit of the insulator–metal transition in magnetite. *Nature materials*, 12(10):882–886, 2013.

[6] Matteo Rini, Ra'anan Tobey, Nicky Dean, Jiro Itatani, Yasuhide Tomioka, Yoshinori Tokura, Robert W Schoenlein, and Andrea Cavalleri. Control of the electronic phase of a manganite by mode-selective vibrational excitation. *Nature*, 449(7158):72–74, 2007.

[7] Michael Först, RI Tobey, Simon Wall, Hubertus Bromberger, Vikaran Khanna, Adrian L Cavalieri, Y-D Chuang, WS Lee, R Moore, WF Schlotter, et al. Driving magnetic order in a manganite by ultrafast lattice excitation. *Physical Review B*, 84(24):241104, 2011.

[8] RI Tobey, D Prabhakaran, AT Boothroyd, and Andrea Cavalleri. Ultrafast electronic phase transition in $La_{1/2}Sr_{3/2}MnO_4$ by coherent vibrational excitation: evidence for nonthermal melting of orbital order. *Physical review letters*, 101(19):197404, 2008.

[9] Daniele Fausti, RI Tobey, Nicky Dean, Stefan Kaiser, A Dienst, Matthias C Hoffmann, S Pyon, T Takayama, H Takagi, and Andrea Cavalleri. Light-induced superconductivity in a stripe-ordered cuprate. *science*, 331(6014):189–191, 2011.

[10] Wanzheng Hu, Stefan Kaiser, Daniele Nicoletti, Cassandra R Hunt, Isabella Gierz, Matthias C Hoffmann, M Le Tacon, T Loew, B Keimer, and Andrea Cavalleri. Optically enhanced coherent transport in $YBa_2Cu_3O_{6.5}$ by ultrafast redistribution of interlayer coupling. *Nature materials*, 13(7):705–711, 2014.

[11] Xian Li, Tian Qiu, Jiahao Zhang, Edoardo Baldini, Jian Lu, Andrew M Rappe, and Keith A Nelson. Terahertz field-induced ferroelectricity in quantum paraelectric $SrTiO_3$. *Science*, 364(6445):1079–1082, 2019.

[12] TF Nova, AS Disa, Michael Fechner, and Andrea Cavalleri. Metastable ferroelectricity in optically strained $SrTiO_3$. *Science*, 364(6445):1075–1079, 2019.

[13] Subir Sachdev. Quantum criticality: competing ground states in low dimensions. *Science*, 288(5465):475–480, 2000.

[14] VJ Emery and SA Kivelson. Importance of phase fluctuations in superconductors with small superfluid density. *Nature*, 374(6521):434–437, 1995.

[15] Subir Sachdev. Colloquium: Order and quantum phase transitions in the cuprate superconductors. *Reviews of Modern Physics*, 75(3):913, 2003.

[16] Thomas Dahm, V Hinkov, SV Borisenko, AA Kordyuk, VB Zabolotnyy, J Fink, B Büchner, DJ Scalapino, W Hanke, and B Keimer. Strength of the spin-fluctuation-mediated pairing interaction in a high-temperature superconductor. *Nature Physics*, 5(3):217–221, 2009.

[17] DM Newns and CC Tsuei. Fluctuating Cu-O-Cu bond model of high-temperature superconductivity. *Nature Physics*, 3(3):184–191, 2007.

Part I

THREE-PULSE SPECTROSCOPY IN COMPLEX SYSTEMS

2

BROADBAND THREE-PULSE SPECTROSCOPY

2.1 MOTIVATION

Time-resolved optical techniques are a well-established tool to study a wide variety of ultrafast non-equilibrium dynamics in atoms, molecules and solids. In a standard pump-probe experiment, the sample under exam is photo-excited by an intense ultrashort pulse (pump) and the subsequent dynamical response is measured by a second, much weaker pulse (probe), properly delayed in time. To improve the temporal resolution, considerable effort has been put in the last decades in developing sub-picosecond sources, whose implementation enabled the investigation of extraordinarily fast processes, such as electron relaxation, charge transfer dynamics and vibrational coherence [2, 3, 4, 5]. Furthermore, the increasing spread of ultrafast optical parametric amplifiers (OPAs), and solutions based on non-linear optical processes in general, enabled a high frequency tunability of the pulsed laser source, so that optical properties of matter can be now probed from the THz to the XUV spectral range, even at high repetition rates [6, 7, 8, 9].

The possibility of properly tuning the energy of the photo-excitation opened up new applications in the field. If the exciting pulse can be chosen to be on resonance with specific properties of the sample under study, different degrees of freedom can be selectively perturbed and monitored. This has a tremendous impact on femtochemistry (where source tunability allows to specifically target electronic transitions and/or molecular vibrations, for instance), but also in condensed matter physics, where there is ample evidence that changing the pump frequency can lead to unexpected phenomena, for example in unconventional superconductors [5, 10, 11, 12].

The photon energy of the probe is also a crucial parameter of the experiment. In order to gain as much information as possible, a broad tunability of the probe is desirable to investigate relevant optical transitions occurring at different wavelengths. While the most intuitive approach would consist in acquiring pump-probe time-traces using a quasi-monochromatic probe beam and systematically changing the probing photon energy, this protocol requires long measuring times and potentially leads to altered measuring conditions, both in terms of laser system stability and sample environment. This has motivated the employment of broadband probe pulses that can encode the sample response over a wide wavelength window, and that can be generated either directly from dedicated OPA systems [13], via photonic

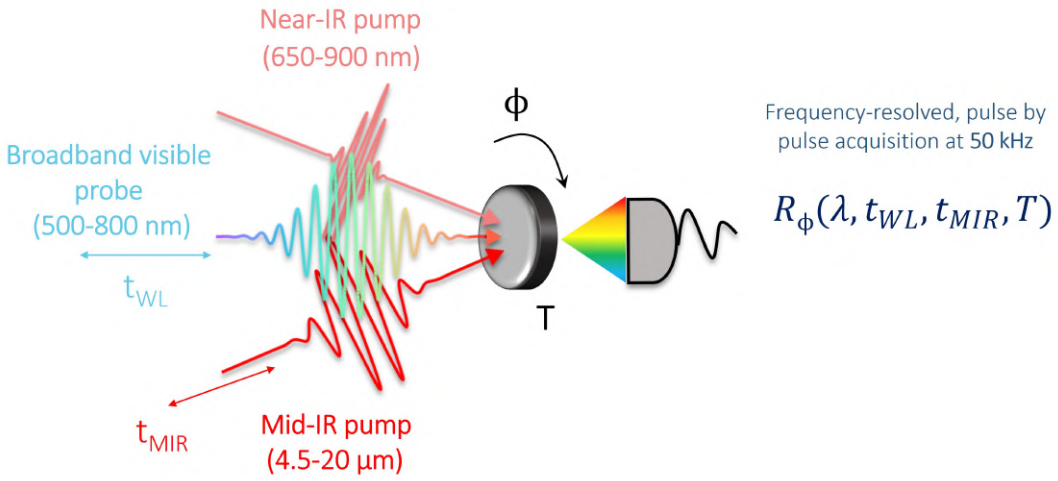

Figure 2.1: **Conceptual idea of the three-pulse experiment.**

crystal fibres [14, 15] or self-phase modulation in appropriate transparent crystals [16, 17, 18, 19, 20]. From an electronic point of view, this has stimulated interest in engineering multichannel detection systems (based either on Si or GaP and PbSe, for instance) providing at the same time a sufficiently high number of pixels to ensure an adequate spectral resolution, and high frame rates to keep up with the increasing delivering rate of current pulsed sources. In this respect, advances in complementary metal oxide semiconductor (CMOS) and charge-coupled device (CCD) technology, enabling image sensors whose pixel readout can be as fast as 50 MHz, boosted the implementation of pump-probe schemes that can perform single-pulse acquisition at high repetition rates [21, 22, 23, 24].

In spite of the impressive variety of phenomena that can be investigated by simply adjusting the photon energy of the pulses involved, a fundamental limitation of standard pump-probe experiments is that they just allow to witness the dynamics of the energy redistribution triggered by the photo-excitation, without the possibility of actively controlling it. This liability inherently lies in the measuring procedure itself: the pump pulse that injects excitations in the sample and is meant to drive the system to off-equilibrium conditions (not adiabatically reachable otherwise), is the same pulse involved in the pump-probe scheme used to measure the effects of the perturbation. The pump-probe response is then embedded with both the order parameter dynamics and the energy relaxation processes, and these two contributions cannot be disentangled. In order to directly exert control and transiently shape the optical properties of matter, it is then crucial to decouple the photo-excitation from the measuring procedure. This has been attempted using a multi-pulse technique to study the emergence of superconducting and charge-density-wave order [25, 26, 27], by using a combination of three quasi-monochromatic pulses, all centered at 800 nm: a first, very intense pulse initially destroys the ordered state and then the subsequent dynamical evolution is monitored by a weaker pump-probe sequence.

2.1.1 *Visible pump–mid infrared pump–broadband probe: a three-pulse setup*

During my PhD project, we have developed a versatile setup to implement a three-pulse scheme to perform non-equilibrium broadband optical spectroscopy. The unique feature of our technique consists in combining, in the very same measurement, two pump pulses having tunable photon energy in two different regions of the electromagnetic spectrum: the first beam can be tuned in the visible range (650-900 nm) to be resonant with the electronic degrees of freedom of the material, while the second one spans the mid-infrared (MIR) region (4.5-20 μm) thus covering low-energy excitations (Figure 2.1). The visible and MIR responses can be either singled out or jointly analysed, allowing for a direct and selective control over different degrees of freedom of the sample and their possible coupling. The system is probed by a supercontinuum white-light (500-800 nm) whose referenced single-pulse detection is enabled by a novel, custom-made acquisition system based on an analog-to-digital converter (ADC) and a field-programmable gate array (FPGA) acquiring up to 50000 spectra/s. The setup has been optimized to perform systematic transient reflectivity or transmittivity studies on crystalline samples over a wide range of temperatures (T = 33-300 K) and sample azimuthal orientations (ϕ = 0-360°).

In the following, we will describe the experimental setup and its characterization. In particular, we will focus on the data structure and illustrate in detail the preliminary analysis of the raw data. This discussion will set the basis for the following chapters in which the three-pulse technique is employed. Finally, we will present a set of transient reflectivity measurements on a slightly underdoped sample of $Bi_2Sr_2Y_{0.08}Ca_{0.92}Cu_2O_{8+\delta}$ (UD Y-Bi2212) across the superconducting phase.

2.2 EXPERIMENTAL SETUP

A block diagram of the optical setup is shown in Figure 2.2. The laser source consists of a Non-Collinear Optical Parametric Amplifier (Orpheus-N by Light Conversion) and a Twin Optical Parametric Amplifier (Orpheus TWIN by Light Conversion). Both systems are pumped by the Pharos Laser (Light Conversion) which delivers 400 μJ pulses with 1.2 eV photon energy (290 fs). The NOPA is pumped with 40 μJ/pp, while the remaining 360 μJ/pp pump the Twin OPAs. The repetition rate of the laser source is tunable from 50 kHz down to single shot using a built-in pulse-picker.

The NOPA output is tunable from a minimum of 650 nm to a maximum of 900 nm and delivers pulses shorter than 25 fs on the entire range. The carrier envelope phase stable MIR pump is obtained through difference frequency generation in a GaSe crystal by mixing the outputs of the Twin OPAs and is tunable from 4.5 to 20 μm.

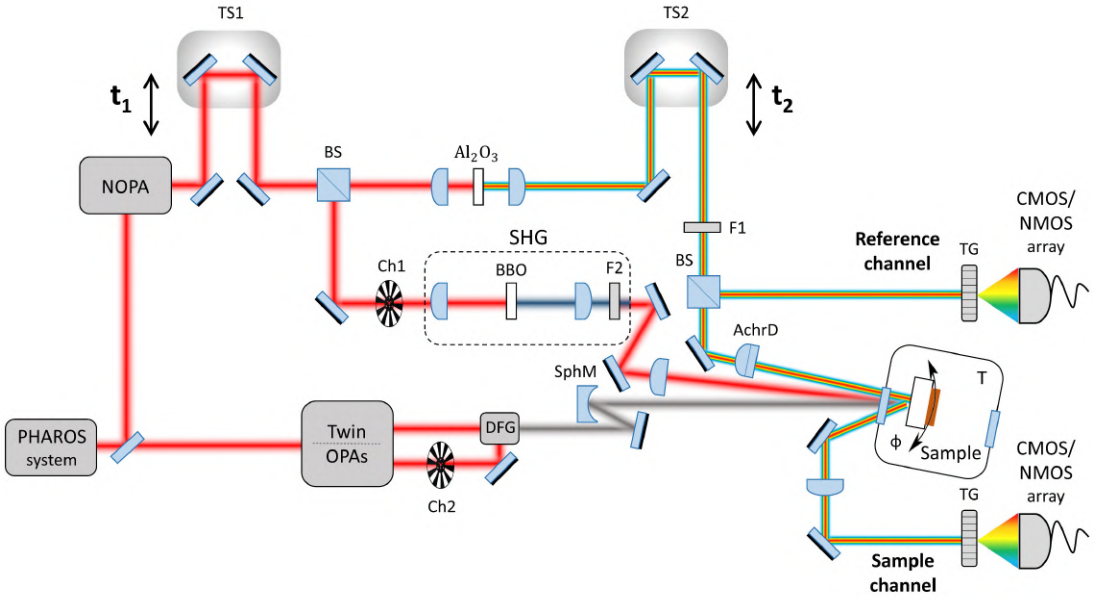

Figure 2.2: **Sketch of the three-pulse setup.** A detailed description of the optical arrangement and the labels assigned to the optical elements is in the text.

2.2.1 *Nonlinear optical phenomena*

The large tunability of our setup - which spans from the visible to the MIR region of the electromagnetic spectum - relies on the implementation of several stages of nonlinear optical processes. When ultrashort pulses interact with matter, the amplitude of the peak electric field is easily high enough for nonlinear phenomena to occur. The linear relation between the electric field ($\tilde{E}$) and the induced polarization ($\tilde{P}$) that we usually experience in our daily life is then replaced by a more general expression in which the higher-order terms become relevant:

$$\tilde{P}_i = \epsilon_0 \chi^{(1)}_{ij} \tilde{E}_j + \epsilon_0 \chi^{(2)}_{ijk} \tilde{E}_j \tilde{E}_k + \epsilon_0 \chi^{(3)}_{ijkl} \tilde{E}_j \tilde{E}_k \tilde{E}_l + \ldots \tag{2.1}$$

where $\hat{\chi}^{(n)}$ is the n-th order nonlinear susceptibility $n+1$-rank tensor. As an immediate effect of Equation 2.1, nonlinear media are characterized by a mixing of different electric fields components. This enables the possibility of engineering suitable experimental conditions for modifying the spectral content of an initial, very intense, quasi-monochromatic light source.

We will focus in the following on the second-order term of Equation 2.1 that gives rise to phenomena such as photon up- and down-conversion, that are used to generate the near-IR and the MIR pumps in our setup. We will then discuss the third-order processes in dispersive media that, by broadening the spectral content of the impinging pulse, enable the generation of the white-light supercontinuum probe.

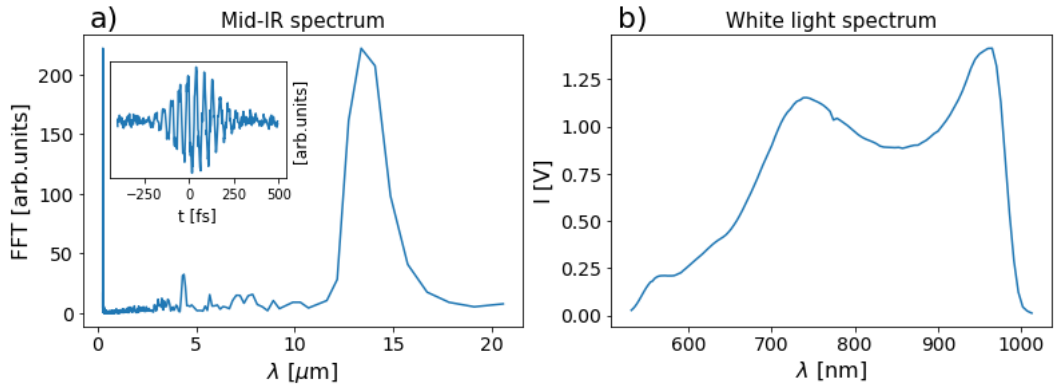

Figure 2.3: **Typical broadband probe and MIR pumps obtained through nonlinear processes. a)** MIR generation @14 μm in a GaSe crystal measured by a Michelson interferometer. The inset shows the interferogram acquired, while its Fourier transform is plotted in the main panel. **b)** White-light generation in a 6 mm thick sapphire crystal from a 1030 nm beam.

SECOND-ORDER NONLINEAR PROCESSES In order to derive the nonlinear effects arising from the second-order term, let us consider an electric field that, before the interaction with the nonlinear medium, contains two spectral components $\tilde{E}(t) = E_1 e^{-i\omega_1 t} + E_2 e^{-i\omega_2 t} + c.c.$. For the sake of clarity, we will drop the indices in Equation 2.1 and consider the one-dimensional problem [28]. The resulting second-order polarization is:

$$\tilde{P}^{(2)}(t) = \epsilon_0 \chi^{(2)} \left[\underbrace{E_1^2 e^{-2i\omega_1 t}}_{\text{SHG}} + \underbrace{E_2^2 e^{-2i\omega_2 t}}_{\text{SHG}} + \underbrace{2E_1 E_2 e^{-i(\omega_1+\omega_2)t}}_{\text{SFG}} + \underbrace{2E_1 E_2^* e^{-i(\omega_1-\omega_2)t}}_{\text{DFG}} + c.c. \right] + 2\epsilon_0 \chi^{(2)} \left[\underbrace{E_1 E_1^* + E_2 E_2^*}_{\text{OR}} \right] \tag{2.2}$$

$\tilde{P}^{(2)}(t)$ acts as the source for the electric field that, depending on the terms in Equation 2.2, will have a different time dependence. There will be two terms oscillating at twice the incoming original frequencies ω_1 and ω_2 that are called *second harmonic generation* (SHG). A component will oscillate at the sum of the two incoming frequencies $\omega_1 + \omega_2$ and is referred to as *sum frequency generation* (SFG). An additional term will oscillate at a frequency which is equal to the difference between the original ones $\omega_1 - \omega_2$ and that is known as *difference frequency generation* (DFG). Finally, some terms do not oscillate in time and give rise to the *optical rectification* (OR) process. The SHG and SFG are usually addressed as photon up-conversion because the resulting frequency is higher than the incoming one; the DFG process is also called photon down-conversion.

Usually, no more than one of these four processes will occur with an appreciable intensity. In order to enhance the desired frequency component, specific phase matching conditions must be met by carefully choosing the polarizations of the incoming beams and the orientation of the nonlinear crystal. In our setup, we generate the MIR pump by DFG in a GaSe crystal, starting from two tunable (0.5-0.8 eV) near-infrared pulses that are in turn obtained via optical parametric amplification. In Figure 2.3a, we plot a typical DFG spectrum measured through a home-made Michelson interferometer, provided with a MCT (Mercury-Cadmium-Telluride) detector (up to 18 μm).

WHITE-LIGHT GENERATION The generation of white-light supercontinuum consists in the spectral broadening of an original light pulse, as illustrated in Figure 2.3b. This phenomenon is mediated by third-order nonlinear processes which have the major consequence of making the refraction index dependent on the intensity $I(t)$ of the impinging light pulse [28]:

$$n(I) = n_0 + \tilde{n}_2 I(t) \tag{2.3}$$

This dependence has two effects that both concur to the generation of broadband pulses. Firstly, since the transverse profile of light pulses is not constant (usually Gaussian), the transverse dependence of $n(I)$ will produce an effective positive lense. As the beam propagates through the nonlinear medium, it collapses into a filament with high intensity. This process is known as *self-focussing* (SF). When a stable filament is produced, other nonlinear processes set in, that are magnified by the SF effect. The one that is directly responsible for the white-light generation is the *self-phase modulation* (SPM), which causes an instantaneous frequency change in the electric field.

In order to understand the temporal and spectral structure of the resulting beam, we will use a simple model in which the beam profile is assumed to be Gaussian [29]:

$$I(t) = I_0 e^{-\frac{t^2}{\tau^2}} \tag{2.4}$$

The intensity-dependent refractive index induces a variation of the optical path through the medium, having thickness d:

$$\Delta L = \tilde{n}_2 d I(t) = \tilde{n}_2 d I_0 e^{-\frac{t^2}{\tau^2}} \tag{2.5}$$

which in turn causes a time-dependent dephasing:

$$\Delta\phi = -\frac{2\pi\Delta L}{\lambda_0} \tag{2.6}$$

Since the angular frequency is simply defined as the time-derivative of the phase, it follows that the instantaneous frequency too experiences a variation:

$$\Delta\omega(t) = \frac{\partial\Delta\phi}{\partial t} = \frac{4\pi\tilde{n}_2 d I_0}{\lambda_0}\frac{t}{\tau^2}e^{-\frac{t^2}{\tau^2}} \tag{2.7}$$

If the phase envelope is much longer than the optical cycle ($t/\tau^2 \ll 1$), the instantaneous frequency can be approximated to:

$$\omega(t) \propto \omega_0\left(1 + \tilde{n}_2 d\frac{t}{\tau^2}\right) \tag{2.8}$$

This equation implies that each spectral component experiences a broadening which is time-dependent. The resulting white-light pulse is *temporally chirped*: the low frequencies travel in the leading edge of the pulse, while the high frequencies travel in the tail. The temporal structure of the white-light probe is clear in our broadband pump-probe measurements: the temporal overlap is frequency-dependent and a post-processing correction of the chirp is carried out (Section2.4.1).

2.2.2 *Optical arrangement*

As sketched in Figure 2.2, the NOPA output is split by a 70/30 beam splitter: most of the power is used to pump the sample and the remaining part to generate the white-light probe. The setup has been designed to work in two main configurations: one can either choose to pump the system directly using the light pulses exiting the NOPA or exploit SHG to achieve higher photon energies. In the latter case, the pump beam is obtained by focusing the NOPA beam in a 0.7 mm thick type I β-Barium Borate (BBO) crystal, optimized for SHG with 900 nm. After collimation, a bandpass coloured filter (F2, 350-700 nm) filters out the remaining near-IR radiation and the blue beam is then focused on the sample surface.

The white-light probe is generated via SPM by focusing (5 cm focal length) the beam in a 2 mm thick sapphire (Al_2O_3) crystal. A stable white light regime is reached by tuning an iris placed in front of the focusing lens. A shortpass filter (F1, edge at 800 nm) filters out the residual component of the generating near-IR light. The final spectrum of the supercontinuum white-light ranges from about 500 to 800 nm. In order to improve the white-light pulse-to-pulse stability, we have introduced a reference channel in the detection scheme. Before impinging the sample, the probe beam is split, and the reflected part (a pristine copy of the probe beam) is routed towards a twin detector to be simultaneously acquired. The transmitted probe beam is instead focused on the sample using an achromatic doublet to avoid chromatic aberrations.

The MIR pump is obtained by filtering the DFG output through a germanium window which absorbs photons with energy above 0.3 eV. The beam is then focused on the sample by means of a silver spherical mirror.

Table 1: Typical performance of the setup.

Pulse	Tunability	Energy per pulse	Time duration	Polarization
Visible pump	650-900 nm (or SHG available)	<1.4 μJ <200 nJ (SHG)	35 fs	Tunable
MIR pump	4.5-20 μm	160 nJ (@17 μm) 1.4 μJ (@9 μm)	150 fs	Vertical
Broadband probe	500-800 nm (gen. @860 nm)	<6 nJ	1.5 ps[1] (chirped)	Tunable

The focus size of the three beams at the sample surface can be measured either by the knife-edge method (5 μm accuracy) or by directly placing a pyro-camera at the sample position. Typical values of the full width at half maximum of the three beam profiles are 100 μm for the visible pump, 150 μm for the MIR pump and 30 μm for the probe. We estimated the visible pump temporal length to be $\sim$35 fs via SHG-FROG. When SHG configuration is used, the visible pump duration slightly increases to reach $\sim$50 fs (measured by cross-correlation measurements). The MIR pump time duration is wavelength-dependent and shorter than 150 fs on the entire energy range. By default, the MIR pump is vertically polarized. The polarizations and the intensity of the probe and the visible pump can be independently adjusted using two pairs of half-wave retardation plates and polarizers. The setup has been designed to work in a non-collinear geometry: the probe beam impinges almost normally to the sample surface; the visible pump propagation direction makes an angle of about 10° with the probe and the MIR beam impinges onto the sample surface at an angle of 20°.

The setup is provided with two translation stages to independently control the time delay between the three beams. A first translation stage (TS1) is placed at the NOPA output, before the first beam splitter, so that TS1 tunes the delay between the two pumps, without affecting the delay between the probe and the visible one. The latter is controlled by a second translation stage (TS2) which modifies the optical path of the white-light probe only. In a standard experiment, for each given position of TS1, a full scan of TS2 is performed.

Finally, we report in Table 1 the standard optical parameters which summarize the performance of the setup.

2.2.3 *Sample environment*

The sample is mounted in a closed cycle liquid helium cryostat (DE 204 by Advanced Research Systems). The cryostat expander is supported by a custom-made structure fixed to the laboratory floor; the cold head is instead fixed to the optical bench. This design allows to efficiently isolate the sample from the strong vibrations experienced by the expander. The custom-made cryostat structure is compatible with adjustments along the x, y and z directions.

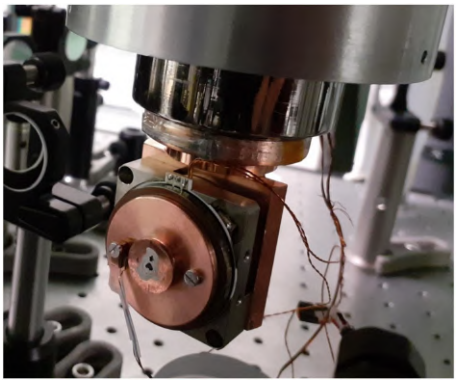

Figure 2.4: **Sample environment.** Single-crystal UD Y-Bi2212 samples mounted on the piezo-electric rotator. A thermocouple is fixed in close proximity of the sample by a small copper clamp.

The sample holder consists of a copper plate which is directly connected to the cold head. On top of this plate, we fixed a piezo-electric rotator (Attocube, ANR240) which allows a rotation of the sample by the azimuthal angle ϕ. Samples are finally mounted on a small copper disk – fixed to the moving part of the rotator - using fast-drying silver paint. We show a picture of the final sample arrangement in Figure 2.4. A thermocouple, fixed in the proximity of the sample, is used to directly measure the sample temperature. Indium foils are interposed at each metallic interface to improve the overall thermal conductivity.

The structure in Figure 2.4 is enclosed in a vacuum chamber that allows optical access through a front 1-inch window. The composition of the window is chosen according to the photon energies of the three beams involved. Because of the presence of the mid-infrared pump, we have chosen to mount a polycrystalline diamond window, which is 0.5 mm thick ($\sim$ 70% transmission). The vacuum chamber is provided with other identical apertures, in correspondence of each chamber's face. This provides the possibility of performing transmittivity measurements, if required. In this respect, it is worth mentioning that the piezo-electric rotator has a hole in the middle so that transmittivity measurements can be performed without compromising the azimuthal degree of freedom.

Vacuum conditions are matched via a standard turbo pumping station (Pfeiffer, HiCube 80 Eco). Pressures as low as 10^{-7} mbar can be reached when working at ambient temperature; at cryogenic temperature, the usual working pressure is 10^{-8} mbar. While the minimum attainable temperature is 12 K when the sample is directly fixed on the first copper plate (so very close to the cold head), it increases up to 33 K when using the piezo-electric rotator. A temperature controller provided with a feedback circuit enables the user to remotely modify the temperature of the sample, so that a full temperature scan, i.e. the acquisition of a simple pump-probe trace for each temperature within a given range, can be performed.

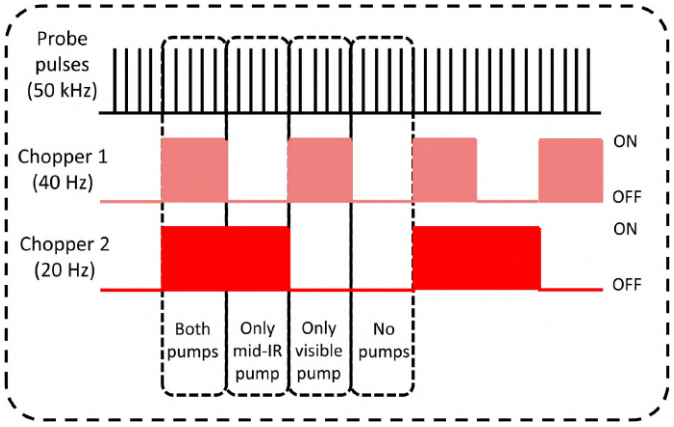

Figure 2.5: **Differential acquisition.** A sketch of the choppers' operation designed to reference the acquisition in different pumping conditions.

2.3 DIFFERENTIAL ACQUISITION OF BROADBAND PULSES AT 50 KHZ

2.3.1 *Chopped detection*

The reflected (or transmitted) probe beam is collimated by a lens and routed towards the acquisition part, designed for a frequency-resolved, pulse-by-pulse detection. The beam is dispersed by a transmission blazed grating (TG, in Figure 2.2) and then focused on the detector. According to the experimental needs, two options of detectors are available: a complementary metal oxide semiconductor (CMOS) linear image sensor (Hamamatsu S11105 [31]) made up of 512 pixels, or a negative channel metal oxide semiconductor (NMOS) linear image sensor (Hamamatsu S8380-128Q [32]) provided with 128 pixels. The detector acquisition is synchronized with the laser repetition rate and can run up to 50 kHz (when CMOS are needed) or up to 5 kHz (when NMOS are installed). A detailed description of the acquisition system and electronics required to achieve this performance is given in Subsection 2.3.2. A new wavelength calibration of the arrays is performed every time the optical alignment is adjusted. To do so, a common coloured filter having distinctive transmittivity features across the white-light bandwidth can be used (FGB67 by Thorlabs, for instance). The filter is usually placed after the collimating lens behind the sample; a spectrum averaged over thousands of pulses is acquired using first the array photodiode detector, and after an already calibrated fiber spectrometer. The final calibration is then achieved by interpolation of the two spectra.

To improve the detection of the signal, two choppers have been inserted along the optical paths of the two pumps. The first chopper (Ch1 in Figure 2.2), periodically blocking the visible pump propagation, runs at 40 Hz, while the second one (Ch2 in Figure 2.2) runs at 20 Hz. The choppers' controllers are both referenced with the same square wave generator, so that the mechanical rotations of the blades are automatically synchronized. A simplified sketch of the chopping scheme is shown in Figure 2.5. Each single probe pulse recorded by the photodiode arrays (sample and

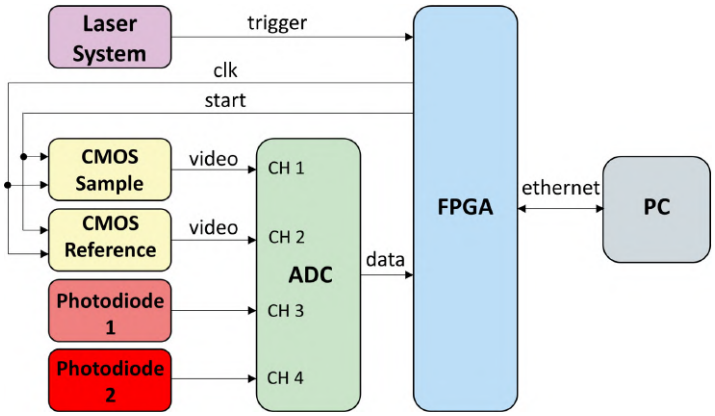

Figure 2.6: **Acquisition scheme.** Schematic representation of the acquisition electronics synchronized with the laser repetition rate.

reference channels) can fall into one of the four dashed boxes drawn in Figure 2.5. In order to sort the pulses according to this scheme, we use two single-photodiode detectors (PhD1 and PhD2). The photodiodes are properly placed to intercept a back-reflection or a residual transmission of the two pump beams, and their signals are digitized by the ADC (CH 3 and CH 4 in Figure 2.6). These signals give a feedback about the chopper status (ON/OFF) and ultimately provide a tool to assign each probe pulse detected by the array detectors with a label, indicating which pump beam has interacted with the sample prior to its arrival.

2.3.2 *Acquisition system*

A dedicated electronic setup has been developed by the Detectors & Instrumentation Laboratory of Elettra Sincrotrone Trieste. A schematic representation of the system is shown in Figure 2.6.

As highlighted above, the setup is provided with two pairs of photodiode arrays, based on CMOS or NMOS linear image sensors. The main difference between the two detection systems lies in the maximum video data rate (and thus the single-shot repetition rate) that can be achieved: while the NMOS data rate is limited to 2 MHz, the CMOS arrays belong to the high-speed Hamamatsu sensor family with video data rate as high as 50 MHz. We will limit here our discussion to the CMOS arrays only, as their acquisition at 50 kHz is the most challenging to handle from an electronic point of view. The same scheme can be adapted to the NMOS detection, with the caveat that an additional external amplifier (Hamamatsu C7884 series) is needed and the clock pulse frequency has to be adjusted.

The CMOS sensors are mounted on custom-made boards. The core part of the acquisition system is the FPGA (Arria 10 GX by Intel) which controls the CMOS sensor operation, coordinates the ADC acquisition and handles data transfer to the PC through an Ethernet link. More precisely, the FPGA continuously generates the 50 MHz clock needed by the sensor and waits for the trigger pulse periodically generated

by the laser system (20 μs, 50 kHz). The start pulse generation is delayed with respect to the trigger, and this delay can be dynamically set in order to synchronize the acquisition with the probe pulse. A rising edge on the CMOS start pin sets the simultaneous integration of all pixels. At falling edge, the collected charge, converted into a voltage through a charge-sensitive-amplifier (CSA), is transferred to the hold circuit and the internal shift register begins to sequentially provide data on video output.

In order to perform referenced measurements and to acquire the output of the two photodiodes (PhD1 and PhD2), we decided to utilize a 4-channel 16-bit analog-to-digital converter (AD9653 by Analog Devices). The sampling frequency has been fixed to 100 MHz and it is generated by a dedicated low-jitter clock generator (SI5340 by Silicon Labs). Therefore, for each analog value provided by CMOS output we acquire 2 samples, thus obtaining 1024 samples.

An appropriate Verilog code takes care of every task: generation of CMOS timing signals, DAC programming, synchronous data acquisition from ADC at every trigger event, storage of captured events in RAM and transmission of collected data through a User Datagram Protocol (UDP) Ethernet link, are performed using a dedicated FPGA hardware. Even if the intrinsic parallel architecture of the FPGA allows to treat large amounts of data sets and their transmission, a great effort has to be done in order to correctly receive and store them. In fact, considering a stream of 1024 16-bit samples multiplied by four channels with a laser repetition rate of 50 kHz, the resulting data rate is 3.3 Gb/s (410 MB/s). A typical point-to-point 1 Gb/s Ethernet connection between FPGA and PC and a standard mechanical hard disk drive cannot handle such a high data rate, so we moved to 10 Gb/s Ethernet and SSD (Solid State Disk) drives. More details on the CMOS synchronous operation and the data transmission can be found in ref. [33].

2.4 DATA ANALYSIS

We underlined above that our setup is suitable for both reflection and transmission geometries, depending on specific requirements set out by the sample under exam (bulk crystal, thin films, solutions). Here, for simplicity, we restrict our discussion to transient reflectivity measurements only.

The measured quantity in our experiment is the $-i^{th}$ frequency-dispersed reflected probe pulse $R_i^s(\lambda, t_1, t_2, T)$, namely the intensity recorded by the linear array detector along the sample channel at each pixel, for a given delay t_1 between the two pumps, a given delay t_2 between the white-light probe and the visible pump, and a given sample temperature T measured by the thermocouple. In Figure 2.7a, we provide a simple scheme which summarizes the degrees of freedom of the measurement and their physical meaning. We recall that we also simultaneously acquire a copy of the pristine probe pulse along the reference channel, $R_i^r(\lambda, t_1, t_2, T)$. Our optical

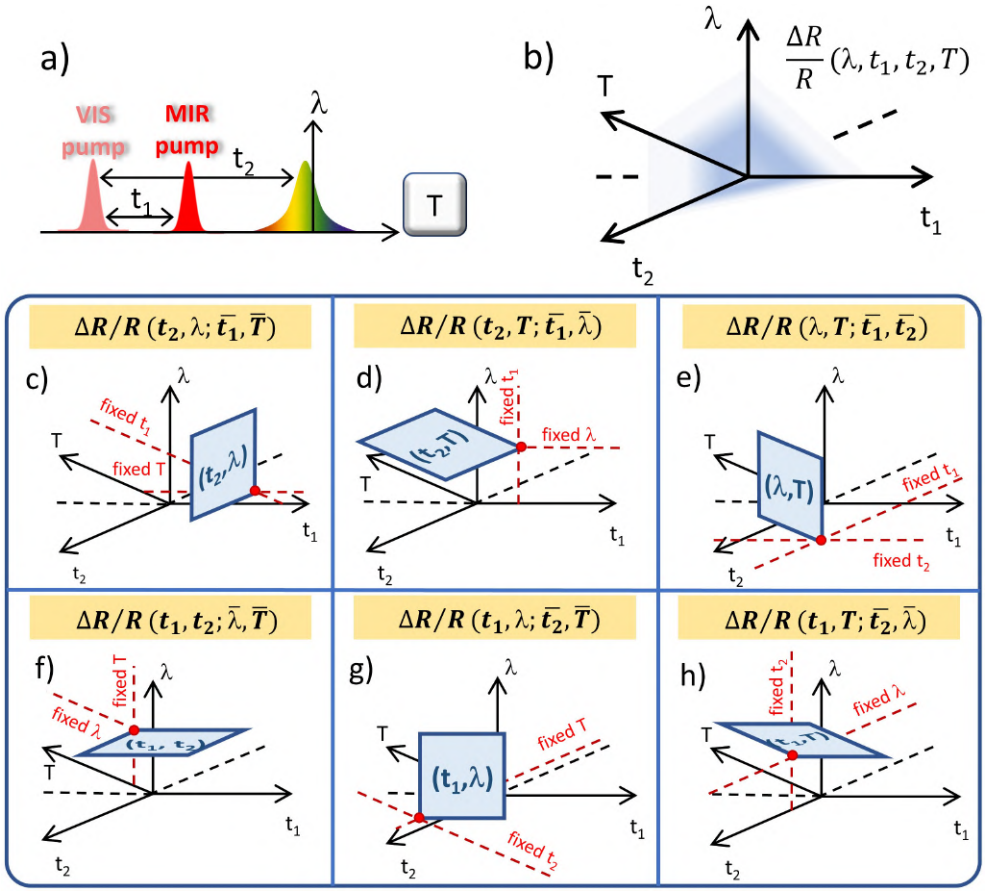

Figure 2.7: **Details of the three-pulse data structure. a)** Depiction of the temporal arrival of the three pulses at the sample (at a given temperature T) and their relative time delays. We highlight that t_1 is < 0 (> 0) when the MIR pulse interacts with the sample before (after) the arrival of the visible pump. **b)** Relevant degrees of freedom of the four-dimensional hypercube representing our dataset. **c-h)** Two-dimensional slices of the full dataset obtained by fixing two parameters at a time; there are six possible combinations. The transient reflectivity can be displayed as function of time delay and wavelength of the probe (c), time delay of the probe and temperature of the sample (d), probe wavelength and temperature (e), relative delay between the two pumps and probe delay (f), probe wavelength (g) and sample temperature (h).

observable is then the referenced average differential reflectivity change, defined as follows:

$$\frac{\Delta R}{R}(\lambda, t_1, t_2, T) = \frac{\sum_{i=1}^{N} R_i^{s,P}(\lambda, t_1, t_2, T)}{\sum_{i=1}^{N} R_i^{r,P}(\lambda, t_1, t_2, T)} - \frac{\sum_{i=1}^{N} R_i^{s,U}(\lambda, t_1, t_2, T)}{\sum_{i=1}^{N} R_i^{r,U}(\lambda, t_1, t_2, T)} \tag{2.9}$$

where N is the number of pulses over which the integration is performed, and the superscripts P, U refer to "pumped" and "unpumped" probe pulses, respectively. By "unpumped" we refer to those pulses reflected by the sample when both pumps are blocked by the choppers (pulses falling in the rightmost dashed box in Figure 2.5). Furthermore, we report that each single curve in Equation 2.9 is systematically corrected for a background spectrum $R_{BG}(\lambda)$ which is acquired before each measurement by blocking the probe beam and let the two pumps open. The background subtraction serves the purpose of cleaning the acquired spectra from any scattered light coming from the pumps and from the environment.

The structure of our data is therefore a four-dimensional hypercube, as depicted in Figure 2.7b, where all the four axes are orthogonal to each other. Given the big amount of data, the most straightforward way to visualize the outcome of measurement consists in dissecting the hypercube into two-dimensional slices, by fixing two parameters at a time.

We show in Figure 2.7-h all the six possible combinations that can be computed in the four-dimensional space. We will refer to these schemes in the following, and use the notation $\Delta R/R(w, x; \bar{y}, \bar{z})$, where (w, x) are the variables whose dependency is studied and $(\bar{y}, \bar{z})$ the ones that have been kept fixed.

Recalling that we perform a sorting of the probe pulses according to the chopping scheme in Figure 2.5, there are three different typologies of "pumped" pulses, so that, for each single measurement, we can construct three different four-dimensional maps: i) a map which contains a two-colour signal only due to the effect of the visible pump (VIS-MAP); ii) a map displaying the two-colour signal due to the interaction of the sample only with the MIR (MIR-MAP); iii) a map showing the effect of applying both pumps (PP-MAP). For each of the three types of maps, an average time-independent signal is calculated over the negative-t_2 region and systematically subtracted. It is worth mentioning that, even though all three typologies of maps are technically four-dimensional hypercubes, the relative delay between the two pumps (t_1) is a relevant degree of freedom only for the PP-MAP, which actually contains a three-colour signal. Consequently, the analysis of the VIS-MAP and the MIR-MAP will not require the computation of the three two-dimensional slices for which t_1 is a variable parameter (i.e. combinations from f to h in Figure 2.7).

We recall that the novelty of our setup consists in being able to uncover possible modifications in the dynamics of the signal due to the combined action of the visible and the MIR pumps. In order to access this information, we perform a point-to-point subtraction between the PP-MAP (which contains the effects of both of them), and the VIS-MAP and MIR-MAP (which contain the effects of the two pumps when they

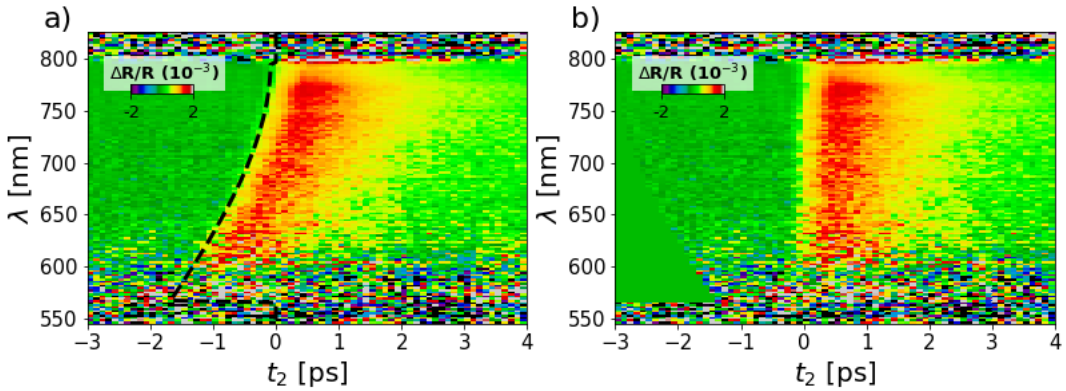

Figure 2.8: **Example of white-light chirp correction. a)** Referenced VIS-MAP measured in UD Y-Bi2212 computed as in Equation 2.9. The black dashed line is the zero-time-delay vector obtained through a polynomial fit of the onset of the signal at the temporal overlap. **b)** Corrected map.

act independently on the sample). We will refer to this new four-dimensional map as "differential map" (DIFF-MAP) in the following.

Finally, our setup is characterized by an intrinsic noise level of 10^{-4} rms over an integration time of 1 s. This signal-to-noise ratio can be further improved statistically by either increasing the number of shots to be averaged over or repeating each experiment many times. Both choices come obviously at the cost of significantly reducing the speed of the measurement. The robust experimental stability of our apparatus, though, easily enables performing experiments lasting even several hours.

2.4.1 *White-light chirp correction*

Since no physical correction of the chirp of the broadband white-light pulses was performed (Equation 2.8), each map has to be post-processed to compensate for the dispersion. After white-light generation, we estimate the probe beam's temporal length to be about 1.5 ps at the sample surface. We stress that, as we are frequency-resolving the signal, the temporal resolution of the setup for a given probe frequency is significantly better than 20 fs [30]. The correction is performed numerically by shifting each line in the four-dimensional dataset $\Delta R/R(\lambda, t_1, t_2, T)$ along the t_2-axis. The amount of the shift is quantified by defining a zero-time-delay vector (one value for each wavelength) by looking at the VIS-MAP, as illustrated in Figure 2.8. We use the onset of the two-colour signal in the VIS-MAP as a reference point for the temporal overlap between the visible pump and the broadband probe[2].

2 We highlight that additional care must be eventually taken when measuring a transmittivity signal, since a further correction must be performed to compensate for the velocity mismatch inside the sample.

2.4.2 *Benchmark measurements on UD Y-Bi2212*

To test the potential of our setup, we performed transient reflectivity measurements on a single crystal of slightly underdoped $Bi_2Sr_2Y_{0.08}Ca_{0.92}Cu_2O_{8+\delta}$ (Y-Bi2212). The crystal has been mounted so that the probe's propagation axis is almost perpendicular to the ab-plane of the unit cell (i.e. the Cu-O planes). In the experiment, we first pump the sample using pulses centered at 1.44 eV (860 nm), and then we further pump it with MIR excitations at 70 meV ($\sim$ 17.5 μm). In order to cover the relevant transitions in the samples, we ran a temperature scan starting from 74 K (superconducting phase) up to 144 K, which is reasonably close to the presumed transition temperature T* at our doping.

As detailed in the previous subsection, one single measurement is sufficient to obtain a great wealth of information. The results of the experiment on UD Y-Bi2212 are summarized in Figure 2.9. In Figure 2.9a-c, we provide simple schemes to clarify which pulses are involved in the colour-maps shown and give details on the time structure of the measurement. In this specific measurement, we chose to investigate just two time-delays between the pumps, $t_1 = \pm 1$ ps: when t_1=-1 ps, the MIR pump impinges on the sample 1 ps before the arrival of the visible one; conversely, when t_1=+1 ps, the MIR pump arrives 1 ps after. From the physical point of view, this corresponds to two different questions. In the former case, we are interested in the effect that low-photon energy excitations may have on the high-energy dynamics; in the latter case, the situation is reversed, and we investigate whether and how visible pulses can alter the dynamics triggered by low-energy excitations. It is thus clear that measurements of this kind could represent a valuable tool to study the intrinsic coupling between degrees of freedom at different energy scales, that lies at the very core of high temperature superconductivity. The detailed interpretation of this specific measurement and its importance to the physics of cuprates, goes beyond the scope of this discussion and will be addressed in Chapter 3. Here we shall confine the discussion to the capabilities of the setup and to the type of information that can be extracted.

On the first row of Figure 2.9, we display the VIS-MAPs, that is the transient reflectivity colour-coded maps that involve just the action of the visible pump. According to the scheme in Figure 2.7, we dissect the four-dimensional dataset into three different two-dimensional matrices and separately study the dependencies. In Figure 2.9d, we show the wavelength-dependent pump-probe traces associated to the superconducting phase, which is consistent with ref. [34]. A second map can be computed by fixing the wavelength and displaying the temperature dependence, as in Figure 2.9e for λ = 786 nm. The horizontal dashed black line highlights the presumed sample's critical temperature, marking the beginning of the pseudogap phase, which is accompanied by a change in both sign and dynamics of the transient reflectivity. Finally, we display in Figure 2.9f $\Delta R/R$ as function of temperature and probe wavelength for a given time delay, showing that we do observe a wavelength-dependent response mainly in the pseudogap region of the phase diagram.

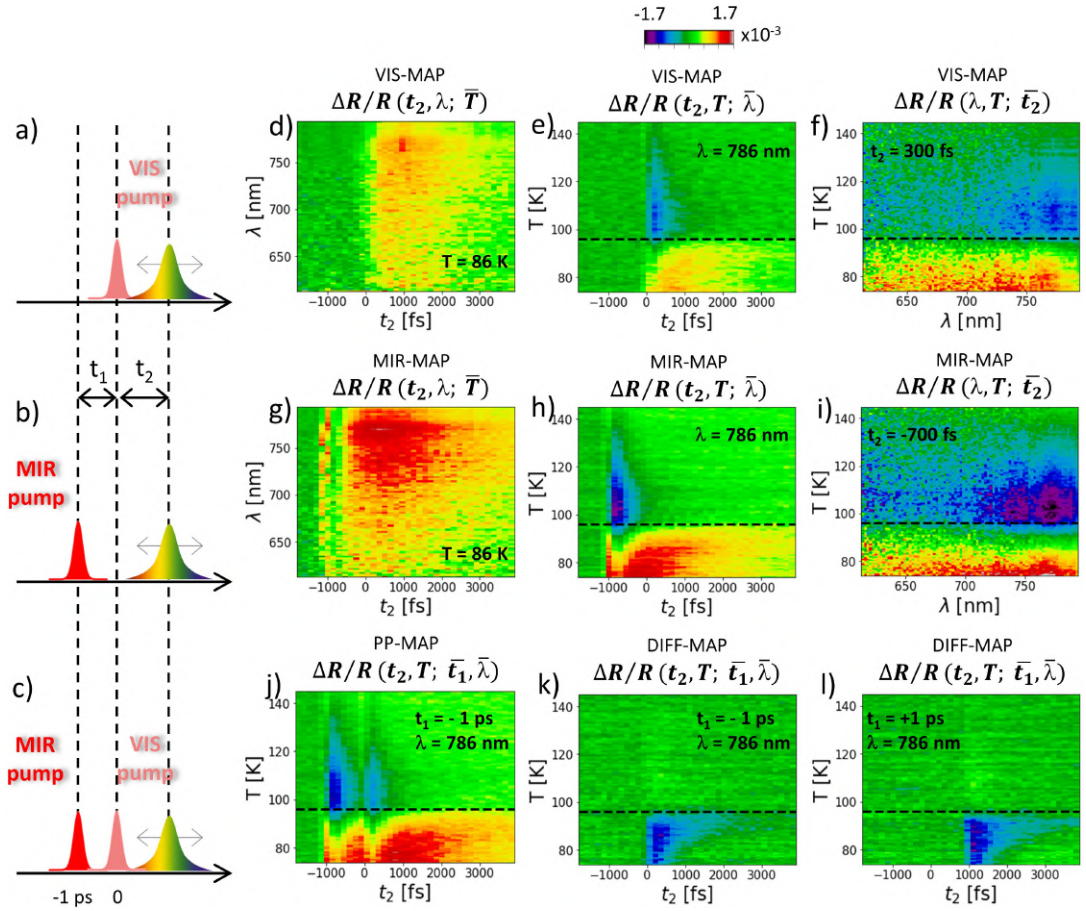

Figure 2.9: **Example of three-pulse data in UD Y-Bi2212. a)**, **b)** and **c)** show a scheme of the pulses involved and their temporal delays. Each scheme refers to the maps that lie in its row. VIS-MAPs (pump-probe signal triggered by the visible pump) are shown in **d)** as function of probe wavelength and temporal delay between the visible pump and the probe at fixed temperature T = 86 K; in **e)** as function of temperature and delay at fixed probe wavelength λ = 786 nm; and in **f)** as function of temperature and probe wavelength at fixed positive delay t_2 = 300 fs. **g)**, **h)** and **i)** follow the same structure as d), e) and f), but they now refer to the MIR pump-probe signal, as shown in b). Note that the dependence on (fixed) t_1 has been dropped in the titles of d-i) as it is not relevant for simple two-colour signals as VIS-MAPs and MIR-MAPs. **j)** is an example of PP-MAP showing the combined time-dependent signal at fixed wavelength λ = 786 nm due to a MIR pump delayed by t_1 = -1 ps with respect to the visible one arriving at t_2 = 0 fs (as pictured in c)). **k)** and **l)** are DIFF-MAPs as function of temperature and delay at fixed wavelength and fixed delay t_2 between the two pumps: the MIR pumps arrives before and after the visible one by 1 ps in k) and l), respectively. Fluences used: ϕ_{VIS} = 40 μJcm^{-2} and ϕ_{MIR} = 100 μJcm^{-2}

The above-discussed structure is the same for the MIR-MAPs in Figure 2.9g-i, with the important difference that now the dynamics is triggered by MIR excitations. By comparing the VIS-MAPs and the MIR-MAPs, clear differences can be spotted that, at least in this measurement, could be attributed to the higher fluence of the MIR pump. Single-colour pump-probe traces (horizontal cuts in Figure 2.9g) are indeed compatible with those observed in ref. [35]. We highlight that Figure 2.9i (and obviously its time dependence, namely cuts at different t_2) represents, to the best of our knowledge, the first MIR pump-broadband probe response ever measured.

In Figure 2.9j, we show the PP-MAP which contains the interaction with both the visible and MIR pumps. Here we show just the two-dimensional cut for a given probe wavelength, as function of time-delay and temperature, but obviously a comprehensive analysis can be carried out according to the scheme in Figure 2.7. It is worth recalling that now a further degree of freedom becomes relevant, namely the relative time-delay of the two pumps, t_1. Figure 2.9j displays just one possible choice of t_1, that is t_1 = -1 ps (as depicted in Figure 2.9c); an additional, similar map must be considered for t_1 = +1 ps, where now the onset of the signal associated to the MIR pulse is shifted to t_2 = 1 ps.

Finally, Figure 2.9k,l show the DIFF-MAPs for $t_1 = \pm 1$ ps, respectively. Again, we limit our discussion to two-dimensional slices at fixed wavelength only. Interestingly, the fact that these maps are not completely zero, is a clear indication that the combined action of the two pumps is not a mere superposition of the signals independently triggered by the visible and MIR pulses. In particular, in both cases, the difference is non-zero below the critical temperature, suggesting that the condensate is mostly affected by the subsequent photo-excitations. This is a hint of an inherent coupling whose nature and dynamics will be discussed in Chapter 3.

REFERENCES

[1] Z Vardeny and J Tauc. Picosecond coherence coupling in the pump and probe technique. *Optics Communications*, 39(6):396–400, 1981.

[2] Jagdeep Shah. *Ultrafast spectroscopy of semiconductors and semiconductor nanostructures*, volume 115. Springer Science & Business Media, 2013.

[3] Ahmed H Zewail. Femtochemistry: Atomic-scale dynamics of the chemical bond. *The Journal of Physical Chemistry A*, 104(24):5660–5694, 2000.

[4] Juan Cabanillas-Gonzalez, Giulia Grancini, and Guglielmo Lanzani. Pump-probe spectroscopy in organic semiconductors: monitoring fundamental processes of relevance in optoelectronics. *Advanced materials*, 23(46):5468–5485, 2011.

[5] Claudio Giannetti, Massimo Capone, Daniele Fausti, Michele Fabrizio, Fulvio Parmigiani, and Dragan Mihailovic. Ultrafast optical spectroscopy of strongly correlated materials and high-temperature superconductors: a non-equilibrium approach. *Advances in Physics*, 65(2):58–238, 2016.

[6] Giulio Cerullo and Sandro De Silvestri. Ultrafast optical parametric amplifiers. *Review of scientific instruments*, 74(1):1–18, 2003.

[7] Christian Bressler and Majed Chergui. Ultrafast X-ray absorption spectroscopy. *Chemical reviews*, 104(4):1781–1812, 2004.

[8] Daniele Brida, Cristian Manzoni, Giovanni Cirmi, Marco Marangoni, Stefano Bonora, Paolo Villoresi, Sandro De Silvestri, and Giulio Cerullo. Few-optical-cycle pulses tunable from the visible to the mid-infrared by optical parametric amplifiers. *Journal of Optics*, 12(1):013001, 2009.

[9] Ryan M Smith and Mark A Arnold. Terahertz time-domain spectroscopy of solid samples: principles, applications, and challenges. *Applied Spectroscopy Reviews*, 46(8):636–679, 2011.

[10] Daniele Fausti, RI Tobey, Nicky Dean, Stefan Kaiser, A Dienst, Matthias C Hoffmann, S Pyon, T Takayama, H Takagi, and Andrea Cavalleri. Light-induced superconductivity in a stripe-ordered cuprate. *Science*, 331(6014):189–191, 2011.

[11] Matteo Mitrano, Alice Cantaluppi, Daniele Nicoletti, Stefan Kaiser, A Perucchi, S Lupi, P Di Pietro, D Pontiroli, M Riccò, Stephen R Clark, et al. Possible light-induced superconductivity in K_3C_{60} at high temperature. *Nature*, 530(7591):461–464, 2016.

[12] F Giusti, A Marciniak, F Randi, G Sparapassi, F Boschini, H Eisaki, Martin Greven, A Damascelli, A Avella, and D Fausti. Signatures of enhanced superconducting phase coherence in optimally doped $Bi_2Sr_2Y_{0.08}Ca_{0.92}Cu_2O_{8+\delta}$ driven by midinfrared pulse excitations. *Physical Review Letters*, 122(6):067002, 2019.

[13] Dario Polli, Larry Lüer, and Giulio Cerullo. High-time-resolution pump-probe system with broadband detection for the study of time-domain vibrational dynamics. *Review of Scientific Instruments*, 78(10):103108, 2007.

[14] John M Dudley, Goëry Genty, and Stéphane Coen. Supercontinuum generation in photonic crystal fiber. *Reviews of modern physics*, 78(4):1135, 2006.

[15] Federico Cilento, Claudio Giannetti, Gabriele Ferrini, Stefano Dal Conte, Tommaso Sala, Giacomo Coslovich, Matteo Rini, Andrea Cavalleri, and Fulvio Parmigiani. Ultrafast insulator-to-metal phase transition as a switch to measure the spectrogram of a supercontinuum light pulse. *Applied Physics Letters*, 96(2):021102, 2010.

[16] NP Ernsting, SA Kovalenko, T Senyushkina, J Saam, and V Farztdinov. Wavepacket-assisted decomposition of femtosecond transient ultraviolet- visible absorption spectra: application to excited-state intramolecular proton transfer in solution. *The Journal of Physical Chemistry A*, 105(14):3443–3453, 2001.

[17] Claudio Giannetti, Goran Zgrablic, Cristina Consani, Alberto Crepaldi, Damiano Nardi, Gabriele Ferrini, Guy Dhalenne, A Revcolevschi, and Fulvio Parmigiani. Disentangling thermal and nonthermal excited states in a charge-transfer insulator by time-and frequency-resolved pump-probe spectroscopy. *Physical Review B*, 80(23):235129, 2009.

[18] Fabio Novelli, Daniele Fausti, Julia Reul, Federico Cilento, Paul HM Van Loosdrecht, Agung A Nugroho, Thomas TM Palstra, Markus Grüninger, and Fulvio Parmigiani. Ultrafast optical spectroscopy of the lowest energy excitations in the Mott insulator compound YVO_3: Evidence for Hubbard-type excitons. *Physical Review B*, 86(16):165135, 2012.

[19] Francesco Randi, Ignacio Vergara, Fabio Novelli, Martina Esposito, Martina Dell'Angela, VAM Brabers, P Metcalf, Roopali Kukreja, Hermann A Dürr, Daniele Fausti, et al. Phase separation in the nonequilibrium Verwey transition in magnetite. *Physical Review B*, 93(5):054305, 2016.

[20] Fabio Novelli, Gianluca Giovannetti, Adolfo Avella, Federico Cilento, Luc Patthey, Milan Radovic, Massimo Capone, Fulvio Parmigiani, and Daniele Fausti. Localized vibrations in superconducting $YBa_2Cu_3O_7$ revealed by ultrafast optical coherent spectroscopy. *Physical Review B*, 95(17):174524, 2017.

[21] AL Dobryakov, Sergey A Kovalenko, A Weigel, José Luis Pérez-Lustres, J Lange, A Müller, and NP Ernsting. Femtosecond pump/supercontinuum-probe spectroscopy: Optimized setup and signal analysis for single-shot spectral referencing. *Review of Scientific Instruments*, 81(11):113106, 2010.

[22] Gerald Auböck, Cristina Consani, Roberto Monni, Andrea Cannizzo, Frank Van Mourik, and Majed Chergui. Femtosecond pump/supercontinuum-probe

setup with 20 khz repetition rate. *Review of Scientific Instruments*, 83(9):093105, 2012.

[23] Florian Kanal, Sabine Keiber, Reiner Eck, and Tobias Brixner. 100-khz shot-to-shot broadband data acquisition for high-repetition-rate pump–probe spectroscopy. *Optics express*, 22(14):16965–16975, 2014.

[24] Edoardo Baldini, Andreas Mann, Simone Borroni, Christopher Arrell, Frank Van Mourik, and Fabrizio Carbone. A versatile setup for ultrafast broadband optical spectroscopy of coherent collective modes in strongly correlated quantum systems. *Structural Dynamics*, 3(6):064301, 2016.

[25] Roman Yusupov, Tomaz Mertelj, Viktor V Kabanov, Serguei Brazovskii, Primoz Kusar, Jiun-Haw Chu, Ian R Fisher, and Dragan Mihailovic. Coherent dynamics of macroscopic electronic order through a symmetry breaking transition. *Nature Physics*, 6(9):681–684, 2010.

[26] Ivan Madan, Toru Kurosawa, Yasunori Toda, Migaku Oda, Tomaz Mertelj, Primoz Kusar, and Dragan Mihailovic. Separating pairing from quantum phase coherence dynamics above the superconducting transition by femtosecond spectroscopy. *Scientific reports*, 4:5656, 2014.

[27] I Madan, P Kusar, VV Baranov, M Lu-Dac, VV Kabanov, T Mertelj, and D Mihailovic. Real-time measurement of the emergence of superconducting order in a high-temperature superconductor. *Physical Review B*, 93(22):224520, 2016.

[28] Robert W Boyd. *Nonlinear optics*. Academic press, 2020.

[29] Anthony E Siegman. *Lasers*. University science books, 1986.

[30] Dario Polli, Daniele Brida, Shaul Mukamel, Guglielmo Lanzani, and Giulio Cerullo. Effective temporal resolution in pump-probe spectroscopy with strongly chirped pulses. *Physical Review A*, 82(5):053809, 2010.

[31] https://www.hamamatsu.com/resources/pdf/ssd/s11105_series_kmpd1111e.pdf.

[32] https://www.hamamatsu.com/resources/pdf/ssd/s8380-128q_etc_kmpd1045e.pdf.

[33] Angela Montanaro, Francesca Giusti, Matija Colja, Gabriele Brajnik, Alexandre MA Marciniak, Rudi Sergo, Dario De Angelis, Filippo Glerean, Giorgia Sparapassi, Giacomo Jarc, et al. Visible pump-mid infrared pump-broadband probe: Development and characterization of a three-pulse setup for single-shot ultrafast spectroscopy at 50 kHz. *Review of Scientific Instruments*, 91(7):073106, 2020.

[34] Claudio Giannetti, Federico Cilento, Stefano Dal Conte, Giacomo Coslovich, Gabriele Ferrini, Hajo Molegraaf, Markus Raichle, Ruixing Liang, Hiroshi Eisaki, Martin Greven, et al. Revealing the high-energy electronic excitations underlying the onset of high-temperature superconductivity in cuprates. *Nature communications*, 2(1):1–7, 2011.

[35] Claudio Giannetti, Giacomo Coslovich, Federico Cilento, Gabriele Ferrini, Hiroshi Eisaki, Nobuhisa Kaneko, Martin Greven, and Fulvio Parmigiani. Discontinuity of the ultrafast electronic response of underdoped superconducting $Bi_2Sr_2CaCu_2O_{8+\delta}$ strongly excited by ultrashort light pulses. *Physical Review B*, 79(22):224502, 2009.

3

DYNAMICS OF NON-THERMAL STATES IN $Bi_2Sr_2Ca_{0.92}Y_{0.08}Cu_2O_{8+\delta}$ REVEALED BY MID-INFRARED THREE-PULSE SPECTROSCOPY

In this chapter we will focus on the study of the non-equilibrium optical properties of a prototype cuprate superconductor, $Bi_2Sr_2Ca_{0.92}Y_{0.08}Cu_2O_{8+\delta}$ (T_C=96 K). The three-pulse spectroscopy described in Chapter 2 will allow us to characterize its broadband transient response to above- and below-gap photo-excitation either at the equilibrium or in tailored non-thermal states. The observation of an anisotropic response in the superconducting phase will be discussed in terms of a non-equilibrium Drude-Lorentz model that will enable us to identify the high-energy electronic transition involved in the superconducting transition. Before discussing our experimental findings, we will review in Section 3.1 some fundamental features of superconductivity in cuprates, with special focus on their optical properties.

3.1 CUPRATE SUPERCONDUCTORS

Since its first experimental observation by Bednorz and Muller in 1986 [1], high-temperature superconductivity in cuprates (HTSC) has been the subject of an intense debate in the scientific community. Still, the mechanism that mediates the electronic pairing in such compounds remains unexplained.

Cuprates are layered ceramic materials displaying a perovskite-like structure. Despite their complex unit cell, cuprates are rather simple materials from a structural point of view. The electronic properties are mainly determined by their peculiar copper oxide layers, in which each copper ion is fourfold coordinated to the oxygen ions (CuO_2 plaquette). The CuO_2 layers are separated by sheets of various chemical composition that act as charge reservoirs. Superconductivity takes place within the CuO_2 planes, suggesting that two-dimensional single-band models might be suitable to capture their fundamental physics.

PHASE DIAGRAM Cuprates give rise to a rich phase diagram. By modifying the doping of the material (p), phases with extremely different macroscopic properties can be attained. A sketch of a typical phase diagram is shown in Figure 3.1. Superconductivity occurs within the area enclosed by the solid red line, the so-called *superconducting dome*. The critical temperature $T_C(p)$ reaches its maximum value at

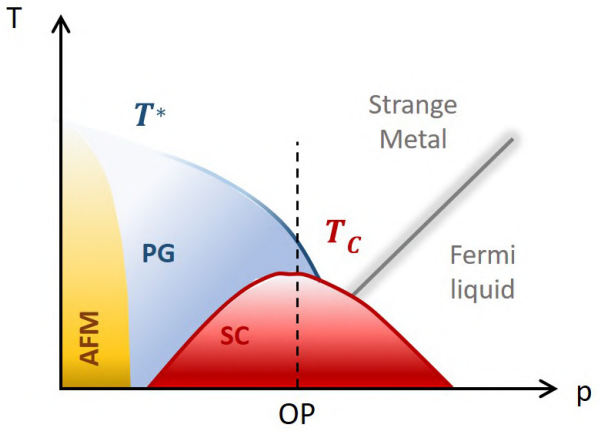

Figure 3.1: **Phase diagram of cuprates.** At very low dopings (p), the cuprates are insulating and antiferromagnetic (yellow area). When the hole concentration is increased, they undergo a superconducting phase transition below the critical temperature (T_C, red dome). At the optimal doping (OP) T_C is maximized. A pseudogap phase, whose boundaries (T^*) are uncertain at low dopings, is observed in the underdoped region of the phase diagram (blue area). Above T^*, cuprates behave as strange metals. A gradual transition from the strange metal phase to the Fermi liquid one occurs at high dopings.

the optimal doping (OP, $p \sim 0.16$) and it decreases on both the underdoped (UD) and overdoped (OD) sides of the phase diagram. Cuprates display peculiar properties also outside the superconducting dome. At low dopings ($p < 0.05$), they are insulating and antiferromagnetic. At high tempatures, they behave as *strange metals* and a crossover to a Fermi-liquid phase is observed at higher doping. The most elusive phase is the pseudogap one (PG, blue-shaded area) [2, 3]. The PG phase occurs only in underdoped and optimally-doped cuprates below $T^*(p)$ and is characterized by intriguing properties which are typical neither of the superconducting (SC) phase nor of the metallic one [4, 5, 6]. Importantly, angle-resolved photo-emission spectroscopy (ARPES) and tunneling measurements revealed the presence of an electronic gap that would be an indication of early pair formation [7, 8, 9, 10]. Whether the PG phase constitues a phase of its own (with its peculiar properties and symmetries) or it is a precursor of the SC one in which Coopers pairs are formed yet lack long-range phase coherence, is still currently debated [11, 12].

ELECTRONIC STRUCTURE The macroscopic properties of cuprates arise from the electronic structure of the CuO_2 plane, sketched in Figure 3.2a. In the parent compound (undoped material), each Cu atom is stripped of $2e^-$ and left in the $3d^9$ configuration because of the oxygen high electronegativity. The Cu ion has therefore a single hole with $d_{x^2-y^2}$ symmetry. While conventional band theory would predict such systems to be metals (odd number of electrons per Cu site), they turn out to be Mott insulators due to the strong electronic correlations. The on-site Coulomb

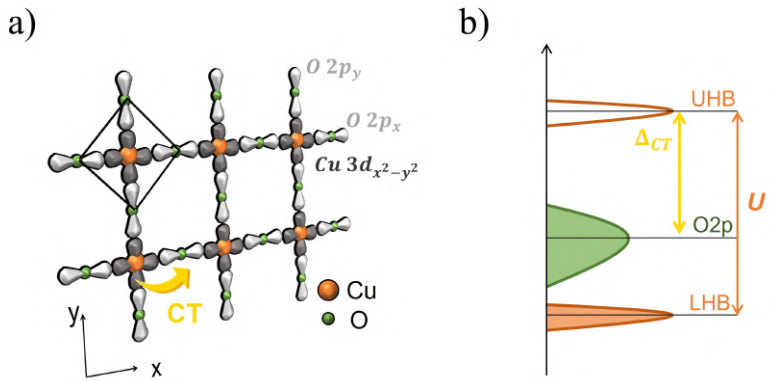

Figure 3.2: **Electronic structure of cuprates. a)** Representation of the Cu $3d_{x^2-y^2}$ and O $2p_{x,y}$ orbitals within the CuO_2 plaquette. The charge-transfer of a Cu $3d_{x^2-y^2}$ hole to its neighbouring O $2p_{x,y}$ states is indicated by the yellow arrow. **b)** Density of states indicating the Hubbard splitting and the charge-transfer transition in the parent compound.

repulsion U splits the Cu d-band into a full lower (LHB) and an empty upper Hubbard band (UHB), as illustrated in Figure 3.2b. The LHB and the UHB are separated in energy by U ∼8-10 eV and the O $2p$ band falls inside this gap, 2 eV below the UHB. In the parent compound, the transition from the O $2p$ band to the UHB is the lowest-energy one and represents the charge-transfer (CT) of the Cu $3d_{x^2-y^2}$ hole to its neighboring O $2p_{x,y}$ states. As a consequence, a charge-transfer gap (Δ_{CT}) emerges in the density of states, which constitutes the lower bound of the electron-hole continuum [13, 14].

Upon doping, the CT-gap is filled with states accounting for the itinerant carriers. These intragap transitions are generally related to many-body mixed Cu-O states involving a local Cu $3d$ hole antiferromagnetically coupled to a $2p$ hole shared among the four surrounding oxygens (Zhang-Rice singlet states) [15, 16]. Dynamical mean field theory calculations show that the Fermi level lies within this hybridized band [17, 18].

3.1.1 *Optical properties of cuprates*

The possibility of probing the sample on a very broad energy range (from the THz to the UV) makes optical techniques exceptional tools to selectively study different degrees of freedom in cuprate systems and their possible involvement in the onset of superconductivity. In Appendix A we review the main optical quantities that will be used in the following and the derivation of the Drude-Lorentz dielectric function that models the equilibrium optical response of HTSC.

The optical properties of cuprates are dictated by the electronic structure discussed above (Figure 3.2b) and the main features are common to most samples. In Figure 3.3a we show the *ab*-plane reflectivity of a prototype cuprate measured at room temperature by spectroscopic ellipsometry [19]. The dressed plasma frequency $\bar{\omega}_P$,

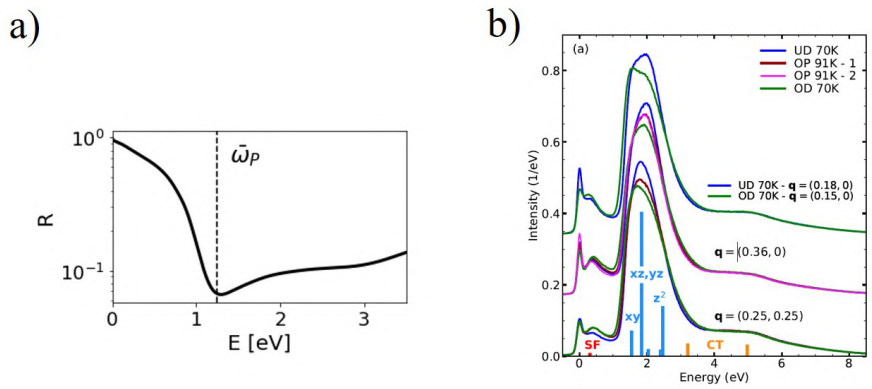

Figure 3.3: **Transfer of spectral weight.** **a)** Reflectivity of a prototype cuprate ($Bi_2Sr_2Ca_{0.92}Y_{0.08}Cu_2O_{8+\delta}$ at T=300 K [19]). The vertical line indicates the dressed plasma frequency $\bar{\omega}_P$. **b)** RIXS spectra of Bi2212 measured in ref. [20] at different dopings.

the frequency at which the real part of the dielectric function vanishes ($\varepsilon_1(\bar{\omega}_P) = 0$), identifies two regions in the plot:

- the low-energy side is dominated by the tail of the zero-frequency Drude response of the free carriers and by additional mid-infrared excitations ($E \sim$ 0.5 eV) that are possibly related to transitions between the Hubbard bands and states close to the Fermi energy [21];
- the high-energy side is instead reminiscent of a CT-like absorption edge ($E >$ 2.5 eV).

The assignment of the excitations that give rise to the structures within the energy window spanning from 1.25 to ∼2 eV is still controversial. It has been proposed that they arise from the transitions involving the Cu-O mixed band and states at the Fermi energy [17, 19]. On the other hand, resonant inelastic x-ray scattering (RIXS) measurements showed that the *dd* orbital transitions dominate the excitation spectrum at these energies (Figure 3.3b) [22, 23] and their possible involvement in the pairing mechanism has been recently suggested [20].

Unconventional spectral weight transfer

As a consequence of the conservation of the total number of charge carriers, the spectral weight contained in the optical conductivity must satisfy the frequency-sum rule:

$$\int_0^\infty \sigma_1(\omega)\, d\omega = \frac{\pi n e^2}{2m} = A \tag{3.1}$$

where σ_1 is the real part of the conductivity and n, e and m are the electronic density, charge and mass, respectively. In Figure 3.4a (top panel) we have indicated with A^N and B^N the spectral weight associated to the low- and high-energies, respectively.

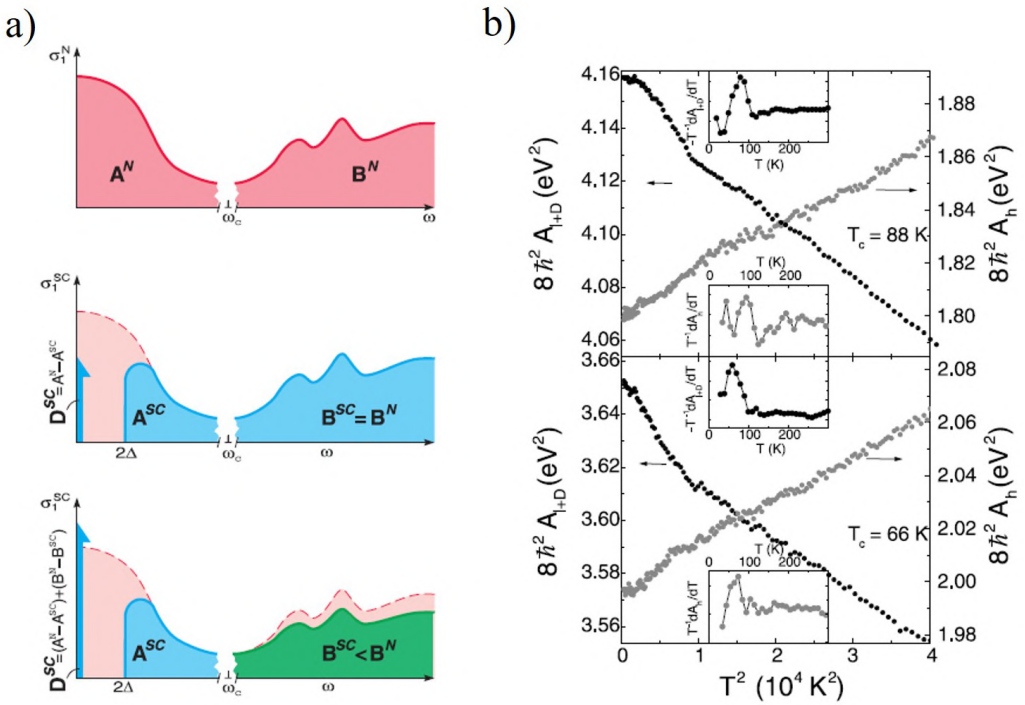

Figure 3.4: **Transfer of spectral weight. a)** Real part of the optical conductivity. Top panel: spectral weight in the normal state at low (A^N) and high (B^N) energy. Middle panel: redistribution of spectral weight in a conventional superconductor. Gapped out weight flows into a δ function at zero frequency. Bottom panel: additional weight in the δ function is transferred from high energies to satisfy the sum rule. Adapted from ref.[24]. **b)** Low-energy (A_{1+D}) and high-energy (A_h) spectral weight as function of temperature in optimally-doped (top) and underdoped (bottom) $Bi_2Sr_2CaCu_2O_{8+\delta}$. The cut-off frequency has been set to 10000 cm^{-1}. The insets show the derivatives. Taken from ref.[25].

Importantly, the frequency-sum rule must hold at every temperature and this has crucial consequences for superconductors.

When the SC condensate is formed below T_C, the optical conductivity (Equation A.16) has to take into account the presence of perfecty conducting charge carriers ($\tau \rightarrow \infty$, where $1/\tau$ is the scattering rate). In this limit, the optical conductivity becomes purely imaginary and proportional to ω^{-1}. An additional δ-like real component at zero frequency must be considered to satisfy the causality of the Kramers-Kronig relations (Equation A.18), resulting in:

$$\sigma_D(\omega) = \frac{ne^2}{m}\left(\pi\delta(\omega) + i\frac{1}{\omega}\right) \tag{3.2}$$

Thus, in the superconducting state, further spectral weight associated to the condensate (D) must be considered (Figure 3.4a, middle panel). As soon as the SC gap (2Δ) is formed, gapped out spectral weight flows into the δ component. A more general conservation rule, the Ferrel-Glover-Tinkham rule [26], holds:

$$D = A^N - A^{SC} + B^N - B^{SC} \tag{3.3}$$

where the superscripts N and SC refer to the normal and the superconducting state, respectively. In conventional BCS superconductors the opening of the SC gap triggers a rearrangement of the excitation spectrum only in an energy range that is comparable with 2Δ, while the high-energy contributions are unaffected by the SC transition ($B^N = B^{SC}$ in Equation 3.3 and middle panel in Figure 3.4a). On the contrary, an anomalous redistribution of spectral weight at energies that are orders of magnitude larger than 2Δ has been observed in cuprates [27, 25, 28, 24, 29, 30]. This means that the sudden emergence of the condensate spectral weight is partially compensated also by high-energy excitations (bottom panel in Figure 3.4a).

This was directly observed in $Bi_2Sr_2CaCu_2O_{8+\delta}$ [25]. The dielectric function of an optimally-doped and an underdoped sample was measured by spectroscopic ellipsometry at different temperatures. In Figure 3.4b the spectral weight of the low-energy (A_{1+D}) and the high-energy (A_h) is reported as function of temperature, showing that they have opposite trends. Below T_C, a slight extra increase (beyond the thermal contribution) in A_{1+D} is observed, while A_h slightly decreases (insets in the panels), demonstrating that there is a transfer of spectral weight from the high- to the low-frequencies in the superconducting state. This further indicates that the pairing mechanism in cuprates is unconventional and hints at a direct involvement of the high-energy electronic excitations in the onset of high-T_C superconductivity.

3.1.2 *Superconducting gap*

Another feature that distinguishes cuprate superconductors is the symmetry of the SC gap. In conventional BCS superconductors, the phonon-mediated Cooper pairing gives rise to a *s*-wave SC gap, that is isotropic across the first Brillouin zone. In

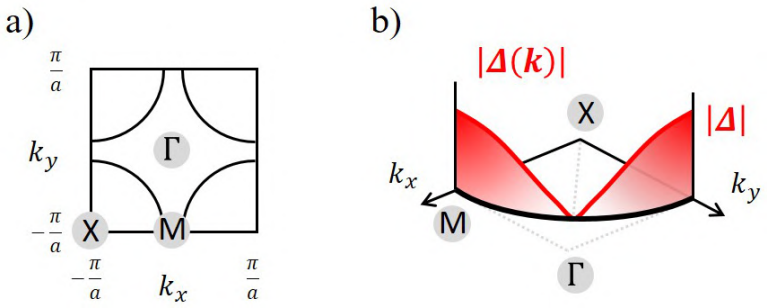

Figure 3.5: ***d*-wave superconducting gap in cuprates. a)** Fermi surface in the first Brillouin zone. **b)** Sketch of the modulus of the d-wave gap in the reciprocal space. $|\Delta|$ is the amplitude of the gap at the antinode. Adapted from ref. [35].

cuprates, it was soon realized through mid-infrared studies of the penetration depth and phase-sensitive measurements that the gap has a strong momentum-dependence that is consistent with a d-wave symmetry [31, 32, 33]. Depending on the direction within the Brillouin zone (Figure 3.5a), the SC gap changes value: it reaches its maximum amplitude (tens of meV) along the ΓM axis (*antinodal* direction) and vanishes along the ΓX axis (*nodal* direction), as sketched in Figure 3.5b where we plot only the modulus of the gap.

This inherent anisotropy has important consequences on the ground state of the condensate because it implies that the amount of energy required to break a Cooper pair into two quasiparticles (QP) depends on its momentum [34]. Superconducting electrons are strongly bound for $\mathbf{k}$ parallel to the Cu-O bond direction, whereas they are not paired at all for $\mathbf{k}$ along the Cu-Cu direction, that is the diagonal of the CuO_2 plaquette. This entails that, while at the antinode electronic transitions are permitted only at energies larger than the SC gap, all transitions are allowed at the nodes. Even in the limit of $T \to 0$, long-lived nodal excitations are always present and dominate the thermodynamical properties at the equilibrium.

In this respect, although momentum-sensitive experimental techniques (such as electronic Raman scattering and ARPES) are convenient tools to resolve the gap symmetry, they have the major drawback - common to all static approaches - of probing the system in its thermal state, in which the presence of a high number of thermal excitations prevents a clear assessment of the nodal excitation spectrum.

3.2 MOTIVATION

Understanding how the momentum distribution of the electronic excitations controls the d-wave SC gap is one of the keys to advance the field and, arguably, a way to distinguish between the many microscopic models proposed for cuprates superconductors [36, 37, 38].

Here, we exploit non-equilibrium optical spectroscopy based on long wavelength pulses to overcome the limitation intrinsic to equilibrium techniques. Photo-excitation by ultrashort laser pulses injects in the system excess QPs, which perturb the initial

equilibrium distribution [39, 40, 41, 42, 43, 44, 45, 46, 47, 48]. We leverage on this aspect to prepare the system into a tailored non-thermal state. While there is direct indication that high-photon energy pulses (>1.5 eV) excite a QP population that is mainly localized in the antinodal regions of the Fermi surface [43, 44, 47], the effect of the photo-excitation by low-photon energy pulses (i.e. smaller than the SC gap) has been little investigated. Evidence of transient SC phases triggered by long-wavelength electric fields has been reported [49, 50, 51, 52, 53, 54], suggesting that low-photon energy excitation may lead to different transient electronic states.

To disentangle the effects of high- and low-photon energy excitation, we employ the three-pulse scheme described in Chapter 2, which combines a near-infrared ($h\nu_{NIR} \gg 2\Delta_{SC}$) pump, a mid-infrared ($h\nu_{MIR} \leq 2\Delta_{SC}$) pump and a white-light probe (1.5-2 eV), as illustrated in Figure 3.6a. The rationale of our approach is to use the first pump to drive the system into a non-thermal state, and then measure the subsequent QP dynamics using the second pump-probe sequence. The broadband detection window enables the measurement of the transient high-energy dielectric function of the sample, thus allowing to directly probe the involvement of the high-energy electronic excitations lying in that spectral range.

3.2.1 *The experiment*

We carried out time-domain optical measurements on a freshly cleaved sample of optimally-doped $Bi_2Sr_2Ca_{0.92}Y_{0.08}Cu_2O_{8+\delta}$ (Y-Bi2212) at different temperatures. The sample displays a SC phase below T_C = 96 K, and a PG pseudogap (PG) phase between T_C and T^* = 135 K. Above T^*, the system behaves as a strange metal [55]. The absolute value of the d-wave gap in reciprocal space is sketched in Figure 3.6d. The antinodal gap amplitude is $2\Delta_{SC} \sim 75$ meV [56].

As sketched in Figure 3.6a, the three pulses propagate along the c-axis (orthogonally to the Cu-O plane). The pump beams are co-polarized, while the probe polarization is orthogonal to the pumps; the polarization of the impinging beams with respect to the CuO_2 plaquette can be adjusted by rotating the sample with a piezoelectric rotator in the vacuum chamber. The sample has been oriented through X-ray diffraction measurements, performed in collaboration with L. Barba and G. Chita at the beamline XRD1 at Elettra Sincrotrone Trieste.[1]

The chopped detection described in Section 2.3.1 allows to measure, for each delay $\bar{t}$ of the probe beam, the broadband transient change in reflectivity induced by the pumps is measured, as illustrated in Figure 3.6b. By tuning the time delay T between the pump pulses, the order of arrival of the pumps can be swapped. This enables to determine, within the very same measurement, how the photo-excitation by the first impinging pump modifies the dynamics measured by the second pump-probe sequence.

1 *Elettra Sincrotrone Trieste S.C.p.A., 34127, Basovizza, Trieste, Italy.*

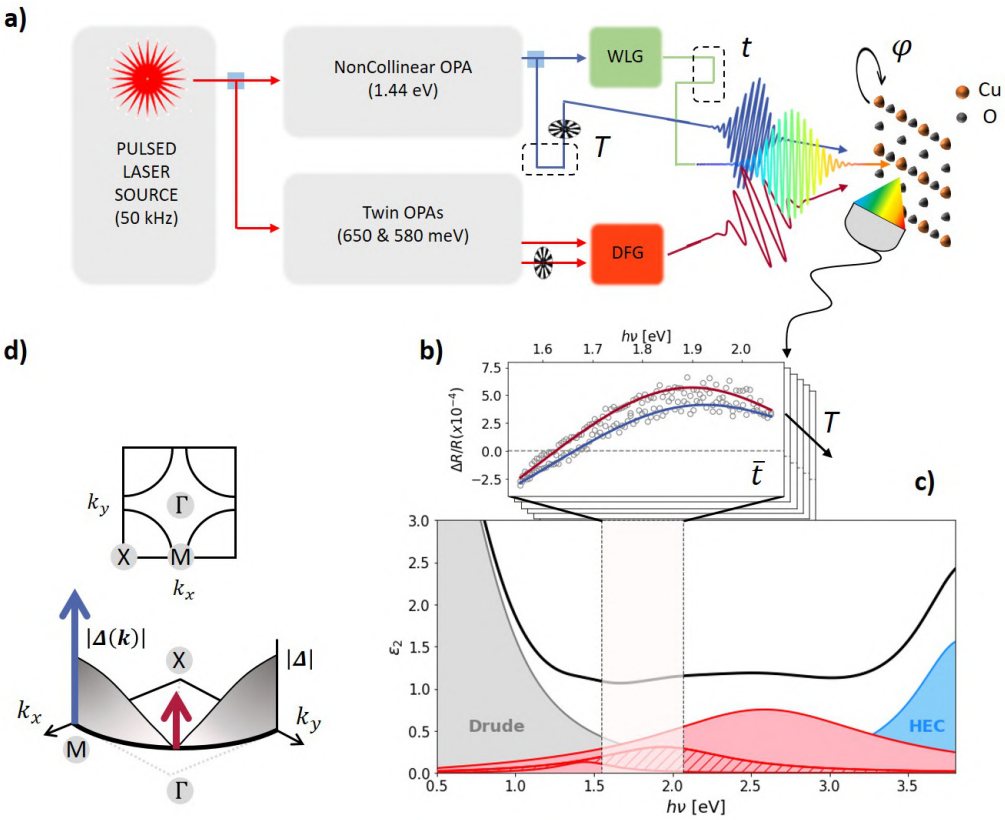

Figure 3.6: **Time-dependent broadband measurements of dielectric function upon photo-excitation above and below the superconducting gap.** **a)** Sketch of the three-pulse experimental setup. "WLG" stands for White-Light Generation, "DFG" for Difference-Frequency Generation. "T" indicates the delay between the two pumps, "t" the delay between the near-infrared pump and the supercontinuum probe. The sample orientation (φ) can be adjusted by a piezoelectric rotator mounted. **b)** Example of a transient reflectivity measurement (grey circles) and corresponding differential fit to the data (solid line) at fixed $\bar{t}$ for the near-infrared (blue) and mid-infrared (red) pumps, simultaneously acquired. This is a representative frame of the full T-dynamics. **c)** Imaginary part of the dielectric function obtained through a Kramers-Kronig constrained Drude-Lorentz fit of the dielectric function of Y-Bi2212 at T=20 K (data published in ref. [19]). The grey-shaded area accounts for the Drude peak and includes the low-energy contributions. The blue-shaded area indicates the high-energy contributions (HEC). The red peaks correspond to the oscillators that overlap with our probing window. The red pattern indicates the oscillator at $\omega_0 = 2$ eV that is the focus of our studies. **d)** First Brillouin zone and absolute value of the superconducting gap in the reciprocal space for a d-wave superconductor. The blue and the red arrows represent the above- and below-gap photo-excitation, respectively.

3.3 EQUILIBRIUM OPTICAL PROPERTIES OF Y-BI2212

As discussed in Section 3.1.1, the equilibrium optical properties of cuprates are mainly determined by the Cu $3d$ and the O $2p$ orbitals within the CuO_2 plaquette. In Figure 3.6c, we plot the imaginary part of the dielectric function of an optimally-doped Y-Bi2212 sample measured at T=20 K by spectroscopic ellipsometry (adapted from ref. [19]). While the low-energy side ($h\nu <$ 1.25 eV) of the dielectric function is dominated by the tail of the Drude response of the free carriers, the high-energy side is reminiscent of a CT-like absorption edge ($h\nu >$ 2.5 eV). The interband transitions give rise to a structured absorption in the region extending from 1.25 to 2 eV. As indicated by the grey-shaded area, our broadband probe overlaps with this window, directly enabling the measurement of the impulsive modification of these states.

3.3.1 *Static Drude-Lorentz fit*

In order to quantitatively estimate the pump-induced changes in the electronic excitations, we fitted the static dielectric function of the material using a Drude-Lorentz model (see Appendix A) consisting of a Drude peak (ε_D) and a sum of Lorentzian oscillators to account for the electronic transitions ($\sum_i \varepsilon_L^i$). We have used the ellipsometry data published in refs. [19, 57], in which the authors measured the dielectric function and the static reflectivity of an optimally-doped Y-Bi2212 sample at three different temperatures (20, 100 and 300 K), corresponding to the SC, PG and normal phases, respectively. Unlike refs. [19, 45], we have used a simple Drude peak instead of an extended Drude model to fit the low-energy side of the spectrum, as the main focus of our study is the optical response in the visible region overlapping with our broadband probe and not the low-energy mid-infrared transitions.

We used the Reffit tool [58] to obtain a Kramers-Kronig constrained fit to the data, using Equation A.15. The Drude peak is included in the sum as an oscillator at ω_0=0 and this parameter is kept fixed during the fitting procedure. The phenomenological parameter ε_∞ accounts for the higher-energy bands outside the measured range and, for consistency, has also been kept fixed and equal to the one given by ref. [19]. We plot in Figure 3.7 the energy-dependent reflectivity at the three temperatures obtained through the Drude-Lorentz fitting and calculated using Equation A.17. The three curves in Figure 3.7 overlap on the high-energy scale and differ mainly below the CT edge (<2 eV). We summarize in Table B.1 the best fitting parameters in the three phases.

In agreement with ref. [19], we found that three oscillators are sufficient to fit the dielectric function in the energy range 1.25-2 eV and they correspond to the three red Lorentzian peaks in Figure 3.6c. We highlighted with a red pattern the transition centered at 2 eV that will be the focus of our time-domain studies.

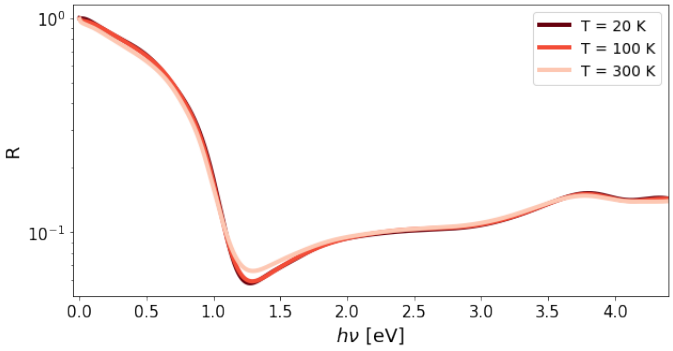

Figure 3.7: **Static reflectivity at different temperatures (logarithmic scale)**. Raw data taken from refs. [19, 57] and fitted via a Drude-Lorentz model. The best fitting parameters are reported in Table B.1.

3.4 SELECTIVE PHOTO-EXCITATION IN THE SUPERCONDUCTING PHASE

The study of the dynamics of the sample in a tailored non-thermal state relies on the knowledge of the QP dynamics in the system that is initially at equilibrium. In this section, we focus on the characterization of the sample response to a single excitation with photon energy either below or above the SC gap.

In Figure 3.8a,c, we compare the broadband transient reflectivity upon photo-excitation in the SC phase by the MIR pump and the NIR pump, respectively. The polarization of both pumps was parallel to the CuCu axis, as illustrated in the top inset. The measurements have been performed at low pumping fluences (ϕ < 30 μJcm^{-2}) to avoid the complete vaporization of the condensate [41]. To guarantee a meaningful comparison between the signal at high- and low-pump photon energy, we tuned the intensity of the pumps to have comparable ΔR/R amplitude at fixed probe energy. An estimation of the errors associated to the time- and energy-dependent reflectivity maps is given in Appendix C. Although the transient change in reflectivity is positive over the entire probing window (in agreement with the one measured in ref. [19] with a 1.55 eV pump pulse), the dynamics of the signal displays a dependence on the photon energy of the pump. This difference is more pronounced at low probe energies, where the black cuts ($h\nu_{pr}$ = 1.59 eV) in Figure 3.8a,c are selected.

Motivated by the distinctive gap anisotropy of the sample and its anisotropic response to long-wavelength pulse excitation that we have recently reported [54, 59], we have investigated how the broadband response changes according to the polarization of the pump beams. In Figure 3.8b,d, we show the time- and spectrally-resolved transient reflectivity for the pump polarizations parallel to the direction of the Cu-O bond (CuO axis). We observe that, in both maps, the transient reflectivity changes sign at approximately 1.7 eV and displays a negative dynamics below this threshold (black cuts in Figure 3.8b,d). We stress that reducing the pumping fluences does not qualitatively affect the spectral dependence of the response in this polarization configuration (Section 3.4.2), confirming that the measurements are performed in the linear regime.

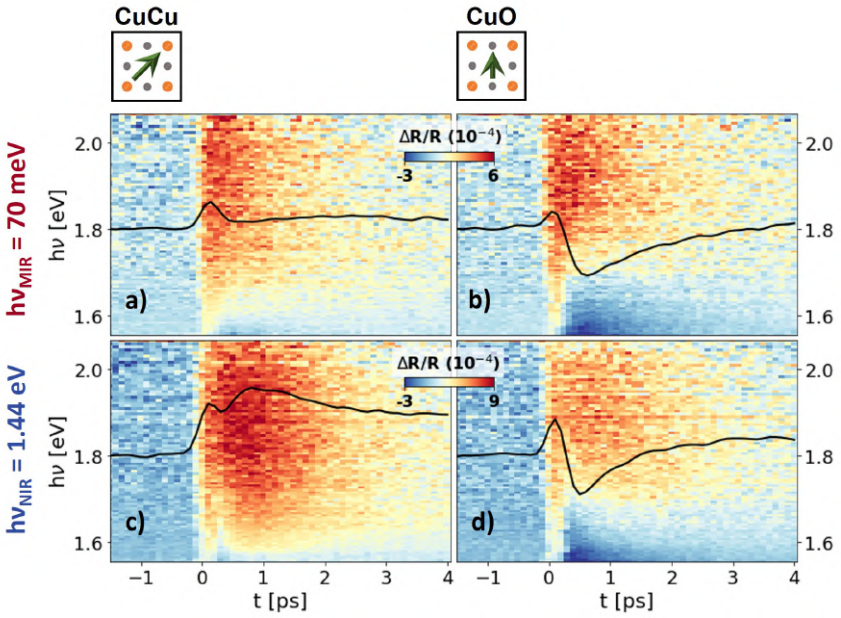

Figure 3.8: **Polarization-dependent pump-probe measurements for below- and above-gap photo-excitation in the superconducting phase. a-b)**. Broadband transient reflectivity upon a photo-excitation by mid-infrared pulses (70 meV) for a pump pulse polarized along the CuCu and the CuO axis, respectively. The black line is a cut at 1.59 eV. The MIR-pump fluence was ϕ_{MIR}=28 μJcm^{-2} and the sample temperature T=74 K. **c-d)** Same as a-b) but for a high-energy near-infrared photo-excitation (1.44 eV) and fluence ϕ_{NIR}=19 μJcm^{-2}.

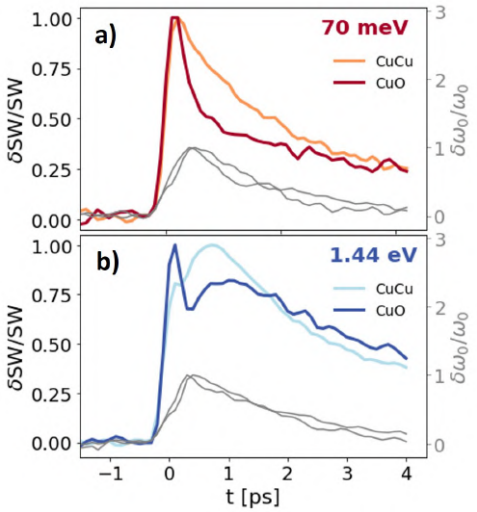

Figure 3.9: **Interband oscillator dynamics in the superconducting phase. a)** Results of the differential fits of the measurements in Figure 3.8a,b. The grey curves show the normalized transient change in the central frequency of the oscillator at ω_0= 2 eV for both the pump polarizations. The orange (red) curve is the normalized transient change in the spectral weight (SW) for the pump polarized along the CuCu (CuO) axis. **b)** Same as a) but for the above-gap photo-excitation.

3.4.1 *Differential fits*

In order to understand the origin of the structured reflectivity observed, we performed a differential fit of the maps based on the equilibrium dielectric function ($\varepsilon_{eq}(\omega)$) discussed in Section 3.3.1. The key idea of the analysis is to modify the minimum number of parameters that model $\varepsilon_{eq}(\omega)$ in order to fit, at every time delay, the transient broadband reflectivity measured. A detailed discussion of the differential fits analysis is given in Appendix D.

The analysis revealed that only a transient change of the Lorentzian oscillator centered at 2 eV is sufficient to reproduce our data. In particular, we found that the photo-excitation results in a blueshift of the central frequency (ω_0) of this oscillator and in a change of its spectral weight (SW), defined as $SW \propto \int_0^\infty \omega\varepsilon_2(\omega)\, d\omega$, where we performed the integration over the whole energy axis of the measured $\varepsilon_{eq}(\omega)$. We stress that the dynamics of ω_0 and SW are uncorrelated and thus these two parameters constitute a good pair of candidates to consistently describe the measurements (Figure D.2).

We show in Figure 3.9 the results of the differential fits for the below- and the above-gap photo-excitation, respectively. We plot the relative change of ω_0 and SW as function of the pump-probe delay for both the pump polarizations in each panel and, to facilitate the comparison between the curves, we normalize the dynamics on the maximum positive value. The maximum pump-induced blueshift of the oscillator is of the order of $\sim$1 meV. The dynamics of the blueshift does not depend neither on the pump photon energy nor on the pump polarization: the dynamics in all the four

combinations (grey curves in Figure 3.9) can be well described by a single-exponential with a decay time equal to ∼1.5 ps. The dynamics of the *SW* is instead more peculiar. When the sample is photo-excited by the above-gap pump (Figure 3.9b), the dynamics is characterized by a fast-decaying component, superimposed to an additional slower decay.

It is interesting to note that this behaviour is reminiscent of the dynamics of the transient single-colour reflectivity (at 1.55 eV) measured in other works [41, 60]. In particular, the fast peak is commonly ascribed to the incipient melting of the SC phase due to the sudden photo-injection of hot QP that non-thermally close the gap. The emergence of the second peak, which is farther delayed in time the more intense the photo-excitation is, is instead associated to the antinodal recovery dynamics of the condensate, that in Bi2212 has been observed to set in within a few ps [61]. However, this peculiar transient reflectivity response is not a universal feature of the sample and ultimately depends on the experimental parameters [35, 60]. Here, by fitting the transient dielectric function and thereby overcoming the limitations intrinsic to single-colour pump-probe measurements, we show that this dynamics is directly mapped into the variation of spectral weight (probe-energy independent quantity) and we thus confirm its general validity.

Interestingly, the absence of such dynamics in the MIR-induced *SW* change (Figure 3.9a) may be an indication that the recombination is different in this case. It is generally accepted that excitation by high photon energy pulses results in the accumulation of photo-injected QP at the antinodes of the SC gap, where the QP recombination rate is faster with respect to the nodal directions [43, 44]. However, photo-excitation by sub-gap pulses might not inject enough energy to excite QP at the antinodes, leading to an anisotropic QP population mostly localized in the nodal regions of the Brillouin zone. We note that increasing the fluence of the MIR pump does not alter the dynamics of the photo-induced change in *SW* (Section 3.4.3), that still lacks the recovery component.

Finally, the *SW* dynamics is also affected by the pump and the probe polarizations. For both pump photon energies, the dynamics is faster when the pump is polarized along the CuO axis, in correspondence with the antinodal direction. This further suggests that, in this condition, the photo-induced quench of the SC gap is more efficient [54, 59].

3.4.2 *Fluence dependence*

In this section, we study the reflectivity maps as function of the fluence of the impinging pulses in the superconducting phase (T=74 K). The purpose of this analysis is to study how the broadband reflectivity dynamics is affected by the increasing intensity of the photo-excitation and to choose the right pumping fluences to work with. In fact, high pumping fluences, in addition to causing effective thermal heating, can drive nonlinear responses in the system, that would obscure the dynamics in the

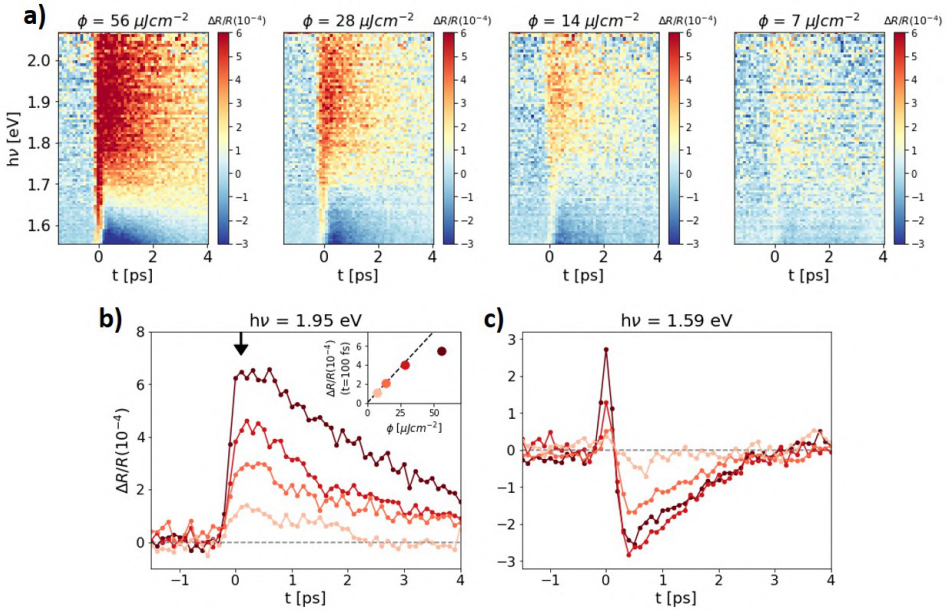

Figure 3.10: **Fluence dependence of the mid-infrared pump. a)**. Color-coded transient reflectivity maps as function of probe energy and pump-probe delay for different mid-infrared pumping fluences (pump polarized along the CuO axis). **b)** Horizontal cuts of the maps in a) at $h\nu$ = 1.95 eV for all the fluences. Inset: fluence dependence of the signal at t=100 fs, as indicated by the black arrow. **c)** Same as b), but for $h\nu$ = 1.59 eV.

linear excitation regime that we are interested in. We will restrict our discussion to the data acquired with the pump polarized along the CuO axis of the sample.

MID-INFRARED PUMP FLUENCE In Figure 3.10a, we plot the time- and energy-dependent transient reflectivity for different mid-infrared (70 meV) pumping fluences. From a qualitative point of view, the photo-excitation fluence does not affect the energy-dependent response: all the maps show a positive signal at probe energies greater than the about 1.68 eV and a negative one below. The pumping fluence that we have used for the measurements discussed in the main text is ϕ=28 μJcm^{-2}.

We plot in Figure 3.10b the positive dynamics at 1.95 eV (averaged over 50 meV) for all the measured fluences. The dynamics is well described by a single exponential decay and, even at the maximum fluence under exam, does not follow the double-exponential decay reported by [41] for high-photon energy pumps (1.55 eV). In the inset we plot the transient reflectivity at t=100 fs (as indicated by the black arrow) as function of the fluence. The signal follows a linear trend for the first three fluences examined and then becomes sub-linear. Importantly, the cuts at 1.59 eV (Figure 3.10, right panel) show that a negative transient reflectivity in this spectral region is observed at all pumping fluences when the MIR pump polarization is parallel to the CuO axis.

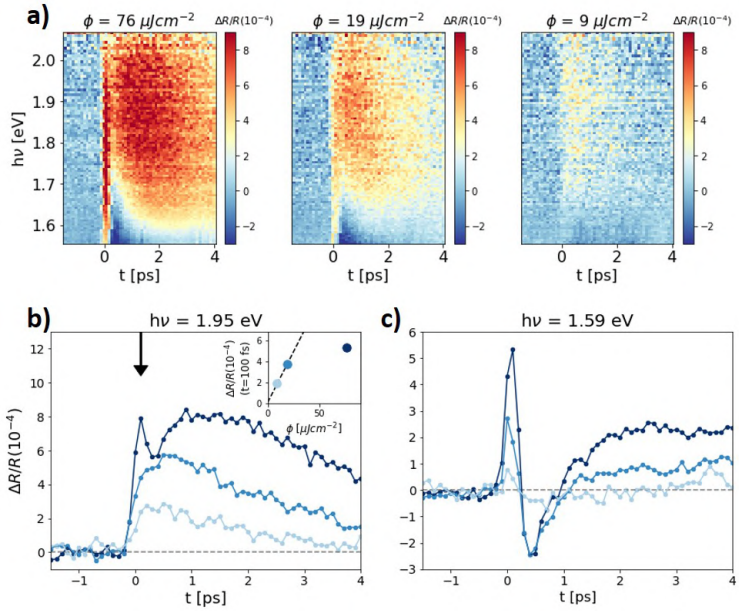

Figure 3.11: **Fluence dependence of the near-infrared pump. a)**. Time- and energy-dependent transient reflectivity upon photo-excitation by near-infrared pulses (polarized along the CuO axis) at different fluences. **b)** Horizontal cuts of the maps in a) at $h\nu$=1.95 eV. Inset: fluence dependence of the signal at t=100 fs. **c)** Same as b), but for $h\nu$=1.59 eV.

NEAR-INFRARED PUMP FLUENCE In Figure 3.11 we carry out the same analysis as in Figure 3.10 but considering a photo-excitation by near-infrared pulses (1.44 eV) with variable fluence. In contrast to the mid-infrared photo-excitation, the highest near-infrared fluence under exam initiates a dynamics at $h\nu$>1.7 eV that is characterized by the emergence of a fast-decaying component at the overlap, as observed in ref. [41] (Figure 3.11b). At lower fluences, the signal scales linearly, as shown in the inset, and a single-exponential decaying dynamics is recovered. We note that the measurements discussed in Figure 3.8 have been acquired with ϕ=19 μJcm^{-2}. At lower probe energies, the negative signal appearing in this polarization configuration is present at all fluences.

It is worth noting that the pair of MIR and NIR pumping fluences used for the discussion in Figure 3.8 are different (ϕ_{MIR}=28 μJcm^{-2} and ϕ_{NIR}=19 μJcm^{-2}), but were chosen according to the following criteria: i) they both drive a linear optical response in the material (as just discussed); ii) they lead to a relative change in reflectivity on the high-energy side of the probe spectrum ($\Delta R/R \sim 5\times10^{-4}$) that is comparable. The fact that the two fluences are different is due to the equilibrium properties of the sample, that is characterized by a lower absorption coefficient in the mid-infrared region of the spectrum.

PROBE LINEARITY We have tuned the probe fluence in order to study a possible dependence of the signal on its intensity. Generally, the probe fluence should be set to the lowest possible value in order to not perturb the sample and act as a

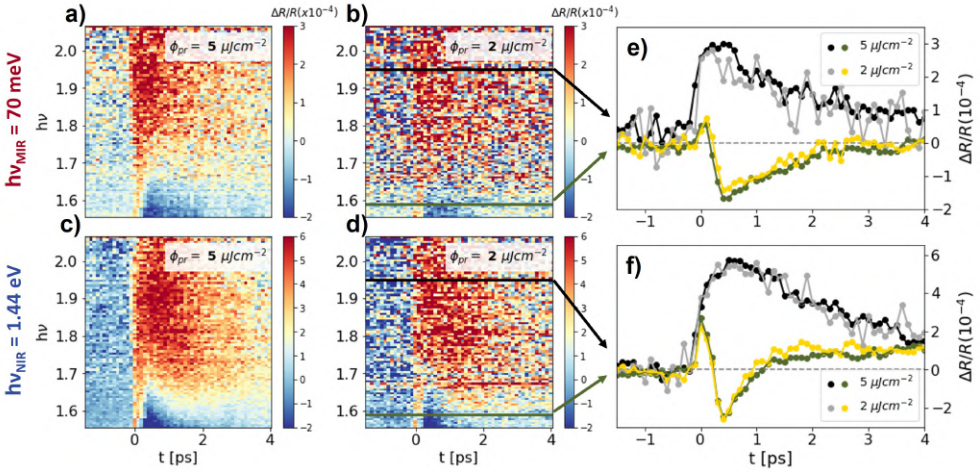

Figure 3.12: **Probe linearity. a)**. Reflectivity maps upon photo-excitation by a MIR pump pulse (ϕ_{MIR}=14 μJcm^{-2}) polarized along the CuO axis for a probe fluence equal to 5 and 2 μJcm^{-2}, respectively. **c-d)** Same as a-b) but for a NIR pump pulse (ϕ_{NIR}=19 c-d)). **e)** The black (green) and the grey (yellow) lines are the dynamics at $h\nu$ = 1.95 eV ($h\nu$ = 1.59 eV) of the MIR-induced reflectivity maps at 5 and 2 μJcm^{-2}, respectively. **f)** Same as e) but for the NIR-induced reflectivity maps.

simple "spectator" of the pump-induced dynamics. When dealing with a white-light supercontinuum instead of a quasi-monochromatic beam, this requirement is harder to satisfy as the probe is diffracted on a multichannel detector in which each photodiode detects just a very small fraction of its intensity.

We have measured the MIR- and NIR-induced dynamics at two different probe fluences (5 and 2 μJcm^{-2}) and studied the dynamics at two probe energies (1.59 and 1.96 eV), as illustrated in Figure 3.12. By comparing the reflectivity maps, it is clear that the probe power does not qualitatively affect the dynamics of the signal upon photo-excitation by neither the MIR pump nor the NIR one. However, reducing the probe fluence by a factor of 2.5 significantly lowers the signal-to-noise ratio of the measurements. The temporal cuts in Figure 3.12e,f show that the transient change in reflectivity (for distinct probe energies) is quantitatively the same for both the probe fluences under exam, as expected in a linear probing regime. For this reason, we have decided to carry out the measurements using a probe fluence ϕ_{pr} = 5 μJcm^{-2}, which ensures, at the same time, a linear optical response and a higher signal-to-noise ratio.

3.4.3 *Spectral weight dynamics at high fluence*

The differential fitting procedure described in Appendix D has been used to study the impulsive modification of the 2 eV oscillator in a linear perturbation regime (Figure 3.9). We found that, while the dynamics of the central frequency of the oscillator is not affected by neither the pump photon energy nor the pump polarization, the dynamics of the spectral weight is markedly different. In order to rule out the possibility that this difference is mostly related to the different photo-excitation fluences used (and so

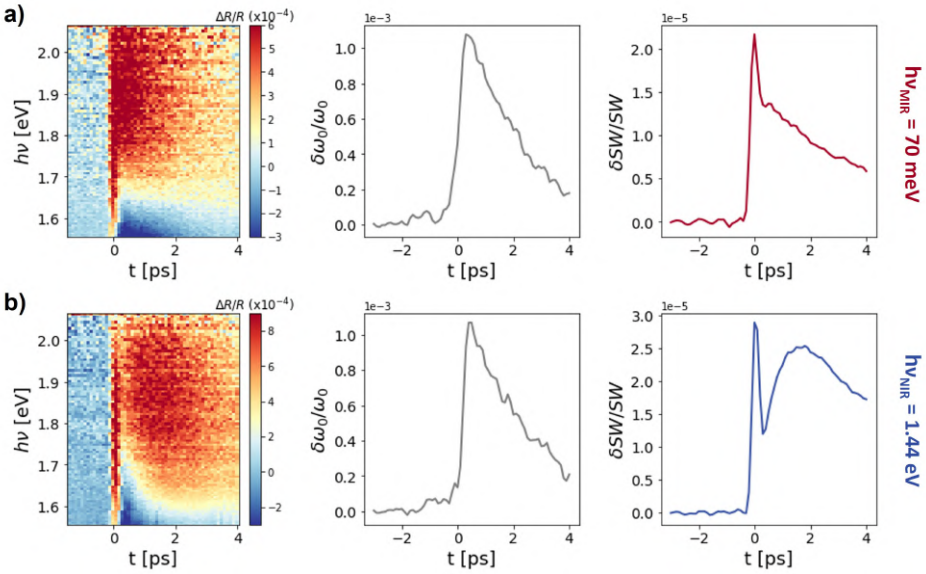

Figure 3.13: **Differential fits at high fluence. a)**. Left panel: time- and spectrally-resolved reflectivity induced by a mid-infrared pump pulse polarized along the CuO axis (ϕ_{MIR} = 56 μJcm^{-2}). Middle and right panels: results of the differential fit as function of the pump-probe delay in terms of the relative shift of the central frequency and the relative change in the spectral weight, respectively. **b)** Same as a) but for a near-infrared pump pulse (ϕ_{NIR} = 76 μJcm^{-2}).

to a thermal effect) rather than to a genuine pump wavelength-dependent effect, we fitted the time- and spectrally-resolved transient reflectivity upon photo-excitation at the highest pumping fluence measured (ϕ_{MIR} = 56 μJcm^{-2}) and ϕ_{NIR} = 76 μJcm^{-2})).

In Figure 3.13 we plot the color-coded reflectivity maps for the below- and the above-gap photo-excitation, and the results of their differential fits. We remind that all the fits have been performed by modifying only the central frequency and the scattering rate of the 2 eV oscillator. We observe that, even in a strong perturbation regime, the dynamics of the blueshift of the oscillator ($\delta\omega_0/\omega_0$) is independent from the photon energy of the pump and follows a single-exponential decay. The spectral weight dynamics ($\delta SW/SW$), however, is again different. While the NIR-induced spectral weight dynamics is characterized by a fast-decaying peak and by the emergence of a delayed and slower dynamics, the MIR-induced response does not display this second feature.

3.5 NORMAL AND PSEUDOGAP PHASES

The dependence of the broadband reflectivity on the photon energy and the polarization of the pump pulse is peculiar of the SC phase. In Figure 3.14a,e we show the time- and spectrally-resolved reflectivity measured in the normal (T=300 K) and in the PG (T=105 K) phase upon photo-excitation by the MIR pump polarized along the CuCu axis. The normal phase is characterized by a positive response, that decays faster than the SC one. This is consistent with the literature and generally attributed

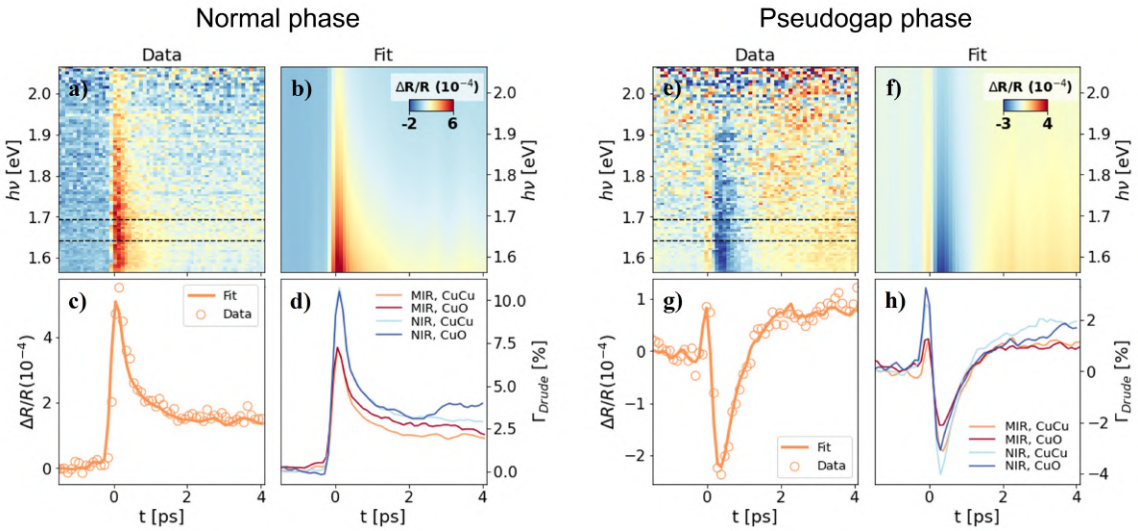

Figure 3.14: **Differential fits in the normal and pseudogap phases. a-b)**. Reflectivity map and corresponding differential fit in the normal phase (T=300 K) upon photo-excitation by a MIR pump pulse polarized along the CuCu axis. **c)** The open circles are a temporal cut of the map in a) averaged over the region within the dashed black lines. The solid line is the corresponding differential fit. **d)** Relative transient change of the Drude scattering rate (Γ) in the four configurations of pump photon energy (MIR or NIR) and pump polarization (//CuCu or //CuO axis). **e-h)** Same as a-d) but in the pseudogap phase (T=105 K).

to the suppression of recombination processes due to the opening of the gap below T_C.

In Figure 3.14c we plot the time trace at $h\nu_{pr}$ = 1.68 eV, averaged over the region within the dashed black lines in the map. The temporal trace at the same probe energy at T=105 K is plotted in Figure 3.14. After an initial positive peak, the reflectivity is negative; after ∼2 ps, a positive signal is restored.

Similarly to the differential analysis carried out in the SC phase, we fitted the maps in Figure 3.14 a,e based on the dielectric function measured at T=300 K and T=100 K in ref. [19]. Our analysis shows that, if the interband oscillators are arbitrarily freezed, the transient reflectivity above T_C can be fitted by modifying only the scattering rate of the Drude peak (Γ_D) in the dielectric function (Figure 3.14b,f), in agreement with other works [19, 47, 62].

It is worth to note that the dynamics of Γ_D is independent from the pump photon energy and the pump polarization. In Figure 3.14d,h the four curves corresponding to different pump wavelength and polarization nearly overlap, apart from a scaling factor that could be due to a slightly difference in the pumping fluences used. This suggests that the **k**-selectivity of the MIR pump photo-excitation is lost above the critical temperature, as a consequence of the closure of the SC gap.

The outcomes of the differential fits above T_C, however, poses the delicate question on how to deal with the superconducting-to-pseudogap transition. When the PG phase is approached from above, one parameter (Γ_D) would seem sufficient to track

the transition from the normal phase. This is not the case at T_C, where the differential fits would instead suggest a discontinuity in our models. By performing a temperature-dependent measurements across the SC transition, we will show in the next section that a transient change of both the central frequency and the spectral weight of the 2 eV oscillator can equivalently account for the signal in the PG phase. The bandwidth of our measurements is not sufficient to conclusively answer this question which we believe stems from the nature of the PG phase itself, that might either compete with the SC order or be its incoherent precursor [12, 63, 64].

3.6 RESPONSE ACROSS THE SUPERCONDUCTING TRANSITION

In order to track the evolution of the spectral weight across the superconducting phase transition, we have carried out temperature-dependent reflectivity measurements. Our setup, which is equipped with a remote temperature control, allows for a full characterization of the transient reflectivity $\Delta R(h\nu, t, T)$ within a single scan. This has the advantage of minimizing possible artifacts (due, for example, to different pumping fluences and pump-probe overlaps) and thus allowing for a more reliable comparison between the reflectivity at different temperatures.

3.6.1 *Measurements*

In Figures 3.15 and 3.16 we plot the time- and temperature-dependent transient reflectivity for four selected probe energies upon photo-excitation by the below- and above-gap photo-excitation, respectively. We stress that, at fixed temperature, these sets of measurements have been performed *at the same time*, by exploting the simultaneous presence of the two pumps and the broad bandwidth of the white-light probe. The polarization of the pump is indicated in the sketch on the left. What clearly emerges from the comparison of all the maps is that the critical temperature (marked by the dashed black line) cannot be univocally inferred from the measurements. A temperature-dependent discontinuity can be detected in all the maps, but its features strongly depend on the probe energies, as well as on the pump polarization and photon energy.

In general, these differences are less distinct at higher probe energies ($h\nu$=1.9 eV) and become more and more evident as the probe photon energy is decreased. At $h\nu$=1.57 eV, the superconducting transition is marked by a change in sign (from positive to negative when T_C is approached from below) when the pump is polarized along the CuCu axis; however, in the other polarization configuration, the transient reflectivity is always negative and the superconducting transition is accompanied instead by a smooth increase in the amplitude of the signal.

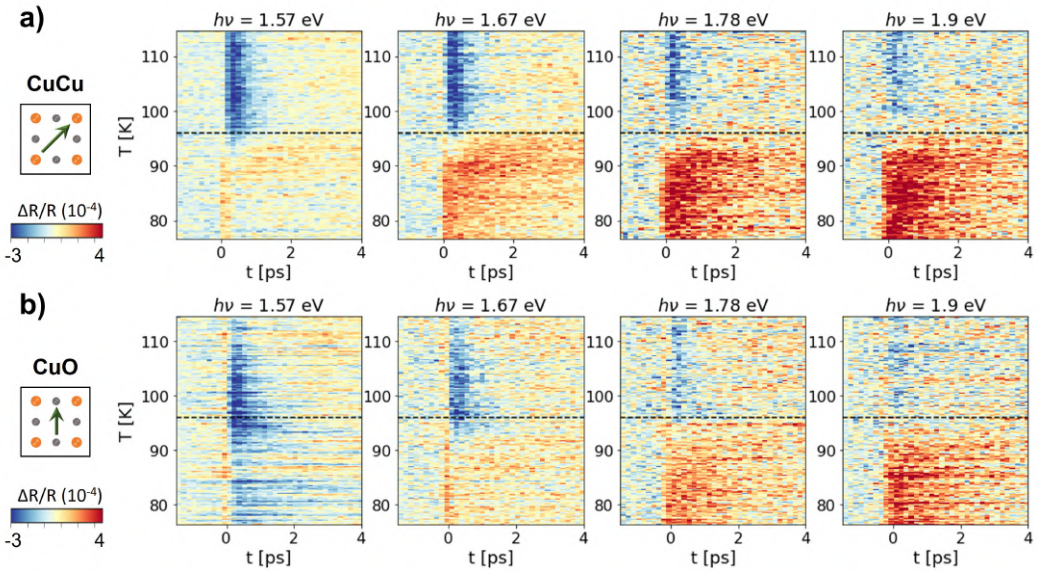

Figure 3.15: **Temperature-dependence upon sub-gap photo-excitation. a)** Transient reflectivity as function of temperature and pump-probe delay following the MIR pump pulse (ϕ_{MIR} = 28 μJcm^{-2}) at different probe energies, indicated in the title of each panel. The pump pulse was polarized along the CuCu axis, as illustrated by the sketch of the CuO_2 plaquette on the left. The black dashed line marks the sample critical temperature. **b)** Same as a) but for the pump polarized along the CuO axis.

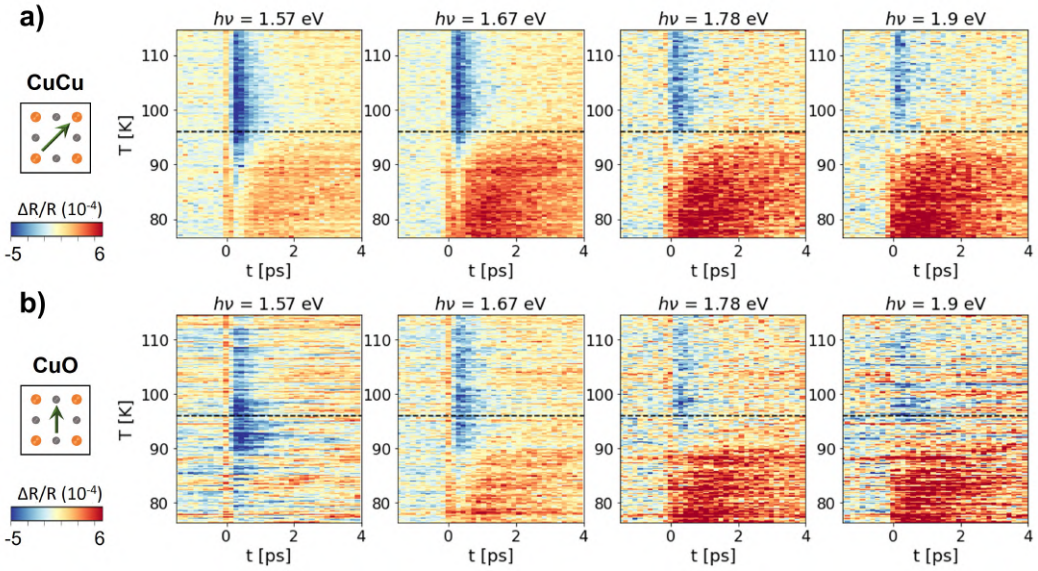

Figure 3.16: **Temperature-dependence upon above-gap photo-excitation. a-b)** Transient reflectivity as function of temperature and delay for different probe energies after photo-excitation by the NIR pump (ϕ_{NIR} = 19 μJcm^{-2}) polarized along the CuCu and CuO axis, respectively.

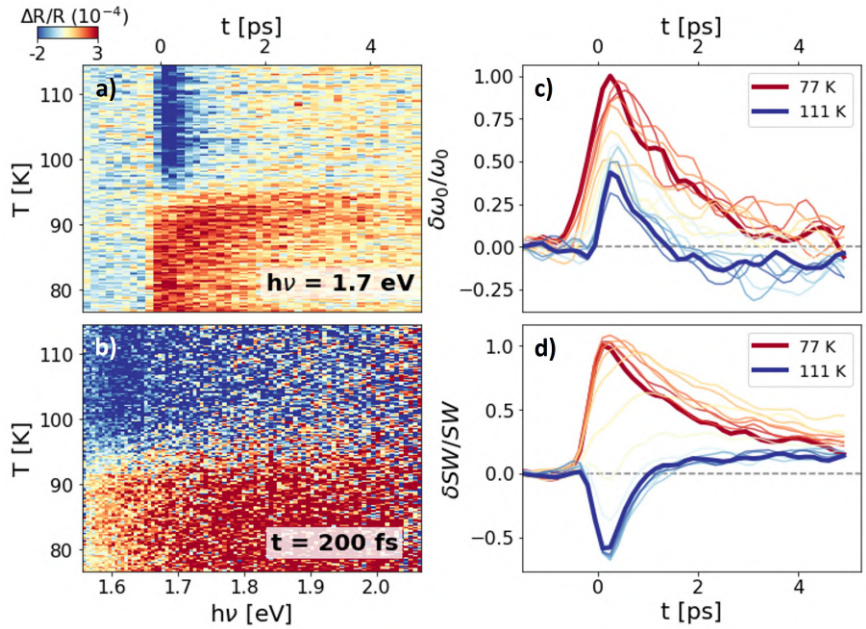

Figure 3.17: **Temperature-dependent dynamics of the interband excitation. a)** Transient reflectivity as function of temperature and time delay at fixed probe energy (1.7 eV) upon photo-excitation by the MIR pump polarized along the CuCu axis (ϕ_{MIR}=28 μJcm^{-2}). **b)** Same as a) but as function of temperature and probe energy at fixed time delay (200 fs). **c)** Time-dependent normalized transient change in the central frequency of the ω_0=2 eV oscillator for selected temperatures measured in a). **d)** Time-dependent normalized transient change in spectral weight for selected temperatures in a).

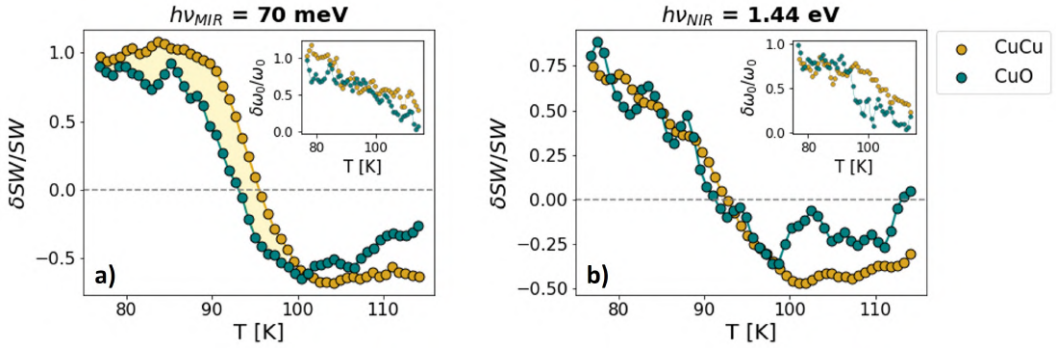

Figure 3.18: **Pump-induced change of the interband excitation across the superconducting transition. a-b)** Transient change of the spectral weight of the 2 eV oscillator at t=250 fs as function of temperature induced by the below- and the above-gap excitation, respectively, polarized along the CuCu (gold) and CuO (green) axis. The insets show the temperature-dependent transient change of the central frequency of the oscillator at t=250 fs.

3.6.2 *Temperature-dependence of the oscillator dynamics*

We fitted the reflectivity maps using the model described in Section 3.4.1. As an example, we plot in Figure 3.17a only the response to the sub-gap pump polarized along the CuCu axis. At each temperature, the broadband response of the sample is measured by the white-light probe (Figure 3.17b) and we select one specific probe energy (1.7 eV) to plot the color-coded map in Figure 3.17a.

The results of the differential analysis are plotted in Figure 3.17c,d, where we show the dynamics of ω_0 and SW, respectively, of the 2 eV transition at different temperatures, from the SC phase (red curves) to the PG one (blue curves). The dynamics of the central frequency of the oscillator does not display a strong dependence on the temperature and remains positive also above T_C. On the contrary, the SW dynamics abruptly changes sign when T_C is approached.

In Figure 3.18 we plot the central frequency and the spectral weight as function of temperature, in correspondence with the maximum pump-induced change (t=250 fs). The insets show the temperature dependence of ω_0, indicating that no sharp transitions occur at T_C regardless of the photon energy of the pump and its polarization. On the other hand, the impulsive change of SW of the 2 eV interband oscillator represents a good indicator of the SC phase transition (Figure 3.18a,b).

This analysis emphasizes once again the interplay between the condensate formation and the high-energy electronic excitations in the material. In fact, it is known that at equilibrium a transfer of spectral weight from the high-energy spectral region to the zero-frequency δ-function of the condensate occurs at T_C, as discussed in Section 3.1.1 [24, 26]. Following the same interpretation, the pump-induced spectral weight change we observe below T_C should be interpreted as a direct consequence of the quench of the SC state, which in our measurements appear to be not directly related to the shift of the central frequency of the 2 eV oscillator.

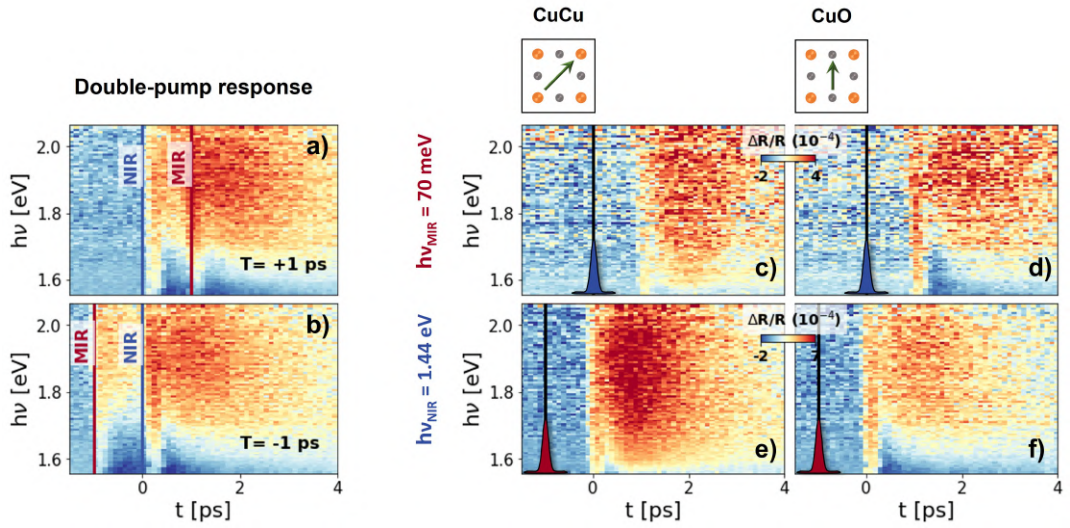

Figure 3.19: **Transient response of non-thermal states at T=74 K. a-b)** Example of the double-pump response measured in the experiment. The MIR pump impinges on the sample 1 ps after (T= + 1 ps) and 1 ps before (T= -1 ps) the NIR pump, respectively. The x-axis is the time delay between the NIR pump and the white-light probe. **c)** Broadband transient reflectivity upon photo-excitation by the MIR pump on a system that has been previously (at t = 0 ps) excited by the above-gap pump, as indicated by the blue Gaussian-shaped pulse. Both the MIR and the NIR polarizations are parallel to the CuCu axis, as illustrated in the top sketch. The pump fluences are ϕ_{MIR} = 28 μJcm^{-2} and ϕ_{NIR} = 19 μJcm^{-2}. **d)** Same as a) but for the pumps' polarization parallel to the CuO axis. **e-f)** Same as c-d) but for a swapped order of arrival of the pumps.

Interestingly, the excitation by above- and below-gap pumps yields different results. While high-photon energy pulses, regardless of their polarization, quench the condensate at temperatures lower than the equilibrium T_C (Figure 3.18b), sub-gap pulses have an anisotropic effect (Figure 3.18a). When the MIR pump is polarized along the CuO axis, the quench is similar to the one induced by high-photon energy pulses. However, when the MIR polarization is parallel to the CuCu axis, the discontinuity in the optical response associated to the SC transition occurs at higher temperatures.

The scenario that emerges is consistent with our previous observation of a SC-like response in single-colour reflectivity measurements enhanced by MIR pulses polarized along the CuCu axis [54]. In this regard, the employment of a broadband probe and thus the use of the spectral weight as an observable enable us to provide a more general result. Importantly, our measurements highlight that the anisotropy of the sub-gap pulses arises from the anisotropic response of the high-energy electronic excitation to the perturbation, which in turn affects the dynamics of the condensate.

3.7 OPTICAL RESPONSE OF NON-THERMAL STATES

The anisotropy found between the excitation through above- and sub-gap pulses suggests that the transient non-thermal states photo-induced by these two perturbations are different. In particular, the single-pump measurements showed that i) the dynamics of the spectral weight of the 2 eV oscillator photo-induced by the NIR and MIR pump is different in the SC phase ii) its temperature-dependence marks the onset of superconductivity and revealed that high-photon energy pulses dynamically quench the condensate more efficiently.

In order to understand the origin of such anisotropy, we study here the dynamical response of a sample previously prepared in a non-thermal state by the photo-excitation with a first impinging pulse. The rationale of the approach is that, depending on the photon energy of the first pump, the resulting non-thermal QP distribution across the Brillouin zone is expected to be different. A second pump-probe sequence is then employed to measure the broadband transient response of the photo-induced non-thermal state. We have delayed the second pump-probe sequence by 1 ps with respect to the first pump: this choice guarantees that the initially excited QP are not completely relaxed before the arrival of the second pump [61] and, at the same time, avoids possible coherent artefacts arising from the temporal overlap of the two pumps.

3.7.1 *Measurements*

Experimentally speaking, the synchronized rotation of the pumps' optical choppers enables the acquisition, at every time delay between the first and the second pump (T), of the double-pump response, as illustrated in Figure 3.19a,b. These maps contain the response to both the MIR and the NIR pumps that are properly delayed in time, as indicated by the coloured vertical lines. At the same time, the single-pump response to both the pumps are also recorded. The direct subtraction between the double-pump maps and the single-pump ones allows for a full characterization of the sample dynamics probed either in its ground or excited state.

As an example, in Figure 3.19c we plot the point-by-point subtraction between the double-pump response at T=+1 ps and the single-pump NIR one (impinging on the sample at t=0, as indicated by the blue Gaussian). The result of the subtraction is the response to the MIR photo-excitation of a system that, at the moment of the interaction with the MIR pump, is no longer in its thermal state, but has been driven into a transiently excited state by the NIR pump. The study of Figure 3.19c represents therefore a direct way to access the dynamics of the excited state.

In Figure 3.19c,d we plot the MIR-induced broadband dynamics in a sample previously excited by the NIR pump. The two maps differ by the polarization configuration used: both the pumps are polarized along the CuCu axis in c) and along the CuO axis in d). In Figure 3.19e,f the order of arrival of the two pumps is swapped, and we plot

instead the NIR-induced change in reflectivity in a sample previously excited by the MIR pump.

The comparison between Figure 3.19 and the single-pump responses in Figure 3.8 highlights once again that the optical response strongly depends on the photon energy of the pump. Specifically, the time- and energy-resolved response to the NIR pump is the same regardless of the initial state of the sample, be it thermal (Figure 3.8c,d) or "prepared" by the MIR pump (Figure 3.19e,f). On the contrary, the response to the MIR pump is different in the two scenarios in both the polarization configurations. In particular, the MIR-induced dynamics is faster when the sample has previously interacted with the NIR pump (Figure 3.19a,b) than when the sample lies in a thermal state (Figure 3.8 a,b). From a qualitative point of view, the maps in Figure 3.19a,b resemble the ones in Figure 3.8c,d, i.e. the transient reflectivity maps upon photo-excitation by the above-gap pump.

3.7.2 *Spectral weight dynamics*

In order to gain a deeper understanding of these dynamics, we have carried out a differential fit of the reflectivity maps in Figure 3.19c-f. We plot in Figure 3.20 the results of the measurements. For clarity, we plot only the dynamics of the *SW* obtained through the differential fits, as we observed no difference in the dynamics of the ω_0 of the 2 eV oscillator.

The comparison of the *SW* dynamics photo-induced by the high-photon energy pulses with or without the previous interaction with the low-photon energy pump reveals that the dynamics is not affected by the initial state of the sample, be it at the equilibrium or driven into a non-thermal state by the excitation with the sub-gap pump (Figure 3.20a,b). On the contrary, if the order of the two pumps is reversed (i.e. the NIR pump prepares a non-thermal state that is subsequently photo-excited by the MIR pump) the *SW* dynamics is markedly different (Figure 3.20c,d). When a QP population is excited by the above-gap pump, the *SW* dynamics revealed by the sub-gap pump, regardless of the pumps' polarization, is qualitatively similar to the one measured by the NIR pump only, featuring an initial fast-decaying response superimposed to a slower delayed dynamics.

Importantly, this difference is peculiar of the SC phase. In Figure 3.20e we plot the differential reflectivity ($\Delta\Delta R/R$) across the SC phase transition, obtained as the difference between the response to the MIR photo-excitation of the sample at the equilibrium and of the sample excited in a non-thermal state by the NIR pump, as illustrated in the sketch on top of the panel. The differential signal vanishes above T_C (dashed black line), indicating that the response in the PG phase is not affected by the previous above-gap photo-excitation.

The picture that emerges is that the anisotropy found between high- and low-photon energy excitations is closely related to the presence of the SC gap. When the gap is open, its *d*-wave symmetry makes the distribution of photo-injected QP dependent on the photon energy of the perturbation. While NIR pulses deliver

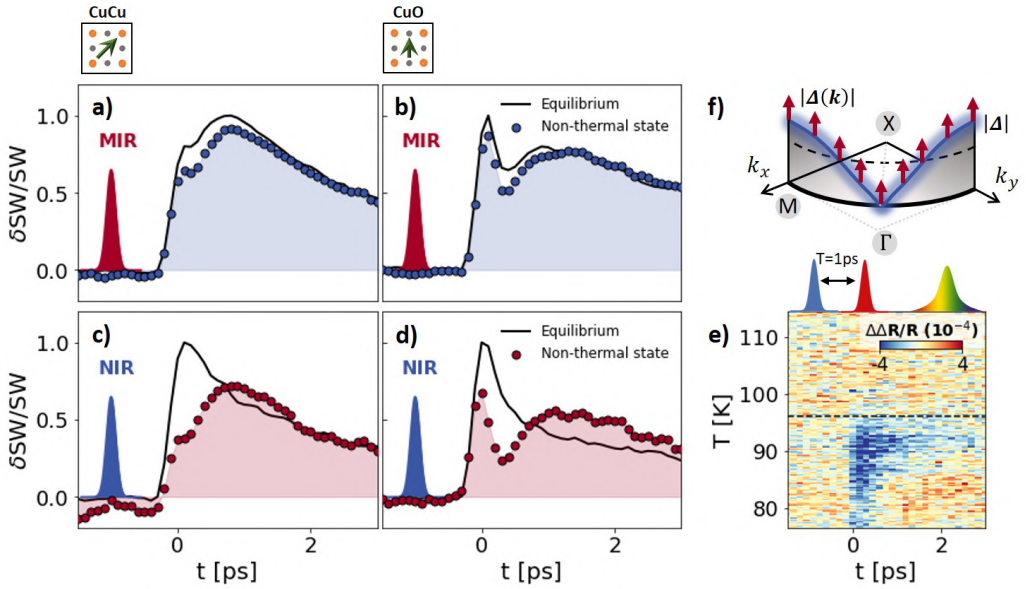

Figure 3.20: **Transient response of non-thermal states at T=74 K. a-b)** The black line indicates the spectral weight dynamics photo-induced by the NIR pump in a sample (T=74 K) initially at the equilibrium (as in Figure 3.8f). The blue dots represent the same dynamics, but for a sample excited 1 ps earlier into a non-thermal state by a sub-gap photo-excitation co-polarized with the NIR pump. The pumps' polarization are sketched on top of the panels. **c-d)** Same as a-b) but for the spectral weight photo-induced by the MIR pump with (red) and without (black) a previous excitation with the NIR pump. **e)** Temperature-dependent differential signal obtained by subtracting the single-pump responses from the joint response measured with both pumps. The NIR pump photo-excites the sample 1 ps before the MIR pump, which interacts with the sample at t=0 (as sketched on top of the panel). The time in the map (horizontal axis) is the delay between the MIR pump and the white-light probe. **f)** Sub-gap photo-excitation of a uniform, non-thermal quasiparticle distribution previously excited by the high-photon energy pump.

sufficient energy to excite QP throughout the entire Brillouin zone, MIR pulses target mostly the nodal regions as they are not energetic enough to initiate transitions at the antinodes. As a consequence, when the sub-gap pump prepares the system in a non-thermal state, the dynamics measured by the NIR pump is not modified because the second pump itself injects a homogeneous QP distribution. However, when the order of arrival is swapped, the dynamics measured in a thermal or in a non-thermal state is clearly different. This is sketched in Figure 3.20f. If the system is previously excited by the NIR pump, a uniform QP distribution is excited (blue glowing line). The subsequent MIR pump (that, at the equilibrium, would not deliver enough energy to excite the antinodes, as indicated by the horizontal dashed black line) can now couple to the pre-excited homogeneous QP distribution, giving rise to a recombination dynamics that is qualitatively similar to the one initiated by the

photo-excitation with high photon energy alone. Above T_C, this difference vanishes and the momentum-selectivity of the MIR excitation is suppressed.

3.8 CONCLUSIONS

In summary, we found that the transient response in optimally-doped Y-Bi2212 below T_C can be fully accounted for by the blueshift and the impulsive change of spectral weight of an interband oscillator at 2 eV. The measurements do not clarify the nature of this excitation, that, based on previous reports, could involve either in-plane Cu-O excitations or *dd* orbital transitions. Importantly, we observe that, while the blueshift of the 2 eV oscillator is not affected by the colour of the pump, the dynamics of its spectral weight is sensitive to both the pump photon energy and the pump polarization, and displays a clear signature of the onset of superconductivity. We used the spectral weight dynamics as an observable to study the response of the sample to the subsequent excitation by the near-infrared and the mid-infrared pumps. Our measurements confirm that, while NIR pulses produce an accumulation of QP at the antinodes, MIR ones mostly inject electronic excitations in the nodal regions. These results indicates that the dynamical control of the momentum-dependent distribution of non-thermal QP may be achieved by the selective tuning of the photo-excitation.

A DRUDE-LORENTZ OSCILLATOR MODEL

The Drude-Lorentz model relates the macroscopic optical properties of materials to their microscopic electronic structure. In this model, electrons are bound to the nuclei via an elastic force and driven by the oscillating electric field [65]. Starting from the equation of motion of electrons in such picture, we will derive in the following the dielectric function and the main optical properties of solids.

Polarization in dielectric materials

In non-conducting isotropic media the macroscopic polarization is the result of the electrons' displacement $\mathbf{r}$ from their equilibrium position:

$$\mathbf{P} = -Ne\mathbf{r} \tag{A.1}$$

where N is the number of electrons per unit volume. When the displacement arises from the application of an external electric field $\mathbf{E}$, the resulting polarization depends on its oscillating frequency ω. In the most simple case of a static field ($\omega = 0$), the force equation for an electron that is bound elastically with force constant K to its nuclues is $-e\mathbf{E} = K\mathbf{r}$, so the polarization reads:

$$\mathbf{P} = \frac{Ne^2}{K}\mathbf{E} \tag{A.2}$$

When dealing with time-varying electric fields, the full differential equation of motion of the electrons must be considered. In the Drude-Lorentz model, the electrons bound to their nuclei behave as classical damped harmonic oscillators:

$$m\frac{d^2\mathbf{r}}{dt^2} + m\gamma\frac{d\mathbf{r}}{dt} + K\mathbf{r} = -e\mathbf{E} \tag{A.3}$$

where m and e are the electron mass and charge, respectively. The damping term $m\gamma(d\mathbf{r}/dt)$ does not have a specific microscopic origin, but accounts for the collisions among the charges and prevents the divergence of the oscillations for a resonant driving field. If we consider the electric field to oscillate in time according to the factor $e^{-i\omega t}$, the equation of motion becomes:

$$(-m\omega^2 - i\omega m\gamma + K)\mathbf{r} = -e\mathbf{E} \tag{A.4}$$

The more general expression of Equation A.2 is therefore:

$$\mathbf{P}(\omega) = \frac{Ne^2}{m}\frac{1}{\omega_0^2 - \omega^2 - i\gamma\omega}\mathbf{E} \tag{A.5}$$

where we have defined $\omega_0 = \sqrt{K/m}$ to be the effective resonance frequency of the electrons.

The Drude-Lorentz dielectric function

In order to derive how the polarization affects the propagation of light in the material, we need to solve the wave equation. In non-magnetic materials with no external charges and currents, the Maxwell equations are:

$$\nabla \times \mathbf{E} = -\mu_0 \frac{\partial \mathbf{H}}{\partial t} \tag{A.6}$$

$$\nabla \times \mathbf{H} = \varepsilon_0 \frac{\partial \mathbf{E}}{\partial t} + \frac{\partial \mathbf{P}}{\partial t} + \mathbf{J} \tag{A.7}$$

$$\nabla \cdot \mathbf{E} = -\frac{1}{\varepsilon_0} \nabla \cdot \mathbf{P} \tag{A.8}$$

$$\nabla \cdot \mathbf{H} = 0 \tag{A.9}$$

By taking the curl of Equation A.6 and substituting the time derivative of Equation A.7, one gets the general wave equation for the electric field:

$$\nabla \times (\nabla \times \mathbf{E}) + \frac{1}{c^2} \frac{\partial^2 \mathbf{E}}{\partial t^2} = -\mu_0 \frac{\partial^2 \mathbf{P}}{\partial t^2} - \mu_0 \frac{\partial \mathbf{J}}{\partial t} \tag{A.10}$$

where the terms on the right side of the equation are the *source terms* due to the presence of polarization and conduction charges, respectively. If we restrict the discussion to dielectric media only ($\mathbf{J} = 0$) and note from Equation A.8 that $\nabla \cdot \mathbf{E} = 0$ due to the linear relationship between $\mathbf{P}$ and $\mathbf{E}$, we get:

$$\nabla^2 \mathbf{E} = \frac{1}{c^2} \left(1 + \frac{Ne^2}{m\varepsilon_0} \frac{1}{\omega_0^2 - \omega^2 - i\gamma\omega} \right) \frac{\partial^2 \mathbf{E}}{\partial t^2} \tag{A.11}$$

If we consider a solution of the form of a plane harmonic wave ($\mathbf{E} = \mathbf{E_0} e^{i(\mathcal{K}(\omega)z - \omega t)}$), we get by substitution that a possible solution is given by:

$$\mathcal{K}(\omega)^2 = \frac{\omega^2}{c^2} \left(1 + \frac{Ne^2}{m\varepsilon_0} \frac{1}{\omega_0^2 - \omega^2 - i\gamma\omega} \right) \tag{A.12}$$

This quantity is directly related to the complex index of refraction through the relation:

$$\mathcal{N}(\omega) = n(\omega) + i\mathrm{k}(\omega) = \frac{c}{\omega} \mathcal{K}(\omega) \tag{A.13}$$

where $n(\omega)$ is the ordinary refractive index and $\mathrm{k}(\omega)$ is the extinction coefficient.

By defining the dielectric function as the square root of the complex refractive index, we get:

$$\varepsilon(\omega) = \varepsilon_1(\omega) + i\varepsilon_2(\omega) = 1 + \frac{\omega_P^2}{\omega_0^2 - \omega^2 - i\gamma\omega} \tag{A.14}$$

where we have defined $\omega_P^2 = \frac{Ne^2}{m\varepsilon_0}$ as the plasma frequency that is proportional to the number of carriers that are involved in the transition. The imaginary part of the dielectric function has a Lorentzian shape which is centered at the transition frequency ω_0 and whose spectral weight (or *oscillator strength*) is proportional to ω_P. Finally, in Equation A.14 we have tacitly assumed that all electrons are subject to the same identical force. In a real material, several optical transitions are allowed that can be all modelled as interband Lorentzian oscillators. The plasma frequencies weight each transition according to the fraction of electrons involved. Moreover, also free carriers contribute to the final expression of the dielectric function and their contribution can be modelled as an oscillator centered at $\omega_0 = 0$. This term is the so-called Drude peak and accounts for the response of unbound charges to the driving electric stimulus. The more general Drude-Lorentz dielectric function can be written as:

$$\varepsilon(\omega) = \varepsilon_\infty - \underbrace{\frac{\omega_{P,D}^2}{\omega^2 + i\gamma_D\omega}}_{\text{Drude peak}} + \underbrace{\sum_i \frac{\omega_{P,i}^2}{\omega_i^2 - \omega^2 - i\gamma_i\omega}}_{\text{Lorentz interband oscillators}} \tag{A.15}$$

where ϵ_∞ is a phenomenological parameter that accounts for the higher energy oscillators that are not included in the summation. Ideally, if all transitions are considered it should be $\varepsilon_\infty = 1$.

Once the dielectric function is known, all the optical properties can be derived. In particular, the optical conductivity and the reflectivity at normal incidence read, respectively:

$$\sigma(\omega) = \sigma_1(\omega) + i\sigma_2(\omega) = i\frac{\omega}{4\pi}\left(\varepsilon(\omega) - 1\right) \tag{A.16}$$

$$R(\omega) = \left|\frac{1 - \sqrt{\varepsilon(\omega)}}{1 + \sqrt{\varepsilon(\omega)}}\right|^2 \tag{A.17}$$

KRAMERS-KRONIG RELATIONS As $\varepsilon(\omega)$ is causal response function, its real and imaginary parts are mutually related by the Kramers-Kronig (KK) relations:

$$\begin{aligned} \varepsilon_1(\omega) &= \varepsilon_\infty + \frac{1}{\pi}\mathcal{P}\int_{-\infty}^{+\infty} d\omega' \frac{\varepsilon_2(\omega')}{\omega' - \omega} \\ \varepsilon_2(\omega) &= -\frac{1}{\pi}\mathcal{P}\int_{-\infty}^{+\infty} d\omega' \frac{\varepsilon_1(\omega') - \varepsilon_\infty}{\omega' - \omega} \end{aligned} \tag{A.18}$$

where $\mathcal{P}$ is the Cauchy's principal value. The KK relations are particularly useful because they allow to retrieve the real/imaginary part of $\varepsilon(\omega)$ if, for example, its counterpart is experimentally available over a broad frequency range. Analogously, if raw reflectivity data are collected over a sufficiently broad range, both $\varepsilon_1(\omega)$ and $\varepsilon_2(\omega)$ can be inferred [66, 67], thus giving access to all the optical properties of the material.

Extended Drude model

The strength of the Drude-Lorentz model is that it has proved adequate to describe a large class of materials, from perfect metals to insulators. However, when many-body effects are dominant, such as in HTSC, an extended version of the formalism can be developed to more appropriately address the low-energy optical response [30, 21]. In this respect, the main limitation of the standard model lies in the treatment of the unbound charges, that are included in Equation A.15 as a uniform free electron gas. In order to account for the band structure, a renormalized effective mass m^* must be considered in the expression of ω_P instead of the bare electron mass m and the damping term must include the scattering rate from the impurities. Moreover, if the electronic degrees of freedom are coupled to bosonic excitations characterized by a typical spectral distribution, the scattering rate must be dependent on the frequency. This physics can be described within the extended Drude model (EDM) in which the frequency-independent scattering rate in Equation A.15 is phenomenologically replaced by a complex frequency-dependent scattering rate (or *memory function* $M(\omega)$) [68]:

$$\gamma_D \rightarrow \tilde{\gamma}_D(\omega) = \gamma_D(\omega) - i\omega\lambda_D(\omega) \tag{A.19}$$

where $1 + \lambda_D(\omega) = \frac{m^*(\omega)}{m}$. The quantities $\gamma_D(\omega)$ and $\lambda_D(\omega)$ account, respectively, for the spectral distribution of the scattering centers and the electron mass enhancement due to the many-body interactions. The Drude intraband contribution $\varepsilon_D(\omega)$ in Equation A.15 can be more conveniently re-written as:

$$\varepsilon_D(\omega) = \frac{\omega^{*2}_{P,D}(\omega)}{\omega^2 + i\gamma^*_D(\omega)\omega} \tag{A.20}$$

where we have defined $\omega^{*2}_{P,D}(\omega) = \frac{\omega^2_{P,D}}{1-\lambda_D(\omega)}$ and $\gamma^*_D(\omega) = \frac{\gamma_D(\omega)}{1-\lambda_D(\omega)}$. In the EDM formalism the single Drude peak centered at $\omega = 0$ is replaced by an infinite sets of Drude peaks that locally describe the dielectric function in proximity of a given ω and that are fully defined by the parameters $\gamma_D(\omega)$ and $\lambda_D(\omega)$.

From the microscopic point of view, the dielectric function in the EDM is fully determined by the memory function $M(\omega)$. Depending on the nature of the bosonic excitations (phonons, spin fluctuations, loop currents) coupled to the electronic degrees of freedom, a coupling function can be defined. Reversely, by modelling the experimentally measured optical conductivity with a EDM (Equation A.20), the electron-boson coupling function can be extracted and shed light on the excitation spectrum of the bosons coupled to the charge carriers. In HTSC, the EDM formalism has been implemented in different experimental techniques that all point to a unified picture in which the bosonic excitation spectrum at low temperature is peaked between 30-60 meV, consistently with both spin fluctuation and phonon coupling [69]. A detailed discussion on the implications of these findings goes beyond the scope of this work, that is mainly focused on the role of high-energy excitations ($\gtrsim$ 1.25 eV) in HTSC.

B FIT OF THE EQUILIBRIUM DIELECTRIC FUNCTION IN Y-BI2212

In order to fit the low-energy side of the spectrum within a simple (not-extended) Drude model, we have included two mid-infrared peaks, whose parameters have not been constrained. These oscillators account for the intraband transitions and are the most affected (along with the Drude peak) by the sample temperature. The visible region of the reflectivity is modelled by three oscillators whose central frequencies are $\omega_0 \sim 1.46$, 2 and 2.72 eV in the superconducting phase. Three higher-energy contributions (>3 eV) model the dielectric function above the CT-edge.

Oscillator	Parameter	T=20K	T=100K	T=300K
Drude peak	ε_∞	2.67	2.62	2.62
	ω_0	0	0	0
	ω_P	10766	11492	10628
	γ	26	180	349
Mid-infrared peaks	ω_0	942	1140	1345
	ω_P	13411	13928	14654
	γ	3985	5532	5526
	ω_0	6309	6530	6626
	ω_P	5102	2279	1174
	γ	4841	2958	1707
Visible peaks	ω_0	11800	12305	12305
	ω_P	2358	2261	2472
	γ	3644	4872	4872
	ω_0	16163	16075	16026
	ω_P	6385	5296	5500
	γ	8304	8160	8097
	ω_0	21947	21947	21947
	ω_P	15026	15600	15603
	γ	13998	13998	14688
Higher-energy contributions	ω_0	31165	31059	30913
	ω_P	17039	17363	18115
	γ	5896	6187	6884
	ω_0	35567	35479	34598
	ω_P	17317	16448	11610
	γ	5765	6224	5758
	ω_0	41677	40614	39715
	ω_P	27979	27430	28795
	γ	5000	5000	6949

Table B.1: Drude-Lorentz parameters obtained via Kramers-Kronig constrained fits [58] of the static reflectivity at different temperatures. All values are expressed in [cm^{-1}].

C DESCRIPTION OF THE ERROR ANALYSIS

We describe here the error analysis performed on the broadband pump-probe measurements. As an example, we limit our discussion to the response upon the photo-excitation of the near-infrared pump polarized along the CuO axis (Figure 3.8d), but it can be similarly extended to all the measurements presented in the chapter.

For each pump-probe time delay (t), we acquire, according to the status of the optical chopper blocking the pump, two spectra as function of the probe photon energy (E_{pr}): a pumped (P) and an unpumped (U) one. We scan all the pump-probe delays and run again the same measurement N times (where N=30 in the measurements discussed in the chapter). For each pump-probe measurement we can thus evaluate two quantities:

$$P(t, E_{pr}) = \bar{P}(t, E_{pr}) \pm \sigma_P(t, E_{pr}) \tag{C.1}$$

$$U(t, E_{pr}) = \bar{U}(t, E_{pr}) \pm \sigma_U(t, E_{pr}) \tag{C.2}$$

where the bar indicates the mean value and σ the standard deviation. We plot $\bar{P}(t, E_{pr})$ in Figure C.1a and $\sigma_P(t, E_{pr})$ in Figure C.1b, where each curve corresponds to a different time delay. The relative error $P_{rel}(t, E_{pr}) = \sigma_P(t, E_{pr})/\bar{P}(t, E_{pr})$ is plotted in Figure C.1c. We observe that the standard deviation is generally proportional to the mean value, indicating a bigger σ for those photodiodes (i.e. E_{pr}) illuminated by a higher number of photons.

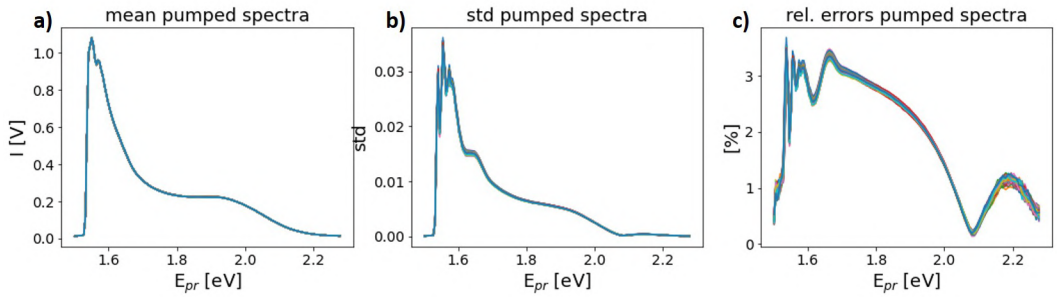

Figure C.1: **Pumped spectra acquired at different time delays. a)** Each curve is the mean (averaged over 30 repetitions) pumped spectrum of the white-light probe acquired at a given pump-probe time delay. The curves corresponding to different time delays are superimposed in the graph. **b)** Standard deviation of the pumped spectra evaluated, at each pump-probe delay, over the 30 repetitions. **c)** Relative errors of the pumped spectra, obtained by dividing each curve in b) by its corresponding curve in a).

We evaluate the transient reflectivity as:

$$\Delta R/R(t, E_{pr}) = \frac{P(t, E_{pr}) - U(t, E_{pr})}{U(t, E_{pr})} \equiv \bar{X} \pm \sigma_X \tag{C.3}$$

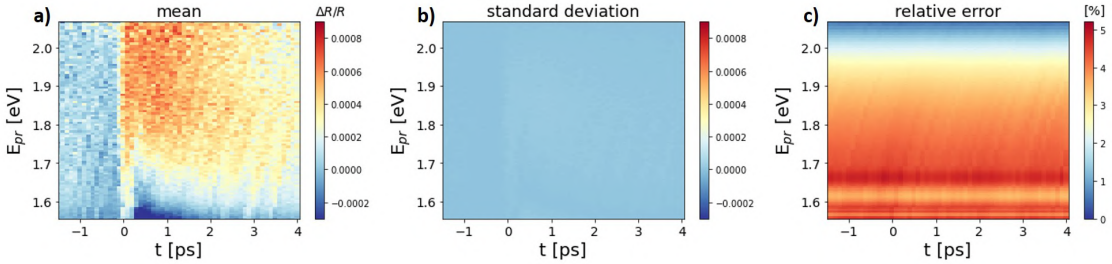

Figure C.2: **Pump-probe maps. a)** Average transient reflectivity map as function of the pump-probe delay and the probe photon energy. **b)** Standard deviation map associated to the map in a). Note that the color scales in a) and b) are the same. **c)** Map of the relative errors.

where, by dropping the dependencies, we have defined:

$$\bar{X} = \frac{\bar{P} - \bar{U}}{\bar{U}} \tag{C.4}$$

$$\sigma_X = |\bar{X}| \sqrt{\left(\frac{\sigma_P}{\bar{P}}\right)^2 + \left(\frac{\sigma_U}{\bar{U}}\right)^2} \tag{C.5}$$

as a result of the propagation of the relative errors.

We plot $\bar{X}$ and σ_X in Figure C.2a,b, respectively. To facilitate the comparison, we have used the same color scale in the two maps. In Figure C.2b, a small increase of the standard deviation is observed in correspondence with the pump-probe overlap, but the relative error (Figure C.2c) is not affected by the arrival of the pump. We obtain a relative error on the pump-probe measurements that is less than 5% over the probe bandwidth that we have considered in the text (1.56-2.06 eV).

In this connection, we highlight that the estimation carried out here holds for the single-pump response. When we perform the point-by-point subtraction of the double-pump and the single-pump responses to obtain the maps in Figure 3.19c-f, the resulting relative error is the square-root of the sum of the relative errors of the individual maps. The relative error associated to the maps in Figure 3.19c-f is thus less than 7%.

In Figure C.3 the grey and the red curves are the standard deviations obtained with Equation C.5 at t=-1 ps and t=100 fs, respectively (i.e. vertical cuts of the map in Figure C.2b). They display only a mild dependence on the probe photon energy.

We stress that we have discussed so far only a purely statistical error. The fact that the photodiodes have a finite (possibly photon energy-dependent) dynamic range is an additional source of noise. The main consequence is that the detection of small, pump-induced intensity changes could be more difficult in those regions of the white-light spectrum that are less intense. This is evident in the reflectivity maps (Figure C.2a for example), where the transient signal is cleaner at lower photon energies, where the intensity of the white-light spectrum is higher (Figure C.1a).

In order to provide an estimate of this effect, we compute at each probe energy the standard deviation among all the negative times at our disposal in Figure C.2a.

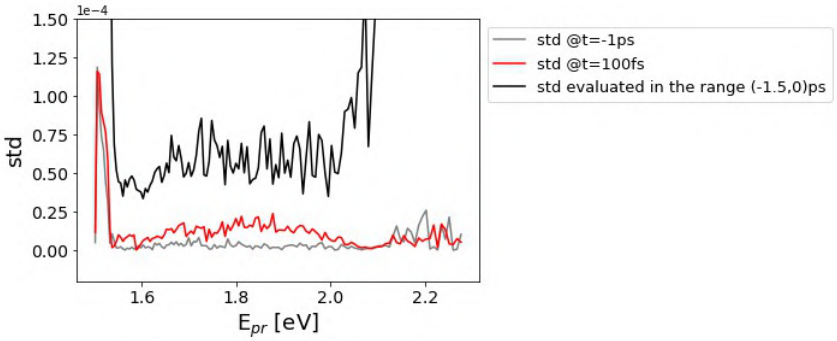

Figure C.3: **Comparison of the standard deviations.** The grey and red curves are the standard deviations at t=-1 ps and t=100 fs, respectively (vertical cuts in Figure C.2b). The black curve is the standard deviation evaluated, at each probe energy, by considering the set of negative times in Figure C.2a.

As all these points should average to zero at $t < 0$, by quantifying how much they deviate from this trend as function of E_{pr}, we can estimate how much we are sensitive to the detection of small intensity changes at different probe photon energies. The black curve in Figure C.3 is the result of this analysis, where it is clear that the standard deviation is higher at higher energies. We will associate this energy-dependent standard deviation to the pump-probe data for all the pump-probe delays. In particular, this analysis will be useful to constrain the differential fits discussed in Appendix D.

D DIFFERENTIAL FITS IN THE SUPERCONDUCTING PHASE

In this Appendix, we describe in detail how the differential fits of the transient broadband reflectivity maps have been performed. As a reference, we will only consider the reflectivity map in Figure 3.8d ($h\nu_{pump}$ = 1.44 eV, pump polarization parallel to the CuO axis).

The procedure is the following: we compute the static reflectivity ($R_{eq}(\omega)$) at a given temperature obtained through the best-fitting Drude-Lorentz model in Table B.1. We duplicate the reflectivity and create a new function ($R_{exc}(\omega, t)$) in which we let selected parameters to change at different pump-probe delays. We finally directly fit the measured $\Delta R/R(\omega, t)$ map using the following equation: $(R_{exc}(\omega, t) - R_{eq}(\omega))/R_{eq}(\omega)$. In this way, the fit returns the pump-induced change in the oscillator parameters that have been modified to fit the transient data.

In Figure D.1a, we illustrate the fit results for a selected time delay (t=200 fs, intergrated over 3 consecutive time delays) for the transient reflectivity upon photo-excitation by the near-infrared pump polarized along the CuO axis. The errorbars indicate the energy-dependent standard deviations estimated in Appendix C (black curve in Figure C.3 divided by a $\sqrt{3}$ factor to account for the integration over 3 time delays). In each panel, we modify a different oscillator in the Drude-Lorentz model, as reported in the title. An impulsive modification of the scattering rate of the Drude peak cannot describe the data in the SC phase (top left panel). In the following panels, we have modified at the same time the three parameters (ω_0, ω, γ) that fully characterize each oscillator. The modification of the mid-infrared peaks and the 1.46 eV one returns fairly good agreement on the low-energy side of our probing window, but it does not provide a good description at higher energies. The two best fits are obtained by modifying either the 2 eV oscillator or the 2.72 eV one.

In order to choose the most reliable description, we have calculated how the reflectivity would dynamically change in these two scenarios on the entire energy axis of the static measurements. In fact, being our detection bandwidth about 0.6 eV wide, a good fit in our probing window could result in strong (larger than the measured ΔR/R) reflectivity variations even outside this region. We have therefore fitted the whole transient reflectivity map (i.e. for all the time delays, and not just a single temporal cut as in Figure D.1a) and obtained a "perturbed" model at each time step ($M_{exc}(t)$). We then used $M_{exc}(t)$ to compute the time-dependent reflectivity over the entire energy range. In Figure D.1b we show the results of this analysis. The panel on the left (right) is obtained by modifying the parameters of just the 2 eV (2.72 eV) oscillator. The solid black curve is the equilibrium reflectivity, while the dashed yellow curve is the computed out-of-equilibrium reflectivity at the pump-probe overlap (t=0). The color-coded lines indicate the relative reflectivity variation at different pump-probe delays (blue/negative times, red/positive times) multiplied by a 10^3 factor. It is clear that, while modifying the oscillator centered at 2 eV results in a 10^{-3} reflectivity change that is mostly localized across our probing window, the time-dependent modification of the 2.72 eV oscillator mostly affects the higher-energy scale and results in a reflectivity change which is 10 times larger than the one we

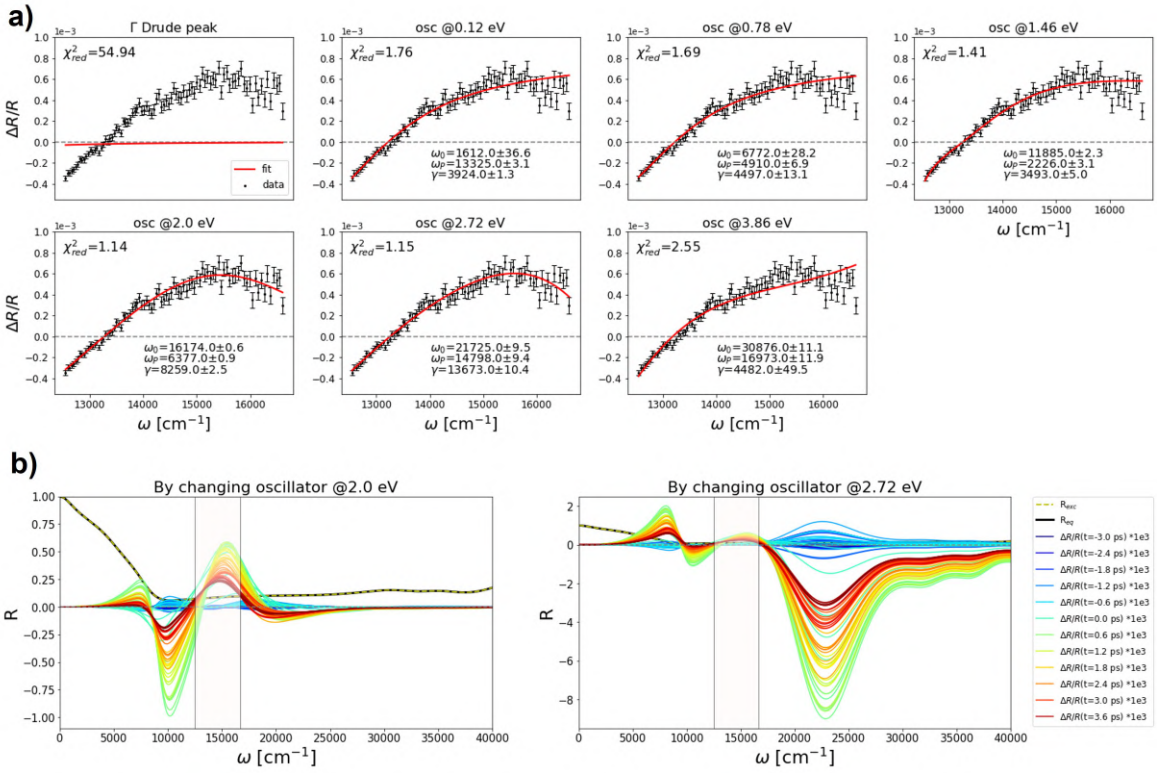

Figure D.1: **Differential fits in the superconducting phase. a)** The black dots are energy-dependent reflectivity cuts at a fixed time-delay (t=200 fs) upon photo-excitation by the 1.44 eV pump polarized along the CuO axis at T=74 K. The red line in each panel is a Drude-Lorentz differential fit obtained by modifying one oscillator at a time (reported in the title of each panel). The reduced χ^2_{red} and the best-fitting parameters are reported in the upper left and lower right corner in each panel, respectively. **b)** Static reflectivity (black curve), out-of-equilibrium reflectivity at the pump-probe overlap (yellow-dashed curve) and relative time-dependent reflectivity changes calculated over a broad frequency axis obtained by modifying the 2 eV (left panel) or the 2.72 eV (right panel) oscillator. The white-shaded area indicates are probing energy window.

measured. For this reason, we will restrict our analysis to a pump-induced variation of the 2 eV oscillator only, which guarantees, at the same time, a good differential fit to our data and a more reasonable behaviour outside the detection window.

In Figure D.2a (left panel), we plot the degrees of correlation among the fitted $(\omega_0, \omega_P, \gamma)$ parameters of the 2 eV oscillator. At each time-delay, we have performed a differential fit as described above. Each point in the plot is, at a given time-delay, one of the off-diagonal elements of the best-fitting symmetric 3x3 covariance matrix. The light green, yellow and dark green lines indicate the degree of correlation between ω_0, ω_P, ω_0, γ, ω_P, γ, respectively. It is clear that the three parameters in the fit are not independent and, in particular, ω and γ display the highest degree of correlation.

For this reason, we have tried to fit the data by modifying only two of the three parameters of the 2 eV oscillator. In the right panel of Figure D.2a, we plot in light

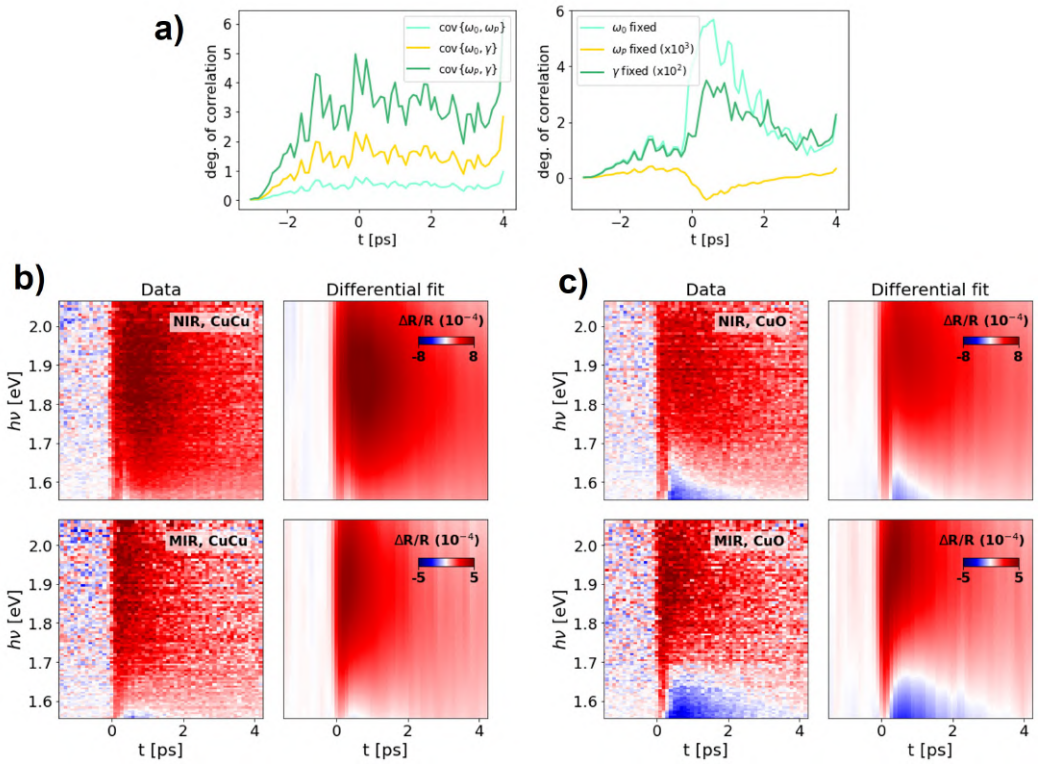

Figure D.2: **Differential fits with constrained parameters. a)** Left panel: off-diagonal elements as function of time-delay of the 3x3 covariance matrix obtained by modifying all the three parameters of the 2 eV oscillator . Each color refers to a different pair of parameters, as indicated in the legend. Right panel: time-dependent off-diagonal element of the 2x2 covariance matrix obtained by keeping fixed one of three parameters of the 2 eV oscillator. **b-c)** Comparison between data and fit keeping ω_P a fixed parameter. The labels in right upper corner of each reflectivity map indicate the photon energy and the polarization of the pump employed. The diverging colormap has been chosen to highlight where sign changes occur (white color).

green (yellow, dark green) the degree of correlation computed by keeping $\omega 0$ (ω_P, γ) fixed in the differential fit (i.e. the only off-diagonal element of the symmetric 2x2 covariance matrix). A joint analysis of the χ^2_{red} and the degree of parameters' correlation obtained in the three models led us to keep ω_P a fixed parameter in the fit. This choice, while does not significantly alter the quality of the fit, guarantees a degree of correlation which is two or even three orders of magnitude lower than in the other two scenarios (Figure D.2a, right panel). We show in Figure D.2b-c the comparison between the data (as in Figure 3.8) and the corresponding differential fits obtained by keeping ω_P fixed.

The conclusion that we draw is that a Drude-Lorentz differential analysis is not able discriminate between an impulsive change in the plasma frequency or in the scattering rate of the oscillator. This is due to the fact that we do not impose any normalization constraint on the time-dependent fitting Lorentzian functions. It is important to highlight, however, that the ω_0 dynamics is not affected by this choice and the central frequency of the oscillator remains an independent parameter of the differential fit.

A more convenient choice to analyse the time-dependent results of the differential fit is therefore to find an observable which is sensitive to the modification of either the plasma frequency or the scattering rate of the oscillator. We have used the spectral weight (SW) defined as follows:

$$SW = \int_0^\infty \sigma_1(\omega)\, d\omega = \frac{1}{4\pi} \int_0^\infty \omega \varepsilon_2(\omega)\, d\omega \tag{D.1}$$

In this framework, a pump-induced change in spectral weight ($\delta SW(t)$) is computed as the difference between the spectral weight calculated using the best-fitting "perturbed" model $M_{exc}(t)$ ($SW_{exc}(t)$) and the one calculated using the equilibrium model M_{eq} (SW_{eq}). The integration is computed over the whole energy axis of the static ellipsometry data in Figure 3.7.

REFERENCES

[1] J George Bednorz and K Alex Müller. Possible high tc superconductivity in the Ba-La-Cu-O system. *Zeitschrift für Physik B Condensed Matter*, 64(2):189–193, 1986.

[2] WW Warren Jr, RE Walstedt, GF Brennert, RJ Cava, R Tycko, RF Bell, and G Dabbagh. Cu spin dynamics and superconducting precursor effects in planes above T_C in $YBa_2Cu_3O_{6.7}$. *Physical review letters*, 62(10):1193, 1989.

[3] H Alloul, T Ohno, and P Mendels. ^{89}Y NMR evidence for a fermi-liquid behavior in $YBa_2Cu_3O_{6+x}$. *Physical review letters*, 63(16):1700, 1989.

[4] JW Lorama, KA Mirza, JR Cooper, and JL Tallon. Specific heat evidence on the normal state pseudogap. *Journal of Physics and Chemistry of Solids*, 59(10-12):2091–2094, 1998.

[5] AV Puchkov, P Fournier, DN Basov, T Timusk, A Kapitulnik, and NN Kolesnikov. Evolution of the pseudogap state of high-T_C superconductors with doping. *Physical review letters*, 77(15):3212, 1996.

[6] H Takagi, B Batlogg, HL Kao, J Kwo, Robert Joseph Cava, JJ Krajewski, and WF Peck Jr. Systematic evolution of temperature-dependent resistivity in $La_{2-x}Sr_xCuO_4$. *Physical review letters*, 69(20):2975, 1992.

[7] T Valla, AV Fedorov, Jinho Lee, JC Davis, and GD Gu. The ground state of the pseudogap in cuprate superconductors. *science*, 314(5807):1914–1916, 2006.

[8] Ch Renner, Bernard Revaz, J-Y Genoud, K Kadowaki, and Ø Fischer. Pseudogap precursor of the superconducting gap in under-and overdoped $Bi_2Sr_2CaCu_2O_{8+\delta}$. *Physical Review Letters*, 80(1):149, 1998.

[9] HJ Tao, Farun Lu, and EL Wolf. Observation of pseudogap in $Bi_2Sr_2CaCu_2O8 + \delta$ single crystals with electron tunneling spectroscopy. *Physica C: Superconductivity*, 282:1507–1508, 1997.

[10] N Miyakawa, P Guptasarma, JF Zasadzinski, DG Hinks, and KE Gray. Strong dependence of the superconducting gap on oxygen doping from tunneling measurements on $Bi_2Sr_2CaCu_2O_{8-\delta}$. *Physical review letters*, 80(1):157, 1998.

[11] VJ Emery and SA Kivelson. Importance of phase fluctuations in superconductors with small superfluid density. *Nature*, 374(6521):434–437, 1995.

[12] Michael R Norman, D Pines, and C Kallin. The pseudogap: friend or foe of high T_C? *Advances in Physics*, 54(8):715–733, 2005.

[13] J Zaanen, GA Sawatzky, and JW Allen. Band gaps and electronic structure of transition-metal compounds. *Physical review letters*, 55(4):418, 1985.

[14] Jacques Ghijsen, Liu-Hao Tjeng, Jan van Elp, Henk Eskes, Jos Westerink, George A Sawatzky, and Marek T Czyzyk. Electronic structure of Cu_2O and CuO. *Physical Review B*, 38(16):11322, 1988.

[15] H Eskes, MBJ Meinders, and GA Sawatzky. Anomalous transfer of spectral weight in doped strongly correlated systems. *Physical review letters*, 67(8):1035, 1991.

[16] FC Zhang and TM Rice. Effective hamiltonian for the superconducting Cu oxides. *Physical Review B*, 37(7):3759, 1988.

[17] Luca de'Medici, Xin Wang, Massimo Capone, and Andrew J Millis. Correlation strength, gaps, and particle-hole asymmetry in high-T_C cuprates: a dynamical mean field study of the three-band copper-oxide model. *Physical Review B*, 80(5):054501, 2009.

[18] Fabio Novelli, Gianluca Giovannetti, Adolfo Avella, Federico Cilento, Luc Patthey, Milan Radovic, Massimo Capone, Fulvio Parmigiani, and Daniele Fausti. Localized vibrations in superconducting $YBa_2Cu_3O_7$ revealed by ultrafast optical coherent spectroscopy. *Physical Review B*, 95(17):174524, 2017.

[19] Claudio Giannetti, Federico Cilento, Stefano Dal Conte, Giacomo Coslovich, Gabriele Ferrini, Hajo Molegraaf, Markus Raichle, Ruixing Liang, Hiroshi Eisaki, Martin Greven, et al. Revealing the high-energy electronic excitations underlying the onset of high-temperature superconductivity in cuprates. *Nature communications*, 2(1):1–7, 2011.

[20] Francesco Barantani, MK Tran, I Madan, Itzik Kapon, Nimrod Bachar, TC Asmara, E Paris, Y Tseng, W Zhang, Y Hu, et al. Resonant Inelastic X-Ray Scattering Study of Electron-Exciton Coupling in High-T_C Cuprates. *Physical Review X*, 12(2):021068, 2022.

[21] Claudio Giannetti, Massimo Capone, Daniele Fausti, Michele Fabrizio, Fulvio Parmigiani, and Dragan Mihailovic. Ultrafast optical spectroscopy of strongly correlated materials and high-temperature superconductors: a non-equilibrium approach. *Advances in Physics*, 65(2):58–238, 2016.

[22] Giacomo Ghiringhelli, NB Brookes, E Annese, H Berger, Claudia Dallera, M Grioni, L Perfetti, Alberto Tagliaferri, and Lucio Braicovich. Low energy electronic excitations in the layered cuprates studied by copper L_3 resonant inelastic x-ray scattering. *Physical review letters*, 92(11):117406, 2004.

[23] M Moretti Sala, Valentina Bisogni, C Aruta, G Balestrino, H Berger, NB Brookes, GM De Luca, D Di Castro, M Grioni, M Guarise, et al. Energy and symmetry of dd excitations in undoped layered cuprates measured by cu L_3 resonant inelastic x-ray scattering. *New Journal of Physics*, 13(4):043026, 2011.

[24] MR Norman and C Pépin. The electronic nature of high temperature cuprate superconductors. *Reports on Progress in Physics*, 66(10):1547, 2003.

[25] HJA Molegraaf, C Presura, D Van Der Marel, PH Kes, and M Li. Superconductivity-induced transfer of in-plane spectral weight in $Bi_2Sr_2CaCu_2O_{8+\delta}$. *Science*, 295(5563):2239–2241, 2002.

[26] Michael Tinkham. *Introduction to superconductivity*. Courier Corporation, 2004.

[27] JE Hirsch. Superconductors that change color when they become superconducting. *Physica C: Superconductivity*, 201(3-4):347–361, 1992.

[28] JE Hirsch. The true colors of cuprates. *Science*, 295(5563):2226–2227, 2002.

[29] AV Boris, NN Kovaleva, OV Dolgov, T Holden, CT Lin, B Keimer, and C Bernhard. In-plane spectral weight shift of charge carriers in $YBa_2Cu_3O_{6.9}$. *Science*, 304(5671):708–710, 2004.

[30] DN Basov and T Timusk. Electrodynamics of high-T_c superconductors. *Reviews of modern physics*, 77(2):721, 2005.

[31] WN Hardy, DA Bonn, DC Morgan, Ruixing Liang, and Kuan Zhang. Precision measurements of the temperature dependence of λ in $YBa_2Cu_3O_{6.95}$: Strong evidence for nodes in the gap function. *Physical Review Letters*, 70(25):3999, 1993.

[32] JR Kirtley, CC Tsuei, JZ Sun, CC Chi, Lock See Yu-Jahnes, A Gupta, M Rupp, and MB Ketchen. Symmetry of the order parameter in the high-tc superconductor $YBa_2Cu_3O_{7-\delta}$. *Nature*, 373(6511):225–228, 1995.

[33] Dale J Van Harlingen. Phase-sensitive tests of the symmetry of the pairing state in the high-temperature superconductors—evidence for $d_{x^2-y^2}$ symmetry. *Reviews of Modern Physics*, 67(2):515, 1995.

[34] Kyle M Shen and JC Seamus Davis. Cuprate high-T_C superconductors. *Materials today*, 11(9):14–21, 2008.

[35] Francesca Giusti. *Intensity and fluctutaion dynamics in pump-probe experiments in complex materials*. PhD thesis, Università degli Studi di Trieste, 2018.

[36] Douglas J Scalapino. The case for $d_{x^2-y^2}$ pairing in the cuprate superconductors. *Physics Reports*, 250(6):329–365, 1995.

[37] CM Varma. Theory of the pseudogap state of the cuprates. *Physical Review B*, 73(15):155113, 2006.

[38] DM Newns and CC Tsuei. Fluctuating cu-o-cu bond model of high-temperature superconductivity. *Nature Physics*, 3(3):184–191, 2007.

[39] L Perfetti, PA Loukakos, M Lisowski, U Bovensiepen, H Eisaki, and M Wolf. Ultrafast electron relaxation in superconducting $Bi_2Sr_2CaCu_2O_{8+\delta}$ by time-resolved photoelectron spectroscopy. *Physical review letters*, 99(19):197001, 2007.

[40] YH Liu, Y Toda, K Shimatake, N Momono, M Oda, and M Ido. Direct observation of the coexistence of the pseudogap and superconducting quasiparticles in $Bi_2Sr_2CaCu_2O_{8+y}$ by time-resolved optical spectroscopy. *Physical review letters*, 101(13):137003, 2008.

[41] Claudio Giannetti, Giacomo Coslovich, Federico Cilento, Gabriele Ferrini, Hiroshi Eisaki, Nobuhisa Kaneko, Martin Greven, and Fulvio Parmigiani. Discontinuity of the ultrafast electronic response of underdoped superconducting $Bi_2Sr_2CaCu_2O_{8+\delta}$ strongly excited by ultrashort light pulses. *Physical Review B*, 79(22):224502, 2009.

[42] Jeff Graf, Chris Jozwiak, Chris L Smallwood, H Eisaki, Robert A Kaindl, Dung-Hai Lee, and Alessandra Lanzara. Nodal quasiparticle meltdown in ultrahigh-resolution pump-probe angle-resolved photoemission. *Nature Physics*, 7(10):805–809, 2011.

[43] Rocia Cortés, L Rettig, Y Yoshida, H Eisaki, Martin Wolf, and Uwe Bovensiepen. Momentum-resolved ultrafast electron dynamics in superconducting $Bi_2Sr_2CaCu_2O_{8+\delta}$. *Physical Review Letters*, 107(9):097002, 2011.

[44] Christopher L Smallwood, James P Hinton, Christopher Jozwiak, Wentao Zhang, Jake D Koralek, Hiroshi Eisaki, Dung-Hai Lee, Joseph Orenstein, and Alessandra Lanzara. Tracking cooper pairs in a cuprate superconductor by ultrafast angle-resolved photoemission. *Science*, 336(6085):1137–1139, 2012.

[45] Stefano Dal Conte, Claudio Giannetti, Giacomo Coslovich, Federico Cilento, Davide Bossini, Tadesse Abebaw, Francesco Banfi, Gabriele Ferrini, Hiroshi Eisaki, Martin Greven, et al. Disentangling the electronic and phononic glue in a high-T_C superconductor. *Science*, 335(6076):1600–1603, 2012.

[46] Giacomo Coslovich, Claudio Giannetti, Federico Cilento, Stefano Dal Conte, Tadesse Abebaw, Davide Bossini, Gabriele Ferrini, Hiroshi Eisaki, Martin Greven, Andrea Damascelli, et al. Competition between the pseudogap and superconducting states of $Bi_2Sr_2Ca_{0.92}Y_{0.08}Cu_2O_{8+\delta}$ single crystals revealed by ultrafast broadband optical reflectivity. *Physical review letters*, 110(10):107003, 2013.

[47] Federico Cilento, Stefano Dal Conte, Giacomo Coslovich, Simone Peli, Nicola Nembrini, Selene Mor, Francesco Banfi, Gabriele Ferrini, Hiroshi Eisaki, Mun K Chan, et al. Photo-enhanced antinodal conductivity in the pseudogap state of high-T_C cuprates. *Nature communications*, 5(1):1–10, 2014.

[48] Christopher L Smallwood, Wentao Zhang, Tristan L Miller, Chris Jozwiak, Hiroshi Eisaki, Dung-Hai Lee, Alessandra Lanzara, et al. Time-and momentum-resolved gap dynamics in $Bi_2Sr_2CaCu_2O_{8+\delta}$. *Physical Review B*, 89(11):115126, 2014.

[49] Daniele Fausti, RI Tobey, Nicky Dean, Stefan Kaiser, A Dienst, Matthias C Hoffmann, S Pyon, T Takayama, H Takagi, and Andrea Cavalleri. Light-induced superconductivity in a stripe-ordered cuprate. *science*, 331(6014):189–191, 2011.

[50] Stefan Kaiser, Cassandra R Hunt, Daniele Nicoletti, Wanzheng Hu, Isabella Gierz, HY Liu, M Le Tacon, T Loew, D Haug, B Keimer, et al. Optically induced coherent transport far above tc in underdoped $YBa_2Cu_3O_{6+\delta}$. *Physical Review B*, 89(18):184516, 2014.

[51] Wanzheng Hu, Stefan Kaiser, Daniele Nicoletti, Cassandra R Hunt, Isabella Gierz, Matthias C Hoffmann, M Le Tacon, T Loew, B Keimer, and Andrea Cavalleri. Optically enhanced coherent transport in $YBa_2Cu_3O_{6.5}$ by ultrafast redistribution of interlayer coupling. *Nature materials*, 13(7):705–711, 2014.

[52] Eliza Casandruc, Daniele Nicoletti, Srivats Rajasekaran, Yannis Laplace, Vikaran Khanna, GD Gu, JP Hill, and Andrea Cavalleri. Wavelength-dependent optical enhancement of superconducting interlayer coupling in $La_{1.885}Ba_{0.115}CuO_4$. *Physical Review B*, 91(17):174502, 2015.

[53] Matteo Mitrano, Alice Cantaluppi, Daniele Nicoletti, Stefan Kaiser, A Perucchi, S Lupi, P Di Pietro, D Pontiroli, M Riccò, Stephen R Clark, et al. Possible light-induced superconductivity in K_3C_{60} at high temperature. *Nature*, 530(7591):461–464, 2016.

[54] F Giusti, A Marciniak, F Randi, G Sparapassi, F Boschini, H Eisaki, M Greven, A Damascelli, A Avella, and Daniele Fausti. Signatures of enhanced superconducting phase coherence in optimally doped $Bi_2Sr_2Y_{0.08}Ca_{0.92}Cu_2O_{8+\delta}$ driven by midinfrared pulse excitations. *Physical review letters*, 122(6):067002, 2019.

[55] H Eisaki, N Kaneko, DL Feng, A Damascelli, PK Mang, KM Shen, Z-X Shen, and M Greven. Effect of chemical inhomogeneity in bismuth-based copper oxide superconductors. *Physical Review B*, 69(6):064512, 2004.

[56] G Yu, Y Li, EM Motoyama, and M Greven. A universal relationship between magnetic resonance and superconducting gap in unconventional superconductors. *Nature Physics*, 5(12):873–875, 2009.

[57] Federico Cilento. *Non-equilibrium phase diagram of $Bi_2Sr_2Y_{0.08}Ca_{0.92}Cu_2O_{8+\delta}$ cuprate superconductors revealed by ultrafast optical spectroscopy*. PhD thesis, Università degli Studi di Trieste, 2011.

[58] AB Kuzmenko. Kramers-kronig constrained variational analysis of optical spectra. *Review of scientific instruments*, 76(8):083108, 2005.

[59] Francesca Giusti, Angela Montanaro, Alexandre Marciniak, Francesco Randi, Fabio Boschini, Filippo Glerean, Giacomo Jarc, Hiroshi Eisaki, Martin Greven, Andrea Damascelli, et al. Anisotropic time-domain electronic response in cuprates driven by midinfrared pulses. *Physical Review B*, 104(12):125121, 2021.

[60] Y Toda, T Mertelj, P Kusar, T Kurosawa, M Oda, M Ido, and D Mihailovic. Quasiparticle relaxation dynamics in underdoped $Bi_2Sr_2CaCu_2O_{8+\delta}$ by two-color pump-probe spectroscopy. *Physical Review B*, 84(17):174516, 2011.

[61] Ivan Madan, Toru Kurosawa, Yasunori Toda, Migaku Oda, Tomaz Mertelj, Primoz Kusar, and Dragan Mihailovic. Separating pairing from quantum phase coherence dynamics above the superconducting transition by femtosecond spectroscopy. *Scientific reports*, 4(1):1–5, 2014.

[62] Simone Peli, S Dal Conte, Riccardo Comin, Nicola Nembrini, Andrea Ronchi, Paolo Abrami, Francesco Banfi, Gabriele Ferrini, Daniele Brida, Stefano Lupi, et al. Mottness at finite doping and charge instabilities in cuprates. *Nature physics*, 13(8):806–811, 2017.

[63] Jhinhwan Lee, K Fujita, AR Schmidt, Chung Koo Kim, H Eisaki, S Uchida, and JC Davis. Spectroscopic fingerprint of phase-incoherent superconductivity in the underdoped $Bi_2Sr_2CaCu_2O_{8+\delta}$. *Science*, 325(5944):1099–1103, 2009.

[64] R Daou, J Chang, David LeBoeuf, Olivier Cyr-Choiniere, Francis Laliberté, Nicolas Doiron-Leyraud, BJ Ramshaw, Ruixing Liang, DA Bonn, WN Hardy, et al. Broken rotational symmetry in the pseudogap phase of a high-T_C superconductor. *Nature*, 463(7280):519–522, 2010.

[65] Grant R Fowles. *Introduction to modern optics*. Courier Corporation, 1989.

[66] Frederick Wooten. *Optical properties of solids*. Academic press, 2013.

[67] Fabio Novelli. *In search of selective excitations for studying out-of-equilibrium properties in strongly correlated electron systems and high temperature superconductors*. PhD thesis, Università degli Studi di Trieste, 2012.

[68] JW Allen and JC Mikkelsen. Optical properties of CrSb, MnSb, NiSb, and NiAs. *Physical Review B*, 15(6):2952, 1977.

[69] Jules P Carbotte, Thomas Timusk, and Jungseek Hwang. Bosons in high-temperature superconductors: an experimental survey. *Reports on Progress in Physics*, 74(6):066501, 2011.

4

SELECTIVE PHOTO-EXCITATION OF THE *dd* ELECTRONIC TRANSITIONS IN THE ANTIFERROMAGNET *TiOCl*

Low-dimensional spin systems in transition metal oxides (TMOs) offer a unique playground to study the interplay between the charge, lattice, orbital and spin degrees of freedom in the presence of strong electronic correlations. This fascinating complexity gives rise to competing orders whose delicate balance determines the rich phase diagram of TMOs [1, 2].

Since the discovery of high-T_C superconductivity in the cuprates, special attention has been reserved to the low-dimensional quantum spin systems based on the $3d^9$ configuration, in view of the possible relevance of quantum magnetism for establishing the superconducting pairing. However, compounds involving early TMOs with a $3d^1$ configuration (such as Ti^{3+} or V^{4+}) exhibit equally exotic properties. In these systems, the orbital degeneracy lies within the t_{2g} triplet, leading to a reduction of the Jahn-Teller effect and, in turn, to the possibility of orbital ordering via superexchange interactions [3].

Among them, TiOCl initially emerged as a potential candidate for hosting an orbital ordered phase [4, 5, 6] and was later discovered to be one of the few examples in nature of inorganic spin-Peierls compounds [7]. At room temperature, TiOCl is a 1D S=1/2 antiferromagnet. At low temperatures, the system undegoes a first-order phase transition to a nonmagnetic spin singlet state, which is accompanied by a dimerization of the crystal structure along the 1D chain.

The evident coupling between the spin and the lattice attributes also involves the orbital degree of freedom. The *d* orbital degeneracy is completely lifted in TiOCl by the crystal field splitting. The only electron present is mainly localized on the Ti non-degenerate *d* orbital having lobes along the atomic chains [4], so that the direct exchange interactions give rise to the peculiar one-dimensional magnetic character of the material.

The study of the *dd* orbital transitions, along with their orbital occupancy, thus represents a poweful approach to indirectly monitor the emergence of competing orders in such systems [8]. At the same time, exerting an active control on the *dd* excitations could provide the means to directly attain new electronic and magnetic functionalities in low-dimensional spin systems [9, 10, 11].

Here, we leverage the breaking of the inversion symmetry in TiOCl to optically stimulate the *dd* intraband transitions. We investigate the non-equilibrium optical response of TiOCl to the selective photo-excitation of two different *dd* transitions

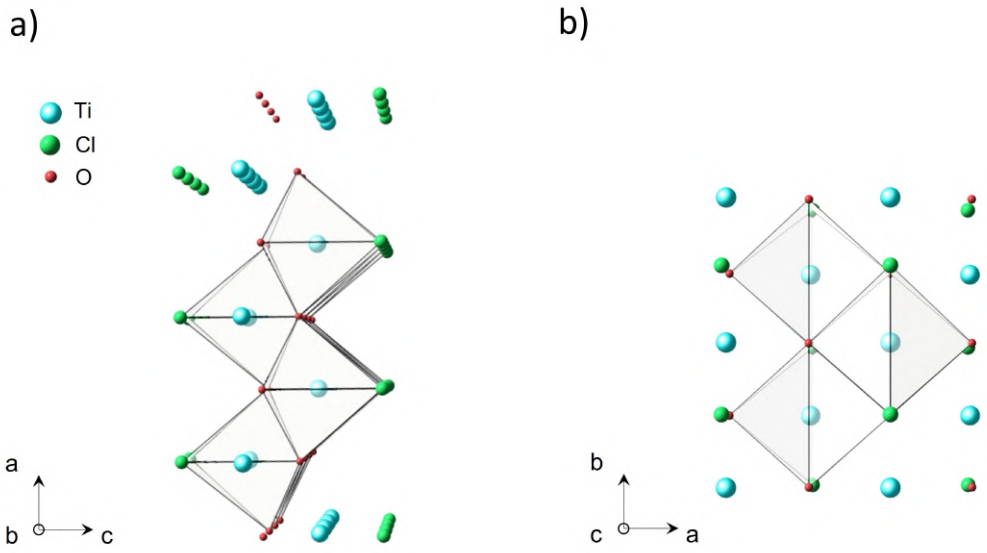

Figure 4.1: **Crystalline structure of TiOCl. a)** Buckled Ti-O layers are stacked along the c-axis and 1D atomic chains are oriented along the b-axis. Only one bilayer is depicted in the figure. The fundamental units are the strongly distorted octahedra $[TiO_4Cl_2]$ enclosing the Ti atoms. **b)** View of the ab-plane, as exfoliated in our sample. The strucure has been realized by means of the software in ref. [12].

in the spin-Peierls phase. After characterizing the transmissivity of the sample at equilibrium, we analyze the transient response of the Mott gap to the resonant photo-excitations. Finally, by employing the three-pulse technique, we investigate how the selective and simultaneous population of different d orbitals modifies the dynamics of the material.

4.1 TITANIUM OXYCHLORIDE

From a structural point of view, TiOCl is a two-dimensional system and, at room temperature, belongs to the $Pmmn$ space group. The structure consists of Ti-O bilayers stacked along the c-axis, as depicted in Figure 4.1a. The Cl atoms mediate the van der Waals coupling between adjacent bilayers. As a result, the compound can be easlily cleaved along the stacking direction; all the experiments discussed in this chapter have been performed with light beams impinging normally to the ab-plane (Figure 4.1b). Despite its two-dimensional structural character, the magnetic interactions in TiOCl have a peculiar quasi one-dimensional character along the b crystallographic direction.

In order to understand the origin of this reduced dimensionality, it is crucial to consider the orbital degree of freedom. The fundamental coordination units of the magnetic interactions are the octahedra that enclose the Ti atoms (Figure 4.2a). Each Ti atom transfers 3 electrons to the Cl and O atoms, resulting in a $3d^1$ configuration

(S=1/2). The only d electron thus resides in a local highly distorted octahedral environment (constituted by four oxygen and two chlorine ions) which breaks the spherical symmetry and partially lifts the d degeneracy. The five-fold degenerate d levels are splitted into the t_{2g} triplet and the e_g doublet (Figure 4.2b). The orbitals having t_{2g} symmetry have the lobes oriented away from the octahedron vertices and, as a consequence, are lower in energy than the e_g ones.

In TiOCl, the t_{2g} and e_g degeneracy is further removed by the co-operative Jahn-Teller effect, resulting from the structural distortion of the octahedral environment[1]. The d orbitals result in five non-degenerate levels that, according to the choice of the local reference frame (x,y,z) that we made, can be depicted as in Figure 4.2c.

The lowest lying orbital is the d_{xy} one, which has lobes at 45° with respect to the x and y axis. In the crystallographic reference frame, this corresponds to lobes oriented along the b and c directions. Thus, in the ground state, d_{xy} orbitals form linear chains along b, connecting neighbouring Ti ions in the same layer [5]. The primary exchange path is the direct exchange interaction between overlapping d_{xy} orbitals along b, while the coupling is weak in the other directions. Accordingly, the magnetic susceptibility in TiOCl can be well described by a one-dimensional S=1/2 Heisenberg chain with an exchange constant of J_b=660 K [5, 14]. The superexchange interaction via the O p orbitals is negligible in the ground state [5].

The magnetic interactions are modified at low temperatures (T_{C_1}=67 K), where TiOCl undergoes a first-order phase transition to a spin-Peierls phase having $P2_1/m$ symmetry [7, 17, 18]. The dimerization of the Ti ions occurs along the b chain, resulting in the formation of nonmagnetic spin singlet states. Early magnetic susceptibility and conductivity measurements initially suggested the presence of a spin-Peierls state [5, 19], that was later corroborated by the observation of a doubled lattice constant along b through x-ray diffraction [7]. Interestingly, the spin-Peierls ground state is reached unconventionally in TiOCl via an intermediate and incommensurate phase at T_{C_2}=91 K, whose nature and origin have been extensively debated. It is now accepted that the frustration of the interchain interactions is the driving force to the incommensurate state that eventually triggers the spin-Peierls mechanism at lower temperatures [20, 14].

4.1.1 *The experiment*

The TiOCl samples have been exfoliated along the c-axis and glued on a holed copper plate to perform transmission measurements. The flakes had typical dimensions of a few mm^2 in the ab plane and <30 μm in the stacking direction. The samples have been mounted in a closed-cycle liquid helium cryostat and measured in the temperature range (8-300) K.

1 It is important to note that, in such compounds, the Jahn-Teller distortion and the orbital ordering are concurrent effects that, although having very different physical origins, are closely linked and produce the same observable consequences, i.e. the removal of the d degeneracy [13].

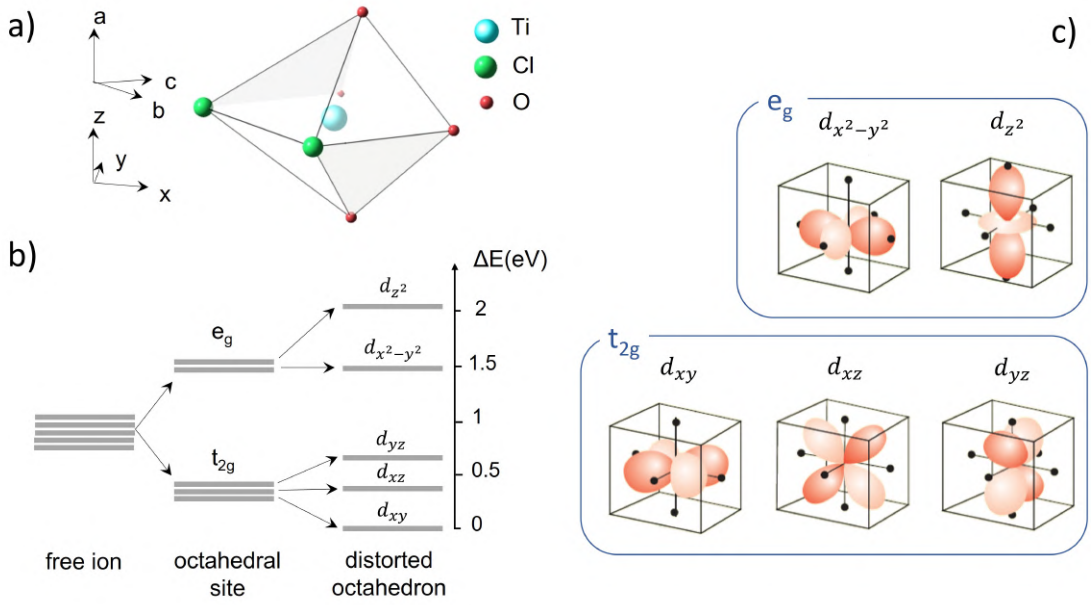

Figure 4.2: **Crystal field splitting of the** $3d$ **orbital levels. a)** Distorted octahedron enclosing a Ti-atom. The orientation of the crystal axes (a,b,c) and the local reference frame (x,y,z) are depicted on the left. Note that x,y are tilted by 45° with respect to b,c, as in ref. [5]. **b)** Splitting of the d degenerate levels as a result of the distorted octahedral environment. The energy levels have been reported according to refs. [4, 15, 8]. **c)** Depiction of the d orbitals having t_{2g} and e_g symmetry, adapted from ref. [16].

We studied the out-of-equilibrium response of TiOCl using the experimental setup described in Chapter 2. In order to selectively excite different dd excitations, we directly pumped the sample with the tunable output of one of the two TOPAs, set at $h\nu_{yz}$=0.7 eV to be resonant with the transition to the d_{yz} orbital. The NOPA has been tuned instead to drive the transition to the $d_{x^2-y^2}$ orbital, $h\nu_{x^2-y^2}$=1.5 eV. The broadband white-light probe extends from 1.35 to 2.2 eV and overlaps with the $d_{x^2-y^2}$ transition and the electronic Mott gap (∼2 eV, ref. [15]). With reference to Figure 4.2c, the $d_{x^2-y^2}$ orbital is the one that lies within the bc plane and has lobes pointing towards the O/Cl atoms. Pump-induced changes in its orbital occupancy could therefore trigger modifications in the superexchange interaction.

The polarizations of all the beams can be adjusted using halfwave plates. We have followed the selection rules in refs. [15, 21] to maximize the absorption related to different dd transitions.

xy	xz	yz	x^2-y^2	z^2
	$E \parallel a$	$E \parallel a$	$E \parallel b,c$	$E \parallel b,c$

Table 4.1: Selection rules for absorption at T=4 K [15].

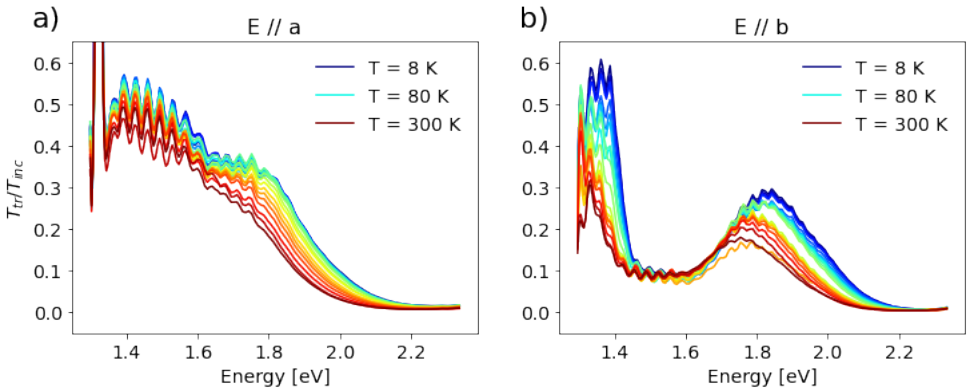

Figure 4.3: **Transmissivity of TiOCl as function of temperature. a)** Transmittance measured with light polarized along the a axis (orthogonal to the chain). **b)** Transmittance measured with light polarized along the b axis (parallel to the chain). A background signal measured with the photodiode array covered has been subtracted to both the incident (T_{inc}) and the transmitted (T_{tr}) spectra prior the division.

4.2 STATIC TRANSMISSIVITY

To characterize the sample, we have performed static transmission measurements at different temperatures. A reference spectrum of the incident white-light probe (T_{inc}) has been acquired by moving the sample away from the beam trajectory and letting it pass through the copper plate's hole. In this way, the optical path of the beam is unmodified. At the lowest temperature (T=8 K) we have rotated the beam polarization within the ab plane to maximize the absorption from the $d_{x^2-y^2}$ transition. According to the selection rules in Table 4.1, this direction identifies the b-axis.

We plot in Figure 4.3 the transmissivity measured in the range T=(8-300)K with the broadband pulse polarized along the a- (Figure 4.3a) and the b- (Figure 4.3b) axis. The transmissivity has been obtained by dividing the transmitted spectrum (T_{tr}) by the incident one, after the subtraction of the array background signal from both of them. In both cases, we observe the presence of Fabry-Perot fringes due to multiple reflections within the thin sample.

Regardless of the light polarization, the transmissivity drops above $\sim$2 eV due to the excitations across the electronic gap. This edge thus identifies the energy of the Mott gap. As expected, when the light is polarized along b, the transmissivity is further suppressed at $\sim$1.5 eV, in correspondence with the $d_{x^2-y^2}$ transition. The flat shape of the absorption feature suggests a bigger thickness of the sample.

The major effect of the temperature increase is the redshift of both the Mott gap and the $d_{x^2-y^2}$ transition. The latter is also broadened at higher temperatures and features an asymmetric shape with a steep drop on the low-energy side that could be attributed to the presence of phonon sidebands [21]. Additionally, we observe an attenuation of the transmissivity for increasing temperature. These results are in agreement with the transmittance spectra measured in refs. [15, 21].

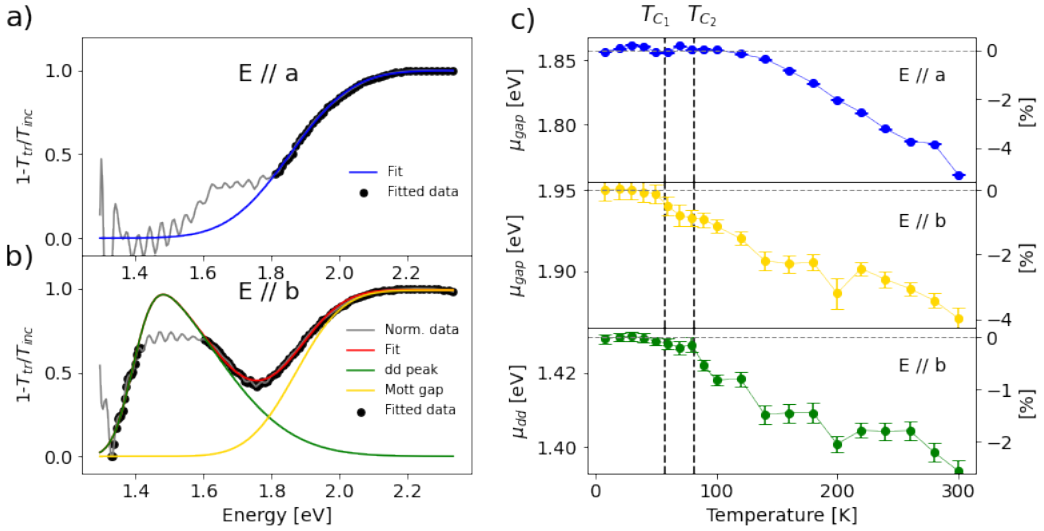

Figure 4.4: **Temperature-dependent fits of the static transmissivity. a)** Normalized absorption measured with light polarized along the a axis ($E \parallel a$) at T=8 K (grey line). The black points have been fitted with an error function (blue line). **b)** Normalized absorption measured with light polarized along the b axis ($E \parallel b$) at T=300 K (grey line). The fit (red line) with the sum of a skewed Gaussian (green) and an error function (gold) has been performed only on the black points to exclude the saturated peak. **c)** Fits results as function of the temperature. Top panel and middle panel: edge of the error function (μ_{gap}) for $E \parallel a$ and $E \parallel b$, respectively. Bottom panel: central energy of the Gaussian (μ_{dd}) for $E//b$. The y-axis on the right indicates the relative change with respect to the value at 8 K.

4.2.1 *Static fits*

In order to quantitatively estimate the effects of the temperature on the optical response of the sample, we fitted each curve in Figure 4.3 to extrapolate the Mott gap energy (μ_{gap}) and the peak energy of the d absorption (μ_{dd}) as function of the temperature.

As an example of the model functions that we used, we plot in Figure 4.4a,b two selected curves for the beam polarized along a and b, respectively. Note that we plotted here 1-T_{tr}/T_{inc}, to highlight the absorption features of the spectra. In the case of $E \parallel a$, we fitted the black points with an error function (blue curve) centered at μ_{gap}. The spectra acquired with $E \parallel b$ have been fitted by combining a skewed Gaussian (green curve) to account for the dd transition and an error function (gold curve) for the Mott gap.

The results of the fits are plotted in Figure 4.4c as function of the temperature. The fits reproduce well the redshift that can be appreciated from the visual inspection of the spectra in Figure 4.3. We find that the dd absorption (green points) redshifts by about 35 meV between 8 and 300 K. This estimate is consistent with the results in ref. [21], which were obtained by measuring the transmittance only at four selected temperatures.

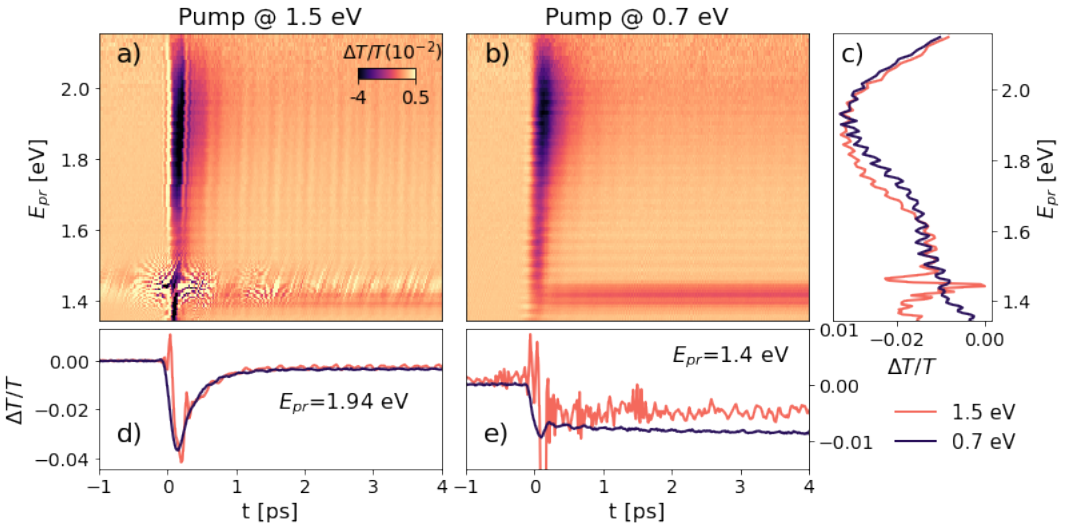

Figure 4.5: **Non-equilibrium transmissivity upon the selective photo-excitation of the *dd* transitions at T=10 K. a-b)** Color-coded maps (same color-scale) of the broadband transient transmissivity upon the photo-excitation with the 1.5 and 0.7 eV pumps, respectively. The pumping fluence is ∼3 mJ cm^{-2} for both pumps. **c)** Spectra of the two maps (pink: 1.5 eV; dark purple: 0.7 eV) averaged over the range 100-300 fs. **d-e)** Time-traces selected in correspondence of the Mott gap (E_{pr}=1.94 eV) and the $d_{x^2-y^2}$ (E_{pr}=1.5 eV) transition, respectively.

By performing a denser temperature scan, we observe that the redshift is not constant in temperature: the peak position of both the *dd* transition and the Mott gap is almost unchanged at low temperatures, and a slow redshift starts only above a given temperature threshold. In particular, when the light is polarized along the *b*-axis (and so along the antiferromagnetic 1D chains), the redshift of μ_{gap} and μ_{dd} starts at temperatures that are compatible with T_{C_1} and T_{C_2}, respectively. [2] This suggests that, at equilibrium, both the electronic gap and the orbital occupancy do depend on the sample temperature and may be coupled to the spin degree of freedom.

4.3 NON-EQUILIBRIUM RESPONSE TO SELECTIVE *dd* TRANSITIONS

Based on the temperature-dependent static transmissivity measurements, we decided to fix the polarization of the white-light probe along the *b*-axis. In this way, we are sensitive not only to the Mott gap energy, but also to the dynamics of the $d_{x^2-y^2}$ transition.

In Figure 4.5a,b we plot the transient transmissivity measured in the spin-Peierls phase (T=10 K) upon the photo-excitation resonant to the $d_{x^2-y^2}$ (1.5 eV) and the d_{yz}

2 Note that the dashed vertical lines have been drawn at T_{C_1}=58 K and T_{C_2}=82 K, so 9 K below the expected phase transitions. These same values have been also extracted from the temperature-dependent measurements of the phonons (Figure 4.10). We thus conclude that the temperature shift that we observe is due to the fact that the sample is warmer than the thermocouple used to measure the sample temperature by about 9 K.

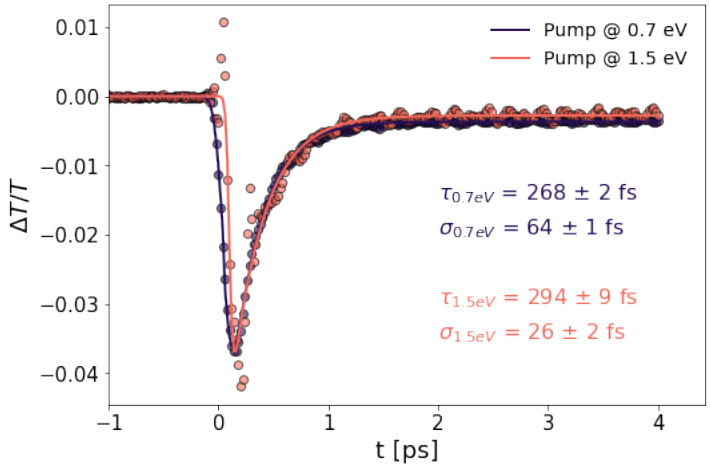

Figure 4.6: **Dynamics at the Mott gap energy.** Dynamics at E_{pr}=1.94 eV induced by the 0.7 (dark purple) and the 1.5 eV pump (pink). The data (filled circles) are fitted (solid lines) using an exponential decay (τ) convoluted with a Gaussian function having width σ. The negative plateau at longer time-delays is accounted for by a step function. The results of the relevant parameters of the fits are displayed in the panel.

(0.7 eV) transitions, respectively. To maximize the pump-absorption, we polarized the former along the b-axis and the latter along the a-axis, according to Table 4.1. We have used this polarization configuration in all the measurements discussed in the chapter.

We observe that both maps are dominated by two elements: a negative transient transmissivity centered at about 1.94 eV and a feature at about 1.4 eV characterized by a longer dynamics. In Figure 4.5a, strong interference fringes are superimposed to the response at 1.4 eV, which is the white-light range that overlaps with the co-polarized pump. In both maps, we resolve oscillations due to the excitation of coherent phonons, whose details will be discussed in Section 4.4.

The comparison between the spectra averaged over the range 100-300 fs (Figure 4.5c) highlights the negative signal at 1.94 eV, that we associate to the transient modification of the electronic gap. In particular, we observe that the spectral response of the gap to the 1.5 eV pump is redshifted with respect to the one associated to the 0.7 eV pump. We quantify this difference in Section 4.3.2.

The time-traces in Figure 4.5d,e compare the dynamics in correspondence of the Mott gap and the $d_{x^2-y^2}$ transition, respectively. In both case, we do not find significant differences between the two resonant excitations. The dynamics of the dd transition (Figure 4.5e) is characterized by a plateau that we have measured up to t=50 ps and that is unmodified at least up to that time.

We analyze the dynamics of the Mott gap in more details in Figure 4.6, where we plot the fits to the data using the convolution of an exponential decay and a Gaussian function to account for the finite temporal duration of the pulses (σ).

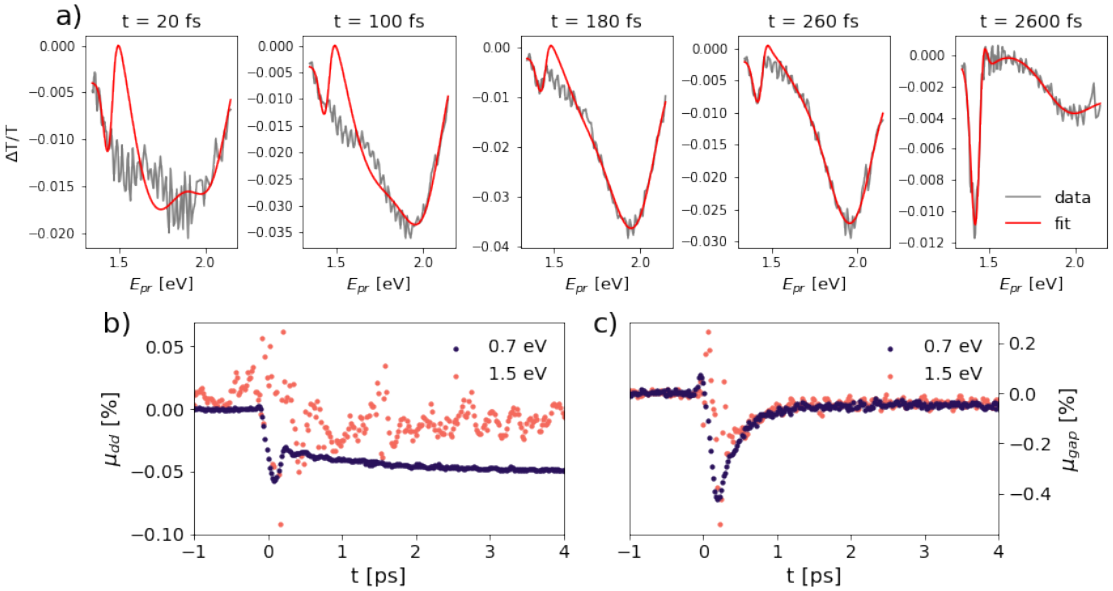

Figure 4.7: **Differential fits of the non-equilibrium response. a)** Data (grey) and differential fits (red) of the broadband transmissivity upon the 0.7 eV pump excitation at different pump-probe delays. **b-c)** Relative pump-induced change of the central energy of the $d_{x^2-y^2}$ excitation (μ_{dd}) and the Mott gap (μ_{gap}) extrapolated from the fit, respectively.

We observe a composite dynamics: at longer time-delays (t>1 ps) the signal is dominated by a negative plateau that is unmodified up to tens of picoseconds (as we measured at t=50 ps); at earlier time-delays, we observe a dynamics that has a characteristic decay time τ similar for both the resonant photo-excitations and that is smaller than 300 fs. We also note that the rising time of the signal is different in the two pumping conditions and, in particular, is longer for the 0.7 eV pump. This is well described by the fits, which return $\sigma_{0.7eV} > \sigma_{1.5eV}$. The values estimated are compatible with the specifics of the OPA sources that we used.

4.3.1 *Non-equilibrium fits*

To gain a physical insight on the transient response measured, we have fitted the transmissivity maps using a differential approach similar to the one described in Appendix D. The key idea of the analysis is to use the static transmissivity measured in the same experimental conditions ($E_{probe} \parallel b$, T=10 K) and modelled in Figure 4.4b. The fit curve to the static data constitutes the "equilibrium model" (T_{eq}) in the differential fits. At each delay, the transient maps in Figure 4.5a,b have been fitted using the model (T_{pert}-T_{eq})/T_{eq}, where T_{pert} has the same functional form of T_{eq} but with varying fitting parameters. In this way, we can estimate which physical parameters are transiently modified upon the photo-excitation.

In Figure 4.7a, we plot the transient transmissivity spectra upon the 0.7 eV pump excitation for different pump-probe delays (grey lines). The red curves are the fits

obtained by using the differential model. The fitting model well describes the data at longer time-delays (rightmost panel), where the time-dependent fit parameters (Figure 4.7b,c) indicate a redshift of both the *dd* transition peak and the Mott gap energy, respectively. Upon the photo-excitation, μ_{dd} and μ_{gap} redshift from their equilibrium value by ∼0.05% for t>1 ps. By comparing this quantity with the temperature-dependent redshift that we measured at the equilibrium (Figure 4.4c), we can deduce that this effect is compatible with a slight, pump-induced temperature increase of the sample. We thus conclude that the dynamics at longer delays has a thermal origin and is therefore coupled to the lattice temperature.

However, the fitting model fails to reproduce the experimental data at early time-delays (t<300 fs), where we observe a clear deviation of the fitting curves (Figure 4.7, left panels). Specifically, the most prominent inconsistencies are found in the probe energy region between the $d_{x^2-y^2}$ transition and the electronic gap energy. In this range, the measured transient transmissivity is more negative than expected. Since the fitting model that we used can only account for modifications of the physical parameters that describe the equilibrium response, the observed deviations from the model can be considered an indication that, within t<300 fs, the lattice temperature and the electronic temperature are decoupled.

A tentative explanation for the quenched transmissivity observed at $E_{pr} \simeq 1.55$ eV could be the formation of intragap states, absent at equilibrium and photo-induced by the sudden injection of excess carriers. A photo-induced gap filling in a prototype Mott–Hubbard compound has been experimentally observed, suggesting the ultrafast formation of a non-thermal transient state in which the system remains trapped before relaxing to the final thermal state [22].

Finally, we note that the fit results for the 1.5 eV pump (pink points in Figure 4.7b,c) are much noiser than the one associated to the 0.7 eV pump. This is due to the presence of the interference fringes on the low-energy side of the probe bandwidth (Figure 4.5a) which affect the quality of the differential fit.

4.3.2 *Dynamics of the Mott gap energy shift*

We pointed out in Figure 4.3c that the spectral dependence of the transient transmissivity is affected by the photon energy of the pump. In particular, the response at the Mott gap energy in the first hundreds of fs undergoes a stronger redshift when the sample is excited by the 1.5 eV pump. This difference, however, is not captured by the non-equilibrium differential fits (Figure 4.7c) as they fail to describe the early-time dynamics.

In order to quantify this redshift, we carried out a model-independent analysis of the transient maps in Figure 4.5a,b. To isolate the transient response of the electronic gap, we have considered only the spectral range 1.5-2.15 eV. An example of the spectra used in the analysis is plotted in Figure 4.8a,b, where cuts, respectively at early and late time delays, have been considered. We note that, while a significant

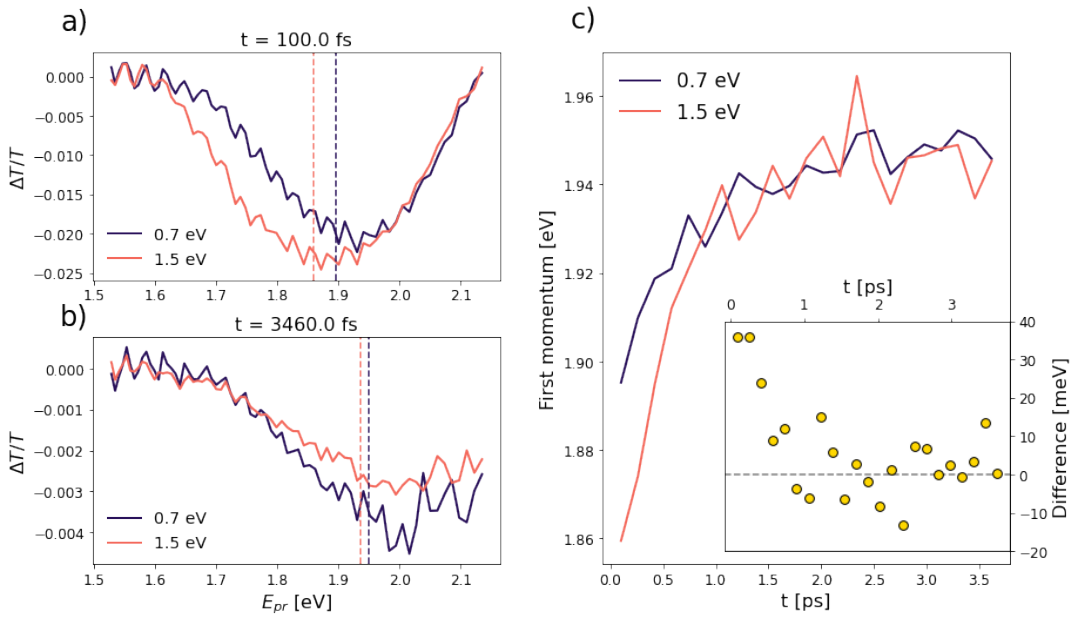

Figure 4.8: **Dynamical redshift of the Mott gap. a-b)** Spectra of the non-equilibrium transmissivity upon the 0.7 eV (dark purple) and the 1.5 eV (pink) photo-excitation at t=100 fs and t=3460 fs, respectively. Each curve is averaged over 160 fs and vertically shifted so that the average $\Delta T/T$ in the range 1.5-1.6 eV is zero. The vertical dashed lines indicate the calculated first momenta of the curves. **c)** First momenta for the two photo-excitations calculated for all the time delays (averaged every 160 fs). The inset shows the difference between the two curves in the main panel.

spectral shift between the purple and the pink curves can be appreciated at t=100 fs, the curves almost overlap at t=3460 fs.

As an indication of the transient Mott gap shift upon the photo-excitation, we have evaluated the first momenta of the curves, denoted by the vertical dashed lines in the graphs. By iterating this procedure for all the pump-probe time delays, we plot in Figure 4.8c the first momenta for the two photon energies as function of time.

In spite of the qualitative nature of this analysis, we argue that it captures well the dynamics of the Mott gap shift. At late time delays, the first momentum analysis returns a gap energy that is $\sim$1.95 eV and so consistent with both the static fits of the transmissivity (Figure 4.4c) and the non-equilibrium fit results (Figure 4.7c). At early time delays, the analysis indicates a substantial difference between the two photo-excitations. Specifically, the redshift induced by the 1.5 eV pump is larger than the one induced by the 0.7 eV for $t \lesssim 1$ ps; at bigger time delays, the two curves converge to approximately the same value.

We stress that the transient redshifts evaluated at t=100 fs upon the 0.7 eV and 1.5 eV photo-excitations correspond, respectively, to a $\sim$2.5% and a $\sim$4.5% modification of the equilibrium value of the Mott gap. By comparison with the temperature-dependent static measurements in Figure 4.4c, these changes are far too large to be

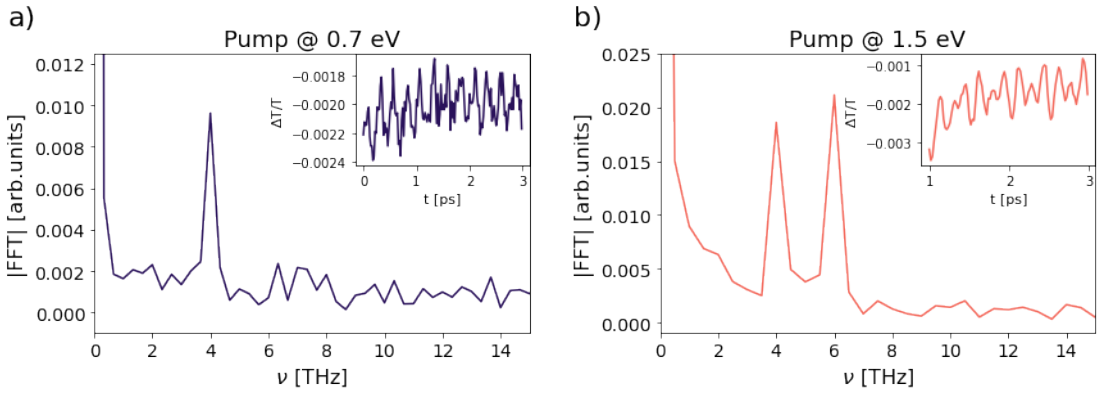

Figure 4.9: **Coherent phonons at T=10 K. a)** Modulus of the Fourier transform performed over the 0.7 eV pump time trace averaged over the range 1.6-2.2 eV (inset). **b)** Same as a) but for the 1.5 eV pump.

ascribed to a pump-induced lattice temperature increase, thus reinforcing our claim that the early-time response is ruled by a non-thermal dynamics.

The inset in Figure 4.8c quantifies the difference between the two curves, that is ∼40 meV at its maximum. The fact that this value is comparable with the energy scale of the direct exchange along the b-axis (J_b=660 K) might suggest that the magnetic interactions are involved in the early-dynamics. However, an interpretation of this experimental evidence will be possible only after the development of a model in which the coupling between the magnetic and the orbital degrees of freedom is included, as it will be discussed in Section 4.5.

4.4 TEMPERATURE-DEPENDENT COHERENT PHONONS

In the transient transmissivity maps in Figure 4.5a,b we highlighted the presence of periodic oscillations, superimposed to the pump-induced relaxation dynamics. In this section, we focus on the analysis of the oscillatory part of the transient response and address its temperature dependence.

In the main panels of Figure 4.9 we plot the modulus of the Fourier transform of the energy-averaged time traces reported in the insets. The Fourier analysis reveals the presence of a 4 THz (133 cm^{-1}) oscillation that modulates the transient response of the sample to the 0.7 eV pump (Figure 4.9a). When the sample is excited by the 1.5 eV pump, a further oscillation emerges at 6 THz (200 cm^{-1}).

These frequencies are consistent with the lowest-energy Raman-active A_g phonons in the spin-Peierls phase, measured by Raman spectroscopy [17] and calculated by DFT simulations [23]. The absence of the faster 6 THz phonon in the transient response induced by the 0.7 eV pump could be due to its larger temporal duration compared to the 1.5 eV pump, as showed in Figure 4.9. In fact, since the phonons observed have both A_g symmetry, we exclude that this difference can be justified by symmetry arguments.

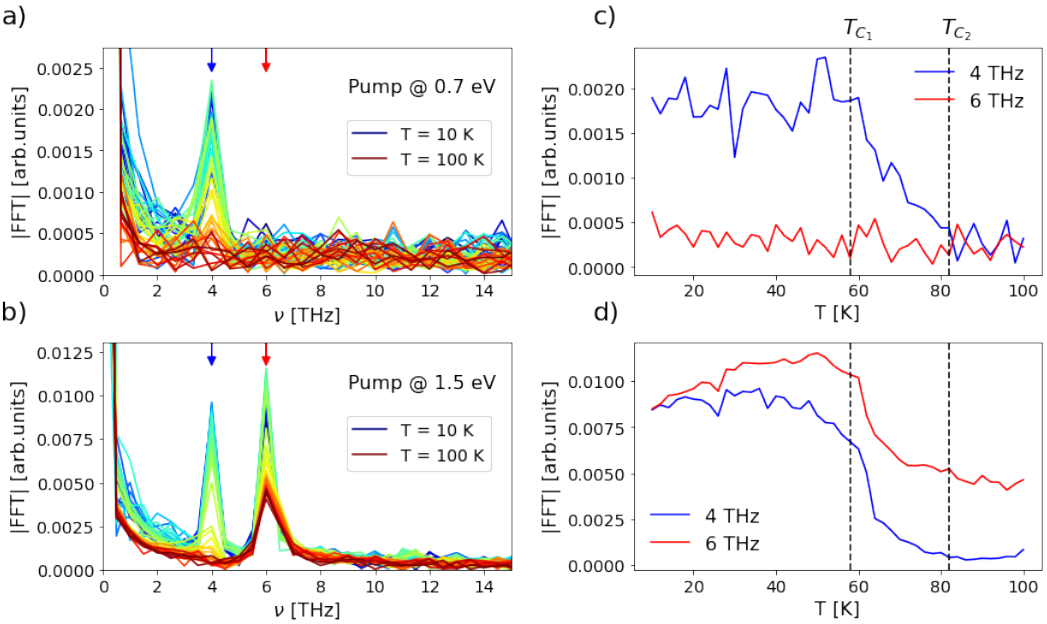

Figure 4.10: **Temperature-dependence of coherent phonons. a-b)** Fourier spectra at different temperatures extrapolated from the transient measurement upon the 0.7 and 1.5 eV photo-excitation, respectively. **c-d)** Temperature-dependent amplitude of the 4 THz (blue) and 6 THz (red) phonons in a) and b), respectively. T_{C_1}=58 K and T_{C_2}=82 K indicate the measured transition temperatures from the Spin-Peierls to the incommensurate phase and from the incommensurate to the high temperature phase, respectively.

However, both phonons are sensitive to the structural changes that accompany the phase transitions in TiOCl [17]. We have thus performed temperature-dependent measurements of the coherent phonons to track the spin-Peierls and the incommensurate phases in our sample. In Figure 4.10a,b we plot the Fourier spectra for different temperatures for the low- and high-energy pump, respectively.

We analyze the temperature-dependence of the two phonons in Figure 4.10c,d. We observe that, in both pumping conditions, the 4 THz phonon (blue line) is weakened above ∼58 K and completely quenched above ∼82 K. Analogously, the 6 THz phonon (red line) is reduced in intensity at ∼58 K, but it then survives at higher temperatures. This trend is consistent with the Raman spectra measured in the spin-Peierls, incommensurate and high-temperature phases [17]. We therefore identify the two phase transitions to occur at T_{C_1}=58 K and T_{C_2}=82 K. A shift of about 9 K with respect to the critical temperatures known in literature could be due to a mismatch between the thermocouple readout and the actual temperature of the sample.

4.4.1 *Coherent control of phonons*

The strength of the three-pulse spectroscopy that we have developed consists in the possibility of simultaneously pumping the material with two photo-excitations in the

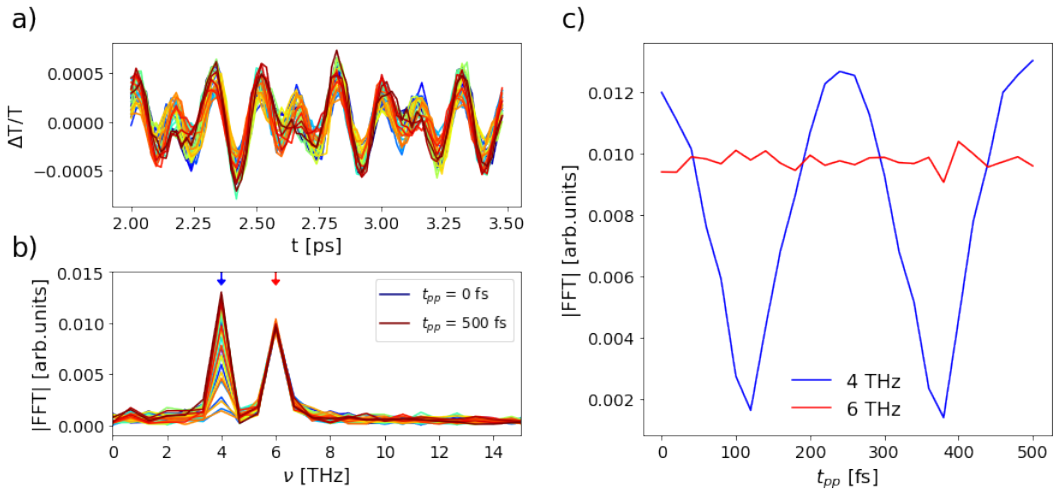

Figure 4.11: **Coherent control of 4 THz phonon through the three-pulse spectroscopy at T=10 K. a)** Time-traces of the two-pump response at different pump-pump delays (t_{pp}). **b)** Modulus of the Fourier transform of the traces in a). **c)** Amplitude of the 4 THz (blue) and 6 THz (red) phonon as function of t_{pp}.

very same experiment. We have seen that, due to the high energy tunability of the pumping sources, this technique is particularly advantageous to study and control the sample dynamics following excitation of selected degrees of freedom. In this section, we show a further application of the technique to exert a coherent control over the optical phonons in the sample.

As both pumps initiate a coherent phonon dynamics in TiOCl at 4 THz, by simply fine tuning the time delay between the two excitations (t_{pp}), it is possible to either enhance or quench the phonon oscillation according to the ratio between t_{pp} and the phonon period [24, 25]. We have attempted this approach and studied the transient transmissivity of the sample after the interaction with both pumps. In Figure 4.11a, we plot the energy-averaged times traces of the two-pump response recorded at different t_{pp}. The relaxation dynamics has been fitted with an exponential decay and only the remaining oscillatory part has been considered. The modulus of the Fourier transform of these traces (Figure 4.11b) reveals that, while the amplitude of the 6 THz phonon remains unaffected by the double pumping, the 4 THz phonon is either amplified or quenched.

To appreciate the dependence on the pump-pump delay, we plot in Figure 4.11c the amplitude of the Fourier spectra at 4 and 6 THz as function of t_{pp}. The amplitude of the 4 THz phonon displays a clear oscillatory behaviour, whose period matches the phonon one (250 fs). This confirms that a coherent control of optical phonons can be attained in TiOCl exploiting our technique.

This is a proof-of-principle demonstration of a further capability of the three-pulse approach. In particular, the possibility of actively controlling the collective behaviour of matter is appealing for the study of correlated materials, where it could be used to disentangle the contributions from other degrees of freedom and tackle their coupling.

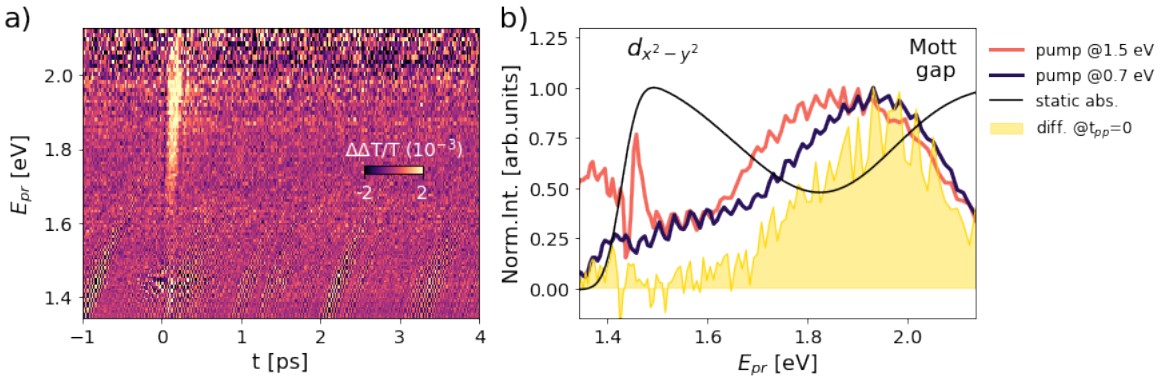

Figure 4.12: **Double-pump resonant excitation at the overlap at T=10 K. a)** Differential map obtained via the direct subtraction of the two-pump response and the single-pump ones. Only t_{pp}=0 (the temporal overlap between the two pumps) is considered. **b)** Spetra of the single-pump responses (pink: 1.5 eV pump; dark purple: 0.7 eV) and the differential response (yellow shaded area). All spectra have been integrated over the range 100-300 fs. For comparison, the black curve is the fit of the static absorption at T=8 K obtained in Figure 4.4.

4.5 DOUBLE-PUMP RESPONSE

We have seen in Section 4.3 that the selective photo-excitation of the d_{yz} and $d_{x^2-y^2}$ orbitals triggers a similar non-equilibrium response in TiOCl. In particular, we have discriminated a non-thermal dynamics in the first hundreds of femtoseconds and a thermal dynamics that sets in at longer time-delays. While the dynamics at the Mott gap energy is similar upon the two photo-excitations (Figure 4.6), the major difference that we have observed is related to the transient spectral dependence of the Mott electronic gap, that is more redshifted at early time delays when the system is excited with the 1.5 eV pump (Figure 4.8). Since the Mott gap Δ is determined by the concurrent Coulomb repulsion U and the hopping integral t

$$\Delta = U - 2zt$$

with z=2 being the number of nearest neighbors in TiOCl, this different gap renormalization may hint at a modified electronic response upon the different orbital occupancy.

We have used the three-pulse approach to study how the simultaneous population of the two d orbitals affects the spectral and temporal response in TiOCl. In Figure 4.12 we plot the time- and energy-resolved transmissivity at T=10 K obtained by subtracting the single-pump responses from the two-pump one; we denote this differential quantity with $\Delta\Delta T/T$. We consider here only the overlap between the 0.7 and 1.5 eV pumps (t_{pp}=0).

We observe that the differential signal is exclusively localized at the Mott gap energies, while is null in correspondence of the $d_{x^2-y^2}$ transition. This is clear in Figure 4.12b, where we compare the differential spectral response (yellow shaded

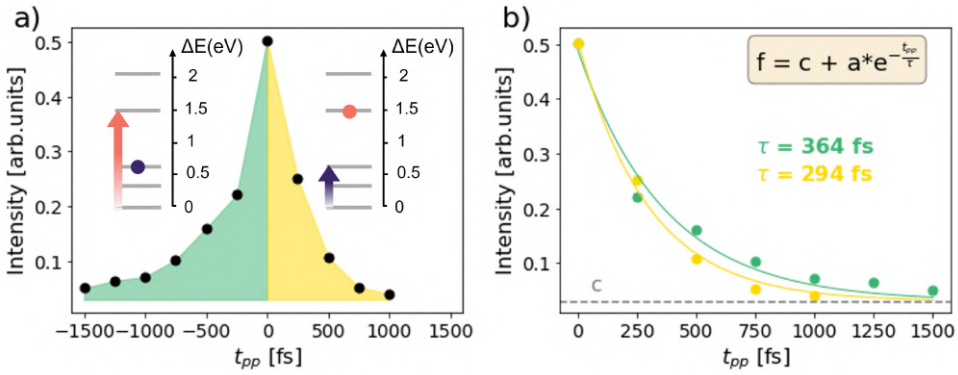

Figure 4.13: **Dynamics of the double-pump excitation. a)** Time- and energy-integrated differential signal as function of the pump-pump delays. At t_{pp}<0, the sample is first excited by the 0.7 eV pump (dark purple circle) and then by the 1.5 eV pump (pink arrow), as illustrated in the energy diagram; At t_{pp}>0, the order is swapped. **b)** Exponential fits of the dynamics at t_{pp}<0 (green) and t_{pp}>0 (yellow). The constant baseline c (dashed grey line) has been kept fixed in the fits.

area) with the spectra of the two single-pump responses. This evidence indicates that the double-pump response is entirely dominated by the Mott gap dynamics, while the thermal dynamics probed in correspondence of the $d_{x^2-y^2}$ transition (Figure 4.5e) is a linear effect and the double excitation results just in the mere superposition of the signals independently triggered by the two pumps (and so vanishes in $\Delta\Delta T/T$).

Figure 4.13 shows the intensity of the $\Delta\Delta T/T$ signal as function of the pump-pump delay. Each point in the plot is the result of an energy-integration of the spectra (similar to Figure 4.12b) acquired at different t_{pp}. The order of arrival of the pumps is sketched in the panel: for t_{pp}<0, the system is first excited resonantly with 0.7 eV dd transition and then further pumped by the 1.5 eV pulse; the order is swapped for t_{pp}>0.

We observe that the differential signal has an asymmetric shape, so its dynamics does depend on the order of arrival of the two photo-excitations. In order to evaluate the dynamics, we have fitted the curves with an exponential decay in Figure 4.13b, where the signal at t_{pp}<0 (green points) is mirrored onto the positive axis to facilitate the comparison with the curve at t_{pp}>0 (yellow points). A fixed baseline c (horizontal grey line) has been included in the fit equation and has been assumed to be the same for both the experimental curves since the system should lie in the same state for $t_{pp} = \pm\infty$. The decay time estimated at t_{pp}>0 is consistent with the single-pump dynamics observed at the Mott gap energy (Figure 4.6), while we find a slower dynamics at t_{pp}<0.

We speculate that this asymmetry might arise from the dispersive character of the d_{yz} orbital transition that has been observed in TiOCl via resonant inelastic x-ray experiments [8]. If the dd excitation is dispersive, a non-null orbital cross-talk between neighboring atoms should be expected, that could in turn lead to different de-excitation pathways in the system. In TiOCl the picture is particularly involved due to the spin-Peierls dimerization at low temperatures. Usually, at equilibrium,

the spin-Peierls phase is formally treated by considering only the spin degree of freedom, because the *dd* splitting is too large for the orbital physics to take place. However, we stress that in non-equilibrium conditions triggered by high photon energy excitation this is no longer the case, and the orbital and the spin excitations should be treated on equal footing. We are currently working with our collaborators on an extension of the Kugel-Khomskii model in a spin-dimerized phase. This could possibly give indications on the decay time of the orbital excitation in presence of a magnon-orbiton coupling.

4.6 CONCLUSIONS

In summary, we have carried out non-equilibrium transmissivity measurements on TiOCl, a transition metal oxide 1D antiferromagnet that undergoes a spin-Peierls dimerization at low temperatures. Specifically, we have studied the optical response of the system in the spin-Peierls phase to the resonant optical stimulation of two *dd* orbital transitions. At equilibrium, temperature-dependent transmissivity measurements revealed that both the $d_{x^2-y^2}$ transition and the Mott electronic gap are sensitive to the low-temperature magnetic order. The transient measurements disclosed an early (t<300 fs) photo-induced dynamics in the system, not explainable by an increase of the lattice temperature, but possibly ascribable to a non-thermal population effect leading to a renormalization of the Mott gap that is dependent on the orbital symmetry. Finally, the selective and simultaneuos excitation of the two *dd* transition via three-pulse spectroscopy indicated that the d_{yz} and $d_{x^2-y^2}$ undergo different de-excitation pathways in the dimerized phase, thus suggesting a coupling between the orbital and the magnetic degrees of freedom whose formal description will be the subject of future work.

REFERENCES

[1] Masatoshi Imada, Atsushi Fujimori, and Yoshinori Tokura. Metal-insulator transitions. *Reviews of modern physics*, 70(4):1039, 1998.

[2] Elbio Dagotto. Complexity in strongly correlated electronic systems. *Science*, 309(5732):257–262, 2005.

[3] Yoshinori Tokura and Naoto Nagaosa. Orbital physics in transition-metal oxides. *Science*, 288(5465):462–468, 2000.

[4] V Kataev, J Baier, A Möller, L Jongen, G Meyer, and A Freimuth. Orbital order in the low-dimensional quantum spin system TiOCl probed by ESR. *Physical Review B*, 68(14):140405, 2003.

[5] Alexander Seidel, Chris A Marianetti, FC Chou, Gerbrand Ceder, and Patrick A Lee. S=1/2 chains and spin-Peierls transition in TiOCl. *Physical Review B*, 67(2):020405, 2003.

[6] T Saha-Dasgupta, Roser Valentí, H Rosner, and Claudius Gros. TiOCl, an orbital-ordered system? *EPL (Europhysics Letters)*, 67(1):63, 2004.

[7] Mohammad Shaz, Sander van Smaalen, Lukas Palatinus, Markus Hoinkis, Matthias Klemm, Siegfried Horn, and Ralph Claessen. Spin-Peierls transition in TiOCl. *Physical Review B*, 71(10):100405, 2005.

[8] Sebastian Glawion, Jakoba Heidler, Maurits W Haverkort, Laurent C Duda, Thorsten Schmitt, Vladimir N Strocov, Claude Monney, KJ Zhou, Andreas Ruff, Michael Sing, et al. Two-spinon and orbital excitations of the spin-Peierls system TiOCl. *Physical Review Letters*, 107(10):107402, 2011.

[9] Semen I Polukeev, Vladimir A Gavrichkov, and Sergey G Ovchinnikov. Effects of optical intra-gap transitions on superexchange interaction in La_2CuO_4 with nonequilibrium photoexcited centers. *Journal of Siberian Federal University. Mathematics & Physics*, 11(2):159–170, 2018.

[10] Filippo Glerean. *Multimode heterodyne detection for ultrafast investigation of quantum materials*. PhD thesis, Università degli Studi di Trieste, 2006.

[11] Alexandre Marciniak, Stefano Marcantoni, Francesca Giusti, Filippo Glerean, Giorgia Sparapassi, Tobia Nova, Andrea Cartella, Simone Latini, Francesco Valiera, Angel Rubio, et al. Vibrational coherent control of localized d-d electronic excitation. *Nature Physics*, 17(3):368–373, 2021.

[12] Tadashi C Ozawa and Sung J Kang. Balls&Sticks: easy-to-use structure visualization and animation program. *Journal of Applied Crystallography*, 37(4):679–679, 2004.

[13] Eva Pavarini. *Orbital Ordering. Quantum Materials: Experiments and Theory.*

[14] Yu-Zhong Zhang, Harald O Jeschke, and Roser Valentí. Microscopic model for transitions from Mott to spin-Peierls insulator in TiOCl. *Physical Review B*, 78(20):205104, 2008.

[15] R Rückamp, E Benckiser, MW Haverkort, H Roth, T Lorenz, A Freimuth, L Jongen, A Möller, GERD Meyer, P Reutler, et al. Optical study of orbital excitations in transition-metal oxides. *New Journal of Physics*, 7(1):144, 2005.

[16] Peter Atkins and Tina Overton. *Shriver and Atkins' Inorganic Chemistry.* Oxford University Press, USA, 2010.

[17] Daniele Fausti, Tom TA Lummen, Cosmina Angelescu, Roberto Macovez, Javier Luzon, Ria Broer, Petra Rudolf, Paul HM van Loosdrecht, Natalia Tristan, Bernd Büchner, et al. Symmetry disquisition on the TiOX phase diagram (X= Br,Cl). *Physical Review B*, 75(24):245114, 2007.

[18] Andreas Schönleber, Galina Shcheka, and Sander van Smaalen. Normal-to-incommensurate phase transition in the spin-Peierls compound TiOCl: An x-ray diffraction study. *Physical Review B*, 77(9):094117, 2008.

[19] G Caimi, L Degiorgi, NN Kovaleva, P Lemmens, and FC Chou. Infrared optical properties of the spin-1/2 quantum magnet TiOCl. *Physical Review B*, 69(12):125108, 2004.

[20] R Rückamp, J Baier, M Kriener, MW Haverkort, T Lorenz, GS Uhrig, L Jongen, A Möller, GERD Meyer, and M Grüninger. Zero-field incommensurate spin-Peierls phase with interchain frustration in TiOCl. *Physical review letters*, 95(9):097203, 2005.

[21] Reinhard Rückamp. *Orbital excitations of transition-metal oxides in optical spectroscopy.* PhD thesis, Universität zu Köln, 2006.

[22] Gabriel Lantz, B Mansart, Daniel Grieger, Davide Boschetto, Niloufar Nilforoushan, Evaggelos Papalazarou, Nicolas Moisan, Luca Perfetti, Vincent LR Jacques, Le Bolloc'h, et al. Ultrafast evolution and transient phases of a prototype out-of-equilibrium Mott-Hubbard material. *Nature communications*, 8(1):1–7, 2017.

[23] L Pisani, R Valentí, B Montanari, and NM Harrison. Density functional study of the electronic and vibrational properties of TiOCl. *Physical Review B*, 76(23):235126, 2007.

[24] AM Weiner, DE Leaird, Gary P Wiederrecht, and Keith A Nelson. Femtosecond pulse sequences used for optical manipulation of molecular motion. *Science*, 247(4948):1317–1319, 1990.

[25] MF DeCamp, DA Reis, PH Bucksbaum, and R Merlin. Dynamics and coherent control of high-amplitude optical phonons in bismuth. *Physical Review B*, 64(9):092301, 2001.

5

ANOMALOUS NON-EQUILIBRIUM RESPONSE IN BLACK PHOSPHORUS TO SUB-GAP MID-INFRARED EXCITATION

5.1 MOTIVATION

Layered van der Waals (vdW) materials have received increasing attention in recent years due to their potential applications in optoelectronics and solar energy harvesting [1, 2, 3]. Due to spatial confinement, the optical response of atomically thin semiconductors is dominated by strongly bound excitons, whose typically large binding energies are drastically reduced by more than an order of magnitude in their bulk counterpart. Understanding how the excitonic structure is affected by the dimensionality crossover from 2D to 3D is of key importance to clarify the role of interlayer coupling and dielectric screening in defining the electronic properties of layered semiconductors.

However, this is intrinsically challenging in most of 2D materials, like transition-metal dichalcogenides (TMDCs) and hexagonal boron nitride (h-BN) semiconductors, mainly because the band gap is direct only in the monolayer, while indirect in the bulk material. Black phosphorus (BP) has recently emerged as a promising candidate to bridge this gap [4]. With a carrier mobility comparable to that of graphene, BP features a direct band gap in both its single-layer (phosphorene) and bulk form [4, 5]. The amplitude of the gap is strongly layer-dependent, spanning from the visible (2 eV) to the mid-infrared (0.3 eV) range as the layer thickness is increased, thereby making BP a unique platform to study the dimensionality crossover from 2D to 3D.

The application of external stimuli, such as electric fields [6], pressure [7, 8], in-plane mechanical strain [9, 10, 11, 12] and dopants [13, 14], has proved an effective way to manipulate the electronic structure of BP. Ultrashort pulses are emerging as an exceptional tool to address the non-equilibrium response and possibly control both its electronic and optical properties on the ultrafast time-scale [15, 16, 17, 18, 19, 20]. In particular, photo-excitation by near-infrared laser pulses has been found to trigger a band gap renormalization in bulk BP due to the transient enhancement of dielectric screening induced by the excited photo-carrier population [21, 22, 23]. However, the non-equilibrium dielectric environment upon photo-injection of a small (i.e., smaller than the band gap) excess energy, remains unexplored. In different complex materials, long-wavelength ac-fields have been shown to hinder electronic excitations

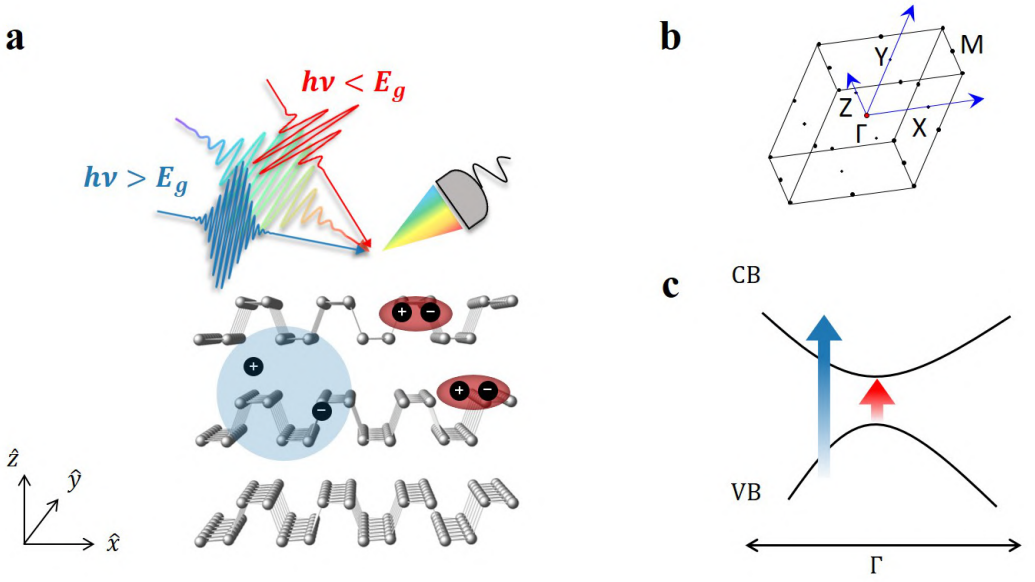

Figure 5.1: **Conceptual idea of the experiment. a)** Sketch of the broadband reflectivity measurements carried out on bulk BP following above- (blue) and below-gap (red) photo-excitation. Mid-infrared photo-excitation triggers an optical resonance that is consistent with the undressed exciton in the monolayer phosphorene. **b)** First Brillouin zone. **c)** Simplified sketch of the electronic structure at the Γ point. The arrows represent the high-photon energy (blue) and sub-gap (red) photo-excitation.

and drive collective, non-adiabatic responses, through phonon-pump [24, 25, 26, 27] and coherent electronic effects [28, 29, 30, 31].

5.1.1 *The experiment*

The aim of our study is to investigate the non-equilibrium response of bulk BP to both above-gap and sub-gap photo-excitation. Experimentally, we photo-excite the sample by ultrashort pulses with photon energy tunable across the equilibrium mid-infrared (MIR) band gap and monitor the photo-induced change in reflectivity over a broad energy range (Figure 5.1).

The major finding of our work is that photo-excitation by high- and low-photon energy pulses yields remarkably different optical responses. While high-photon energy excitation leads to a broadband light-induced transparency in the visible range due to phase space filling, excitation with photon energies comparable to the band gap triggers an anomalous response, which is solely localized at the energies of the single-layer exciton resonance. We characterize this response as function of the MIR photon energy, the photo-excitation intensity and the sample temperature.

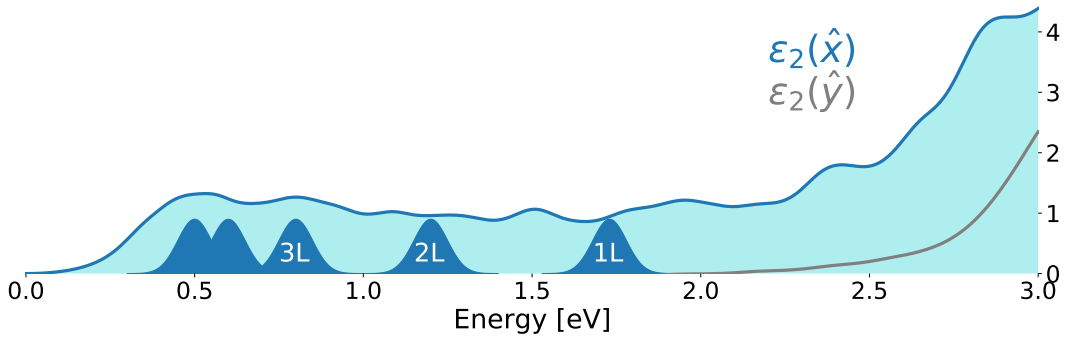

Figure 5.2: **Optical fingerprint of 3D screening in bulk black phosphorus.** Calculated imaginary part of the dielectric function in bulk BP along the armchair ($\hat{x}$, blue) and zigzag ($\hat{y}$, grey) direction, convoluted with a numerical broadening of 100 meV. The blue peaks denote the lowest-energy exciton resonances (E_{11}) in monolayer (1L), bilayer (2L), trilayer (3L) etc. BP, adapted from ref. [37].

5.2 EQUILIBRIUM DIELECTRIC ENVIRONMENT IN BLACK PHOSPHORUS

BP is an elemental semiconductor which crystallizes in a layered orthorhombic structure, where, because of sp_3 orbital hybridization, phosphorus atoms are arranged in a puckered honeycomb lattice [32]. As shown in Figure 5.1a, the resulting layers have two inequivalent high-symmetry directions, the so-called armchair ($\hat{x}$) and zigzag ($\hat{y}$) directions. This strong in-plane anisotropy has macroscopic consequences on both the electronic and optical properties of BP [5, 33, 34].

We show in Figure 5.2 the single-particle optical absorption in bulk BP calculated through first-principle hybrid-functional DFT theory, as discussed in Appendix A. As a result of the symmetry selection rules, light polarized along the zig-zag direction is expected to be absorbed only above ∼2 eV. Conversely, when the polarization is parallel to the armchair direction, the computed absorption threshold is 0.345 eV. This agrees with previous experimental and theoretical studies [5, 35], and corresponds to a direct electronic band gap at the Γ point (Figure 5.1c)[1].

In order to identify the optical transitions that give rise to the structured absorption in Figure5.2, it is crucial to consider the evolution of the optical properties of BP as function of the sample thickness. The direct band gap energy in the monolayer phosphorene is ∼2 eV, and the optical absorption is dominated by excitons with binding energies as large as hundreds of meV [37, 38, 39, 40, 41]. Although higher-energy exciton states are theoretically predicted in the single-layer limit [5], the most prominent one is the lowest-energy 1s resonance of the E_{11} exciton transition, that has been identified by photoluminescence and absorption spectroscopy, and lies at ∼1.73 eV [37, 42].

Importantly, as the layer number (L) is increased, the E_{11} resonance (along with the band gap) monotonically shifts to lower energies, as a consequence of the strong

1 It should be noted that we used in the calculation a conventional unit cell with double sized interlayer distance, as in ref. [36].

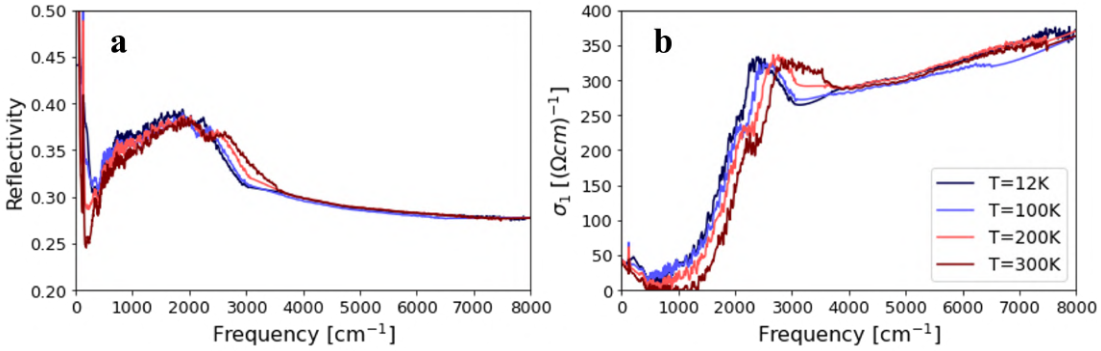

Figure 5.3: **FTIR static measurements. a)** Steady-state reflectivity measurements for a variety of temperatures in the mid- and far-infrared spectral range. **b)** Temperature-dependence of the optical conductivity extracted from panel a through the Kramers-Kronig relations.

interlayer interactions. As denoted by the position of the blue peaks in Figure 5.2, the singlet exciton red-shift does not scale linearly with the layer number and eventually reaches a plateau at ∼15L, giving rise to the absorption edge in the bulk limit (0.34 eV) [38]. This critical thickness is consistent with the theoretically predicted screening length of 10 nm, which is roughly 20 atomic layers [5].

The optical absorption of bulk BP is thus the result of the strong interlayer interactions that arise from the reduced perpendicular quantum confinement. In particular, the optical transitions within 0.34 eV (gap energy in bulk BP) and 2 eV (gap energy in the monolayer) are intrinsically related to the three-dimensional nature of the material [43]. This is evident in our DFT calculations, which confirm that absorption in this optical range is dominated by transitions involving solely the lowest energy bands dispersing along the stacking direction, as detailed in Appendix A.1.

In our time-domain measurements, we leverage on this characteristic and use a white-light supercontinuum (1.3-2.2 eV) to monitor the transient reflectivity in this spectral region that is expected to be the most sensitive to pump-induced changes of the 3D screening environment.

5.2.1 *Static reflectivity measurements*

We characterized the sample by performing steady-state reflectivity measurements in the far- and mid-infrared spectral range at different temperatures. The measurements were performed by P. Di Pietro and A. Perucchi at the SISSI infrared beamline [44] of the Elettra Synchrotron in Trieste (Italy).[2] Reflectivity data were collected using a Bruker Vertex 70v interferometer.

The reflectivity is rather flat above 4000 cm^{-1} and reaches a value close to 0.3 for all the temperatures examined (Figure 5.3a). In the mid-infrared region, from 500 to 4000 cm^{-1}, we observe an increase in the reflectivity which features a mild

2 *Elettra Sincrotrone Trieste S.C.p.A., 34127, Basovizza, Trieste, Italy.*

dependence on the sample temperature. In the far-infrared range, the reflectivity is dominated by a peak localized at $\sim$130 cm^{-1}, that we assign to the B_{1u} IR-active optical mode, in agreement with previous studies [45, 46, 47, 48].

From the reflectivity data, we retrieved the optical conductivity for the whole set of temperatures through the Kramers-Kronig relations, as shown in Figure 5.3b. On top of the phonon mode (more prominent at low temperatures), we reveal a Drude-like contribution in the low-frequency range, due to the presence of free charge carriers. At higher frequency, a significant rise in the conductivity marks the gap energy of the sample at approximately 2250 cm^{-1} ($\sim$280 meV). The edge clearly shifts towards higher frequencies as temperature increases, confirming the anomalous temperature-dependence of the band gap that has been widely reported [49, 50, 51, 52] and only recently related to the temperature-dependence of the interlayer vdW coupling [53]. Our results are in good agreement with previous optical studies (see ref. [32] and references therein, and refs. [51, 37]), although we observe a less sharp step-like edge, which is probably due to the use of unpolarized light in our measurements.

5.3 TRANSIENT RESPONSE TO ABOVE- AND SUB-GAP EXCITATION

The broadband transient reflectivity measurements were carried out on freshly cleaved bulk BP, employing the experimental setup described in Chapter 2. From the steady-state Fourier transform infrared (FTIR) measurements reported in Figure 5.3, we identified the gap energy at room temperature to be $\sim$0.33 eV. In contrast to most of semiconductors, the band gap in bulk BP redshifts at lower temperatures, to reach $\sim$0.28 eV at 12 K. We investigated two distinct regimes: a) the photo-injected excess energy is larger than the band gap ($h\nu > E_g$), so a carrier population is excited in the material; b) the sample is photo-excited by MIR pulses ($h\nu < E_g$) that are not energetic enough to initiate electronic transitions.

We show in Figure 5.4c the time- and energy-resolved transient reflectivity change upon high photon-energy excitation. The measurement reported was performed at T=10 K, but we stress that this result is not affected by the sample temperature (Section 5.4.4). For probe photon energy (E_{pr}) below 2 eV, the pump-probe time traces are characterized by an initial negative change in reflectivity, followed – after approximately 1 ps – by a less intense positive signal (Figure 5.4d). These results are consistent with previous quasi-monochromatic pump-probe experiments in the near-infrared range, in which the early-time signal is ascribed to photo-bleaching due to Pauli blocking and the subsequent one to photo-induced absorption by the excited free carrier population [15, 16, 18].

Our broadband measurements, however, put these interpretations in a new perspective and show that the early-time photo-induced transparency is not a universal feature of the ultrafast response of bulk BP, but that it vanishes for $E_{pr} > 2$ eV. This is an indication that the Pauli blockade effect induced by above-gap photo-excitations targets only the lowest energy optical band associated to the dispersion along the stacking direction.

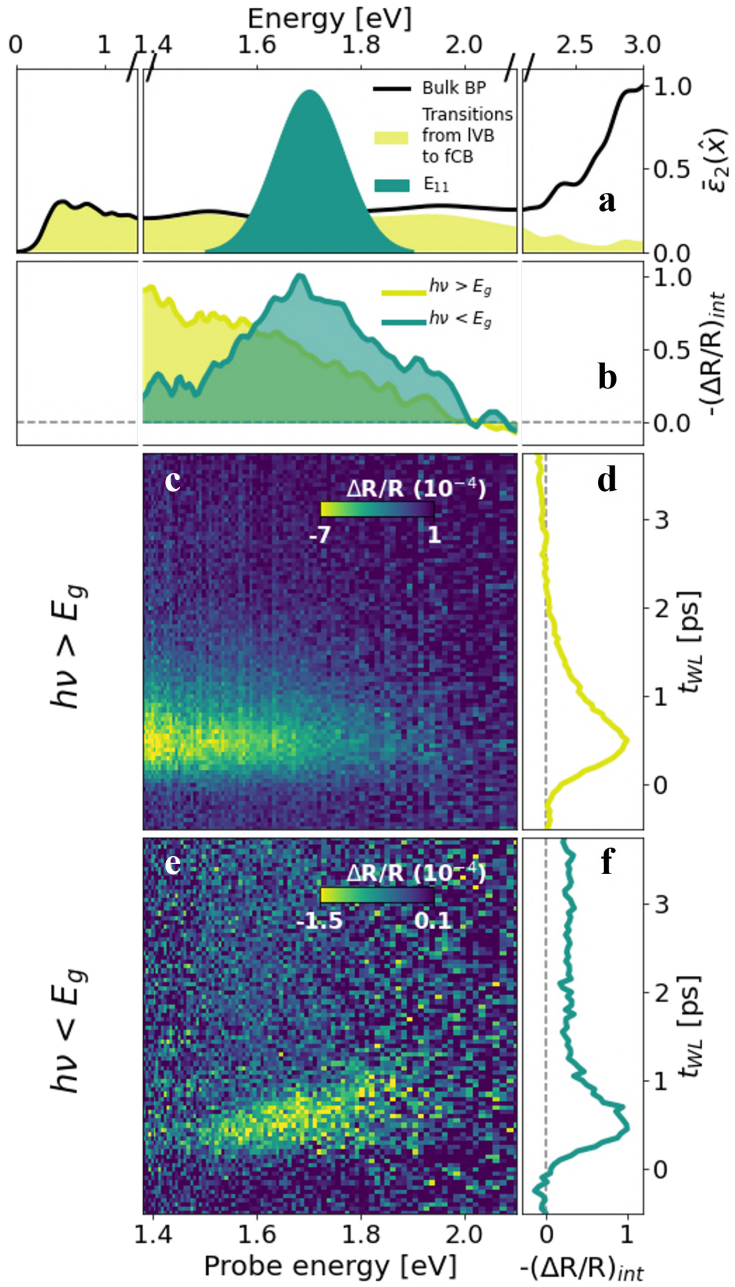

Figure 5.4: **Above- and below-gap photo-excitation in bulk black phosphorus. a)** Normalized DFT-calculated total optical absorption of bulk BP (thick black line). The yellow area indicates the optical absorption obtained when only the transitions from the last valence band (lVB) to the first conduction band (fCB) are included in the calculation. The green Gaussian shape indicates the lowest-energy exciton resonance in the single-layer limit. The energy scale is uniformly spaced from 1.34 eV up to 2.1 eV (probe energy window), and it is shrinked below 1.38 eV and above 2.1 eV. **c,e)** Transient reflectivity map measured on bulk BP at 10 K upon photo-excitation by high-photon energy (3.1 eV > E_g) and sub-gap (275 meV < E_g) pulses, respectively. The pumping fluences were 21 μJ cm^{-2} and 130 μJ cm^{-2}. **b)** Normalized spectra at fixed t_{WL}=700 fs of the maps in c and e. A Gaussian smoothing (σ=1) has been applied to both traces. **d,f)** Normalized pump-probe traces of the maps in c and e integrated over the region (1.4-1.7 eV) and (1.5-1.8 eV), respectively.

To clarify this point, we compare in Figure 5.4a the DFT optical absorption computed including in the calculation all the optical transitions (black line), and only the transitions between the last valence band (lVB) and the first conduction band (fCB) (yellow-shadowed area). The two curves overlap up to approximately $\sim$1.7 eV and then start to deviate, until the contribution of the optical transitions from lVB to fCB is almost suppressed. As transitions to other bands dominate above 2 eV, the probe can be absorbed even if the lVB and fCB are already occupied by the photo-excited carrier population, thereby overcoming the Pauli blocking effect. We stress that this effect is not related to a specific pump photon energy and photo-excitation by pumps with smaller photon energy (0.65 eV) but still larger than the band gap, induces a similar spectral response (Section 5.4.3).

The broadband photo-induced transparency below 2 eV is not present when the sample is excited by pulses with photon energy smaller than the MIR gap (Figure 5.4e). Strikingly, the spectral response with long wavelength pumps displays a qualitatively different response, that is characterized by a negative feature peaked at $\sim$1.7 eV (Figure 5.4b). The suppression of the Pauli blocking effect is an indication that no optical transitions occur along the stacking direction upon the photo-excitation. Moreover, the emergence of a transient response that is well localized in frequency is in stark contrast with the calculated optical absorption of bulk BP (Figure 5.4a), that does not display any particular resonance at 1.7 eV. Based on these arguments and the assignments in refs. [37, 42, 54], we tentatively identify this signal with the appearance of a transient absorption from the lowest-energy exciton resonance in the monolayer phosphorene, whose energy exactly matches the observed MIR-induced signal (Figure 5.4a, green curve).

In contrast to previous transient absorption measurements in few-layer BP that reported a derivative-like signal at the exciton resonance [18], our measurements display a signal centered at the expected E_{11} transition, with no significant energy shifts within the time window considered in Figure 5.4e. This may be an indication that, at least at early-times, many-body interactions (such as renormalization of the band gap and exciton binding energy, which would determine a pump-induced energy shift in the data) are negligible.

5.4 CHARACTERIZATION OF THE ABOVE-GAP EXCITATION

In this section, we characterize the response of the sample to above-gap excitations. Specifically, we analyze the dynamics at long time delays and study the transient response as function of the pumping fluence, the pump photon energy and the sample temperature.

5.4.1 *Coherent longitudinal acoustic phonons generation in BP*

Figure 5.5a shows the time- and spectrally-resolved relative reflectivity induced by a 3.1 eV photo-excitation for pump-probe delays up to 100 ps. After the initial photo-

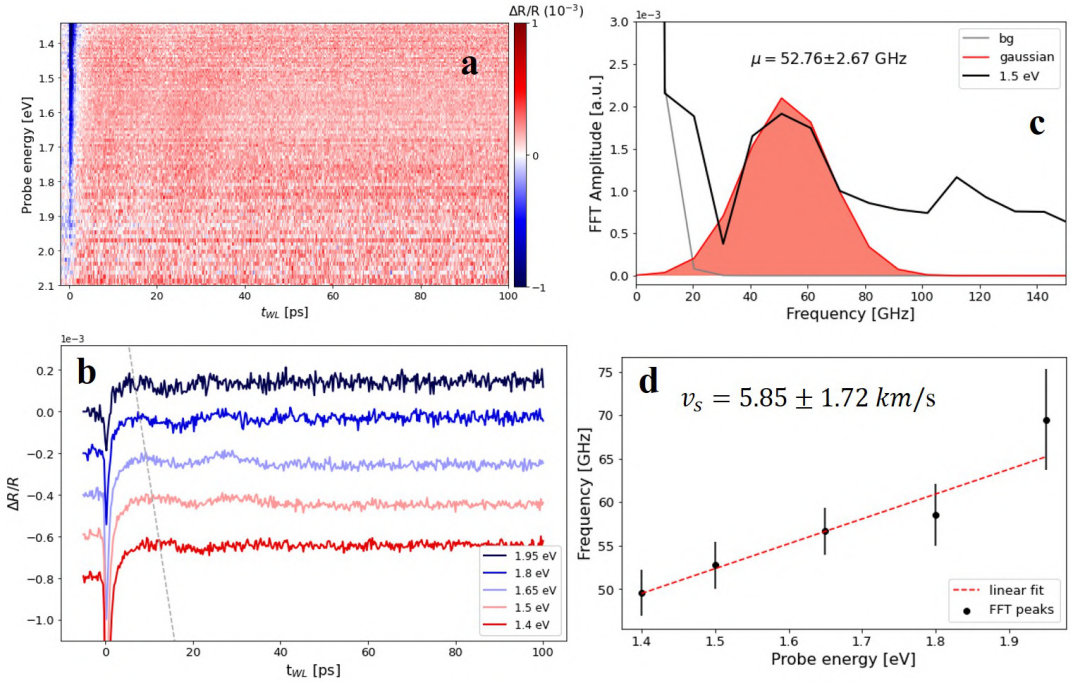

Figure 5.5: **Longitudinal sound velocity revealed by Coherent Longitudinal Acoustic Phonon (CLAP) creation. a)** Transient change in reflectivity induced by visible ultrashort pulses as function of time-delay and spectral content of the white-light supercontinuum probe. **b)** Horizontal cuts of the map in a for a selection of probe photon energies, each averaged over 70 meV (±35 meV with respect to the value indicated in the label). The traces are arbitrarily shifted for clarity. The dashed grey line is a guide for the eye to highlight the linear dependence of the CLAP frequency on the photon energy of the probe. **c)** Fourier transform (black line) of the 1.5 eV curve in b. The Fourier transform calculation has been performed avoiding the early-time negative dynamics of the signal. The peak arising at about 50 GHz was fitted by a gaussian-like function (red shape) to estimate its central frequency. **d)** Central frequency of the Fourier-transform estimated as in c as function of the selected probe photon energies (black bullets). The dashed red line indicates a linear fit to the data, whose slope gives an estimation of the longitudinal sound velocity of black phosphorus through Equation 5.1 [55].

bleaching observed in Figure 5.4, at longer time scales, the reflectivity is modulated by oscillations, whose frequency increases with increasing probe photon energies. This is better highlighted in Figure 5.5b where we plot pump-probe traces for selected probe photon energies averaged over 70 meV. We attribute this energy-dependent modulation of the reflectivity to the onset of Coherent Longitudinal Acoustic Phonons (CLAP) in bulk BP. CLAP detection via pump-probe spectroscopy is a largely studied phenomenon and a well-established tool to measure the longitudinal sound velocity in crystals [56, 55, 57, 58].

In this framework, the pump pulse initiates a travelling strain wave which propagates away from the surface at the longitudinal sound velocity of the material and periodically shapes its dielectric function. When the probe impinges on the sample, reflection from both the surface and the CLAP oscillations will contribute to the measured reflectivity, resulting in interferential processes that cause the oscillatory behaviour observed in Figure 5.5b. Being the result of an interferential process, the oscillating frequency (f) depends on the wavelength (λ) of the probe pulses, according to the following relation [55]:

$$f = \frac{2nv_s}{\lambda} \tag{5.1}$$

where n is the refractive index and v_s the longitudinal velocity.

The technique has been applied recently to bulk BP to study how the in-plane anisotropy affects the CLAP generation [59]. Here, we use the wavelength-dependent reflectivity oscillations to estimate the sound velocity and provide a characterization of the sample. For this purpose, we estimate the oscillating frequency by Fourier-transforming the time-traces in Figure 5.5b. We discard in the calculation the initial transient response. An example of the Fourier analysis is given in Figure 5.5c, where the black line is the Fourier-transform of the oscillating reflectivity measured at $h\nu$=1.5 eV. We fit the peak arising at about 50 GHz with the sum of a gaussian function (red shape) and an exponential decay to account for the incoherent contributions. By repeating the same procedure for all the time-traces in Figure 5.5b, we get the oscillating frequencies that we plot in Figure 5.5d as function of the probe photon energy. A linear fit to the data estimates the longitudinal sound velocity in our sample to be v_s = 5.85±1.72 km/s, in agreement with the literature [59, 60]. In the calculation, we considered the refractive index calculated in ref. [61].

5.4.2 *Fluence-dependence of the visible pump-probe signal*

We show in Figure 5.6 the transient reflectivity upon photo-excitation by 3.1 eV pulses with different fluence. Both the photo-induced transparency by photo-bleaching (Figure 5.6b) and the photo-induced absorption (Figure 5.6c) scale linearly in pump fluence, as shown in the insets. This is an indication that we work in a regime in which the photo-excited free carrier population is proportional to the absorbed power.

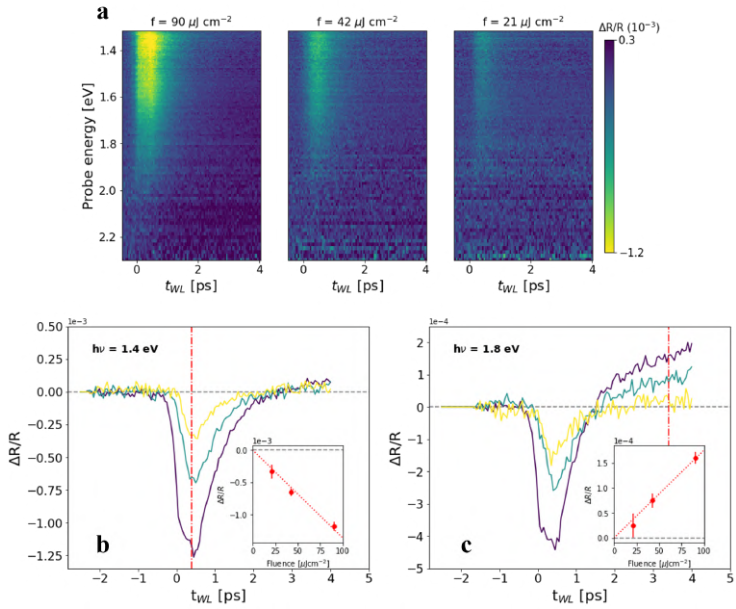

Figure 5.6: **Fluence-dependent visible pump-probe measurements. a)** Color-coded maps of transient change in broadband reflectivity after photo-excitation by visible ultrashort pulses with variable fluence at 10 K. **b-c)** Time-traces at selected probe photon energies ($h\nu$=1.4 eV and $h\nu$=1.8 eV, respectively) for all the three fluences under study. The insets show the fitted linear dependence of the transiently induced transparency at t_{WL}= 400 fs and t_{WL}= 3.5 ps.

5.4.3 *Above-gap photo-excitation by near-infrared pulses*

In order to explore the non-equilibrium optical response upon injection of different amounts of excess energy, we photo-excited the sample with near-infrared ultrashort pulses. Considering the characteristic mid-infrared band gap of bulk BP, these photon energies are large enough to excite a photo-carrier population. At the same time, they are much lower than the visible photo-excitation discussed in Section 5.3 that may eventually initiate higher-order electronic transitions.

We used one of the two near-infrared outputs of the Twin Optical Parametric Amplifier as pump and tuned it in the range 0.65-0.83 eV. We show in Figure 5.7 the results of the experiment. There is no appreciable difference neither in the spectral shape nor in the dynamics of the signal upon photo-excitation by different photon energies (Figure 5.7a,b). The spectral dependence of the transient reflectivity is very similar to the one photo-excited by visible pulses: at early times, there is a broadband photo-bleaching (negative differential reflectivity). Similar to the optical response to 3.1 eV photo-excitation discussed in Section 5.3, the photo-bleaching is confined below ∼2 eV.

Above this threshold, the optical absorption is dominated by higher-order transitions, which are not affected by Pauli blocking. However, when compared to Figure 5.5a, the dynamics of the early-time photo-induced transparency due to phase space filling is slower at smaller pump photon energy. This difference could be explained

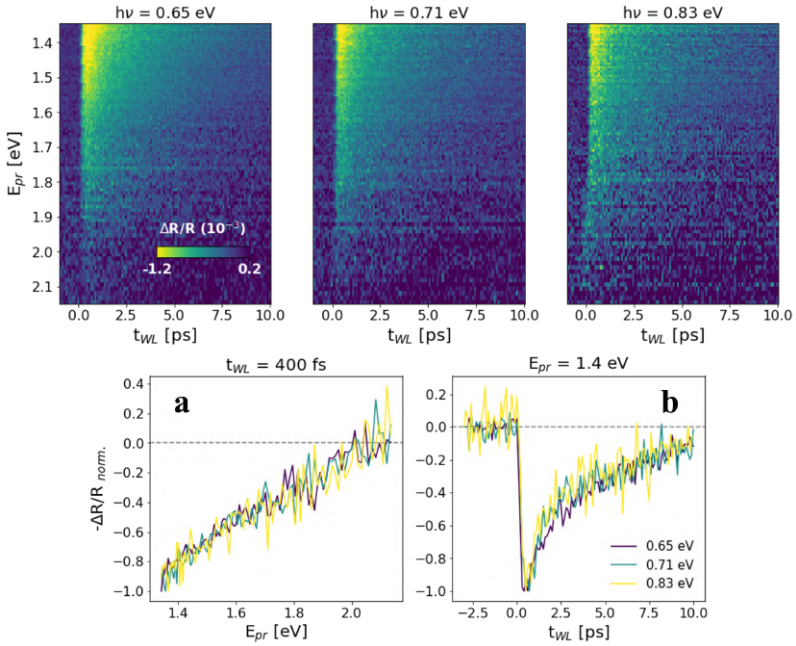

Figure 5.7: **Photo-excitation by near-infrared ultrashort pulses.** Transient reflectivity color-coded maps upon photo-excitation by near-infrared pulses with tunable photon energy. **a)** Normalized probe energy-dependent spectra at fixed time delay (t_{WL}=400 fs) for different pump photon energy. **b)** Normalized pump-probe traces at fixed probe energy (E_{pr}=1.4 eV).

as follows. The photo-bleaching by Pauli blocking is ultimately due to the fact that the probing energy levels are already occupied by the pump-excited carriers. On a picosecond time scale, intra-band scattering with phonons leads to a relaxation of the free photo-carriers that results in a reduction of the Pauli blocking contribution to the optical signal. As the pump photon energy is decreased, also the number of de-excitation channels available for the free carrier population is reduced. This could result in a slower electron-phonon scattering dynamics and, in turn, in the observed slower dynamics of the bleach signal (Figure 5.7b). The broadband near-infrared pump-probe measurements are a clear indication that the overall optical response of the sample to above-gap photo-excitations is similar, no matter how large the photon energy is. Only sub-gap photo-excitations unveil a response peaked at the monolayer exciton resonance.

5.4.4 *Temperature-dependence of the pump-probe signal*

As highlighted in Section 5.2.1, BP features anomalous thermoelectric properties and its gap energy monotonically increases with increasing temperature (Figure 5.3b).

The optical response to visible and near-infrared pulses does not have strong dependence on the sample temperature. We summarize in Figure 5.8 the pump-probe measurements performed on bulk BP at different temperatures upon visible (Figure 5.8a) and near-infrared (Figure 5.8b) photo-excitation. The normalized visible

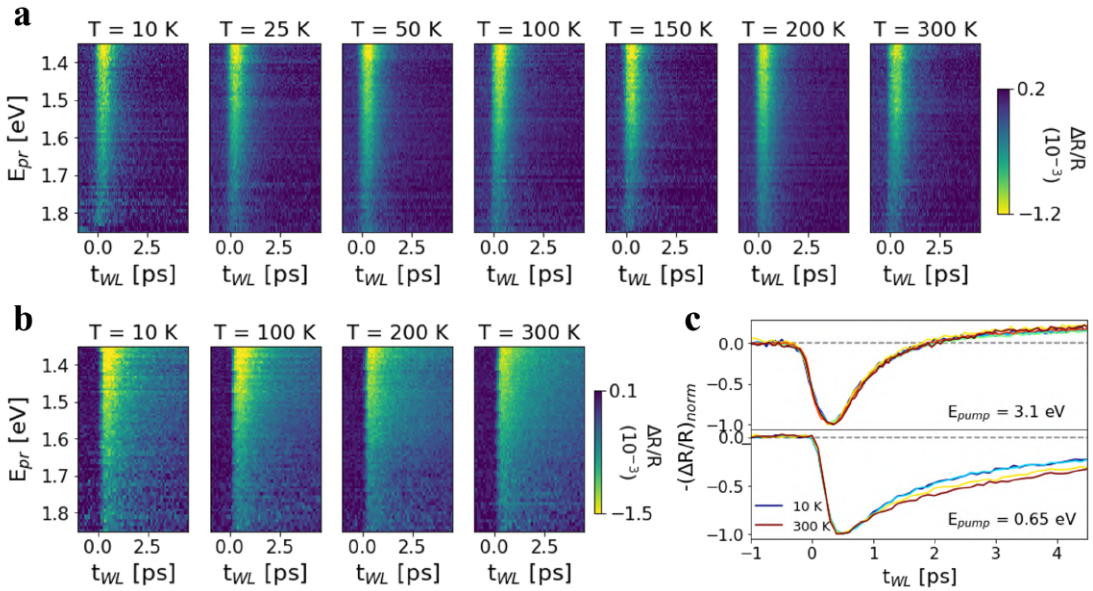

Figure 5.8: **Transient reflectivity maps at different temperatures. a-b)** Transient change in reflectivity at different temperatures upon photo-excitation by visible (E_{pump} = 3.1 eV) and near-infrared (E_{pump} = 0.65 eV) pulses, respectively. **c)** Normalized pump-probe traces at different temperatures integrated over the range 1.35-1.85 eV following a visible (top) and near-infrared (bottom) photo-excitation.

pump-probe traces integrated over a broad energy range almost overlap at different temperatures (Figure 5.8c, top panel). The same analysis on the reflectivity maps following a near-infrared photo-excitation (Figure 5.8c, bottom panel) shows that also in this case the overall signal is similar at different temperatures. We observe a slower decay time of the photo-bleaching at higher temperatures, possibly due to a modified electron-phonon scattering rate.

5.5 CHARACTERIZATION OF THE SUB-GAP EXCITATION

We present in this section a characterization of the transient response to sub-gap excitations. In particular, we address the fluence-, photon energy- and temperature-dependence of the transient response of BP to MIR pulses.

5.5.1 *Fluence-dependence of the MIR pump-probe signal*

We analyze in Figure 5.9 the differential reflectivity following photo-excitation by MIR pulses with tunable fluence. The optical response at the lowest fluence under exam is the one discussed in Figure 5.4, where the only contribution to the signal is well localized in frequency and matches the exciton resonance. When the MIR pump fluence is increased (up to almost an order of magnitude), a background signal arises on top of the resonance, whose spectral dependence (Figure 5.9b) is similar to

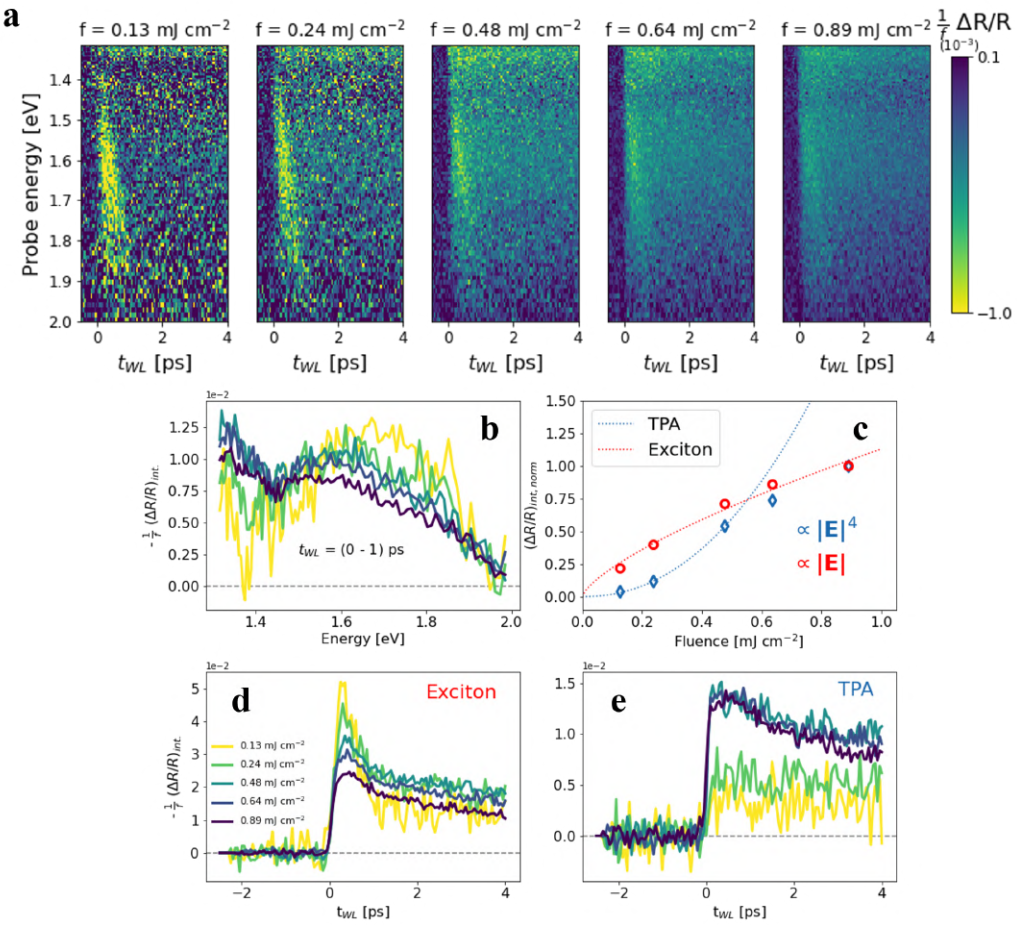

Figure 5.9: **Fluence-dependent MIR pump-probe measurements. a)** Transient reflectivity maps at 10 K upon photo-excitation by mid-infrared (275 meV) with different fluences (f). To highlight the exciton resonance at low fluences, all maps have been rescaled by the corresponding pump intensity ($1/f(\Delta R/R)$). **b)** Energy spectra of the maps in panel a integrated over 1 ps after the photo-excitation and normalized over the pump fluence. **c)** Normalized fluence dependence of the exciton and TPA contribution. Each point in the graph is obtained by integrating the spectra in b over the region 1.45-1.9 eV for the exciton, and 1.3-1.45 eV for the TPA signal. The dotted lines are power law fits to the data. We included in the TPA fit only the three measurements at lowest fluences. **d)** Time-traces integrated over the exciton resonance (1.45-1.9 eV) normalized over the corresponding pump fluence. **e)** Time-traces integrated over the energy region 1.3-1.45 eV to highlight the two-photon absorption (TPA) contribution.

the one measured upon above-gap photo-excitation (Figure 5.4b, yellow trace). We ascribe this frequency-broad background to nonlinear two-photon absorption (TPA).

In order to isolate the two contributions, we integrated the differential maps in Figure 5.9a over two different energy regions: the exciton resonance lies in the range 1.45-1.9 eV, while the TPA signal dominates the low-energy side of the spectrum (1.3-1.45 eV). We plot in Figure 5.9d,e the pump-probe traces integrated over these two spectral regions and normalized over the corresponding fluences. While the exciton resonance is characterized by a fast decay of approximately 1 ps, the TPA dynamics at high fluences features a slower decay time, which is very similar to the one measured upon near-infrared (0.65 eV) photo-excitation (Figure 5.7c bottom panel). This reinforces our assignment of the TPA signal.

A further confirmation comes from the fluence dependence of the resonance and TPA contributions (Figure 5.9c). We fitted the points in the plot with a power law function (βx^{α}) to extract the fluence dependence. While the TPA signal scales as the square of the fluence (α_{TPA}=2.17$\pm$0.09), in agreement with a two-photon process, the resonance is consistent with a square root-like dependence (α_{exc}=0.71$\pm$0.07). This may be an indication that the peaked transient absorption is the result of a coherent effect that scales with the amplitude of the electric field ($\sqrt{f} \sim |E|$).

It should be noted that the two points at highest fluences of the TPA signal deviate from the expected quadratic power law. This behaviour can be explained by the saturation of optical absorption that has been observed in BP under strong illumination. Due to the Pauli blockade effect, interband transitions become forbidden and this results in a nonlinear enhancement of transmittance in both few-layer and bulk BP [62].

5.5.2 *Reflectivity maps as function of MIR pump photon energy*

We show in Figure 5.10a the time- and energy-resolved transient reflectivity upon photo-excitation by MIR pulses with photon energy tunable across the bulk BP band gap. The measurement at the highest MIR photon energy displays a prominent contribution of the spectral feature peaked at 1.7 eV and assigned to the monolayer lowest-energy exciton resonance. A spectrally-flat background is present, along with a replica of the signal at t_{WL} $\sim$2 ps that arises from a partial reflection of the copper substrate. As the MIR photon energy is decreased, the contribution of the exciton is reduced in intensity, but the flat background is not suppressed.

In order to isolate the exciton contribution and quantify it as function of the MIR photon energy, we performed a bi-exponential fit of the pump-probe traces at each probe energy. We identified a fast-decaying component associated to the resonance, and a slow-decaying component that is associated to the background and that has been subtracted. We show in Figure 5.10b the energy-integrated pump-probe traces after the subtraction of the background.

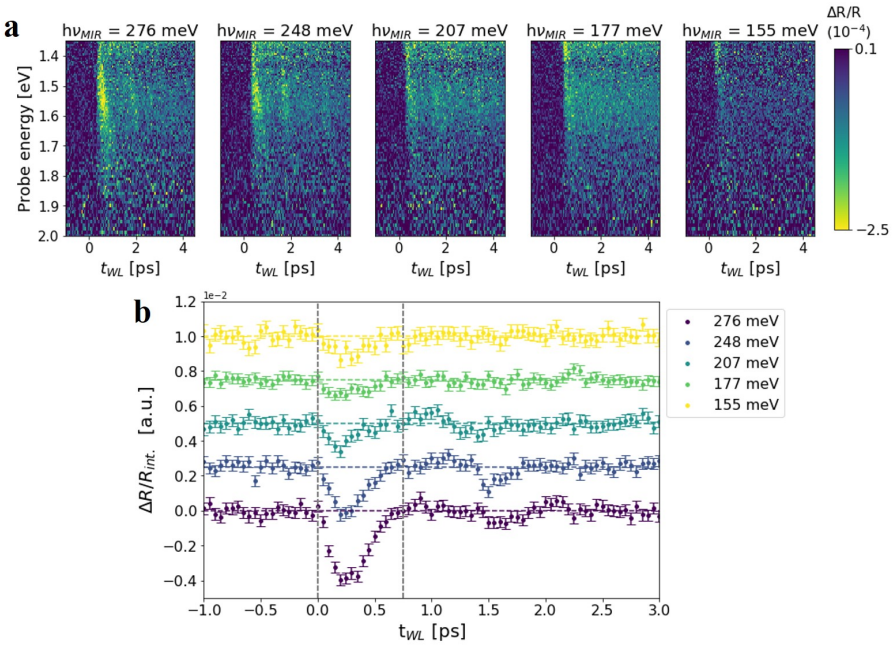

Figure 5.10: **Photon energy-dependent MIR pump-probe measurements. a)** Transient reflectivity maps upon photo-excitation by MIR pulses with tunable photon energy at constant fluence (160 μJcm^{-2}). **b)** Pump-probe traces integrated over the spectral region (1.45-1.65) eV after the subtraction of a slow-decay component through bi-exponential fitting of the data in panel a.

5.5.3 *MIR pump-probe signal as function of temperature*

We plot in Figure 5.11a the time- and energy-resolved transient reflectivity maps upon photo-excitation by MIR pulses ($h\nu$=275 meV) at different sample temperatures. The $\Delta R/R$ map at low temperature consists of the frequency-localized signal associated to the phosphorene E_{11} exciton resonance and a spectrally-flat background.

Similarly to the MIR photon-energy dependent measurements (Figure 5.10a), the resonance disappears at higher temperatures, while the background persists, even if reduced in intensity. In order to study the temperature-dependence of the two contributions independently, we analyzed the data as follows. Firstly, we performed an integration of the pump-probe traces over the spectral range of the resonance (1.45-1.8 eV) and subtracted the spurious replica of the signal at $t_{WL} \simeq 3$ ps coming from the back-reflection of the copper substrate. The result is the black curve plotted in Figure 5.11b for a representative map at T=150 K. We fitted this curve with the sum of a fast-decaying exponential (yellow curve), which reproduces well the dynamics of the exciton, and an error function (grey curve) to fit the background. By performing the same analysis on all the maps in Figure 5.11a, we plotted in Figure 5.11c the temperature-dependent amplitude of the resonance signal (light blue curve) and of the background (pink curve). The latter is consistent with a fit-independent integration of the pump-probe traces at positive time delays (3-4 ps, dashed black curve).

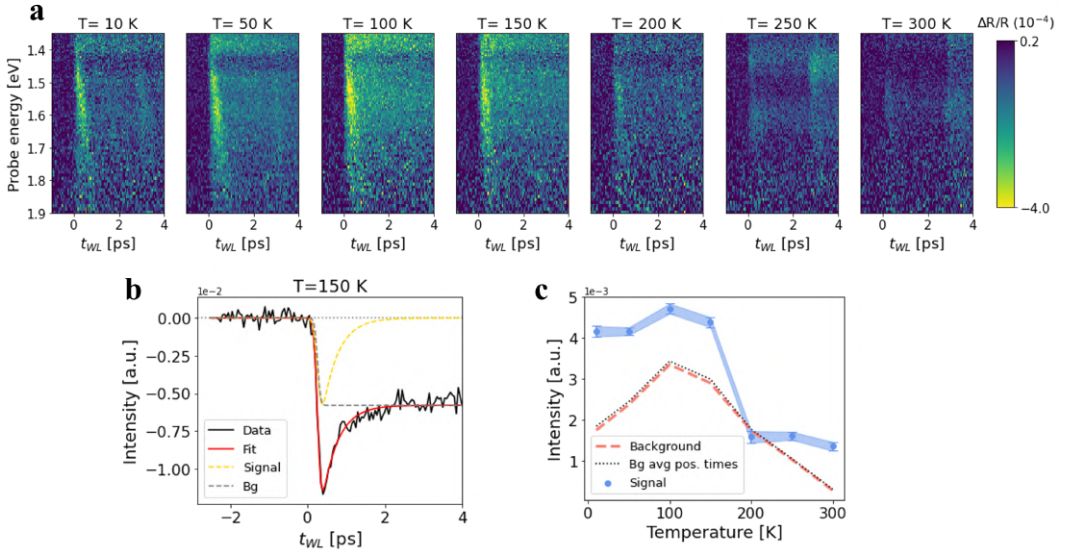

Figure 5.11: **Temperature-dependent MIR pump-probe measurements. a)** Transient reflectivity maps upon MIR photo-excitation ($h\nu$=275 meV) at different temperatures. The fluence has been kept constant and equal to 160 μJcm^{-2}. **b)** Example at T=150 K of the analysis performed. The black curve is the pump-probe traces integrated over the spectral region 1.45-1.8 eV. The red curve is a fit to the data that is the sum of a fast exponential decay (yellow curve) and a slow-decaying background component (error function, grey curve). **c)** Fitted amplitude of the signal (light blue) and of the background (pink) as function of sample temperature. The dashed black curve indicates the fit-independent background obtained by integration of the pump-probe traces at positive times (3-4 ps).

5.6 MIR-INDUCED RESONANCE

In order to shed light on the mechanism leading to the observed resonance, we summarize here the main results obtained from the characterization discussed in Section 5.5. As detailed in Section 5.5.2, we quantified the intensity of the transient signal associated to the resonance at each pump photon energy.

We plot in Figure 5.12a the results of this analysis for two different fluence regimes of the MIR pump pulse. We observe that the signal is quenched at small pump photon energies. In particular, the resonance is suppressed at approximately 200 meV at low MIR fluences, while the cut-off edge is redshifted at higher pumping fluences. We associate this cut-off to the effective band gap energy of the material upon the MIR photo-excitation, which is found to trigger a transient gap closure.

While it would be tempting to ascribe the redshift of the response to a carrier-induced band gap renormalization, as observed in ref. [22], we stress that the photo-injected excess energy here is smaller than the equilibrium band gap and no above-gap free-carrier population is excited in the linear response. In fact, according to the study of the MIR pump fluence-dependence (Section 5.5.1), population effects due to two-photon absorption can be ruled out. As evidenced in Figure 5.9, the signal

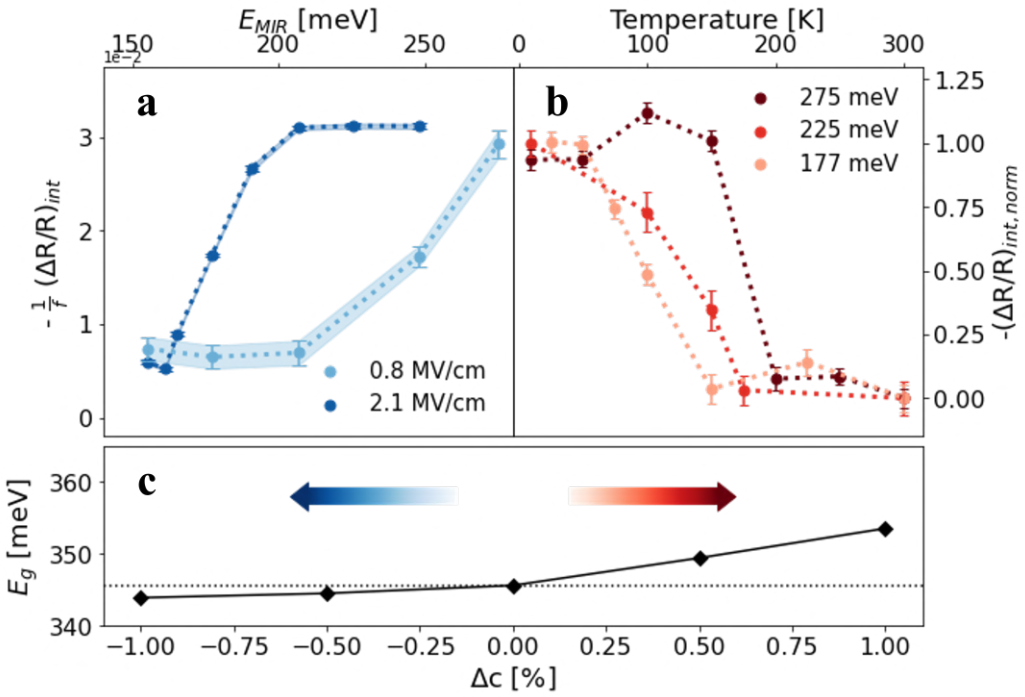

Figure 5.12: **Non-adiabatic control of the black phosphorus gap with MI pulses. a)** Intensity of the MIR-driven resonance at 10 K as function of the photon energy of the MIR pump in a low (130 μJ cm^{-2}, light blue line) and high (890 μJ cm^{-2}, dark blue line) field strength regime. Each point in the plot is the result of an integration over a specific probe energy- and time-range (1.4-1.8 eV and 0-750 fs, respectively). The curves are divided by the corresponding fluence. **b)** Normalized intensity of the resonance as function of the sample temperature for three different photon energies of the MIR pump. **c)** DFT-calculated band gap energy in bulk BP with modified interlayer distance (c). Negative (positive) values of Δc correspond to a compression (expansion) along the stacking direction.

associated to the exciton resonance does not scale as the square of the fluence (as it would be expected if two-photon absorption processes were involved), but it is consistent with a coherent effect that scales with the amplitude of the electric field.

While the further redshift of the band gap at higher MIR fluence (Figure 5.12a) could suggest a thermally driven effect, temperature-dependent measurements at fixed MIR pump photon energy rule out also this possibility. In Figure 5.12b, each point indicates the intensity of the resonance measured at a given temperature and pump photon energy (as explained in Section 5.5.3). For all the three examined MIR photon energies, the resonance disappears at high temperature, hence providing a clear indication that its emergence is related to the equilibrium band gap energy. Importantly, the high temperature cut-off for the dynamical resonance signal occurs at higher temperature when the MIR photon energy is larger. The temperature-dependence of the gap energy is then consistent with the equilibrium thermoelectric properties of BP, but follows an opposite trend with respect to the MIR fluence-dependent measurements in Figure5.12a.

5.6.1 *Double-pump response*

In order to further rule out thermal effects, we carried out double-pumped pump-probe experiments employing the three-pulse scheme described in 2.

In these experiments, the three-pulse scheme is adopted to study the broadband transient reflectivity of the sample in its excited state. The sample is simultaneously photo-excited by both the visible (3.1 eV) and MIR (275 meV) pumps (whose time delay τ can be arbitrarily set), and probed by the white-light supercontinuum, as depicted in Figure 5.13a. Two optical choppers placed along the optical path of the pumps and synchronized to run one at double the frequency of the other, repeatedly block the pumps, as sketched in the top of Figure 5.13a. The probe pulses (repetition rate = 5 kHz) are sorted according to the chopping scheme, so that they fall into one of the four dashed boxes in Figure 5.13a ("U" = unpumped spectra, "DP" = double-pumped spectra, "MIR" = MIR pump-excited spectra, "VIS" = visible-pump excited spectra). This differential acquisition allows to isolate, within the very same measurement, the dynamical response of the sample to just the visible pump ($R_{VIS} = (VIS - U)/U$), just the MIR pump ($R_{MIR} = (MIR - U)/U$) and the joint response to the double photo-excitation ($R_{DP} = (DP - U)/U$).

In Figure 5.13b,c we plot as a reference the transient reflectivity maps upon photo-excitation by MIR (R_{MIR}) and VIS (R_{VIS}) pulses, which show, respectively, the MIR-driven exciton resonance at 1.7 eV and the broadband photo-bleaching by Pauli blocking (same data discussed in Figure 5.4). The strength of our three-pulse approach is the possibility to measure how the sample responds to MIR fields after a previous photo-excitation by the visible pump. The panels d,e in Figure 5.13 ($R_{DP} - R_{VIS}$) show that, if BP is previously excited by the above-gap pump at t_{WL}=0 (white arrows), the MIR-driven resonance is suppressed and a broadband photo-induced transparency, similar to that in Figure 5.13e, is observed.

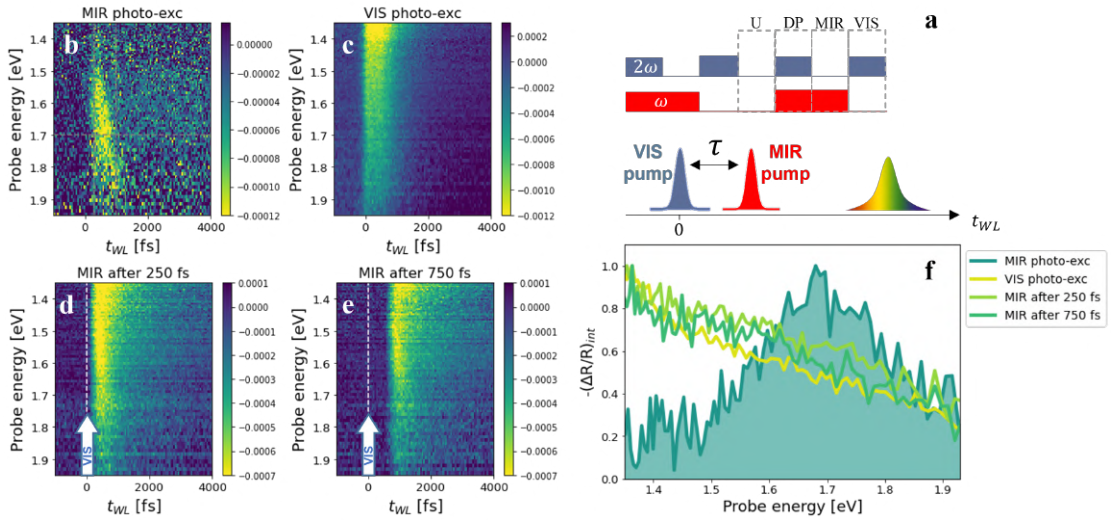

Figure 5.13: **Double-pumped pump-probe measurements. a)** Conceptual scheme of the three-pulse experiment. The blue and red squares on the top indicate the status (ON/OFF) of the optical choppers that cut the visible and MIR pumps, respectively. The blades run synchronously (ω=45 Hz), so that the response to both the pumps (DP), to only the mid-infrared one (MIR) and to only the visible one (VIS) can be isolated. The unpumped spectra (U) are also acquired as reference, when both the choppers block the pump beams. **b-c)** Transient reflectivity maps upon MIR ($h\nu$=275 meV) and visible ($h\nu$=3.1 eV) photo-excitation, respectively. **d-e)** Transient reflectivity maps upon MIR photo-excitation when the sample was previously photo-excited by visible pulses. The delay between the arrival of the two pumps is 250 and 750 fs, respectively. The white arrows indicate when the above-gap photo-excitation occurs. **f)** Normalized energy cuts of the maps in b-e. The spectra are averaged over 400 fs.

We compare in Figure 5.13f the transient spectra in the four configurations considered (maps in b-e). The suppression of the resonance in the double-pumped response reveals that its emergence takes place only in the pristine sample, where there are no free carriers. This evidence indicates that, whenever absorption occurs (being from the ground or the excited state), the photo-injected carriers screen the resonance and modulate the optical response through Pauli blocking. This is a further indication that the observed resonance is related to a coherent non-adiabatic effect, rather than a population one.

5.7 DISCUSSION

The experimental observation of a MIR-driven narrow resonance at 1.7 eV in BP constitutes the major discovery of this work. This is rather unexpected in the equilibrium response function of the bulk material, which is flat and featureless in that spectral region. Such a dramatic change in the response function exactly in correspondence of the energy of the single-layer exciton, suggests that the interlayer interactions are impulsively perturbed and thus the 3D screening environment is modified.

The nonlinear response to sub-gap excitation indicates that the transient emergence of a visible MIR-driven resonance is accompanied by a non-thermal closure of the infrared band gap (Figure 5.12a). To identify a mechanism that could rationalise our experimental evidence, we ran a set of simulations with modified interlayer spacing (c) in bulk BP at equilibrium. The rationale of this approach is that the 3D screening (along with the corresponding band structure and gap energy) at equilibrium is ultimately set by the interlayer distance in the simulated material. By freezing the in-plane atomic distances, we calculated the band gap energy when the crystalline structure is compressed ($\Delta c<0$) or strained ($\Delta c>0$) along the stacking direction up to 1% (Figure 5.12c). We found that when the interlayer distance is increased, the gap energy increases as well, in agreement with previous calculations [5]. This scenario is qualitatively analogous to an adiabatic thermal expansion, which, as observed both at equilibrium (Figure 5.3) and in temperature-dependent pump-probe measurements (Figure 5.12b), is related to an enlargement of the infrared optical gap. The observed MIR-driven collapse of the band gap (Figure 5.12a) is instead compatible with a contraction along the stacking direction.

We stress, however, that such comparison is only qualitative, while quantitatively the observed dynamical collapse of the infrared gap remains unexplained and cannot be rationalized solely as an adiabatic compression of the lattice. On the one hand, the calculated gap energy is much larger than the one extracted by the pump wavelength-dependent experiments. In this regard, it should be noted that in the simulated adiabatic compression the in-plane lattice parameters have been kept fixed, while further in-plane contractions could result in a larger band gap closure [48], as detailed in Appendix A.2 where hydrodynamic pressure-dependent simulations are discussed. On the other hand, the most relevant aspect distinguishing the observed MIR-driven response from an adiabatic contraction of the c-axis is the fact that the

latter is expected to increase the screening of excitonic resonances, while the optical measurements revealed the transient emergence of a resonance which is instead compatible with a dynamical reduction of screening.

Based on the evidence collected so far, we speculate that the sudden reduction of the 3D screening that possibly unveils the single-layer exciton in our measurements could be related to a non-adiabatic coherent redistribution of the charge carriers driven by MIR pulses. In a simple picture, the bulk material at equilibrium can be seen as an electron bath in which the single-layer excitons are largely screened due to the high carrier mobility. Upon photo-excitation by MIR pulses, the material interacts with a long-wavelength in-plane electric field, which forces the electrons to a coherent motion, resulting in light-driven ac-currents. Due to the sudden charge redistribution, the electron bath is then less effective in screening the exciton, whose transient absorption is then detected by the broadband probe. Moreover, the establishment of such currents might also affect the layered structure of the material. Analogously to the magnetic attraction experienced by wires carrying homodirectional dc-current (Biot-Savart law), the driven in-plane transport of charge carriers may result in a contraction along the stacking direction, that, based on our DFT simulations, could justify the observed band gap closure. In this regard, investigating the coherent response triggered by intense THz fields might be decisive to assess the role of light-driven ac-currents in a layered semiconductor prototype such as BP.

Finally, we stress that it cannot be excluded that other processes, not directly involving the single-layer excitonic structures, may give rise to a similar response. For example, a peaked response may arise from photo-induced perturbation of indirect band gaps. However, this seems a more unlikely scenario as significant structural changes would be required to justify such an impulsive modification of the material band structure. Moreover, motivated by our experimental evidence, we have considered that the emergence of the MIR-driven resonance and the non-thermal collapse of the gap are related phenomena. If we ease this assumption, other pictures could be considered. While the gap collapse might be related to a bulk effect, the resonance peaked at the single-layer exciton could be an indication of a photo-induced expansion of the material, eventually leading to a transient structural detachment of the surface layers. We deem this scenario unlikely for two reasons: i) the deformation needed to completely decouple the external layers would be massive and yet reversible; ii) the response is peculiar for sub-gap excitation, while energy absorption is far larger for high photon energy. Nevertheless, time-resolved structural determination (X-ray or electrons diffraction) would be needed to unequivocally rule out such effects.

5.8 CONCLUSIONS

In conclusion, we have studied the non-equilibrium dielectric environment in bulk BP upon photo-excitation by energy-tunable ultrashort pulses. Our *ab-initio* DFT calculations have shown that the optical absorption below 2 eV is dominated by tran-

sitions involving energy bands dispersing along the stacking direction, making this spectral region intrinsically linked to the enhanced 3D screening in the bulk material. We have found that high-photon energy excitations uniformly target this whole band, leading to a spectrally flat photo-induced transparency through Pauli blocking. This bulk-like spectral response is suppressed when the sample is photo-excited by sub-gap mid-infrared pulses, which reveal instead a peaked transient response, that matches the lowest-energy exciton resonance in the monolayer phosphorene. By unveiling how low energy ac-currents may modify the screening of excitonic resonances in quantum materials, our findings potentially enable an ultrafast control of screening in layered semiconductors, which is of paramount importance for 2D materials-based optoelectronic applications.

A *AB-INITIO* CALCULATIONS

The DFT calculations have been carried out by M. Zanfrognini, D. Varsano, M. Rontani and E. Molinari at the University of Modena.[3]

The ground state structural and electronic properties of bulk BP have been evaluated at the DFT level, using the Quantum Espresso package [63]. The structural relaxation has been performed using the PBE [64] approximation for the exchange correlation potential together with the plane wave basis set, while ONCVPSP [65] norm-conserving pseudopotentials have been adopted to model the electron–ion interaction; the kinetic energy cutoff for the wave-functions has been fixed to 90 Ry, while the Brillouin zone has been sampled with a 16x16x8 k-point grid. Van der Waals interactions between layers has been included using the Grimme-D2 parametrization [66].

Both atomic positions and lattice parameters (a conventional orthogonal unit cell has been used, with eight atoms per cell) were relaxed up to when forces acting on each atom were below 3×10^{-4} eV/Å. The obtained lattice parameters a = 4.43 Å, b = 3.33 Å, c = 10.48 Åare in good agreement with experimental [67] and theoretical results [68].

Hybrid-DFT (using Gau-PBE hybrid functional [69]) has been used to perform electronic band structure calculations. The equilibrium charge density and electronic Kohn-Sham states have been computed using a 20x20x10 k-point grid to sample the Brillouin zone, in combination with a 4x4x2 grid for the sampling of the Fock operator. The obtained direct electronic band gap of 0.34 eV (located at the Γ point) turns out to be in reasonable agreement with the experimental one [70].

Optical properties have been evaluated using the Yambo code [71], at the independent-particle level. The dielectric function has been calculated as:

$$\varepsilon_\alpha(E) = 1 + \frac{16\pi}{\Omega} \sum_{c,v} \sum_{k} \frac{1}{E_{c\mathbf{k}} - E_{v\mathbf{k}}} \frac{|r^\alpha_{vc}|^2}{(E_{c\mathbf{k}} - E_{v\mathbf{k}})^2 - (E + i\gamma)^2} \tag{A.1}$$

where $E_{c\mathbf{k}}$ ($E_{v\mathbf{k}}$) are the conduction (valence) electronic states computed at the Gau-PBE level, r^α_{vc} are the interband electric dipoles between a valence and a conduction state projected along direction α (the direction of light polarization) and computed using Covariant approach [71]; finally, γ is a broadening, here always fixed to 0.1 eV.

A.1 *Contributions to calculated optical absorption*

In this section, we identify the electronic transitions responsible for the absorption spectrum (computed at the independent particle level) in the range [0-3.0] eV for bulk BP. Specifically, we consider various sub-regions of the absorption spectrum and determine the pairs ($c\mathbf{k}$,$v\mathbf{k}$) of a conduction and a valence state at a given $\mathbf{k}$-point in the Brillouin zone, for which:

3 *Dipartimento FIM, Università degli Studi di Modena e Reggio Emilia, 41125, Modena, Italy*; *Consiglio Nazionale delle Ricerche—Istituto Nanoscienze, 41125, Modena, Italy.*

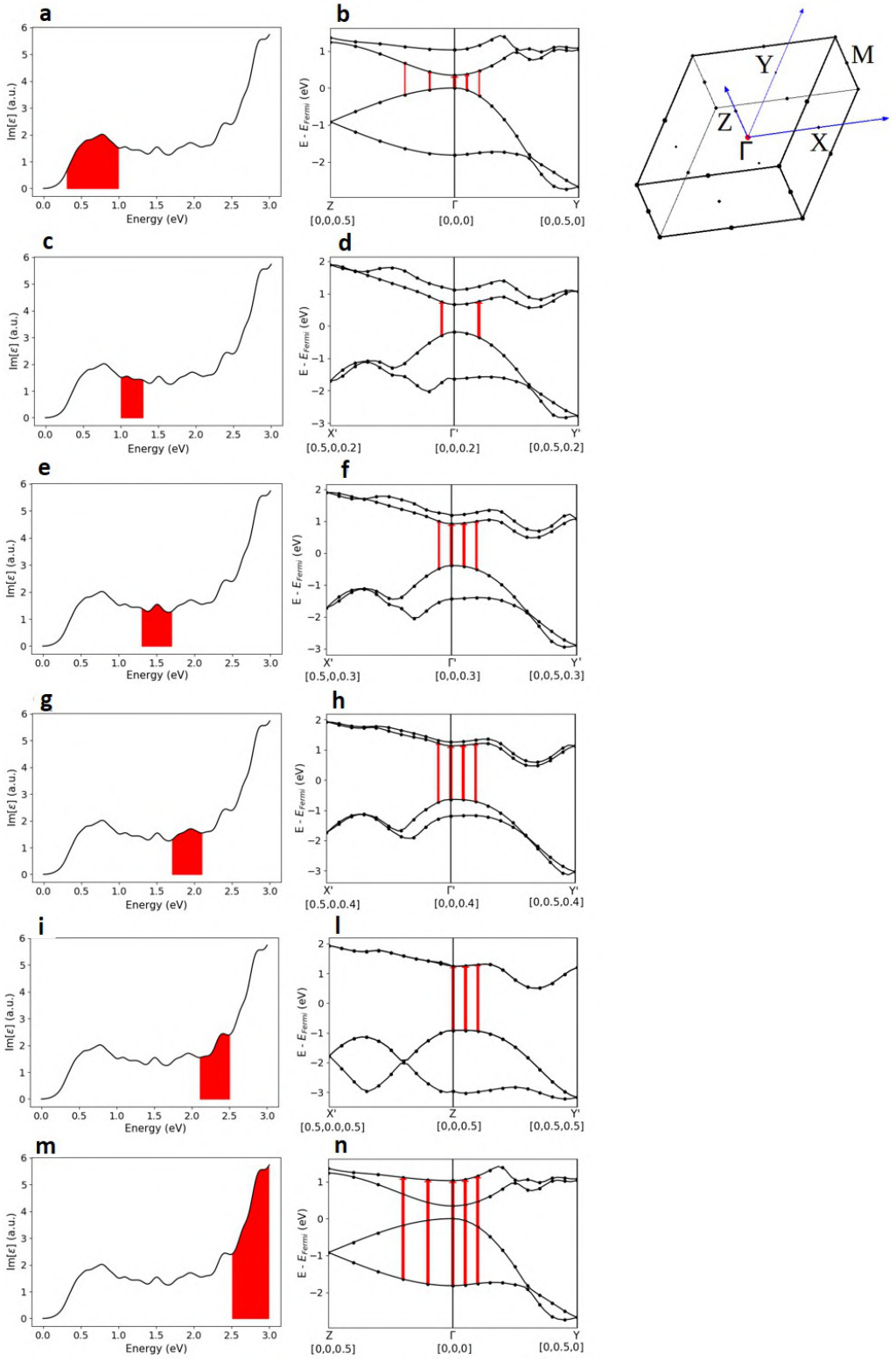

Figure A.1: **Contributions to calculated optical absorption.** Left panels show the absorption spectrum (i.e. the imaginary part of the dielectric function) for light polarized along the x-axis. In the right panels, we highlight the transitions along the high symmetry directions in the Brillouin zone that are responsible for the absorption in the red-shaded area of the spectrum in the corresponding left panels. See text for details. The high symmetry points are expressed in reciprocal lattice units.

- The energy difference $E_c(\mathbf{k}) - E_v(\mathbf{k})$ (transition energy) is within the energy range of the considered sub-interval of the absorption spectrum;
- The dipole matrix elements $|r^x_{vc}|$ (computed along the x-direction) are the most intense.

In this way, it is possible to identify which regions of the Brillouin zone contribute to a given portion of the absorption spectrum, selecting transitions characterized by a high dipole strength.

The left panels in Figure A.1 show the absorption spectrum computed for light polarized along the x direction: in each subfigure we highlight in red the portion of spectrum mainly determined by the transitions between valence and conduction states denoted by the arrows in the band structures shown in the corresponding panels on the right; the width of the arrows (denoting different transitions) is proportional to $|r^x_{vc}|$, normalized to the largest dipole matrix element in a given region. Further, the **k**-points, along which the band dispersions are shown, are expressed in reciprocal lattice units (rlu).

Figure A.1a,b show that the main contribution to absorption in the range [0.3,1.0] eV comes from transitions between the last occupied valence and the first unoccupied conduction bands, with both k parallel to the ΓY direction in the k_z = 0.0 plane and with k parallel to the ΓZ direction.

At higher photon energies (Figure A.1c,d, Figure A.1e,f and Figure A.1g,h), the absorption is explained in terms of transitions between the same valence-conduction band pairs considered before but characterized by wave vectors with progressively increasing k_z (the in-plane component remains close to Γ and mostly parallel to ΓY direction).

Looking at Figure A.1i,l, we can rationalize the absorption structure at about 2.2 eV as a transition between the penultimate occupied valence and the second unoccupied conduction bands, in the k_z = 0.5 rlu plane of the Brillouin zone, where the last two valence bands (along with the first two conduction bands) are degenerate in energy.

Finally, Figure A.1m,n demonstrate that the main contributions to the absorption peak between 2.7 and 3.0 eV come from transitions between the penultimate valence and the second unoccupied conduction band, at the wave vectors at which the transitions responsible for the absorption in the [0.3,1.0] range occur.

A.2 *Hydrodynamic pressure-dependent DFT calculations*

We present in this section the effect of external hydrodynamic compression on the electronic properties of BP. More precisely, we focus on applied pressure values in the range between 0.2 GPa up to 1.0 Gpa. The lattice parameters in presence of an external hydrodynamic pressure have been determined by minimizing the enthalpy of the structure. This has been done at the DFT level using PBE exchange correlation functional. The atomic positions within the unit cell have been relaxed following the procedure outlined in 'Methods' section. Finally, the electronic properties as

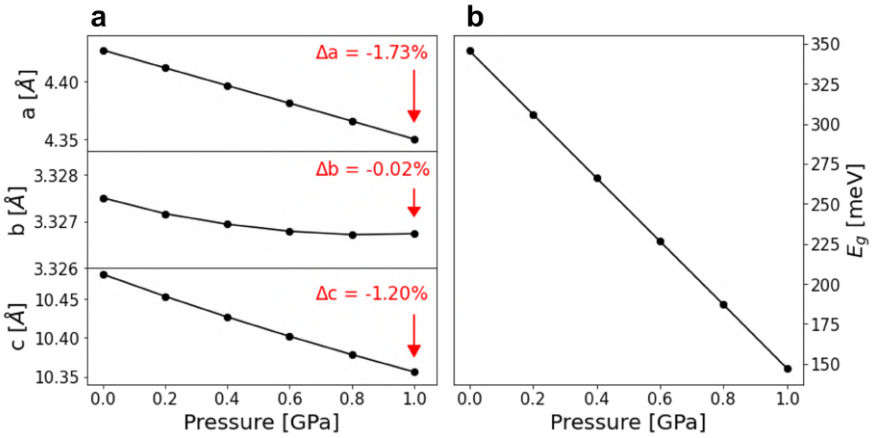

Figure A.2: **Pressure-dependent simulations. a)** Compression of the lattice parameters as function of the applied external pressure. We highlighted the relative changes in the lattice parameters corresponding to the highest applied pressure, as denoted by the red arrows. **b)** Corresponding band gap energy plotted as function of the pressure.

a function of the external pressure have been computed with Hybrid DFT, using GAU-PBE hybrid functional.

In Figure A.2a we summarize the effect of the application of an external pressure on the lattice parameters. The resulting in-plane contraction is anisotropic: it is more prominent along the armchair direction (a), while less important along the zigzag direction (b). The electronic band gap is significantly reduced upon the hydrodynamic compression (Figure A.2b).

REFERENCES

[1] KS Novoselov, o A Mishchenko, o A Carvalho, and AH Castro Neto. 2d materials and van der Waals heterostructures. *Science*, 353(6298):aac9439, 2016.

[2] Jinbing Cheng, Chunlan Wang, Xuming Zou, and Lei Liao. Recent advances in optoelectronic devices based on 2D materials and their heterostructures. *Advanced Optical Materials*, 7(1):1800441, 2019.

[3] Bin Luo, Gang Liu, and Lianzhou Wang. Recent advances in 2D materials for photocatalysis. *Nanoscale*, 8(13):6904–6920, 2016.

[4] Jingsi Qiao, Xianghua Kong, Zhi-Xin Hu, Feng Yang, and Wei Ji. High-mobility transport anisotropy and linear dichroism in few-layer black phosphorus. *Nature communications*, 5(1):1–7, 2014.

[5] Vy Tran, Ryan Soklaski, Yufeng Liang, and Li Yang. Layer-controlled band gap and anisotropic excitons in few-layer black phosphorus. *Physical Review B*, 89(23):235319, 2014.

[6] Qihang Liu, Xiuwen Zhang, LB Abdalla, Adalberto Fazzio, and Alex Zunger. Switching a normal insulator into a topological insulator via electric field with application to phosphorene. *Nano letters*, 15(2):1222–1228, 2015.

[7] ZJ Xiang, GJ Ye, C Shang, B Lei, NZ Wang, KS Yang, DY Liu, FB Meng, XG Luo, LJ Zou, et al. Pressure-induced electronic transition in black phosphorus. *Physical review letters*, 115(18):186403, 2015.

[8] Chun-Hong Li, Yu-Jia Long, Ling-Xiao Zhao, Lei Shan, Zhi-An Ren, Jian-Zhou Zhao, Hong-Ming Weng, Xi Dai, Zhong Fang, Cong Ren, et al. Pressure-induced topological phase transitions and strongly anisotropic magnetoresistance in bulk black phosphorus. *Physical Review B*, 95(12):125417, 2017.

[9] Yan Li, Shengxue Yang, and Jingbo Li. Modulation of the electronic properties of ultrathin black phosphorus by strain and electrical field. *The Journal of Physical Chemistry C*, 118(41):23970–23976, 2014.

[10] AS Rodin, A Carvalho, and AH Castro Neto. Strain-induced gap modification in black phosphorus. *Physical review letters*, 112(17):176801, 2014.

[11] Zuocheng Zhang, Likai Li, Jason Horng, Nai Zhou Wang, Fangyuan Yang, Yijun Yu, Yu Zhang, Guorui Chen, Kenji Watanabe, Takashi Taniguchi, et al. Strain-modulated bandgap and piezo-resistive effect in black phosphorus field-effect transistors. *Nano letters*, 17(10):6097–6103, 2017.

[12] Shenyang Huang, Guowei Zhang, Fengren Fan, Chaoyu Song, Fanjie Wang, Qiaoxia Xing, Chong Wang, Hua Wu, and Hugen Yan. Strain-tunable van der

Waals interactions in few-layer black phosphorus. *Nature communications*, 10(1):1–7, 2019.

[13] Jimin Kim, Seung Su Baik, Sae Hee Ryu, Yeongsup Sohn, Soohyung Park, Byeong-Gyu Park, Jonathan Denlinger, Yeonjin Yi, Hyoung Joon Choi, and Keun Su Kim. Observation of tunable band gap and anisotropic dirac semimetal state in black phosphorus. *Science*, 349(6249):723–726, 2015.

[14] N Ehlen, A Sanna, BV Senkovskiy, L Petaccia, AV Fedorov, G Profeta, and A Grüneis. Direct observation of a surface resonance state and surface band inversion control in black phosphorus. *Physical review B*, 97(4):045143, 2018.

[15] Shaofeng Ge, Chaokai Li, Zhiming Zhang, Chenglong Zhang, Yudao Zhang, Jun Qiu, Qinsheng Wang, Junku Liu, Shuang Jia, Ji Feng, et al. Dynamical evolution of anisotropic response in black phosphorus under ultrafast photoexcitation. *Nano letters*, 15(7):4650–4656, 2015.

[16] Ryan J Suess, Mohammad M Jadidi, Thomas E Murphy, and Martin Mittendorff. Carrier dynamics and transient photobleaching in thin layers of black phosphorus. *Applied Physics Letters*, 107(8):081103, 2015.

[17] Vasudevan Iyer, Peide Ye, and Xianfan Xu. Mid-infrared ultrafast carrier dynamics in thin film black phosphorus. *2D Materials*, 4(2):021032, 2017.

[18] Xianchong Miao, Guowei Zhang, Fanjie Wang, Hugen Yan, and Minbiao Ji. Layer-dependent ultrafast carrier and coherent phonon dynamics in black phosphorus. *Nano letters*, 18(5):3053–3059, 2018.

[19] Kangpeng Wang, Beata M Szydłowska, Gaozhong Wang, Xiaoyan Zhang, Jing Jing Wang, John J Magan, Long Zhang, Jonathan N Coleman, Jun Wang, and Werner J Blau. Ultrafast nonlinear excitation dynamics of black phosphorus nanosheets from visible to mid-infrared. *ACS nano*, 10(7):6923–6932, 2016.

[20] Wenzhi Wu, Yongjian Zhou, Jun Wang, Yabin Shao, Degui Kong, Yachen Gao, and Yaguo Wang. The pump fluence and wavelength-dependent ultrafast carrier dynamics and optical nonlinear absorption in black phosphorus nanosheets. *Nanophotonics*, 9(7):2033–2043, 2020.

[21] Zhesheng Chen, Jingwei Dong, Evangelos Papalazarou, Marino Marsi, Christine Giorgetti, Zailan Zhang, Bingbing Tian, Jean-Pascal Rueff, Amina Taleb-Ibrahimi, and Luca Perfetti. Band gap renormalization, carrier multiplication, and Stark broadening in photoexcited black phosphorus. *Nano letters*, 19(1):488–493, 2018.

[22] S Roth, A Crepaldi, M Puppin, G Gatti, D Bugini, I Grimaldi, TR Barrilot, CA Arrell, F Frassetto, L Poletto, et al. Photocarrier-induced band-gap renormalization and ultrafast charge dynamics in black phosphorus. *2D Materials*, 6(3):031001, 2019.

[23] H Hedayat, A Ceraso, G Soavi, S Akhavan, A Cadore, C Dallera, G Cerullo, AC Ferrari, and E Carpene. Non-equilibrium band broadening, gap renormalization and band inversion in black phosphorus. *2D Materials*, 8(2):025020, 2021.

[24] Matteo Rini, Ra'anan Tobey, Nicky Dean, Jiro Itatani, Yasuhide Tomioka, Yoshinori Tokura, Robert W Schoenlein, and Andrea Cavalleri. Control of the electronic phase of a manganite by mode-selective vibrational excitation. *Nature*, 449(7158):72–74, 2007.

[25] Roman Mankowsky, Alaska Subedi, Michael Först, Simon O Mariager, Matthieu Chollet, HT Lemke, Jeffrey S Robinson, James M Glownia, Michael P Minitti, Alex Frano, et al. Nonlinear lattice dynamics as a basis for enhanced superconductivity in $YBa_2Cu_3O_{6.5}$. *Nature*, 516(7529):71–73, 2014.

[26] Tobia F Nova, Andrea Cartella, Alice Cantaluppi, Michael Först, Davide Bossini, Rostislav V Mikhaylovskiy, Aleksei V Kimel, Roberto Merlin, and Andrea Cavalleri. An effective magnetic field from optically driven phonons. *Nature Physics*, 13(2):132–136, 2017.

[27] Alexandre Marciniak, Stefano Marcantoni, Francesca Giusti, Filippo Glerean, Giorgia Sparapassi, Tobia Nova, Andrea Cartella, Simone Latini, Francesco Valiera, Angel Rubio, et al. Vibrational coherent control of localized d-d electronic excitation. *Nature Physics*, 17(3):368–373, 2021.

[28] Dmytro Afanasiev, JR Hortensius, BA Ivanov, Alireza Sasani, Eric Bousquet, YM Blanter, RV Mikhaylovskiy, AV Kimel, and AD Caviglia. Ultrafast control of magnetic interactions via light-driven phonons. *Nature materials*, 20(5):607–611, 2021.

[29] F Giusti, A Marciniak, F Randi, G Sparapassi, F Boschini, H Eisaki, M Greven, A Damascelli, A Avella, and Daniele Fausti. Signatures of enhanced superconducting phase coherence in optimally doped $Bi_2Sr_2Y_{0.08}Ca_{0.92}Cu_2O_{8+\delta}$ driven by midinfrared pulse excitations. *Physical review letters*, 122(6):067002, 2019.

[30] Francesca Giusti, Angela Montanaro, Alexandre Marciniak, Francesco Randi, Fabio Boschini, Filippo Glerean, Giacomo Jarc, Hiroshi Eisaki, Martin Greven, Andrea Damascelli, et al. Anisotropic time-domain electronic response in cuprates driven by midinfrared pulses. *Physical Review B*, 104(12):125121, 2021.

[31] Daniele Fausti, RI Tobey, Nicky Dean, Stefan Kaiser, A Dienst, Matthias C Hoffmann, S Pyon, T Takayama, H Takagi, and Andrea Cavalleri. Light-induced superconductivity in a stripe-ordered cuprate. *science*, 331(6014):189–191, 2011.

[32] A Morita. Semiconducting black phosphorus. *Applied Physics A*, 39(4):227–242, 1986.

[33] Fengnian Xia, Han Wang, and Yichen Jia. Rediscovering black phosphorus as an anisotropic layered material for optoelectronics and electronics. *Nature communications*, 5(1):1–6, 2014.

[34] Shoufeng Lan, Sean Rodrigues, Lei Kang, and Wenshan Cai. Visualizing optical phase anisotropy in black phosphorus. *Acs Photonics*, 3(7):1176–1181, 2016.

[35] Hongtao Yuan, Xiaoge Liu, Farzaneh Afshinmanesh, Wei Li, Gang Xu, Jie Sun, Biao Lian, Alberto G Curto, Guojun Ye, Yasuyuki Hikita, et al. Polarization-sensitive broadband photodetector using a black phosphorus vertical p-n junction. *Nature nanotechnology*, 10(8):707–713, 2015.

[36] Alexander N Rudenko and Mikhail I Katsnelson. Quasiparticle band structure and tight-binding model for single-and bilayer black phosphorus. *Physical Review B*, 89(20):201408, 2014.

[37] Likai Li, Jonghwan Kim, Chenhao Jin, Guo Jun Ye, Diana Y Qiu, H Felipe, Zhiwen Shi, Long Chen, Zuocheng Zhang, Fangyuan Yang, et al. Direct observation of the layer-dependent electronic structure in phosphorene. *Nature nanotechnology*, 12(1):21–25, 2017.

[38] Guowei Zhang, Shenyang Huang, Andrey Chaves, Chaoyu Song, V Ongun Özçelik, Tony Low, and Hugen Yan. Infrared fingerprints of few-layer black phosphorus. *Nature communications*, 8(1):1–9, 2017.

[39] Guowei Zhang, Andrey Chaves, Shenyang Huang, Fanjie Wang, Qiaoxia Xing, Tony Low, and Hugen Yan. Determination of layer-dependent exciton binding energies in few-layer black phosphorus. *Science advances*, 4(3):eaap9977, 2018.

[40] Yushuang Zhang, Shaowei Wang, Shula Chen, Qinglin Zhang, Xiao Wang, Xiaoli Zhu, Xuehong Zhang, Xing Xu, Tiefeng Yang, Mai He, et al. Wavelength-tunable mid-infrared lasing from black phosphorus nanosheets. *Advanced Materials*, 32(17):1808319, 2020.

[41] Vy Tran, Ruixiang Fei, and Li Yang. Quasiparticle energies, excitons, and optical spectra of few-layer black phosphorus. *2D Materials*, 2(4):044014, 2015.

[42] Han Liu, Adam T Neal, Zhen Zhu, Zhe Luo, Xianfan Xu, David Tománek, and Peide D Ye. Phosphorene: an unexplored 2D semiconductor with a high hole mobility. *ACS nano*, 8(4):4033–4041, 2014.

[43] Yukihiro Takao, Hideo Asahina, and Akira Morita. Electronic structure of black phosphorus in tight binding approach. *Journal of the Physical Society of Japan*, 50(10):3362–3369, 1981.

[44] Stefano Lupi, Alessandro Nucara, Andrea Perucchi, Paolo Calvani, Michele Ortolani, Luca Quaroni, and Maya Kiskinova. Performance of SISSI, the infrared beamline of the ELETTRA storage ring. *JOSA B*, 24(4):959–964, 2007.

[45] Shinichi Terada, Tuyoshi Hattori, Michihiro Kobayashi, Yuichi Akahama, Shoichi Endo, and Shin-ichiro Narita. Infrared investigation of lattice vibration in black phosphorus. *Journal of the Physical Society of Japan*, 52(8):2630–2633, 1983.

[46] Toshiya Nagahama, Michihiro Kobayashi, Yuichi Akahama, Shoichi Endo, and Shin-ichiro Narita. Optical determination of dielectric constant in black phosphorus. *Journal of the Physical Society of Japan*, 54(6):2096–2099, 1985.

[47] S Sugai and IJSSC Shirotani. Raman and infrared reflection spectroscopy in black phosphorus. *Solid state communications*, 53(9):753–755, 1985.

[48] P Di Pietro, M Mitrano, S Caramazza, F Capitani, S Lupi, P Postorino, F Ripanti, B Joseph, N Ehlen, A Grüneis, et al. Emergent dirac carriers across a pressure-induced Lifshitz transition in black phosphorus. *Physical review B*, 98(16):165111, 2018.

[49] Mamoru Baba, Yoshitaka Nakamura, Kiyotaka Shibata, and Akira Morita. Photoconduction of black phosphorus in the infrared region. *Japanese journal of applied physics*, 30(7A):L1178, 1991.

[50] Cesar EP Villegas, AR Rocha, and Andrea Marini. Anomalous temperature dependence of the band gap in black phosphorus. *Nano letters*, 16(8):5095–5101, 2016.

[51] N Ehlen, BV Senkovskiy, AV Fedorov, A Perucchi, P Di Pietro, A Sanna, G Profeta, L Petaccia, and A Grüneis. Evolution of electronic structure of few-layer phosphorene from angle-resolved photoemission spectroscopy of black phosphorous. *Physical Review B*, 94(24):245410, 2016.

[52] Chen Chen, Feng Chen, Xiaolong Chen, Bingchen Deng, Brendan Eng, Daehwan Jung, Qiushi Guo, Shaofan Yuan, Kenji Watanabe, Takashi Taniguchi, et al. Bright mid-infrared photoluminescence from thin-film black phosphorus. *Nano letters*, 19(3):1488–1493, 2019.

[53] Shenyang Huang, Fanjie Wang, Guowei Zhang, Chaoyu Song, Yuchen Lei, Qiaoxia Xing, Chong Wang, Yujun Zhang, Jiasheng Zhang, Yuangang Xie, et al. From anomalous to normal: temperature dependence of the band gap in two-dimensional black phosphorus. *Physical Review Letters*, 125(15):156802, 2020.

[54] Jiong Yang, Renjing Xu, Jiajie Pei, Ye Win Myint, Fan Wang, Zhu Wang, Shuang Zhang, Zongfu Yu, and Yuerui Lu. Optical tuning of exciton and trion emissions in monolayer phosphorene. *Light: Science & Applications*, 4(7):e312–e312, 2015.

[55] C Thomsen, Holger T Grahn, Humphrey J Maris, and Jan Tauc. Surface generation and detection of phonons by picosecond light pulses. *Physical Review B*, 34(6):4129, 1986.

[56] C Thomsen, J Strait, Z Vardeny, Humphrey J Maris, J Tauc, and JJ Hauser. Coherent phonon generation and detection by picosecond light pulses. *Physical review letters*, 53(10):989, 1984.

[57] Shaofeng Ge, Xuefeng Liu, Xiaofen Qiao, Qinsheng Wang, Zhen Xu, Jun Qiu, Ping-Heng Tan, Jimin Zhao, and Dong Sun. Coherent longitudinal acoustic phonon approaching THz frequency in multilayer molybdenum disulphide. *Scientific reports*, 4(1):1–7, 2014.

[58] M Vinod, G Raghavan, and V Sivasubramanian. Fano resonance between coherent acoustic phonon oscillations and electronic states near the bandgap of photoexcited GaAs. *Scientific Reports*, 8(1):1–9, 2018.

[59] Shengjie Meng, Hongyan Shi, Hu Jiang, Xiudong Sun, and Bo Gao. Anisotropic charge carrier and coherent acoustic phonon dynamics of black phosphorus studied by transient absorption microscopy. *The Journal of Physical Chemistry C*, 123(32):20051–20058, 2019.

[60] Yasushi Kôzuki, Yoichi Hanayama, Masaki Kimura, Teruo Nishitake, and Shoichi Endo. Measurement of ultrasound velocity in the single crystal of black phosphorus up to 3.3 GPa gas pressure. *Journal of the Physical Society of Japan*, 60(5):1612–1618, 1991.

[61] Xiaomu Wang and Shoufeng Lan. Optical properties of black phosphorus. *Advances in Optics and photonics*, 8(4):618–655, 2016.

[62] Diao Li, Henri Jussila, Lasse Karvonen, Guojun Ye, Harri Lipsanen, Xianhui Chen, and Zhipei Sun. Polarization and thickness dependent absorption properties of black phosphorus: new saturable absorber for ultrafast pulse generation. *Scientific reports*, 5(1):1–9, 2015.

[63] Paolo Giannozzi, Stefano Baroni, Nicola Bonini, Matteo Calandra, Roberto Car, Carlo Cavazzoni, Davide Ceresoli, Guido L Chiarotti, Matteo Cococcioni, Ismaila Dabo, et al. QUANTUM ESPRESSO: a modular and open-source software project for quantum simulations of materials. *Journal of physics: Condensed matter*, 21(39):395502, 2009.

[64] John P Perdew, Kieron Burke, and Matthias Ernzerhof. Generalized gradient approximation made simple. *Physical review letters*, 77(18):3865, 1996.

[65] DR Hamann. Optimized norm-conserving Vanderbilt pseudopotentials. *Physical Review B*, 88(8):085117, 2013.

[66] Stefan Grimme. Semiempirical GGA-type density functional constructed with a long-range dispersion correction. *Journal of computational chemistry*, 27(15):1787–1799, 2006.

[67] Allan Brown and Stig Rundqvist. Refinement of the crystal structure of black phosphorus. *Acta Crystallographica*, 19(4):684–685, 1965.

[68] S Appalakondaiah, G Vaitheeswaran, S Lebegue, Niels Egede Christensen, and Axel Svane. Effect of van der Waals interactions on the structural and elastic properties of black phosphorus. *Physical Review B*, 86(3):035105, 2012.

[69] Jong-Won Song, Koichi Yamashita, and Kimihiko Hirao. Communication: A new hybrid exchange correlation functional for band-gap calculations using a short-range Gaussian attenuation (Gaussian-Perdue-Burke-Ernzerhof). *The Journal of chemical physics*, 135(7):071103, 2011.

[70] Robert W Keyes. The electrical properties of black phosphorus. *Physical Review*, 92(3):580, 1953.

[71] Davide Sangalli, Andrea Ferretti, Henrique Miranda, Claudio Attaccalite, Ivan Marri, Elena Cannuccia, P Melo, Margherita Marsili, Fulvio Paleari, Antimo Marrazzo, et al. Many-body perturbation theory calculations using the yambo code. *Journal of Physics: Condensed Matter*, 31(32):325902, 2019.

Part II

TIME-RESOLVED ELECTRONIC RAMAN SCATTERING IN CUPRATES: A COVARIANCE-BASED APPROACH

WHY NOISE MATTERS

Since the advent of the early technological devices, the presence of random noise has always been considered detrimental to the detection of signals. This perception also stems from our own daily experience: the annoying buzz that we happen to hear in our headphones, or the blurring of the radio signal in our car, all originate from concomitant different kinds of noises that eventually lead to the signal degradation. In the attempt to improve the communication systems, engineers have put a lot of effort ever since in trying to realize noise-limited devices.

However, in a few fascinating cases, the presence of noise can surprisingly enhance the signal detection, rather than being a nuisance. The phenomenon of *stochastic resonance* is a perfect example of this condition [1, 2]. The stochastic resonance is a nonlinear cooperative effect in which a weak periodic signal is amplified by the presence of environmental noise, which effectively makes the system "resonating" at a given noise threshold. Initially formulated in the attempt to explain the ice-age cycles [3], stochastic resonance has been later observed in many biological systems, from crayfish (which leverage the environmental noise to detect the coherent pressure variations caused by the approach of a predator [4]) to humans (whose tactile sense is enhanced when an appropriate level of touching noise is added [5]).

The idea of using noise as an additional source of information has recently started to be envisioned also in experimental physics. In photoionization electron spectroscopy [6, 7] and mass spectrometry [8], for instance, the implementation of a covariance-based detection has allowed to analyse the fluctuations in the detected signals and to extract information otherwise prevented in the mean-value observables.

Nonlinear optical spectroscopies are ideal candidates for such approach. In nonlinear optics, the signals are typically extremely weak, and complex experimental solutions are often adopted to separate them from the more prominent linear contributions. In addition, femtosecond laser sources are characterized by several stages of amplification that unsettle the pulse-to-pulse stability, on which the success of the mean-value detections relies. From an alternate perspective, however, one could take advantage of the intrinsic fluctuations of the laser source. In a noise-assisted framework, each ultrashort pulse delivered by the source can be considered as a unique realization of the experiment, rather than just one of the multiple repetitions

on which the average is performed. By separately recording a large set of pulses, the computation of higher-order momenta can be then used to search the noise and uncover correlations that standard mean-value approaches would miss.

The use of higher-order statistical tools is especially appealing for studying correlated materials in which fluctuations of diverse nature play a major role [9]. In these systems, in fact, standard mean-value measurements would flatten not only the environmental noise, but also the intrinsic photonic fluctuations (either classical or quantum) that can carry instead genuine information on the material properties [10, 11, 12, 13]. The phase diagram of high temperature cuprate superconductors well exemplifies the relevance of developing experimental approaches suitable for probing fluctuations. In both underdoped and optimally-doped cuprates, superconducting fluctuations survive well above the critical temperature [14, 15], where either the presence of a competing charge order or the pair phase incoherence yet hinder the formation of a macroscopic superconducting state. Furthermore, also magnetic [16, 17] and atomic lattice fluctuations [18] have been proposed to play an active role in the Cooper pairing of the cuprates.

In this second part of the dissertation we combine a pump-probe scheme with a noise-assisted covariance-based detection for studying electronic Raman scattering in cuprates. In developing such approach, we capitalize on the peculiar strengths of each technique to pursue a time-resolved, momentum-sensitive investigation of the Cooper pair breaking in an optimally-doped sample of $Bi_2Sr_2CaCu_2O_{8+\delta}$.

REFERENCES

[1] Kurt Wiesenfeld and Frank Moss. Stochastic resonance and the benefits of noise: from ice ages to crayfish and SQUIDs. *Nature*, 373(6509):33–36, 1995.

[2] Luca Gammaitoni, Peter Hänggi, Peter Jung, and Fabio Marchesoni. Stochastic resonance. *Reviews of modern physics*, 70(1):223, 1998.

[3] Roberto Benzi, Giorgio Parisi, Alfonso Sutera, and Angelo Vulpiani. Stochastic resonance in climatic change. *Tellus*, 34(1):10–16, 1982.

[4] John K Douglass, Lon Wilkens, Eleni Pantazelou, and Frank Moss. Noise enhancement of information transfer in crayfish mechanoreceptors by stochastic resonance. *Nature*, 365(6444):337–340, 1993.

[5] James J Collins, Thomas T Imhoff, and Peter Grigg. Noise-enhanced tactile sensation. *Nature*, 1996.

[6] LJ Frasinski, K Codling, and PA Hatherly. Covariance mapping: A correlation method applied to multiphoton multiple ionization. *Science*, 246(4933):1029–1031, 1989.

[7] Jochen Mikosch and Serguei Patchkovskii. Coincidence and covariance data acquisition in photoelectron and-ion spectroscopy. I. Formal theory. *Journal of Modern Optics*, 60(17):1426–1438, 2013.

[8] Michael E Sigman and Mary R Williams. Covariance mapping in the analysis of ignitable liquids by gas chromatography/mass spectrometry. *Analytical chemistry*, 78(5):1713–1718, 2006.

[9] Subir Sachdev. Quantum criticality: competing ground states in low dimensions. *Science*, 288(5465):475–480, 2000.

[10] Martina Esposito, Kelvin Titimbo, Klaus Zimmermann, Francesca Giusti, Francesco Randi, Davide Boschetto, Fulvio Parmigiani, Roberto Floreanini, Fabio Benatti, and Daniele Fausti. Photon number statistics uncover the fluctuations in non-equilibrium lattice dynamics. *Nature communications*, 6(1):1–7, 2015.

[11] Francesco Randi, Martina Esposito, Francesca Giusti, Oleg Misochko, Fulvio Parmigiani, Daniele Fausti, and Martin Eckstein. Probing the fluctuations of optical properties in time-resolved spectroscopy. *Physical Review Letters*, 119(18):187403, 2017.

[12] Christopher Stahl and Martin Eckstein. Noise correlations in time-and angle-resolved photoemission spectroscopy. *Physical Review B*, 99(24):241111, 2019.

[13] Jonathan Owen Tollerud, Giorgia Sparapassi, Angela Montanaro, Shahaf Asban, Filippo Glerean, Francesca Giusti, Alexandre Marciniak, George Kourousias, Fulvio Billè, Federico Cilento, et al. Femtosecond covariance spectroscopy. *Proceedings of the National Academy of Sciences*, 116(12):5383–5386, 2019.

[14] VJ Emery and SA Kivelson. Importance of phase fluctuations in superconductors with small superfluid density. *Nature*, 374(6521):434–437, 1995.

[15] John Corson, R Mallozzi, J Orenstein, JN Eckstein, and I Bozovic. Vanishing of phase coherence in underdoped $Bi_2Sr_2CaCu_2O_{8+\delta}$. *Nature*, 398(6724):221–223, 1999.

[16] Thomas Dahm, V Hinkov, SV Borisenko, AA Kordyuk, VB Zabolotnyy, J Fink, B Büchner, DJ Scalapino, W Hanke, and B Keimer. Strength of the spin-fluctuation-mediated pairing interaction in a high-temperature superconductor. *Nature Physics*, 5(3):217–221, 2009.

[17] Yuan Li, M Le Tacon, M Bakr, D Terrade, D Manske, R Hackl, L Ji, MK Chan, N Barišić, X Zhao, et al. Feedback effect on high-energy magnetic fluctuations in the model high-temperature superconductor $HgBa_2CuO_{4+\delta}$ observed by electronic Raman scattering. *Physical review letters*, 108(22):227003, 2012.

[18] DM Newns and CC Tsuei. Fluctuating Cu-O-Cu bond model of high-temperature superconductivity. *Nature Physics*, 3(3):184–191, 2007.

6

RAMAN SCATTERING IN CUPRATES

In this chapter we shall review the fundamentals of Raman spectroscopy, mainly focusing on the electronic Raman scattering in cuprates and its application for the momentum-resolved study of the d-wave superconducting (SC) gap. In the first section, we will provide an intuitive description of the Raman processes based on classical arguments. We will then resort to a fully quantum treatment to describe the process in terms of creation/annihilation of elementary excitations. This will lead us to the derivation of the Raman tensor of D_{4h} cuprates, whose symmetries will be exploited to study the SC order parameter projected onto different regions of the Brillouin zone. This discussion will set the basis for the time-resolved stochastic Raman measurements presented in Chapter 8.

6.1 FUNDAMENTALS OF RAMAN SCATTERING

When light impinges on a molecule or a solid, most photons elastically scatter from the material. However, a tiny portion of them (typically 1 over 10^8) may scatter inelastically, thereby shifting away from the incident light. This is what the physicist C.V. Raman dubbed as *"A new radiation"* in his inaugural speech almost a century ago [1], and that it was later named after him.

Although Raman spectroscopy has been historically associated to the study of the vibrational spectrum of materials, its applicability is much more general. Inelastic scattering can in fact originate also from the coupling of light to other fundamental excitations, such as magnons and electrons. Here, we will deal in particular with the electronic Raman scattering, that has proven a valuable tool in experimental condensed matter for studying correlated systems. The great advantage of the technique is that, by simply selecting the polarization of the incoming and the scattered photons, it allows to single out the electron dynamics projected into specific regions of the Brillouin zone, thereby accessing the **k**-resolved two-particle correlation function that is prevented in other single-particle **k**-resolved techniques, such as ARPES and electron tunneling [2].

In the 1980s, direct electronic Raman scattering by SC Cooper pairs was observed and theoretically formulated [3, 4]. The advent of SC cuprates in 1986 [5] finally unlocked the full potential of the technique, that has provided unique insights into

the anisotropy of the SC order parameter and the behaviour of competing orders that arise from the strong electronic correlations [2].

Bearing in mind that the aim of this discussion is to introduce the reader to theoretical concepts that will be used in the following chapters, we will start by giving an intuitive picture of classical Raman scattering from a molecule and in a solid. A more general quantum approach will be then presented to derive the Raman tensor in our cuprate sample.

6.1.1 *Classical description*

From a classical point of view, Raman scattering can be interpreted as originating from a perturbation in the electronic polarizability due to the presence of the nuclear modes [6]. If we consider a two-atom molecule on which an electric field $E(\omega)$ is applied, the polarizability α_0 results into a dipole moment $P_D(\omega) = \alpha_0 E(\omega)$ which acts as the source of the evanescing wave. If the molecule vibrates at the frequency Ω, the polarizability, at the first order, will be periodically modulated at the same frequency by an additional term as $\mathbf{P}(\omega) = (\alpha_0 + \alpha_1 \cos\Omega t)\mathbf{E_0}\cos\omega t$, that can be re-written in the following clearer form:

$$\mathbf{P}(\omega) = \alpha_0 \mathbf{E_0}\cos\omega t + (\alpha_1 \mathbf{E_0}/2)\left[\cos(\omega+\Omega)t + \cos(\omega-\Omega)t\right] \tag{6.1}$$

As a result, light is scattered not only at the frequency ω of the incoming field (Rayleigh scattering), but also at the Raman sidebands $\omega - \Omega$ (*Stokes process*) and $\omega + \Omega$ (*Anti-Stokes process*), that are many orders of magnitude weaker than the elastic contribution.

In solids, the presence of the periodic crystalline potential causes the waves scattered in different directions of the crystal to interfere. As a result, for a given incident wavelength and a nuclear mode, light is scattered in a well-defined direction via constructive interference. To obtain an expression of the Raman intensity in solids, the susceptibility tensor χ_{jl} has to be considered instead of the molecular scalar polarizability. Moreover, the atoms' displacements are replaced by the normal coordinates Q_k of the oscillations. The susceptibiltiy can be expanded in a power series of the normal coordinates:

$$\chi_{jl} = (\chi_{jl})_0 + \sum_k \left(\frac{\partial \chi_{jl}}{\partial Q_k}\right)_0 Q_k + high.ord. \tag{6.2}$$

where the coefficient $\frac{\partial \chi_{jl}}{\partial Q_k} \equiv \chi_{jl,k}$ is a component of the so-called *Raman tensor* R. Each component of the tensor has three indices: j and l run over the coordinates 1 to 3, while k runs over the $3(N-1)$ normal coordinates of the crystal, being N the number of atoms in the unit cell.

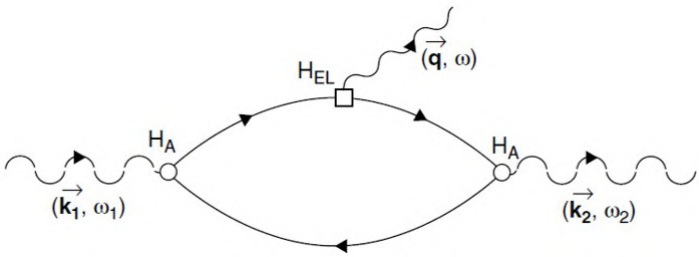

Figure 6.1: **Feynamn diagram of a Stokes process.** $\mathbf{k}_{1,2}$,$\omega_{1,2}$ are the wavevector and the frequency of the incident (1) and the scattered (2) photon, while $\mathbf{q}$,ω those of the elementary excitation (phonon) created. H_A and H_{EL} represent the electron interaction with the field and the lattice, respectively [7].

In analogy with Equation 6.1, the induced dipole moment that is responsible for the Raman sidebands is

$$P^s_{Dj}(\omega \pm \Omega_k) = \chi_{jl,k}\epsilon_0 V E^i_{l0} Q_{k0} \cos(\omega \pm \Omega_k)t \tag{6.3}$$

where V is the unit cell volume and we have defined $Q_k = Q_{k0}\cos\Omega_k t$ in Equation 6.2. The Raman scattering intensity can be readily evaluated as the absolute square of the projection of $\mathbf{P}^s_D$ on a selected direction of polarization $\mathbf{e}^s$ of the scattered light:

$$\phi(k) = C\,|\mathbf{e}^s\mathbf{P}^s_D|^2 = C\left|\sum_j e^s_j P^s_{Dj}(k)\right|^2 \propto \left|\sum_{jl} e^s_j \chi_{jl,k} e^i_l\right|^2 E_0^2 \tag{6.4}$$

where it is clear that any component of the Raman tensor can be singled out by a proper selection of the incident (e^i) and the scattered (e^s) light polarization.

6.1.2 *Electronic coupling to light: quantum treatment*

From a quantum mechanical point of view, the Raman scattering process can be interpreted as the creation (Stokes) or the annihilation (Anti-Stokes) of an elementary excitation in the solid. The Stokes process is illustrated in Figure 6.1 and can be described in three fundamental steps [7]:

- The impinging electric field couples to the electronic system of the material. The absorption of a photon results in the creation of an electron-hole pair that brings the electronic system into a virtual intermediate state.
- The electron-hole pair migrates to another state, leading to the creation of an elementary excitation.
- The electron and the hole recombine and emit the scattered photon.

A fully quantum treatment of the Raman scattering can be obtained through the second-order perturbation theory, considering the vector potential of the electromag-

netic fields as a perturbation [2]. The Hamiltonian of N electrons with mass m and charge e interacting with the electromagnetic fields:

$$H = \sum_i^N \frac{\left[\hat{\mathbf{p}}_i + (e/c)\hat{\mathbf{A}}(\mathbf{r}_i)\right]^2}{2m} + H_C + H_F \tag{6.5}$$

where $\hat{\mathbf{p}}$ is the momentum operator and $\hat{\mathbf{A}}(\mathbf{r}_i)$ is the vector potential of the fields at the spatial-temporal coordinate $\mathbf{r}_i$. H_C and H_F represent the hamiltonian of the Coulomb interaction between electrons and hamiltonian of the free electric fields, respectively. By expanding the kinetic term containing the minimal coupling to the the fields, Equation 6.5 can be further re-written in the following form:

$$\begin{aligned} H &= \tilde{H} + \frac{e}{2mc}\sum_i \left[\hat{\mathbf{p}}_i \cdot \hat{\mathbf{A}}(\mathbf{r}_i) + \hat{\mathbf{A}}(\mathbf{r}_i)\cdot\hat{\mathbf{p}}_i\right] + \frac{e^2}{2mc^2}\sum_i \hat{\mathbf{A}}(\mathbf{r}_i)\cdot\hat{\mathbf{A}}(\mathbf{r}_i) \\ &\equiv \tilde{H} + H'_{INT} + H''_{INT} \end{aligned} \tag{6.6}$$

where we have defined $\tilde{H} = H_0 + H_F$ and $H_0 = (1/2m)\sum_i \hat{\mathbf{p}}_i^2 + H_C$. H_0 is the total hamiltonian of the material and we denote with $|\alpha\rangle$ its eigenstates as $H_0|\alpha\rangle = E_\alpha|\alpha\rangle$. The eigenstates are labelled with all the relevant degrees of freedom (band index, spin and orbital quantum numbers) and their exact expression (Bloch waves or Hubbard states) depends on the potential included in H_C.

The observable of an electronic Raman scattering measurement is the total cross section for scattering from all electrons illuminated by the incident light source. From scattering theory, the differential cross section, i.e. the probability that an incident photon having momentum $\mathbf{q}_i$, frequency ω_i and polarization $\hat{\mathbf{e}}_{\mathbf{q}}^{(i)}$ is scattered within a solid-angle interval $(\Omega, \Omega + d\Omega)$ and a scattered energy window $(\omega_s, \omega_s + d\omega_s)$, is evaluated by the Fermi's golden rule:

$$\frac{\partial^2\sigma}{\partial\Omega\partial\omega_s} \propto \frac{\omega_s}{\omega_i}\frac{1}{\mathcal{Z}}\sum_{I,F} e^{-\frac{E_I}{k_B T}}|M_{F,I}|^2\delta(E_F - E_I - \hbar(\omega_i - \omega_s)) \tag{6.7}$$

where k_B is the Boltzmann constant and $\mathcal{Z}$ the partition function, so that the factor $\frac{1}{Z}\sum e^{-\frac{E_j}{k_B T}}$ represents the probability for the system to be in the j^{th} microstate. I,F represent the initial and the final state of the electronic system, having energy E_I,E_F respectively. $|M_{F,I}|^2$ indicates the matrix elements that determine the light scattering, that can be obtained as $\langle F; \mathbf{q}_s, \omega_s, \hat{\mathbf{e}}_{\mathbf{q}}^{(s)}|H'_{INT} + H''_{INT}|I; \mathbf{q}_i, \omega_i, \hat{\mathbf{e}}_{\mathbf{q}}^{(i)}\rangle$. The matrix elements can be analytically computed by using second-order perturbation theory [8]. Looking at Equation 6.6, it can be noted that the two terms of the interacting hamiltonian behave differently. While H'_{INT} couples the electron's current to a single photon, in H''_{INT} the electron's charge is coupled to two photons. By expanding the

vector potential into Fourier modes and using a second-quantization formalism for the electronic states, the scattering matrix elements can be expressed as follows:

$$\begin{aligned} M_{F,I} =& \mathbf{e}_i \cdot \mathbf{e}_s \sum_{\alpha,\beta} \rho_{\alpha,\beta}(\mathbf{q}) \langle F|c_\alpha^\dagger c_\beta|I\rangle + \\ &+ \frac{1}{m} \sum_{\nu} \sum_{\alpha,\alpha',\beta,\beta'} p_{\alpha,\alpha'}(\mathbf{q}_s) p_{\beta,\beta'}(\mathbf{q}_i) \times \\ &\times \left(\frac{\langle F|c_\alpha^\dagger c_{\alpha'}|\nu\rangle \langle \nu|c_\beta^\dagger c_{\beta'}|I\rangle}{E_I - E_\nu + \hbar\omega_i} + \frac{\langle F|c_\beta^\dagger c_{\beta'}|\nu\rangle \langle \nu|c_\alpha^\dagger c_{\alpha'}|I\rangle}{E_I - E_\nu - \hbar\omega_s} \right) \end{aligned} \tag{6.8}$$

where $|I\rangle$, $|F\rangle$ and $|\nu\rangle$ are the initial, final and intermediate many-electron states having energy E_I, E_F and E_ν, respectively. We have denoted with $\mathbf{q} = \mathbf{q}_i - \mathbf{q}_s$ the momentum transfer and with c_γ ($c_\gamma^\dagger$) the annihilation (creation) operator of the electron state $|\gamma\rangle$, which is an eigenstate of H_0. In second quantization, $\rho_{\alpha,\beta}(\mathbf{q}) = \langle \alpha|e^{i\mathbf{q}\cdot\mathbf{r}}|\beta\rangle$ is the matrix element for single-particle density fluctuations, while $p_{\alpha,\beta}(\mathbf{q}_{i,s}) = \langle \alpha|\mathbf{p}\cdot\mathbf{e}_{i,s}e^{\pm i\mathbf{q}_{i,s}\cdot\mathbf{r}}|\beta\rangle$ is the momentum density matrix element. The first term in Equation 6.8 arises from first-order perturbation of the two-photon term in Equation 6.6. The remaining terms come from the second-order perturbation of the single-photon terms via intermediate states $|\nu\rangle$, while the first-order corrections vanish.

The first term is referred to as nonresonant Raman scattering and describes the process in which the photon gives away part of its energy to create an electron-hole pair. In the second term, an intermediate state is involved, which decays into the final state via the emission of scattered photons. The latter process can be resonant, thereby significantly enhancing the Raman cross section, if the incident or scattered photon energy matches the energy difference between the initial and the intermediate states (denominators approaching zero). From this simple picture, it follows that excitations lying near the Fermi surface are mainly probed by the nonresonant Raman process, while excitations involving transitions between different bands are probed via the intermediate state pathway [2].

6.2 SELECTION RULES IN CUPRATES

The computation of Equation 6.8 for a given materials can be significantly simplified by symmetry arguments. Since the charge density fluctuations are modulated along directions determined by the polaizations of the incident and the scattered photons, they satisfy the symmetry rules for the given scattering geometry. As a consequence, the Raman matrix element is non-zero only when the whole system (incident photon, scattered photon, Raman excitation) is even under the symmetry operations that characterize the crystal symmetries.

The Raman matrix element can be therefore decomposed into basis functions of the irreducible point group of the crystal ϕ_μ:

$$M_{F,I} \rightarrow \sum_\mu M_\mu \phi_\mu \tag{6.9}$$

where the μ indicates an irreducible representation of the point group. The sum runs over all the contributions for a given scattering geometry. In practice, the decomposition in Equation 6.9 is fully determined by the character table of the point group of the crystal, which lists all the possible irreducible representations in Mulliken notation and their peculiar symmetries [9].

Most cuprates belong, with a good approximation, to the D_{4h} group of the tetragonal lattice. They have inversion centers, so the modes can be classified as odd (u, *ungerade*, IR-active) or even (g, *gerade*, Raman-active) if they change or do not change sign upon inversion [7]. So, the Raman matrix element in cuprates can be written as:

$$\begin{aligned} M_{F,I} = & \frac{1}{2}[R_{A_{1g}^{(1)}}(e_i^x e_s^x + e_i^y e_s^y) + R_{A_{1g}^{(2)}}(e_i^z e_s^z) + \\ & + R_{B_{1g}}(e_i^x e_s^x - e_i^y e_s^y) + R_{B_{2g}}(e_i^x e_s^y + e_i^y e_s^x) + \\ & + R_{A_{2g}}(e_i^x e_s^y - e_i^y e_s^x) + R_{E_g^{(1)}}(e_i^x e_s^z + e_i^z e_s^x) + R_{E_g^{(2)}}(e_i^y e_s^z + e_i^z e_s^y)] \end{aligned} \tag{6.10}$$

where R_μ are operators projected in the μ-representation and $e_{i,s}^\alpha$ denote the polarization of the incident and scattered photons, respectively. By making explicit the outer products of the polarization vectors, Equation 6.10 can be re-written in the more intuitive form [7, 10]:

$$\begin{array}{cccc} \begin{pmatrix} a & & \\ & a & \\ & & b \end{pmatrix} & \begin{pmatrix} c & & \\ & -c & \\ & & \end{pmatrix} & \begin{pmatrix} & d & \\ d & & \\ & & \end{pmatrix} & \begin{pmatrix} & d & \\ -d & & \\ & & \end{pmatrix} \\ A_{1g} & B_{1g} & B_{2g} & A_{2g} \end{array}$$

$$\begin{array}{cc} \begin{pmatrix} & e & \\ & & \\ e & & \end{pmatrix} & \begin{pmatrix} & & \\ & e & \\ e & & \end{pmatrix} \\ E_g & E_g \end{array} \tag{6.11}$$

A proper selection of the incoming and the scattered polarizations allows to single out specific projections. However, it is worth to note that for polarizations in the $a-b$ plane in D_{4h} crystals the irreducible representations cannot be accessed individually and subtraction procedures are needed. For example, if the incident photons are polarized along $\hat{x}$ ($\hat{y}$) and the scattered photons are measured along the same

polarization direction, it follows from Equation 6.10 that both the A_{1g} and the B_{1g} are simultaneously measured.

EXPERIMENTAL CONFIGURATION In our experiment, the incident beam propagates along the c-axis, i.e. orthogonally to the CuO_2 plaquette. In this experimental configuration, the number of contributing irreducible representations is reduced as follows [11]:

$$M_{F,I} = \frac{1}{2}\begin{bmatrix} R_{A_{1g}} + R_{B_{1g}} & R_{B_{2g}} \\ R_{B_{2g}} & R_{A_{1g}} - R_{B_{1g}} \end{bmatrix} \tag{6.12}$$

It can be easily proved that in this experimental configuration the individual detection of the B modes is possible. By defining the x-axis parallel to the CuO bond, it can be seen that the B_{1g} mode can be isolated by impinging with photon polarized along the CuCu axis ($e^i = \binom{1}{1}$) and detecting the cross-polarized scattered photons ($e^s = \binom{1}{-1}$). On the contrary, the B_{2g} mode can be selected with incident photon polarized along the CuO axis ($e^i = \binom{1}{0}$) and cross-polarized scattered photons ($e^s = \binom{0}{1}$). The A_g mode cannot be instead isolated, but, due to its high intensity, it dominates when the incident and the scattered photons are co-polarized and all other contributions are therefore negligible.

Referring to the Mulliken notation, the A and B representations are, respectively, even and odd with respect to the C_4 symmetry. In order to gain insight on the $\mathbf{k}$-projections of the A and B modes, it is useful to write their corresponding representative basis functions $\phi_\mu(\mathbf{k})$ taken from the complete set of the Brillouin zone (BZ) harmonics for the D_{4h} space group [2]

$$\begin{aligned} A_{1g} &\leftrightarrow \frac{1}{2}\left[\cos(k_x a) + \cos(k_y a)\right] \\ B_{1g} &\leftrightarrow \frac{1}{2}\left[\cos(k_x a) - \cos(k_y a)\right] \\ B_{2g} &\leftrightarrow \sin(k_x a)\sin(k_y a) \end{aligned} \tag{6.13}$$

As a consequence, each mode corresponds to a different projection within the BZ, enabling the examination of charge excitations in different regions of the BZ. In particular, we plot in Figure 6.2 the sensitivity to the excitations in the BZ for the three different Raman symmetries. From the color-coded maps, it is clear that, while the A_{1g} mode is the total-symmetric one, the B modes are sensitive to specific directions in the reciprocal space. Importantly, scattered light transforming as the B_{1g} symmetry couples to charge excitations along the axes of the BZ (k_x or $k_y = 0$), while the B_{2g} symmetry couples to excitations along the BZ diagonals ($k_x = \pm k_y$).

Given the d-wave symmetry of the SC gap, the B_{1g} mode probes the antinodal directions of the gap, while the B_{2g} one the nodal regions. Therefore, Raman scattering from paired electrons having different momentum in the reciprocal space can directly map the amplitude of the d-wave SC gap, as discussed in Section 6.3.

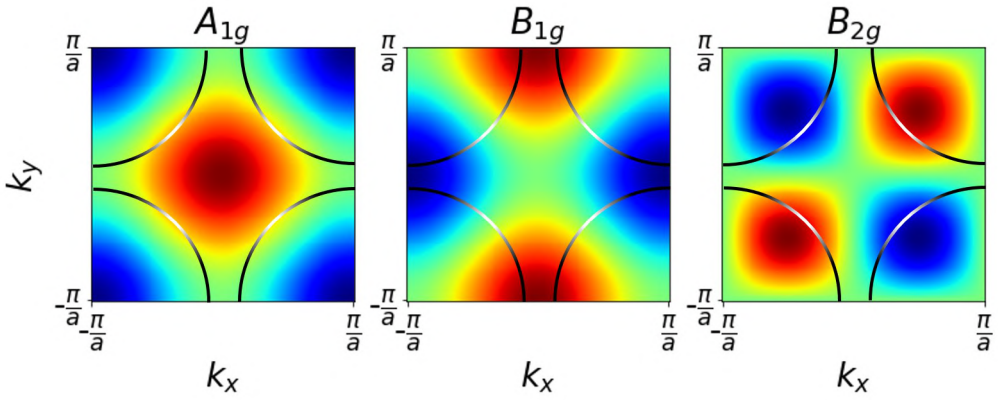

Figure 6.2: **Momentum-dependent sensitivity of the Raman modes.** The **k**-dependent representative basis functions are plotted within the Brillouin zone for the A_{1g}, B_{1g} and B_{2g} symmetries. The curved lines in each panel denote the Fermi surface; the color gradient indicates the amplitude of the d-wave gap: black at the antinodes and white at the nodes.

6.2.1 *Third-order Raman tensor in cuprates*

So far, we have considered Raman scattering from a system that is at equilibrium before the interaction with the incident light. In a pump-probe experiment, this is not the case and a more complete expression of the Raman tensor should take into account also the pump pulse and its polarization. From a theoretical point of view, this can be done by expanding the interacting hamiltonian in Equation 6.6 up to the third-order to include the interaction with the pump fields. The full process can be described by a fourth rank Raman tensor that, if both the pump and the probe beams propagate orthogonally to the CuO_2 plane, can be expressed as

$$R^{(3)}_{ijkl} = R^{ij}_{A_{1g}} R^{kl}_{A_{1g}} + R^{ij}_{B_{1g}} R^{kl}_{B_{1g}} + R^{ij}_{B_{2g}} R^{kl}_{B_{2g}} \tag{6.14}$$

where i, j, k, l=1,2 [12]. By making explicit the symmetry of each mode as in Equation 6.11, the Raman tensor can be cast in the following form:

$$R^{(3)}_{ijkl} = \begin{pmatrix} \begin{pmatrix} a^2+c^2 & 0 \\ 0 & a^2+c^2 \end{pmatrix} & \begin{pmatrix} 0 & d^2 \\ d^2 & 0 \end{pmatrix} \\ \begin{pmatrix} 0 & d^2 \\ d^2 & 0 \end{pmatrix} & \begin{pmatrix} a^2-c^2 & 0 \\ 0 & a^2+c^2 \end{pmatrix} \end{pmatrix} \tag{6.15}$$

where the first two indices (outer rows and columns) indicate the pump polarization, while the remaining ones (inner rows and columns) are associated to the polarization of the incoming and the scattered probe, respectively. Experimentally, the polarizations of the pump and the probe beams can be properly adjusted before the interaction with the sample. The polarization of the scattered probe, which is also known as

emitted field in nonlinear spectroscopy, can be rotated afterwards and selected with a polarizer (*analyser*) before the detection.

Starting from the third-order Raman tensor (Equation 6.15), the proper polarization configuration can be chosen following three steps. We will explicitly consider only the polarizations needed to isolate the B_{1g} mode, but the generalization to the A_{1g} and B_{2g} symmetries is straightforward.

1. Let us choose the pump polarization to be parallel to the CuO axis and defined by the ket $|\uparrow\rangle = \begin{pmatrix} \mathbb{I} \\ 0 \end{pmatrix} = \begin{pmatrix} 1 & 0 \\ 0 & 1 \\ 0 & 0 \\ 0 & 0 \end{pmatrix}$. The action of the pump can be evaluated as:

$$\langle\uparrow | R^{(3)}_{ijkl} | \uparrow\rangle = \begin{pmatrix} a^2 + c^2 & 0 \\ 0 & a^2 - c^2 \end{pmatrix} \tag{6.16}$$

2. By taking the probe beam polarized along the CuCu axis, its state can be described by the ket $|\nearrow\rangle = \frac{1}{\sqrt{2}} \begin{pmatrix} 1 \\ 1 \end{pmatrix}$. The interaction with the probe selects the following Raman elements:

$$\xrightarrow{\text{probe //CuCu}} \frac{1}{\sqrt{2}} \begin{pmatrix} a^2 + c^2 & 0 \\ 0 & a^2 - c^2 \end{pmatrix} \begin{pmatrix} 1 \\ 1 \end{pmatrix} = \frac{1}{\sqrt{2}} \begin{pmatrix} a^2 + c^2 \\ a^2 - c^2 \end{pmatrix} \tag{6.17}$$

3. The polarization of the emitted field finally isolates the mode. If we select the component of the scattered field that is cross-polarized to the probe $|\nwarrow\rangle = \frac{1}{\sqrt{2}} \begin{pmatrix} -1 \\ 1 \end{pmatrix}$, the final Raman element is

$$\xrightarrow{\text{polarizer} \perp \text{CuCu}} \frac{1}{2} \begin{pmatrix} -1 & 1 \end{pmatrix} \begin{pmatrix} a^2 + c^2 \\ a^2 - c^2 \end{pmatrix} = \frac{1}{2}(-a^2 - c^2 + a^2 - c^2) = -c^2 \tag{6.18}$$

   so the B_{1g} mode can be measured.

Figure 6.3 summarizes the results. While the A_{1g} dominates when no polarization selection is applied (probe and analyser are co-polarized), the B modes can be singled out by fixing to 45° the angle between the the pump and the probe polarizations and measuring the cross-scattered photons. Experimentally, once the polarization configuration is fixed, it is sufficient to rotate the sample by 45° to distinguish between the B_{1g} and B_{2g} symmetries.

6.3 RAMAN MEASUREMENTS OF THE d-WAVE GAP

Due to its intrinsic momentum-sensitivity, Raman scattering soon became instrumental in the experimental investigation of the SC order symmetry in cuprates. Initially,

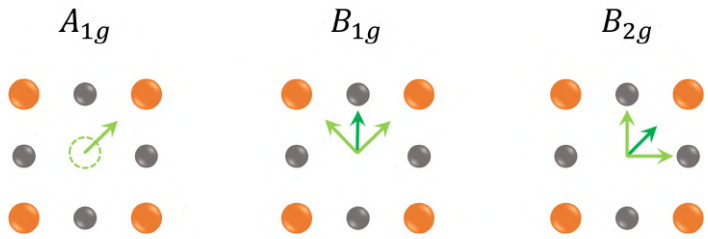

Figure 6.3: **Polarization-sensitive third-order Raman tensor.** The arrows indicate the polarizations of the beams within the CuO_2 plaquette (Cu atoms in gold and O atoms in grey). The dark green arrow refers to the pump, while the light green arrows denote the probe and the analyser. The A_{1g} contribution is dominant when no polarization selection is applied.

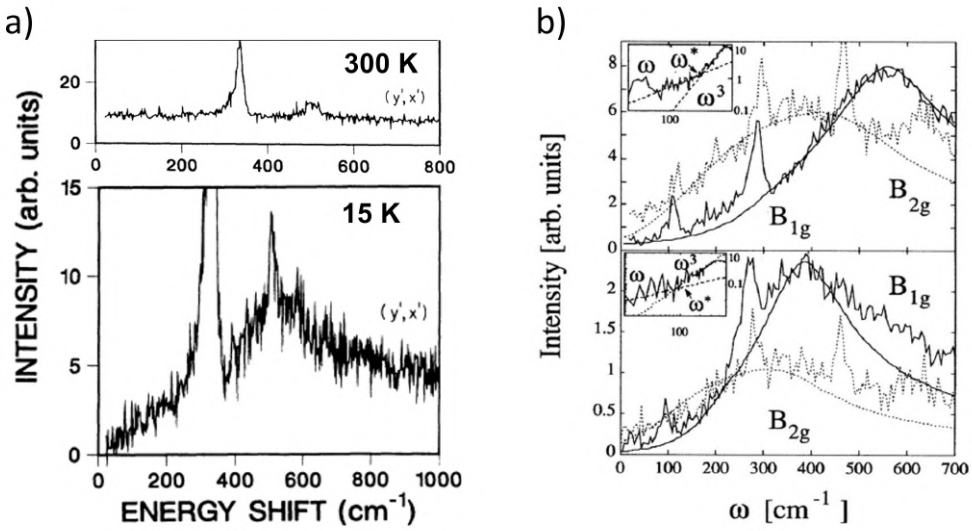

Figure 6.4: **Raman spectra in cuprates. a)** Raman spectra in B_{1g} symmetry (y', x' scattering geometry) in single-crystal $YBa_2Cu_3O_{7-\delta}$ in the normal (top) and in the superconducting (bottom) phase. Adapted from ref. [13]. **b)** Data and fits of the B_{1g} (black line) and B_{2g} (grey line) modes in $Bi_2Sr_2CaCu_2O_{8+\delta}$ having different oxygen content (top: T_C=86 K; bottom: T_C=79 K) [14].

no differences in the Raman scattered electronic continuum were observed above and below T_C, mainly because of the presence of a high number of defects in early synthesized samples [2].

The situation significantly improved when flux-grown purer cuprate samples became available. This technical advance led to the first observation of direct light-scattering from Cooper pairs in the SC state [15]. In Figure 6.4a we report the Raman spectra of $YBa_2Cu_3O_{7-\delta}$ measured in ref. [13] in B_{1g} symmetry. While the electronic continuum - on which narrow phonon contributions are superimposed - is generally flat in the normal state (top panel), a spectral weight reorganization is observed below T_C, where a gap opens in the excitation spectrum (bottom panel). Contrarily to the sharp spectroscopic onset of the gap in conventional BCS superconductors, residual electronic scattering is present in cuprates well below the expected 2Δ gap ($\sim$500 cm^{-1} in Figure 6.4a), due to the presence of nodes along specific directions in the momentum space [16].

The study of Raman scattering in different polarization geometries enabled the first spectroscopic evidence of the gap anisotropy [13, 16, 17]. In Figure 6.4b we report the B_{1g} and B_{2g} spectra measured in $Bi_2Sr_2CaCu_2O_{8+\delta}$ (Bi2212) with different oxygen content [18, 14]. The major differences between the two symmetries are the following. i) The B_{1g} peak arises at higher energies (usually greater than $\sim$30% [2, 13]) than the B_{2g} one, suggesting an anisotropic amplitude of the gap in the reciprocal space. ii) The two spectra approach the zero-frequency differently: while the B_{2g} mode scales linearly, the B_{1g} mode scales as ω^3 above a certain threshold ω^*, as shown in the insets. Even if electronic Raman scattering can only probe directly the amplitude of the gap (and not its eventual sign changes), these two features were found quantitatively compatible only with a gap having $d_{x^2-y^2}$ symmetry rather than an anisotropic s-wave pairing [19, 14].

6.3.1 *Time-resolved Raman measurements of the gap*

The advent of pulsed laser sources in the 1990s has dramatically boosted the field of ultrafast spectroscopy. The possibility of exploring the sub-ps dynamics of materials out of their equilibrium conditions has progressively led to the development of the "time-resolved version" of the most common static techniques, such as reflectivity/transmittivity, absorption, photoemission, and fluorescence to name a few. The field of strongly correlated materials has particularly benefited from these studies as they allow to access the dynamics of competing order parameters and elucidate their potential interplay [21].

Nevertheless, the implementation of time-resolved Raman spectroscopy has been particularly hampered by the intrinsic requirements of the technique. A high time resolution can be obviously achieved at the cost of the monochromaticity of the incident pulse, that is nonetheless essential to ensure a high frequency resolution. In general, compromises must be made to face this challenge [22, 23, 24].

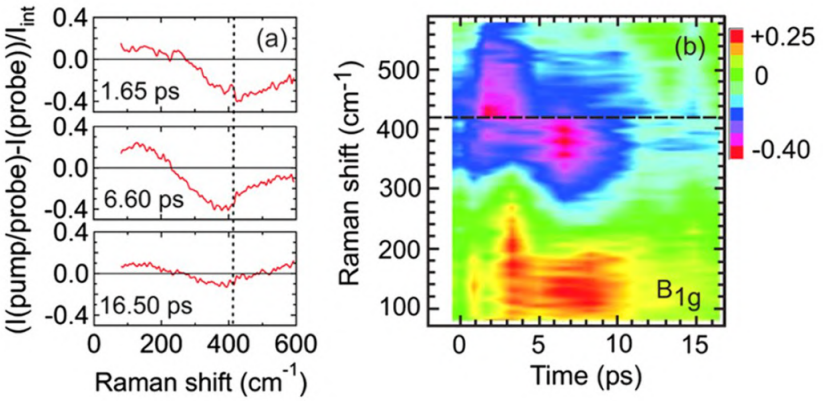

Figure 6.5: **Time-resolved measurement in B_{1g} symmetry in Bi2212. a)** Differential Raman spectra at three different pump-probe delays. **b)** Color-coded map of 12 differential Raman spectra plotted as function of the temporal delay (horizontal axis) and the Raman shift (vertical shift). Taken from ref. [20].

The first direct measurement of the dynamics of the SC order parameter $\Delta(\mathbf{k})$ in cuprates through time-resolved Raman scattering was obtained by Saichu et al. [20]. The authors employed ultraviolet (pump) and visible (probe) pulses to track the dynamics of the B_{1g} mode, as reported in Figure 6.5. As a consequence of the pair-breaking initiated by the pump pulse, they observed a decrease in the intensity of the Raman scattering at twice the maximum value of the gap ($\sim$420 cm^{-1}). Charge conservation is responsible for an increase of the spectral weight of quasiparticles within the gap that leads instead to a positive signal at lower frequencies. However, the time-resolution of the experiment was set to 0.9 ps (FWHM of the probe pulse). This restricted the authors' investigation to the characteristic timescale of the hole-phonon coupling [20, 25] and prevented the study of the dynamics on shorter timescales, where the coupling to other bosonic excitations (such as spin fluctuations and loop currents) is supposed to play a major role [21, 26].

In the following chapter, we will explain how the technique we have developed, *Femtosecond Covariance Spectroscopy* (FCS) [27], overcomes this limitation by disentangling the time and the frequency resolution in a covariance-based Raman scattering experiment.

REFERENCES

[1] Chandrasekhara Venkata Raman. A new radiation. *Indian Journal of physics*, 2:387–398, 1928.

[2] Thomas P Devereaux and Rudi Hackl. Inelastic light scattering from correlated electrons. *Reviews of modern physics*, 79(1):175, 2007.

[3] SB Dierker, MV Klein, GW Webb, and Z Fisk. Electronic Raman scattering by superconducting gap excitations in Nb_3Sn and V_3Si. *Physical review letters*, 50(11):853, 1983.

[4] MV Klein and SB Dierker. Theory of Raman scattering in superconductors. *Physical Review B*, 29(9):4976, 1984.

[5] J George Bednorz and K Alex Müller. Possible high T_C superconductivity in the Ba-La-Cu-O system. *Zeitschrift für Physik B Condensed Matter*, 64(2):189–193, 1986.

[6] Hans Kuzmany. *Solid-state spectroscopy: an introduction*. Springer, 2009.

[7] C Thomsen and G Kaczmarczyk. Vibrational raman spectroscopy of high-temperature superconductors, 2002.

[8] Jhih-An Yang. *Conventional and Ultrafast Pump-Probe Time-Resolved Raman Spectroscopy of Strongly Correlated Systems*. PhD thesis, University of Colorado at Boulder, 2017.

[9] Marcus Frederick Charles Ladd. *Symmetry of crystals and molecules*. Oxford University Press, USA, 2014.

[10] Rodney Loudon. The Raman effect in crystals. *Advances in Physics*, 13(52):423–482, 1964.

[11] Y Toda, F Kawanokami, T Kurosawa, M Oda, I Madan, T Mertelj, VV Kabanov, and D Mihailovic. Rotational symmetry breaking in $Bi_2Sr_2CaCu_2O_{8+\delta}$ probed by polarized femtosecond spectroscopy. *Physical Review B*, 90(9):094513, 2014.

[12] Francesco Randi. *Low-energy physics in strongly correlated materials via nonlinear spectroscopies*. PhD thesis, Università degli Studi di Trieste, 2017.

[13] SL Cooper, F Slakey, MV Klein, JP Rice, ED Bukowski, and DM Ginsberg. Gap anisotropy and phonon self-energy effects in single-crystal $YBa_2Cu_3O_{7-\delta}$. *Physical Review B*, 38(16):11934, 1988.

[14] TP Devereaux. Theory of electronic Raman scattering in disordered unconventional superconductors. *Physical review letters*, 74(21):4313, 1995.

[15] SL Cooper, MV Klein, BG Pazol, JP Rice, and DM Ginsberg. Raman scattering from superconducting gap excitations in single-crystal $YBa_2Cu_3O_{7-\delta}$. *Physical Review B*, 37(10):5920, 1988.

[16] R Hackl, W Gläser, P Müller, D Einzel, and K Andres. Light-scattering study of the superconducting energy gap in $YBa_2Cu_3O_7$ single crystals. *Physical Review B*, 38(10):7133, 1988.

[17] Akio Yamanaka, Toshinori Kimura, Fujio Minami, Kuon Inoue, and Shunji Takekawa. Superconducting gap excitations in $Bi-Sr-Ca-Cu-O$ superconductor observed by Raman Scattering. *Japanese journal of applied physics*, 27(10A):L1902, 1988.

[18] T Staufer, R Nemetschek, R Hackl, P Müller, and H Veith. Investigation of the superconducting order parameter in $Bi_2Sr_2CaCu_2O_8$ single crystals. *Physical review letters*, 68(7):1069, 1992.

[19] TP Devereaux, D Einzel, B Stadlober, R Hackl, DH Leach, and JJ Neumeier. Electronic Raman scattering in high-T_C superconductors: A probe of $d_{x^2-y^2}$ pairing. *Physical review letters*, 72(3):396, 1994.

[20] RP Saichu, I Mahns, A Goos, S Binder, P May, SG Singer, B Schulz, A Rusydi, J Unterhinninghofen, D Manske, et al. Two-component dynamics of the order parameter of high temperature $Bi_2Sr_2CaCu_2O_{8+\delta}$ superconductors revealed by time-resolved Raman scattering. *Physical review letters*, 102(17):177004, 2009.

[21] Claudio Giannetti, Massimo Capone, Daniele Fausti, Michele Fabrizio, Fulvio Parmigiani, and Dragan Mihailovic. Ultrafast optical spectroscopy of strongly correlated materials and high-temperature superconductors: a non-equilibrium approach. *Advances in Physics*, 65(2):58–238, 2016.

[22] Daniele Fausti and Paul HM van Loosdrecht. Time-Resolved Raman Scattering. In *Optical Techniques for Solid-State Materials Characterization*, pages 530–555. CRC Press, 2016.

[23] Daniele Fausti, Oleg V Misochko, and Paul HM van Loosdrecht. Ultrafast photoinduced structure phase transition in antimony single crystals. *Physical Review B*, 80(16):161207, 2009.

[24] Makoto Nakajima, Kenji Kazumi, Masahiko Isobe, Yutaka Ueda, and Tohru Suemoto. Time-resolved Raman spectroscopy applied to the photoinduced phenomena in NaV_2O_5. In *Journal of Physics: Conference Series*, volume 21, page 033. IOP Publishing, 2005.

[25] L Perfetti, PA Loukakos, M Lisowski, U Bovensiepen, H Eisaki, and M Wolf. Ultrafast electron relaxation in superconducting $Bi_2Sr_2CaCu_2O_{8+\delta}$ by time-resolved photoelectron spectroscopy. *Physical review letters*, 99(19):197001, 2007.

[26] Stefano Dal Conte, Claudio Giannetti, Giacomo Coslovich, Federico Cilento, Davide Bossini, Tadesse Abebaw, Francesco Banfi, Gabriele Ferrini, Hiroshi Eisaki, Martin Greven, et al. Disentangling the electronic and phononic glue in a high-T_C superconductor. *Science*, 335(6076):1600–1603, 2012.

[27] Jonathan Owen Tollerud, Giorgia Sparapassi, Angela Montanaro, Shahaf Asban, Filippo Glerean, Francesca Giusti, Alexandre Marciniak, George Kourousias, Fulvio Billè, Federico Cilento, et al. Femtosecond covariance spectroscopy. *Proceedings of the National Academy of Sciences*, 116(12):5383–5386, 2019.

7

FEMTOSECOND COVARIANCE SPECTROSCOPY

We present in this chapter the covariance-based technique we have developed to study nonlinear optical processes, *Femtosecond Covariance Spectroscopy* (FCS) [1]. We first give an intuitive description of the method by explaining how randomized pulses and covariance-based detection can be combined to retrieve spectroscopic information on nonlinear processes. As a proof of principle, we discuss the application of the technique to Impulsive Stimulated Raman Scattering in transparent media, which has been the focus of my project as a master student [1, 2, 3, 4]. The last two sections are devoted to the description of the experimental setup we have developed during my PhD project for extending FCS to the study of electronic Raman scattering in cuprates. We will reserve special focus to the polarization pulse shaper we have designed to attain arbitrary control of the amplitude, phase and polarization state of each spectral component within an ultrashort light pulse.

7.1 NONLINEAR SPECTROSCOPY WITH RANDOMIZED PULSES

The major experimental challenge when dealing with nonlinear processes is posed by their weak intensity compared to the linear contributions. The desired signal-to-noise ratio is usually reached by i) reducing the experimental noise as much as possible ii) performing the mean of repeated iterations of the same experiment. When working with femtosecond laser sources, this approach relies strongly on pulse-to-pulse consistency and has thus motivated significant efforts in pursuit of perfect experimental stability.

On the other hand, in different contexts, noise can act as a source of additional information rather than a liability to be mitigated [5, 6, 7, 8, 9, 1, 2]. In this framework, each single pulse, rather than being considered a stroboscopic repetition of the same experiment, can be regarded as a new experiment, taking place in different conditions with respect to the previous one and therefore carrying different information. By flattening out all the spectral features peculiar to each pulse, the mean-value loses significance; other statistical tools are needed to search the random noise and extract the hidden information, such as covariance.

This conceptual scheme is illustrated in Figure 7.1, in which each pulse has unique spectral features. A frequency-resolved shot-to-shot detection enables the acquisition of the entire spectral content. By evaluating the covariance between pairs of spectral

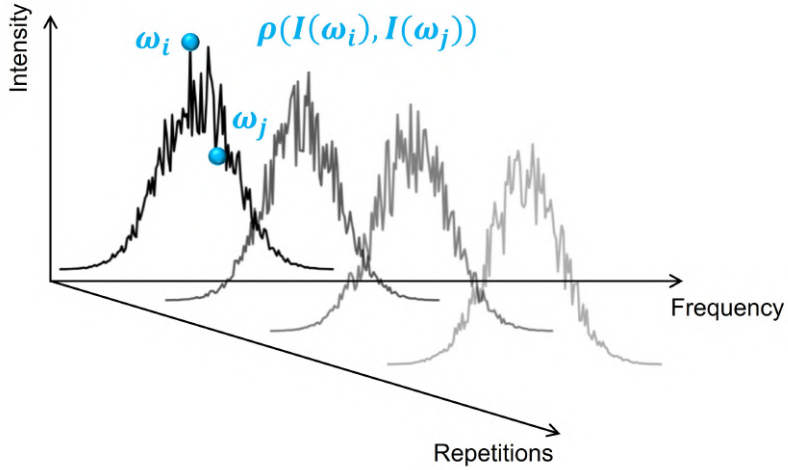

Figure 7.1: **Measurements with randomized pulses.** Each repetition with a stochastic pulse is seen as a new experiment, rather than an iteration to be averaged over. Information is encoded in the correlation coefficient ρ between different spectral components.

components, it is possible to uncover the correlations between the intensities at different frequencies and therefore quantifying the photon correlations imparted by the light-matter interaction.

In this respect, it is crucial to highlight that the stability of the laser source is no longer a requirement, but is rather detrimental to the success of the FCS technique. If the pulses employed in the experiment are characterized by a high degree of coherence, their intrinsic correlations might conceal the ones imprinted by the nonlinear interaction. For this reason, FCS relies on the introduction of spectrally narrow stochastic fluctuations across the bandwidth of the impinging pulses, so that the spectral components are completely uncorrelated prior the interaction with the sample. As it will be discussed in detail in Section 7.3.1, we have employed femtosecond pulse shaping based on a liquid crystal spatial light modulator to achieve this task.

7.1.1 *Pearson Correlation coefficient*

In order to quantify the correlations among the spectral components after the light-matter interaction, we will use throughout this thesis the Pearson correlation coefficient ρ, which evaluates the degree of linear correlation between two stochastic variables. In our experiment, the variables considered are the intensities measured at two given spectral components ω_i,ω_j. By definition,

$$\rho(I(\omega_i), I(\omega_j)) = \frac{\langle I(\omega_i) I(\omega_j) \rangle - \langle I(\omega_i) \rangle \langle I(\omega_j) \rangle}{\sigma_i \sigma_j} \tag{7.1}$$

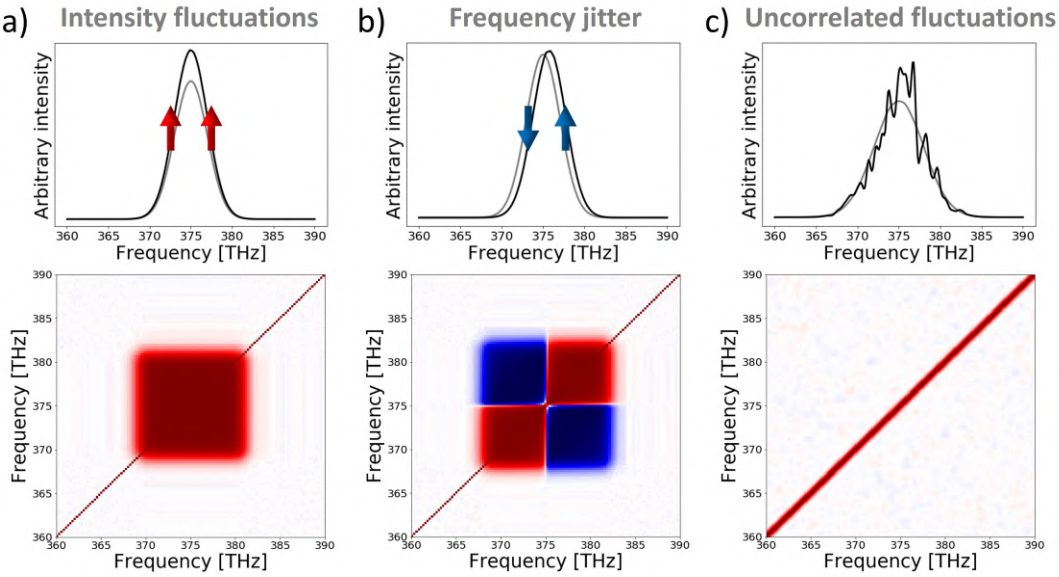

Figure 7.2: **Simulated covariance maps.** Set of 1000 simulated light pulses in which intensity (**a**), central frequency (**b**) and uncorrelated (**c**) stochastic fluctuations are introduced. In the top panels, the black line represents one realization, while the grey line the average over the entire set. In the bottom panels, the corresponding Pearson correlation maps are plotted in false colors. Adapted from the thesis [4].

where $\langle \dots \rangle$ indicates the mean over all the repetitions of the set (i.e. the number of pulses employed in the experiment) and σ_i denotes the standard deviation over the set at frequency ω_j.

The numerator of Equation 7.1 is nothing but the covariance between the variables considered; the denominators normalizes the Pearson coefficient, so that it can assume values ranging from -1 (negatively correlated variables) and 1 (positively correlated variables). When $I(\omega_i)$ and $I(\omega_j)$ are independent variables, $\rho = 0$.

With reference to Figure 7.1, the Pearson correlation coefficient must be computed for each pair of frequencies within the spectral content of the pulse. The computation over all the possible combinations results in a two-dimensional symmetric map, in which both axes are the pulse frequency range and the colormap indicates the degree of correlation for a specific point in the grid, i.e. for a specific pair of spectral intensities.

We present in Figure 7.2 the result of a set of simulations of incident pulses in which specific noise characteristics are arbitrarily introduced across the bandwidth. This preliminary study is particularly useful to get familiar with the statistical tool and to understand which correlation structures obtained in the experimental data can be eventually traced back to the intrinsic noise of the laser source rather than the light-matter interaction. In particular, we consider two kinds of noise that are peculiar to femtosecond sources: intensity fluctuations (Figure 7.2a) and jitter in the central frequency of the pulse (Figure 7.2b). The former gives rise to a positive Pearson map because all the modes have the same sign shift with respect to the average pulse (grey line). In the latter case, the Pearson map is checkered because two modes lying

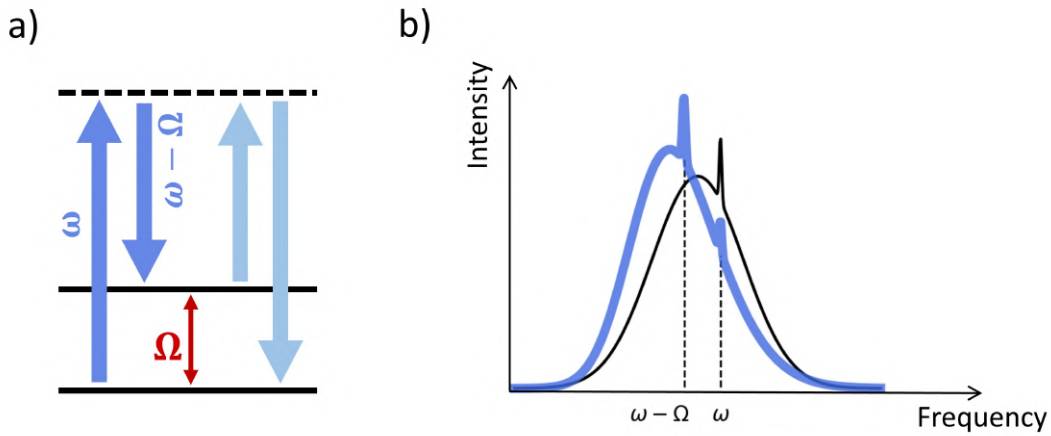

Figure 7.3: **ISRS process. a)** Depiction of a Stokes (dark blue) and Anti-Stokes (light blue) process involving a vibrational excitation Ω and a pair of photons (ω,$\omega + \Omega$). **b)** A localized narrow fluctuation is introduced in the incoming pulse (black curve) and imprints distinguishable features at the frequencies involved in the Stokes process in the transmitted pulse (blue curve).

on the same side (with respect to the central frequency of the pulse) deviate similarly from the mean, while two modes on the opposite sides are anti-correlated. In both cases, the maps display a positively-correlated diagonal line that indicates the trivial correlation between each frequency and itself.

In Figure 7.2c we consider a dataset in which uncorrelated fluctuations have been inserted. The resulting Pearson map displays only the diagonal line, while the rest of the values are centered around zero. The width of the diagonal line is set by the correlation length (Δ_{corr}) of the fluctuations manually introduced in the pulse: the larger Δ_{corr}, the broader the diagonal. We stress that using spectrally uncorrelated pulses as the ones in Figure 7.2c has the advantage of suppressing the correlations intrinsic to the source Figure (7.2a,b) and enhancing instead the photon correlations imprinted by the light-matter interaction.

7.2 APPLICATION TO IMPULSIVE STIMULATED RAMAN SCATTERING

We have demonstrated the feasibility of the FCS technique by studying the vibrational spectrum of crystalline α-quartz via Impulsive Stimulated Raman Scattering (ISRS) [10]. ISRS is a Raman process which takes place whenever sufficiently short light pulses propagate through transparent media. The impulsive character of the process is due to the temporal duration of the pulses that, being shorter than the typical vibrational lifetimes, are responsible for an instantaneous perturbation of the atoms that coherently vibrate around their equilibrium positions. Its stimulated nature is related instead to the way the Raman resonance is established [11]. In a stimulated process, the Raman mode is driven into resonance by two incident (off-resonance) fields, so that the initial phase of the oscillation matches the relative phase difference

of the incoming fields. Due to the broad spectral content of ultrashort pulses, both the fields involved in the stimulated process can be found within the bandwidth of the pulse and the coherent excitation occurs through the optical mixing of its Fourier components.

In a fully quantum effective description up to the first-order, ISRS can be formalized by the following hamiltonian, which involves photonic ($\hat{a}$) and phononic ($\hat{b}$) degrees of freedom [12, 13]:

$$\hat{H}_{ISRS} = \sum_{\omega,\omega'=-J}^{J} (\underbrace{\hat{a}^\dagger_\omega \hat{a}_{\omega'} \hat{b}^\dagger_\Omega}_{\text{Stokes}} + \underbrace{\hat{a}_\omega \hat{a}^\dagger_{\omega'} \hat{b}_\Omega}_{\text{AntiStokes}}) \tag{7.2}$$

where the only non-vanishing terms are for the pairs j and j' whose frequency difference is Ω (i.e. the phonon frequency), and the sum runs over all the optical modes within the pulse. The first term of the hamiltonian describes a Stokes process in which, as illustrated in Figure 7.3a (dark blue arrows), a photon is annihilated at frequency ω, one is created at frequency $\omega - \Omega$ and a vibrational excitation is simultaneously created in the system. The second term describes an Anti-Stokes process (light blue arrows) resulting in the annihilation of a phonon.

In order to understand the role played by the noise in FCS, let us consider an incident pulse in which a spectrally narrow fluctuation has been introduced at a given frequency ω (black curve in Figure 7.3b). When such pulse propagates through a transparent medium, ISRS takes place and, if we consider for simplicity only a Stokes process, the transmitted pulse will be shifted at lower frequencies (blue curve in Figure 7.3b). However, the entity of such shift depends not only on the energy of the phonon modes involved, but also on the scattering cross section of the process; as a result, the shift does not directly maps the vibrational spectrum of the material. Nevertheless, the fluctuation inserted at ω in the incident pulse will be mapped into a distinguishable feature at $\omega - \Omega$. By repeating the measurement many times introducing different unique fluctuations, a correlation between the frequencies involved in the process will be established.

7.2.1 *Measurements on α-quartz*

In Figure 7.4 we plot the results of the FCS experiments carried out in crystalline α-quartz [1]. After the introduction of stochastic fluctuations, the beam is splitted and a small portion (*reference*) is routed around the sample and recorded by an array of photodiodes. The covariance map (Equation 7.1) of the reference beam is plotted in Figure 7.4 and confirms that only the trivial auto- correlation $\omega_i = \omega_j$ is present.

In contrast, when the randomized pulse is transmitted by the sample, the Pearson map is evidently structured (Figure 7.4b). In particular, we observe off- diagonal sidebands whose distances from the diagonal exactly match the Raman shift of the main phonon modes in α-quartz. This means that optical modes that differ by the frequency of the Raman modes have been correlated by the ISRS process.

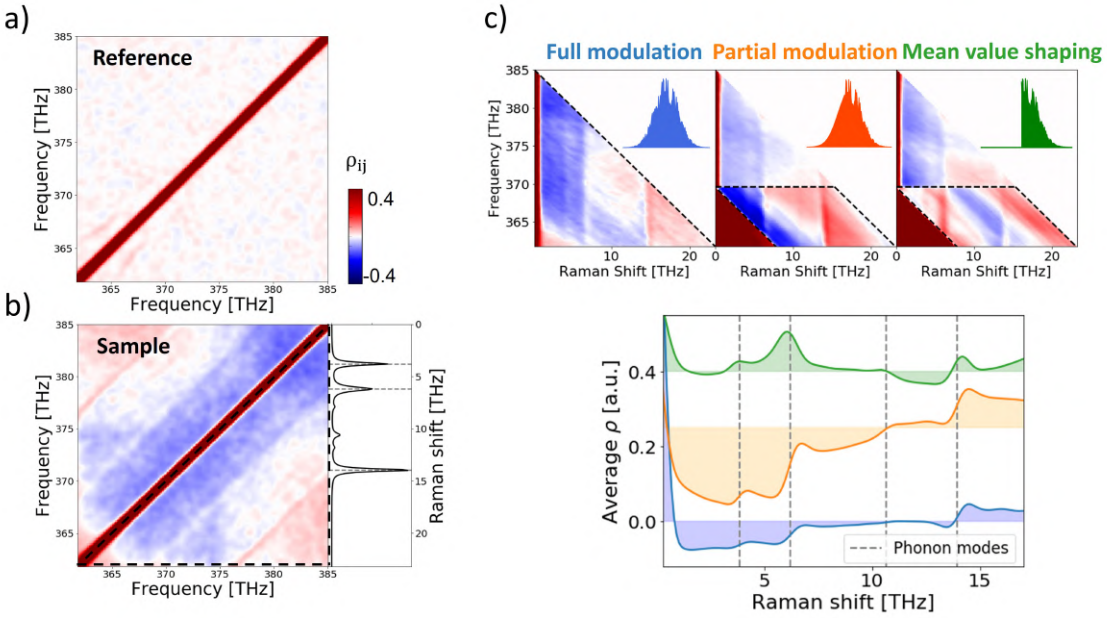

Figure 7.4: **FCS in transparent α-quartz.** Pearson map computed over 50k noise realizations of the uncorrelated incoming pulse (**a**) and the pulse transmitted by the sample (**b**). The spontaneous Raman spectrum has been adapted from [14]. **c)** Rotated quadrants of the Pearson maps in different noise configurations and their integration over the dashed boxes as function of the Raman shift.

A more detailed analysis of the noise configurations that can be applied to the incident pulses, shows that FCS is a phase-sensitive technique. We consider in Figure 7.4c three variations: i) *full modulation*: spectral fluctuations are introduced across the entire bandwidth; ii) *partial modulation*: the pulse is Gaussian below a certain frequency and randomized above; iii) *mean value shaping*: the intensity is zero below a certain edge and fluctuating above. By integrating the corresponding Pearson maps, it is evident that the lineshape of the Raman features depends on the noisy pattern applied, as a consequence of the self-heterodyning character of the ISRS process. When there is a heterodyning field at the emission energy (full or a partial modulation) the lineshape is dispersive, while in the absence of a heterodyning field (mean-value shaping) we observe a completely positive lineshape. Furthermore, it is worth to note that the visibility of the Raman features in the heterodyning configurations (full and partial) benefits from the presence of an unmodulated portion of the spectrum: the correlations are enhanced by the high degree of coherence of the stable low-energy side of the pulse (orange line), while they result attenuated when the optical modes at the emission energies are also randomized (blue line).

Finally, we have recently demonstrated that, by implementing the FCS technique into a pump-probe scheme, it is possible to recover the amplitude, phase and energy of each phonon mode as function of the coherent pump-randomized probe temporal delay [2].

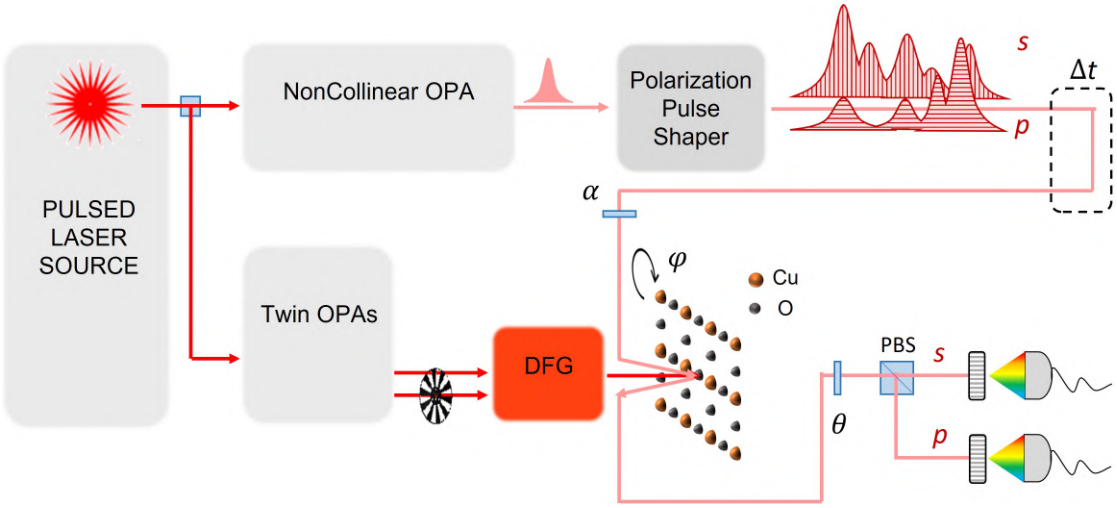

Figure 7.5: **Sketch of the FCS pump-probe setup.** The mid-infrared pump is obtained via DFG, while the probe (750 nm) is generated in a noncollinear OPA and properly shaped by the polarization pulse shaper. A motorized translation stage adjusts the temporal overlap (Δt) between the pump and the probe beams, which impinge non-collinearly on the cuprate sample. A polarizing beam splitter (PBS) splits the reflected probe into the s- and p-polarized components that are dispersed by two transmission gratings and focused on two linear arrays of silicon photodiodes (NMOS). α,θ are half-waveplates and φ denotes the orientation of the sample, adjustable by means of a piezoelectric rotator.

7.3 EXPERIMENTAL REALIZATION

In this section, we describe the experimental setup we have developed to study time-resolved electronic Raman scattering in cuprates by means of the FCS approach.

The main blocks of the setup are sketched in Figure 7.5. Similarly to the measurements discussed in Chapter 3, we have pumped the cuprate sample, an optimally-doped $Bi_2Sr_2CaCu_2O_{8+\delta}$ (Bi2212), with mid-infrared (MIR) pulses obtained through DFG as explained in Chapter 2. The probe is a 750 nm pulse (20 fs) generated by the non-collinear optical parametric amplifier.

The core part of the setup consists of an optical pulse shaper based on a liquid crystal spatial light modulator (LC-SLM) (by Meadowlark Optics). The pulse shaper has been designed with the purpose of exerting complete control over the amplitude, phase and polarization state of all the optical modes within the probe pulses in order to introduce stochastic fluctuations. In particular, the possibility of controlling the polarization state is especially advantageous in view of the study of the superconducting order parameter projected onto the Raman symmetries, as emphasized in Chapter 6. We stress that, while the amplitude and the phase degrees of freedom in ultrashort pulses are commonly handled by adopting rather standard schemes [15, 16], the spectrally independent manipulation of the polarization is a less explored route. We will explain in detail in Section 7.4 how we achieved it using an interferometric scheme.

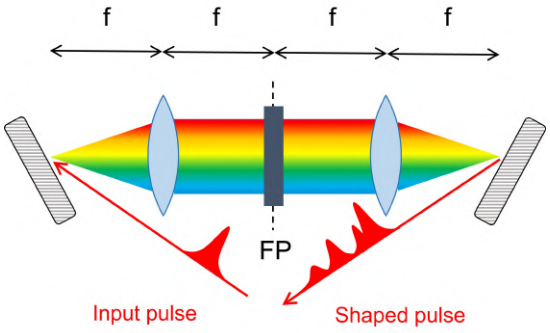

Figure 7.6: **Pulse shaping in a $4f$-scheme.** The spacing between all the optical elements equals the focal length f of the lens. The spatial mask is placed in the Fourier plane (FP).

The half-waveplate α in front of the sample is used to define the input polarization geometry needed to isolate specific symmetry modes in the sample, with reference to Figure 6.3. The reflected probe beam is collected and splitted into orthogonal components by a polarizing beam splitter cube, where the half-waveplate θ is used to balance the two channels at the equlibrium. The s- and p-components are independently diffracted and detected by two linear arrays of photodiodes.

7.3.1 *Femtosecond pulse shaping with spatial light modulators*

In order to discuss the operation of the polarization pulse shaper we have designed, we will introduce here some fundamental concepts on femtosecond pulse shaping.

In general, with the term *pulse shaping* one refers to a broad class of techniques that are employed to arbitrarily manipulate the electric field of optical pulses. Due to their sub-ps temporal duration, direct shaping in time is not a viable option and most schemes work in the frequency domain. A widely used approach consists in the $4f$-scheme, depicted in Figure 7.6, in which all the relevant optical elements are spaced by the focal length f of the lens [16]. The input pulse is dispersed by a reflection grating and the angularly separated optical modes are focused by a lens into the Fourier plane, where the frequency components are spatially separated into diffraction-limited spots. By placing a spatial mask that acts separately on every Fourier component, a spectrally-resolved manipulation is achieved. The pulse is then collimated and recombined by the second pair of lens and grating.

It is clear that the crucial point lies in the choice of the spatial mask. While static masks (slabs with a varying transmission coefficient, phase retarders, etc) can be fabricate via lithography, they have the obvious drawback of being unmodifiable by the user. Programmable masks are instead more desirable options and several dynamical masks are nowadays available [15]. The device we have employed is a spatial light modulator based on liquid crystals (LC-SLM).

A LC-SLM exploits the birefringent properties of nematic liquid crystals placed between two electrodes with varying voltage (Figure 7.7a). When no voltage is

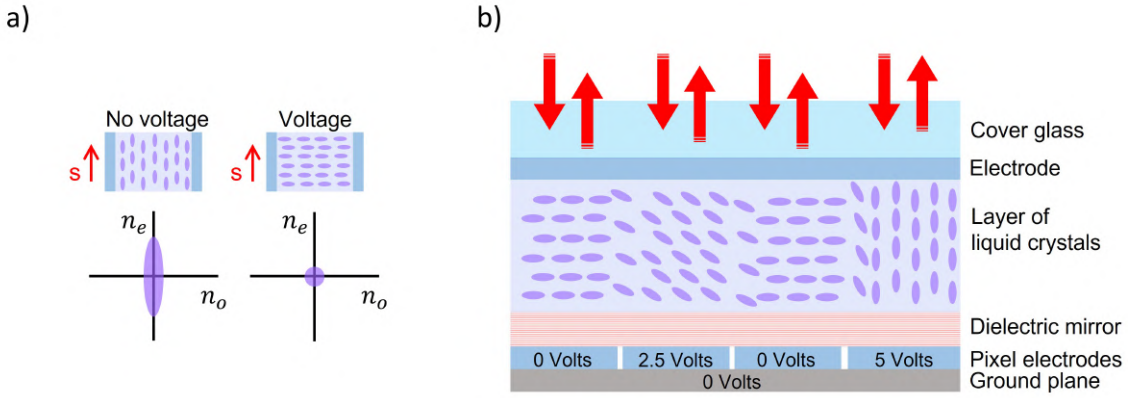

Figure 7.7: **Femtosecond pulse shaping with liquid crystals. a)** The birefringent optical properties of nematic liquid crystals modulate a light beam linearly polarized along the extraordinary axis. The maximum phase shift (largest difference between the ordinary and extraordinary refractive indices) is obtained when no voltage is applied between the electrodes. **b)** Side-view of a liquid crystal spatial light modulator in a reflection geometry. Adapted from [4].

applied, an electric field polarized along the director of the liquid crystals experiences the largest difference between the ordinary (n_o) and the extraordinay (n_e) refractive indices. The application of a voltage between the electrodes tilts the molecules and attenuates the birefringence. By tuning the voltage V, the liquid crystals behave as an adjustable waveplate which is responsible for a phase delay ϕ equal to

$$\phi(\omega, V) = \frac{\omega \Delta n(\omega, V) d_{LC}}{c} \tag{7.3}$$

where Δn is the difference between n_o and n_e, ω is the frequency of the impinging electric field and d_{LC} is the thickness of the liquid crystals layer.

In a more general framework, one of the electrodes is pixelated so that different voltages can be applied and light beams impinging on different regions on the mask can experience a different phase delay. A side view of a LC-SLM is sketched in Figure 7.7b. The four fields impinging on distinct pixels will be phase delayed each by a different amount according to the four voltages applied. It is worth to note, however, that the layer of liquid crystals is not partitioned, but uniform. As a consequence, neighbouring pixels cannot be regarded as completely independent, and a certain degree of correlation is always present at the edges and must be properly handled, as explained in Section 7.4.2.

DIFFRACTION-BASED SPATIAL LIGHT MODULATORS While a device like that in Figure 7.7b would allow to control only the spectral phase, the simultaneous shaping of both the phase and the amplitude of the pulse can be achieved using a two-dimensional LC mask in a diffraction geometry [17]. The optical arrangement is

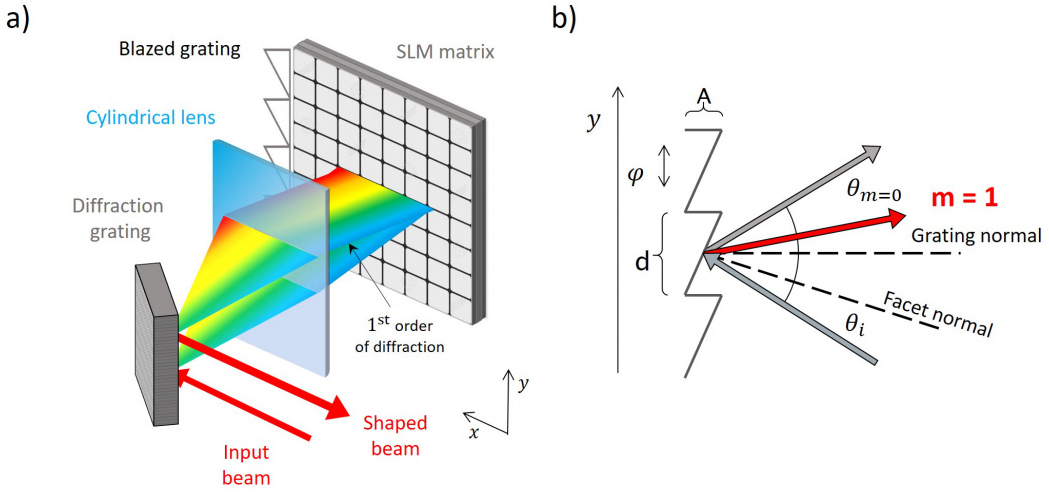

Figure 7.8: **Diffraction-based pulse shaping. a)** Optical arrangement of a diffraction-based spatial light modulator. **b)** Diffraction of an incoming monochromatic beam from a blazed grating with amplitude A, period d and vertical position φ. Adapted from [4].

illustrated in Figure 7.8a. Instead of using a $4f$-scheme, a single grating-lens[1] pair is employed which acts as both dispersive and collimating element (*folded* $4f$-line). By tuning the voltages in each pixel column of the SLM matrix, a blazed grating is applied. The input beam is diffracted back and the first order of diffraction is collected by the lens and recombined. The SLM matrix is software-programmable: the 2D mask can be regarded as a collection of several blazed gratings (as many as the pixels along the horizontal direction x). A full control over the first-order diffracted light can be then achieved by modifying the parameters of each blazed grating extending along the vertical direction y.

The choice of the parameters can be understood in terms of the Fraunhofer diffraction [17]. We consider a phase modulation as the one depicted in Figure 7.8b and described as:

$$\phi(\omega, y) = \alpha\left\{\frac{1}{2} + A(\omega)S_d[\varphi(\omega), y]\right\} \tag{7.4}$$

where S_d is a sawtooth function oriented along the vertical axis y of the SLM matrix. The sawtooth has amplitude $A(\omega)$, period d and phase $\varphi(\omega)$. The amplitude of the first-order diffracted beam is then [17]:

$$E(\omega) \propto e^{-i\varphi(\omega)}\text{sinc}\left[\pi - \frac{\alpha}{2}A(\omega)\right] \tag{7.5}$$

where α is the maximum phase shift achievable by the SLM.

1 A cylindrical lens is used instead of a convex one to focus the dispersed beam only along the horizontal axis. The beam is not focused along the vertical axis to illuminate multiple periods of the blazed grating.

Equation 7.5 effectively rules the properties of the shaped beam: the amplitude of the diffracted pulse can be arbitrarily modified by changing the efficiency of the blazed grating (which scales as the sinc of the sawtooth amplitude), whereas its phase can be controlled by varying the spatial phase (i.e. the vertical position) of the sawtooth.

7.4 POLARIZATION PULSE SHAPER

The achievement of a complete vector-field control of ultrashort pulses relies on the independent manipulation of four degrees of freedom for each frequency component: the spectral intensity, the spectral amplitude ratio between the two orthogonal polarization components, their common spectral phase and their spectral phase difference. There are two distinct approaches to accomplish this task [18]. The first method is based on the use of multiple one-dimensional SLM layers: the phase delays independently introduced by each layer can be properly combined to attain the desired state. A pair of SLM layers was initially employed to simultaneously control the common phase and the amplitude ratio (but not the orientation of the major axis of the elliptical polarization) [19, 20] and later, a scheme with four consecutive liquid crystal arrays was designed to realize full control without this limitation [21].

The second approach consists in the independent shaping of the spectral amplitudes and the phases of the two orthogonal components of the pulse in an interferometric scheme. The input beam is splitted into the s- and $p-$components, whose amplitude and phase are simultaneously shaped by two independently controllable LC 1D layers [22, 23, 24]. The orthogonal components are then spatially and temporally recombined.

Our pulse shaper design combines a diffraction-based SLM (a 2D single layer LC mask) with an interferometric setup. We decided to employ a single-layer 2D mask instead of a two-layer 1D one for i) suppressing the unwanted temporal replica that are a common drawback in dual LC-SLMs ii) achieving a higher frame rate that is a crucial parameter to realize thousands of stochastic noise patterns in FCS. We used a 2D LC-SLM fabricated by Meadowlark Optics with an active matrix of 1920x1152 pixels (17.7x10.6 mm) and characterized by a refresh rate of $\sim$200 Hz.

In Figure 7.9 we show a picture of the optical arrangement of the pulse shaper. The input beam (750 nm, FWHM$\simeq$55 nm) is generated by the NOPA and goes through a telescope (out of the picture) to reduce the spot size. The polarization is vertical to be parallel to the director of the LC within the SLM and is selected by a polarizer. A 50:50 beam splitter separates the two beams that are routed towards a folded $4f$-line. The beams impinge on the same spot of the reflection grating, but with a different incident angle so that the first-order diffracted beams are spatially separated and their dispersions do not overlap. A cylindrical lens focuses the two frequency-dispersed beams on different areas of the SLM matrix, so that they can be independently shaped.

By adjusting the period of the SLM blazed grating and the blazing direction, the first-order diffracted beams are vertically tilted to impinge back on the reflection

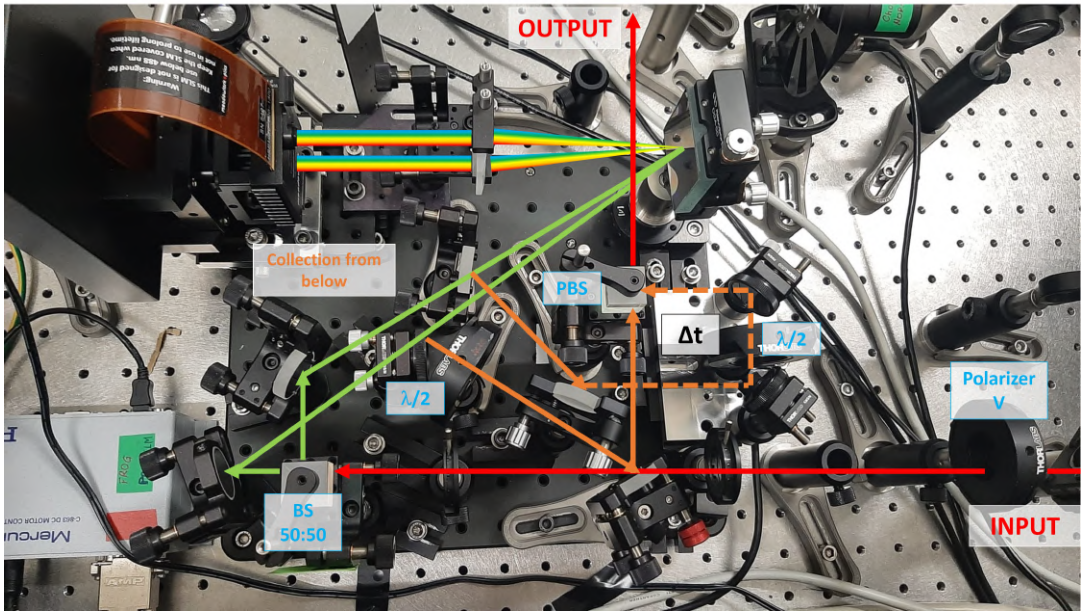

Figure 7.9: **Polarization pulse shaper board.** An input *s*-polarized beam is equally splitted by a beam splitter (BS) and the two components enter a common folded $4f$-line. The diffracted beams are temporally (translation stage Δt) and spatially recombined by a polarizing beam splitter (PBS) after rotating by 90° the polarization of one of them.

grating ∼1 cm below the spot of the incoming path. Two mirrors intercept from below the shaped beams outgoing the $4f$-line, that still have at this point the same polarization. A half-waveplate rotates by 90° the polarization of one arm, while the other one goes through a mechanical translation stage to adjust the temporal overlap between the two components.[2] The beams are finally recombined by a polarizing beam splitter.

Usually, in a diffraction-based SLM geometry, a beam splitter (or a wedged window) is used to select the portion of the beam to be routed in the $4f$-line. Then, the shaped pulse is diffracted back along the same path of the incoming beam and goes through the beam splitter once again, so that its reflection is deviated from the incoming direction. In the best case scenario, the double passage through the beam splitter leads to a 75% reduction of the initial power. We highlight that, in our arrangement, the vertical tilt of the diffracted beams allows the collection of the shaped pulses with almost no losses.

2 In principle, the delay between the two arms can be adjusted by adding a linear term in the spectral phase shaped by the SLM, without the need of a translation stage. However, the geometry of the $4f$ line imposes limits on the maximum temporal window that is available for shaping, as a consequence of the space-time coupling that affects these experimental schemes by construction [15, 16]. The duration or the temporal delay of the shaped pulse should stay below this threshold to avoid distortions. The maximum temporal window T is inversely related to the finest achievable spectral feature (spot size at the SLM for a single colour). In our design, T<5 ps, so it is not sufficient to compensate for the mismatch of the optical paths experienced by the two arms. A translation stage is then needed to overlap the pulses; the SLM can be eventually employed for fine-tuning.

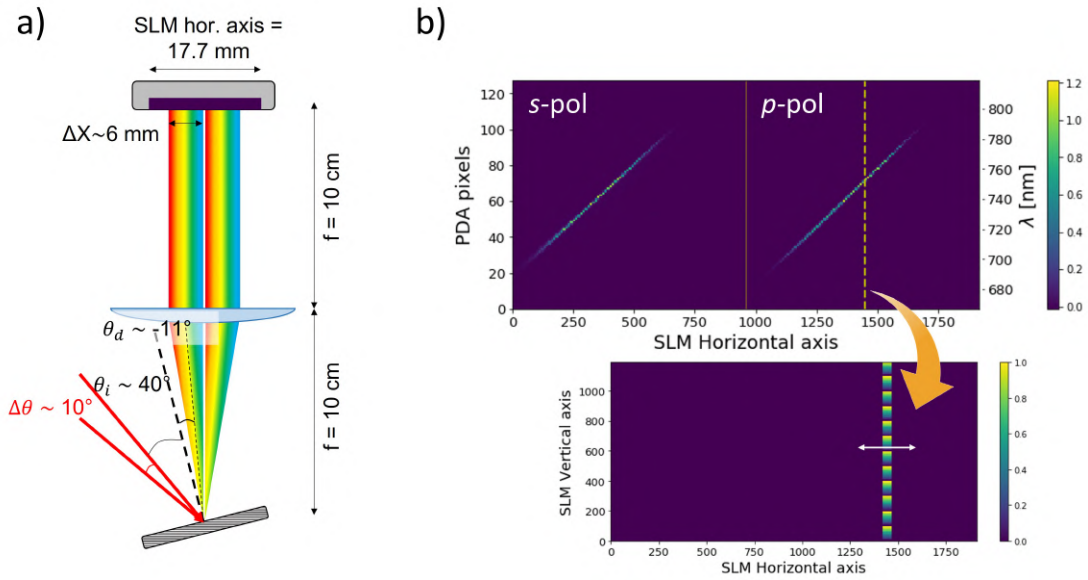

Figure 7.10: **Double-shaping of the probe pulse. a)** Geometry of the $4f$-line for polarization shaping. **b)** Shaping of a single frequency component within the probe pulse measured by the photodiode arrays (PDA). The arrow indicates the blazed diffraction grating imprinted on the SLM matrix for a specific frequency and polarization component. The period of the grating and its horizontal extension have been enlarged for clarity.

The $4f$-line has been designed according to the following requirements: i) illuminating the largest possible portion of the full width of the SLM matrix to improve the frequency resolution of the shaping; ii) providing a sufficient gap between the SLM areas illuminated by the two beams to avoid overlaps. Given the spectral content of the incoming pulse and the optical elements commercially available, we have employed a reflection grating with 600 grooves/mm ($1/d$, being d the grating period) and a cylindrical lens with a 10 cm focal length f. Considering an incoming Gaussian beam with central wavelength λ_0 and assuming a linear dispersion [16], the frequency ω_k is located at the Fourier plane of the $4f$-line at the spatial coordinate

$$X_k = \frac{\lambda_0^2 f}{2\pi c d \cos\theta_d}\omega_k \tag{7.6}$$

where θ_d is the first-order diffracted angle at λ_0, given by the grating equation $d[\sin\theta_d + \sin\theta_i] = \lambda_0$ with θ_i the incident angle.

The geometry of the $4f$-line is sketched in Figure 7.10a. We used $\theta_i \sim 40°$ (with respect to the normal of the grating) and we separated the two components by $\Delta\theta_i \sim 10°$. This choice ensures that the spectral dispersion at the Fourier plane, estimated with Equation 7.6, is ΔX ~6 mm, and so smaller than half of the SLM width.

In Figure 7.10b we plot the measured dispersion across the SLM pixels projected onto the photodiode arrays. With reference to Figure 7.5, after the interferometric

recombination in the pulse shaper board, the orthogonal components of the pulse are splitted again by a polarizing beam splitter prior the detection. Therefore, each array measures the polarization component that has been shaped by one half of the SLM matrix. As shown in the bottom map, we have applied a SLM pattern in which a blazed grating along the vertical SLM axis extends only for 2 pixels along the horizontal SLM axis. In this way, by programming the grating at a specific position along the horizontal axis, only light at a given frequency and polarization is diffracted and measured by the arrays. The top map in Figure 7.10b is the result of 192 measurements, each for a different position of the 2 pixel-wide blazed grating that has been shifted by 10 pixels every time. The two components do not overlap on the SLM horizontal axis and their dispersion is roughly 650 pixels wide ($\sim$6 mm, being 9.2 μm the SLM pixel pitch), as theoretically estimated. Finally, by measuring the spectral content of the shaped pulse with an already calibrated fiber spectrometer, we have built a one-by-one correspondence between the SLM horizontal axis and the wavelength axis. We used this relation to calibrate in turn the photodiode arrays.

7.4.1 *Characterization of the pulse shaper*

The interferometric recombination of the two shaped orthogonal components of the pulse strongly relies on a stable spatial and temporal overlap. To suppress air currents and thus possible spatial drifts, we have enclosed the pulse shaper board in a closed box. We will explain in the following how we routinely adjust the overlap between the beams. Moreover, the use of beam splitter cubes in the pulse shaper setup leads to a broadening of the pulse temporal duration. We will describe how we compress the probe using the SLM.

TEMPORAL OVERLAP To recombine the beams after the SLM, we exploit the interference between them. In order for interference to take place, we place a 45° oriented polarizer on the outgoing beam to create two pulses with the same polarization originating from the shaped s- and p-components. We focus the resulting beam into a fiber spectrometer and measure the spectrum while scanning the position of the translation stage (Figure 7.11a). In proximity of the temporal overlap, the scanning step of the stage is 5 μm ($\sim$17 fs). When the pulses are delayed in time, interference peaks can be observed. The spacing between the peaks is inversely proportional to the time separation of the beams. The zero delay can be thus identified when either no peaks (destructive interference) or one peak (constructive interference) are observed. By plotting the spectra in a false-color 2D map (Figure 7.11b), the position of the translation stage for which the temporal overlap is reached can be determined.

PULSE COMPRESSION The dispersive elements of the pulse shaper lead to a temporal chirp of the pulse. We use the pulse shaper to introduce an opposite chirp which re-compresses the pulse by properly modifying its spectral phase. In order to achieve a good compression of the shaped pulse at the sample position, we have used

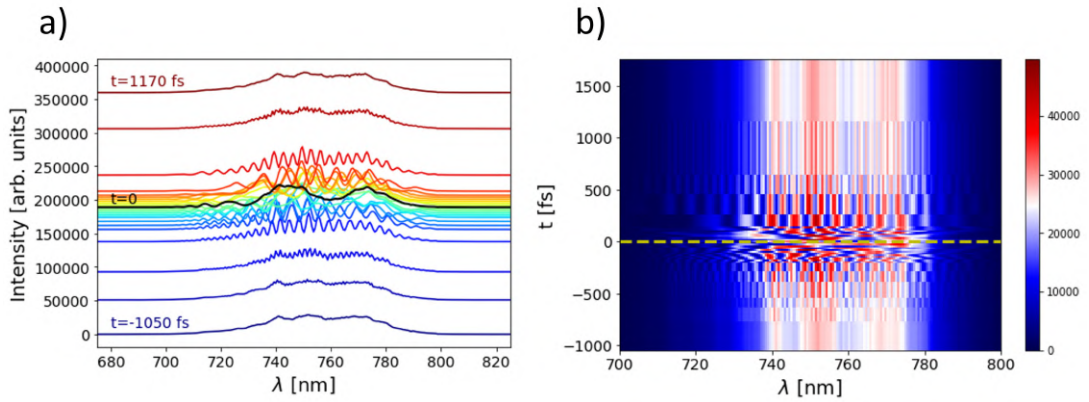

Figure 7.11: **Temporal overlap between the shaped beams. a)** Spectra after a 45° polarizer acquired by a fiber spectrometer for several stage positions (converted in time delay t). The curves around the overlap t=0 (black line) are equally spaced by ∼17 fs. A vertical offset proportional to the corresponding delay has been added to each curve for clarity. **b)** Color-coded map of the spectra as function of measured wavelength (x-axis) and stage position converted in temporal delay (y-axis).

as feedback signal the transient broadband reflectivity in a reference YBCO sample, which is characterized by a quasi-instantaneous response. With reference to Figure 7.5, the sample has been excited with the DFG pump and the transient reflectivity along both the vertical and horizontal polarization components has been acquired by the array detectors. We illustrate in Figure 7.12 the compression procedure for one arm of the pulse shaper (only the horizontal polarization) and thus just one half of the SLM width (960 pixels over the whole 1920 axis). If no corrections are applied on the spectral phase (i.e. the SLM pattern is made of blazed gratings with the same depth across the SLM horizontal axis and not displaced along the vertical axis, Figure 7.12a), the resulting broadband reflectivity is strongly chirped, meaning that the probe pulse is temporally stretched (∼400 fs). By introducing a second-order correction (a quadratic spectral phase, Fibure 7.12b), the chirp can be compensated. However, also cubic corrections (Figure 7.12c) are needed to finally obtain a flat dispersion. We have calibrated both arms of the pulse shaper to adjust the correction coefficients up to the third-order. These parameters are saved and always superimposed to any 2D pattern written on the SLM matrix.

7.4.2 *Introduction of stochastic fluctuations*

We have stressed that in a FCS experiment thousands of pulses are employed and the signal is obtained by evaluating the covariance over the whole set. The strength of the method relies on the stochasticity of the incident pulses, that are spectrally uncorrelated prior the interaction with the sample. Each pulse is shaped by a randomized SLM pattern. Specifically, an array of 1920 numbers (the width of the SLM matrix) is randomly generated with a uniform distribution and used to modify the

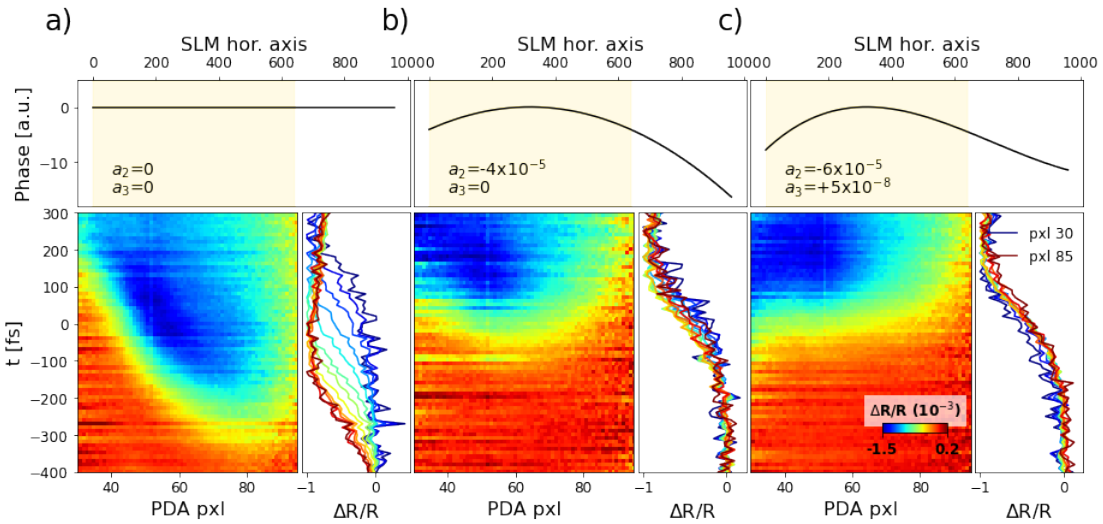

Figure 7.12: **Compression of the shaped pulse.** Spectral phase imparted by the SLM after the introduction of no corrections (**a**), only a second-order correction (**b**) and non-null second- and third-order corrections (**c**. In each of the three scenarios, the top panel is the spectral phase across the SLM horizontal axis and the coefficients of the corresponding corrections are reported. The gold-shaded area indicates the SLM region that it is illuminated by the pulse dispersion (Figure 7.10b). The color-coded map is the time- and frequency-dependent pump-probe reflectivity signal measured on a reference YBCO sample. The time-traces on the right of each map are the normalized $\Delta R/R$ signal at different pixels of the photodiode array (different frequencies).

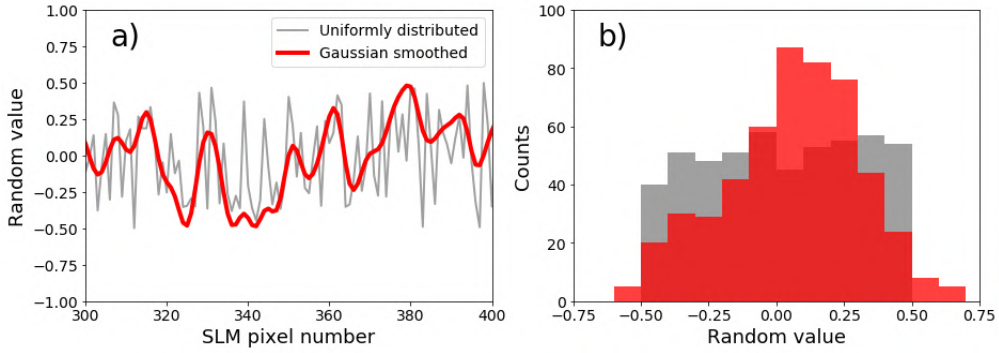

Figure 7.13: **Example of Gaussian-smoothed stochastic fluctuations. a)** Comparison between a uniform (grey) and a Gaussian-smoothed (red) distribution of random values for a portion a 100 SLM pixels. **b)** Histogram of the random numbers generated in a single realization (uniform in grey, Gaussian-smoothed in red).

efficiency of each SLM blazed grating. In this way, as different frequency components are diffracted by different gratings, the spectral amplitude of the pulse is randomized.

Because of the inherent coupling of the liquid crystals in adjacent pixels, we apply a Gaussian-smoothing on the uniformly distributed random array. Precisely, we replace each uniformly distributed value with the sum of its neighbouring values weighted by a Gaussian function with a fixed variance (Δ_{corr}). The procedure is illustrated in Figure 7.13, where the red line represents the Gaussian-smoothed distribution with Δ_{corr}=2 pixels.

As a consequence of the smoothing, neighbouring pixels can no longer be considered independent, as a Gaussian correlation function has been introduced (Figure 7.13b). Two frequency components can be regarded as statistically independent only if they impinge on pixels that are farther apart than Δ_{corr}, which thus sets the frequency resolution of the spectral fluctuations that can be introduced. In our design, Δ_{corr} = 5 SLM pixels, that, considering the wavelength distribution in Figure 7.10b, corresponds to $\sim$ 1 nm.

RESOLUTION OF THE TECHNIQUE It is important to note, however, that the final frequency resolution of the method is determined by the convolution of Δ_{corr} and the spectral resolution of the photodiode arrays ($\sim$ 1.5 nm). Taking into account the spectral content of the pulse (375-430 THz), the resolution is <1.5 THz over the entire bandwidth. Moreover, as correlations can be established among all the optical modes within the pulse, the pulse bandwidth also sets the maximum energy of the excitations that can be probed by the technique, that is $\sim$55 THz (18000 cm^{-1}) in our configuration. This means that Cooper pair breaking in cuprates (<500 cm^{-1}) is well within this limit.

In this respect, particular attention must be paid on the temporal profile of the randomized pulses. We have shown in the previous section that second- and third-order corrections of the spectral phase are needed to compress the pulse after the shaping. When we generate the random patterns, these corrections are superimposed

to the stochastic blazed gratings to preserve the phase profile of the initially transform limited pulses. However, the introduction of noisy fluctuations results, over repeated realizations, in a broad tail [1], that can be directly measured through Frequency Resolved Optical Gating (FROG) [3]. The time profile is thus the superposition of a ps-long tail and a short coherent component; the latter provides the impulsive excitation and sets, combined with the pump pulse duration, the temporal resolution of the experiment.

It is thus clear that, as anticipated in Chapter 6, the FCS technique allows to circumventing the uncertainty principle by disentagling the frequency and the time resolution, whose connection represents a major limitation in time-resolved Raman scattering measurements. *In a time-resolved FCS experiment, while the temporal resolution is dictated by the convolution of the sub-ps duration of the pump and the probe, the frequency resolution is set by the spectral dispersion on the SLM.* Without affecting the temporal resolution, the spectral resolution can be thus improved by increasing the resolving power of the diffraction grating in the folded $4f$ line. It should be noted that, considering a fixed bandwith of the incoming beam, the only practical limitation lies in the finite horizontal size of the SLM matrix, that would eventually cut the dispersed beam and thus introduce spectral fluctuations over a smaller frequency range. By reducing the bandwidth of the randomized pulses, this would in turn lead to a decrease in the maximum energy of the excitations measurable by the technique. In general, a compromise between the spectral resolution and the broadness of the bandwidth must be made according to the nonlinear processes that are subject to investigation.

Finally, as each pulse has to be shaped by a randomized SLM pattern, the repetition rate of the experiment is set by the refresh rate of the SLM ($\sim$200 Hz[3]), rather than the full repetition rate of the laser (set to 5 kHz). The acquisition of the photodiode arrays is synchonized with the SLM rate, so that no copies of the same shaped pulse are measured. When a new pattern has been written on the SLM matrix, a flag is raised and the acquisition starts.

3 In addition to the $\sim$5 ms needed to re-orientate the liquid crystals, 8 ms must be further considered to generate the 2D SLM patter. This currently lowers the speed of the experiment to $\sim$70 Hz.

REFERENCES

[1] Jonathan Owen Tollerud, Giorgia Sparapassi, Angela Montanaro, Shahaf Asban, Filippo Glerean, Francesca Giusti, Alexandre Marciniak, George Kourousias, Fulvio Billè, Federico Cilento, et al. Femtosecond covariance spectroscopy. *Proceedings of the National Academy of Sciences*, 116(12):5383–5386, 2019.

[2] Giorgia Sparapassi, Stefano M Cavaletto, Jonathan Tollerud, Angela Montanaro, Filippo Glerean, Alexandre Marciniak, Fancesca Giusti, Shaul Mukamel, and Daniele Fausti. Transient measurement of phononic states with covariance-based stochastic spectroscopy. *Light: Science & Applications*, 11(1):1–8, 2022.

[3] Giorgia Sparapassi. *Femtosecond covariance spectroscopy*. PhD thesis, Università degli Studi di Trieste, 2019.

[4] Angela Montanaro. *Noise correlation spectroscopy*. Master's thesis, Università degli Studi di Trieste, 2018.

[5] LJ Frasinski, K Codling, and PA Hatherly. Covariance mapping: A correlation method applied to multiphoton multiple ionization. *Science*, 246(4933):1029–1031, 1989.

[6] Luca Gammaitoni, Peter Hänggi, Peter Jung, and Fabio Marchesoni. Stochastic resonance. *Reviews of modern physics*, 70(1):223, 1998.

[7] Filippo Caruso, Alex W Chin, Animesh Datta, Susana F Huelga, and Martin B Plenio. Highly efficient energy excitation transfer in light-harvesting complexes: The fundamental role of noise-assisted transport. *The Journal of Chemical Physics*, 131(10):09B612, 2009.

[8] Xiaoji G Xu, Stanislav O Konorov, John W Hepburn, and Valery Milner. Noise autocorrelation spectroscopy with coherent Raman scattering. *Nature Physics*, 4(2):125–129, 2008.

[9] Jochen Mikosch and Serguei Patchkovskii. Coincidence and covariance data acquisition in photoelectron and-ion spectroscopy. I. Formal theory. *Journal of Modern Optics*, 60(17):1426–1438, 2013.

[10] Yong-Xin Yan, Edward B Gamble Jr, and Keith A Nelson. Impulsive stimulated scattering: General importance in femtosecond laser pulse interactions with matter, and spectroscopic applications. *The Journal of chemical physics*, 83(11):5391–5399, 1985.

[11] Eric Olaf Potma and Shaul Mukamel. Theory of coherent Raman scattering. *Coherent Raman Scattering Microscopy*, pages 3–42, 2012.

[12] Martina Esposito, Kelvin Titimbo, Klaus Zimmermann, Francesca Giusti, Francesco Randi, Davide Boschetto, Fulvio Parmigiani, Roberto Floreanini, Fabio Benatti, and Daniele Fausti. Photon number statistics uncover the fluctuations in non-equilibrium lattice dynamics. *Nature communications*, 6(1):1–7, 2015.

[13] Filippo Glerean, Stefano Marcantoni, Giorgia Sparapassi, Andrea Blason, Martina Esposito, Fabio Benatti, and Daniele Fausti. Quantum model for impulsive stimulated Raman scattering. *Journal of Physics B: Atomic, Molecular and Optical Physics*, 52(14):145502, 2019.

[14] Andy Rundquist, Jon Broman, David Underwood, and David Blank. Polarization-dependent detection of impulsive stimulated Raman scattering in α-quartz. *Journal of Modern Optics*, 52(17):2501–2510, 2005.

[15] Andrew M Weiner. Femtosecond pulse shaping using spatial light modulators. *Review of scientific instruments*, 71(5):1929–1960, 2000.

[16] Antoine Monmayrant, Sébastien Weber, and Béatrice Chatel. A newcomer's guide to ultrashort pulse shaping and characterization. *Journal of Physics B: Atomic, Molecular and Optical Physics*, 43(10):103001, 2010.

[17] Joshua C Vaughan, Thomas Hornung, T Feurer, and Keith A Nelson. Diffraction-based femtosecond pulse shaping with a two-dimensional spatial light modulator. *Optics letters*, 30(3):323–325, 2005.

[18] Kazuhiko Misawa. Applications of polarization-shaped femtosecond laser pulses. *Advances in Physics: X*, 1(4):544–569, 2016.

[19] Tobias Brixner and G Gerber. Femtosecond polarization pulse shaping. *Optics letters*, 26(8):557–559, 2001.

[20] T Brixner, G Krampert, P Niklaus, and G Gerber. Generation and characterization of polarization-shaped femtosecond laser pulses. *Applied Physics B*, 74(1):s133–s144, 2002.

[21] Fabian Weise and Albrecht Lindinger. Full control over the electric field using four liquid crystal arrays. *Optics letters*, 34(8):1258–1260, 2009.

[22] Mateusz Plewicki, Fabian Weise, Stefan M Weber, and Albrecht Lindinger. Phase, amplitude, and polarization shaping with a pulse shaper in a Mach-Zehnder interferometer. *Applied optics*, 45(32):8354–8359, 2006.

[23] Masaaki Sato, Takayuki Suzuki, and Kazuhiko Misawa. Interferometric polarization pulse shaper stabilized by an external laser diode for arbitrary vector field shaping. *Review of Scientific Instruments*, 80(12):123107, 2009.

[24] Christoph Schwarz, Ole Hüter, and Tobias Brixner. Full vector-field control of ultrashort laser pulses utilizing a single dual-layer spatial light modulator in a common-path setup. *JOSA B*, 32(5):933–945, 2015.

8

CLOCKING SUPERCONDUCTING FLUCTUATIONS IN THE PSEUDOGAP PHASE

We have proved in Chapter 7 the feasibility of *Femtosecond Covariance Spectroscopy* (FCS) for studying the vibrational spectrum of transparent media. As ultrashort randomized pulses are transmitted, the Fourier components involved in stimulated Raman processes become correlated and the evaluation of their degree of correlation ultimately uncovers the frequency of the phononic excitations. In the present chapter, we extend this conceptual framework to the study of time-resolved electronic Raman scattering in a cuprate superconductor.

The main difference between the two applications arises from the scattering process that mediates the optical mixing within the pulse: while in α-quartz is the creation/annihilation of phonons that imparts the correlations, here we aim at directly probing the scattering from the electronic continuum. To do so, we combine the FCS approach with a pump-probe scheme. We excite the cuprate by means of an intense coherent pump and measure the spectral correlations imprinted in the incident randomized probe pulses at different time delays. A covariance map is computed at each temporal step to address the dynamical evolution of the correlations.

We stressed in Chapter 6 that the strength of the standard Raman techniques lies in the possibility of isolating the contributions from different regions of the Brillouin zone. In a similar manner, by properly defining the polarization geometry of the covariance-based experiment, we are able to track the dynamics of the electronic excitations having different symmetry.

In the first section of the chapter, we present the time-resolved reflectivity measurements performed on a sample of optimally-doped $Bi_2Sr_2CaCu_2O_{8+\delta}$ (Bi2212, T_C=90 K) in different polarization-dependent geometries. These are mean-value measurements involving a coherent probe pulse, rather than a randomized one. The aim of these preliminary measurements is to characterize the non-equilibrium response of the electronic excitations of different symmetries and set the basis for the time-resolved covariance measurements that are discussed in Section 8.2.

8.1 COHERENT TIME-RESOLVED MEASUREMENTS

In order to isolate the dynamics associated to the electronic excitation of different symmetry, a proper polarization selection must be defined according to the third-

order Raman tensor of the sample (Equation 6.15). With reference to the setup sketched in Figure 7.5, the polarizations of the mid-infrared (MIR) pump, the incident probe and the scattered beam are adjusted, respectively, by means of the sample orientation φ[1], the probe half-waveplate α and the analyser half-waveplate θ.

By explicitly computing the Raman tensor elements for a specific polarization geometry, we have showed that the isolation of the B_{1g} (antinodal) and B_{2g} (nodal) contributions can be achieved by cross-polarizing the analyser with respect to the probe beam (Figure 6.3). However, this requirement is rather challenging from an experimental point of view, as in an extinction geometry i) the desired signal has a very low intensity ii) the unwanted contributions from the parallel polarization are always present due to the imperfect extinction coefficient of the polarizers. We will show in the following that, by re-writing the third-order Raman tensor in a convenient form, we can envision a polarization scheme that is experimentally advantageous [1, 2].

8.1.1 *Birefringence measurements*

The calculations of the Raman elements in Section 6.2.1 can be generalized to an arbitrary polarization. If we consider the degrees of freedom of our setup, the polarization of the pump (P), the probe (p) and the analyser (A) can be described by the following vectors:

$$|P\rangle = \begin{pmatrix} \cos\varphi \\ \sin\varphi \end{pmatrix} = \begin{pmatrix} \cos\varphi & 0 \\ 0 & \cos\varphi \\ \sin\varphi & 0 \\ 0 & \sin\varphi \end{pmatrix}; |p\rangle = \begin{pmatrix} \cos\alpha \\ \sin\alpha \end{pmatrix}; |A\rangle = \begin{pmatrix} \cos\theta \\ \sin\theta \end{pmatrix} \tag{8.1}$$

where the $|P\rangle$ has been expanded in a 4x2 matrix to act on the outer level indices of the third-order Raman tensor $R^{(3)}_{ijkl}$ (Equation 6.15).

The reflectivity signal measured in the experiment is proportional to the Raman elements isolated by the polarization geometry [3]. The action of the pump can be formally described by the matrix

$$R^{(pump)} = \langle P|R^{(3)}_{ijkl}|P\rangle = \begin{pmatrix} a^2 + c^2\cos 2\varphi & d^2\sin 2\varphi \\ d^2\sin 2\varphi & a^2 - c^2\cos 2\varphi \end{pmatrix} \tag{8.2}$$

on which the probe ket acts

$$R^{(probe)} = R^{(pump)}\,|p\rangle = \begin{pmatrix} (a^2 + c^2\cos 2\varphi)\cos\alpha + d^2\sin 2\varphi\sin\alpha \\ d^2\sin 2\varphi\cos\alpha + (a^2 - c^2\cos 2\varphi)\sin\alpha \end{pmatrix} \tag{8.3}$$

1 The MIR pump is vertically polarized. Because of its low photon energy, the rotation of the sample is a cleaner solution than the use of waveplates specifically designed for the MIR spectral range.

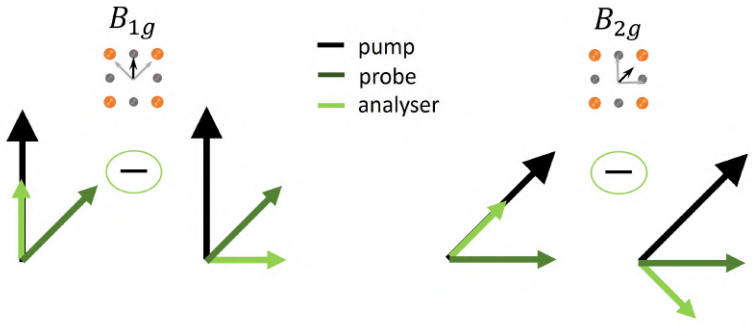

Figure 8.1: **Birefringence measurements of the B_{1g} and B_{2g} symmetries.** The "standard" cross-polarization geometry (top) and the differential birefringent acquisition (bottom) are compared. On the sketch in each figure the orange (grey) circles represent the Cu^{2+} (O^{2-}) ions.

The final reflectivity signal is finally worked out by considering the analyser after the sample ($\langle A| R^{(probe)}$) and we finally get:

$$\Delta R(\varphi,\alpha,\theta) \propto A_{1g}\cos(\alpha-\theta) + B_{1g}\cos 2\varphi\cos(\alpha+\theta) + B_{2g}\sin 2\varphi\sin(\alpha+\theta) \tag{8.4}$$

where we have replaced the matrix elements (a,c,d) with the Mulliken symbols representing the symmetry of the excitations.

From Equation 8.4 it is easy to show that in a cross-polarized geometry ($\theta \perp \alpha$) the A_{1g} contribution can be suppressed and, depending on the orientation of the sample, either the B_{1g} or the B_{2g} mode can be isolated.

However, the same result can be obtained if we consider a different geometry in which the desired signal is obtained as the subtraction of two components. Specifically, if we place a polarizing beam splitter (PBS) after the sample, the two orthogonal projections of the reflected probe beam can be simultaneously acquired. In this way, the A_{1g} signal is splitted into two equal contributions and is canceled out. The differential reflectivity can be treated with the same formalism and if the half-waveplate after the sample is rotated according to the incoming probe polarization so that the orthogonal projections are always splitted by the (fixed) PBS ($\theta = \alpha \pm 45°$), the two detected signals are

$$\Delta R_{+,-}(\varphi,\alpha) \propto \frac{A_{1g}}{\sqrt{2}} + B_{1g}\cos 2\varphi\cos(2\alpha\pm 45°) + B_{2g}\sin 2\varphi\sin(2\alpha\pm 45°) \tag{8.5}$$

and their difference reads:

$$\Delta R(\varphi,\alpha) = \Delta R_+ - \Delta R_- \propto B_{2g}\sin 2\varphi\cos 2\alpha - B_{1g}\cos 2\varphi\sin 2\alpha \tag{8.6}$$

The two polarization geometries needed to isolate the B_1g and the B_{2g} modes are sketched in Figure 8.1, where on the top we have illustrated the "standard" cross-polarization configuration (Figure 6.3) and on the bottom the differential acquisition

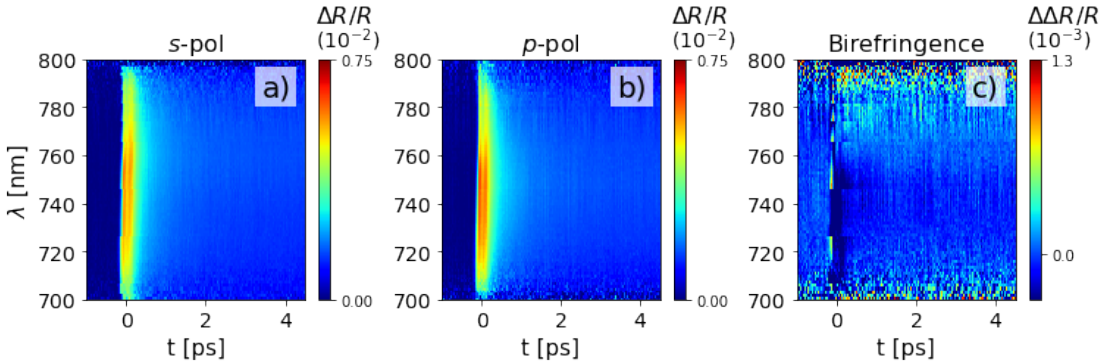

Figure 8.2: **Birefringence at room temperature in B_{1g} symmetry. a-b)** Vertical and horizontal projections, respectively, of the reflected probe beam as function of the pump-probe delay and the probe wavelength. **c)** Subtraction of the maps in a) and b) to get the B_{1g} contribution. The MIR pump pulse has the following features: $h\nu_{MIR}$=70 meV and ϕ_{MIR}=0.2 mJ cm^{-2}.

as described by Equation 8.6. In the following, we will refer to the measurements done in the differential configuration as *birefringent* measurements. In fact, the time-resolved differential acquisition of the two projections of the reflected beam is a measure of the variation of the beam polarization due to the interaction with the excited sample.

The birefringent approach has been adopted in other works with quasi-monochromatic probe beams [4, 1], but it was never applied to a broadband detection, so the spectral dependence of the birefringence in cuprates is missing in literature. In the following sections, we will characterize the time-dependent B_{1g} and B_{2g} signals in Bi2212 as function of the sample temperature and the MIR pump wavelength over a spectral range extending from 700 to 800 nm.

8.1.2 *Measurements in the normal phase*

The measurements have been performed using the setup sketched in Figure 7.5. The spatial light modulator (SLM) has been programmed so that the spectral content of the probe beam (λ_0=750 nm, FWHM=$\sim$55 nm) is not modified in the pulse shaper board. In particular, we have used blazed gratings with the same diffraction efficiency for all the spectral components. A quadratic and a cubic correction of the spectral phase have been applied to compress the pulse (Section 7.4.1)[2]. An optical chopper (45 Hz) placed along the optical path of the pump allows to sort the pumped/umpumped probe spectra and compute the relative transient reflectivity $\Delta R/R$.

In Figure 8.2 we plot the results of a birefringent measurement performed in the B_{1g} symmetry in the normal phase (T=300 K). The panels a) and b) show the transient reflectivity measured, respectively, along the vertical and the horizontal projections

2 Because the temporal chirp of the pulse is corrected by the pulse shaper, the pump-probe maps are not corrected in post-processing as explained in Section 2.4.1.

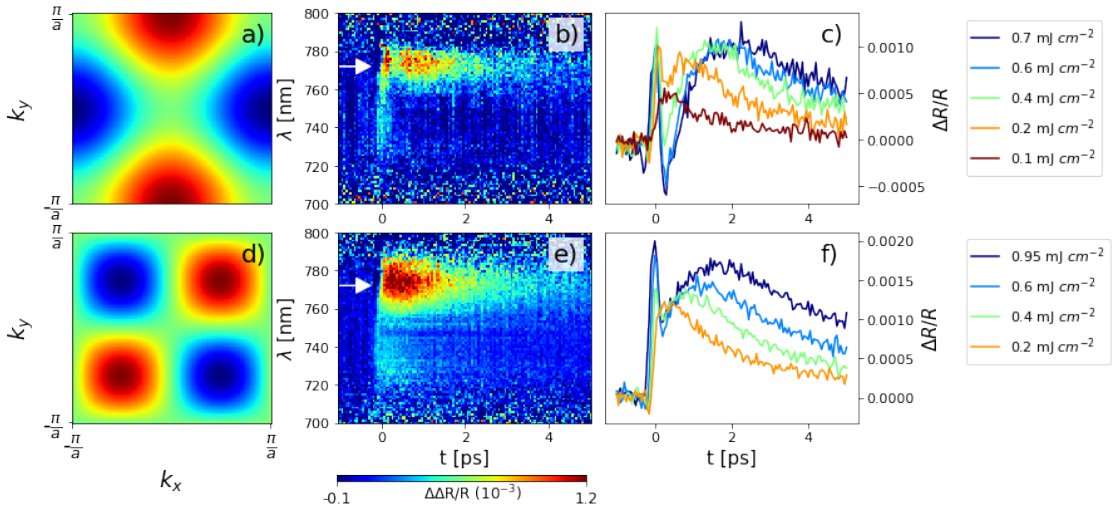

Figure 8.3: **Dynamics of the B modes at T=40 K. a),d)** Sensitivity of the B_{1g}/B_{2g} symmetries to the antinodal/nodal directions, respectively, in the Brillouin zone. **b),e)** Color-coded $\Delta\Delta R/R$ maps of the B_{1g},B_{2g} symmetries upon the photo-excitation by a MIR pulse ($h\nu_{MIR}$=70 meV) with fluence $\phi_{MIR} = 0.2$ mJ cm^{-2}. **c),f)** Time-traces at different pumping fluences in correspondence with the probe wavelength indicated by the white arrows in the maps.

of the probe. The dynamics and the spectral dependence are similar to the ones measured in Y-Bi2212 and discussed in Section 3.5. No significant differences can be appreciated between the signal measured in two projections. Following Equation 8.6, their difference ($\Delta\Delta R/R$, Figure 8.2c) returns the signal associated to the B_{1g} mode, that, except for a slightly negative signal in correspondence with the pump-probe overlap which can be associated to cross-phase modulation between the pump and the probe, is null. Similar measurements performed in the B_{2g} symmetry produce the same result, indicating that the sample is not birefringent in the normal state.

8.1.3 B_{1g} and B_{2g} modes in the superconducting phase

In the superconducting (SC) phase (T=40 K), a birefringent signal arises in both the B_{1g} and B_{2g} geometries (Figure 8.3b,e). In both configurations, the signal has a strong spectral dependence, being mostly localized at approximately 770 nm ($\sim$ 1.6 eV). In this spectral region, the dynamics is a few picoseconds long while the signal vanishes at lower probe wavelengths.

It is worth mentioning that the sign of the birefringent signal has only a relative importance. As we can derive from Equation 8.6, the signal has a π periodicity, while its sign changes every $\pi/2$. We have decided here to plot $\Delta\Delta R/R$ as a positive signal, but the sign can be reversed either by rotating the probe polarization by 90° or by swapping the orthogonal projections onto the PBS.

The signals in the two scattering geometries have different dependence on the pumping fluence. In Figure 8.3c,f we plot the time-traces averaged over the spectral

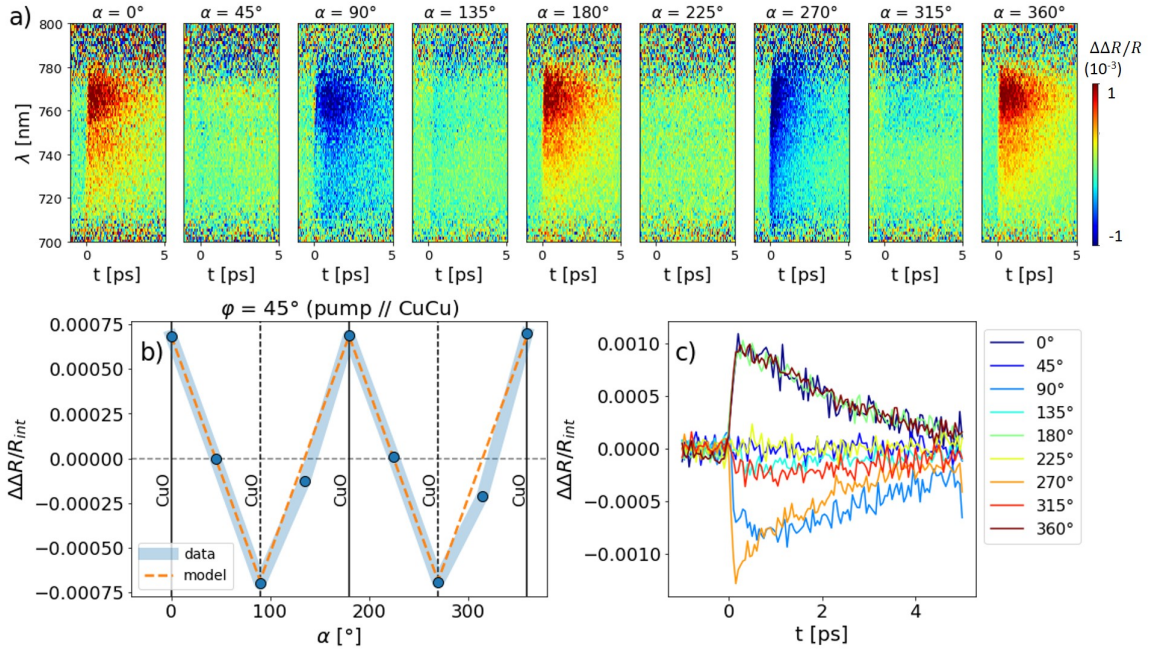

Figure 8.4: **Probe polarization dependence at T=40 K. a)** Birefringence color-coded maps for different probe polarization α and fixed pump polarization along the CuCu axis (φ=45°). **b)** Time- and wavelength-averaged birefringence (blue bullets) as function of the probe polarization. The orange dashed line indicates the model predictions based on Equation 8.6. The point at α=0 has been arbitrarily chosen to coincide with the first experimental point. **b)** Time-traces of the birefringent signal at different probe polarizations.

region centered at 775 nm in different excitation regimes. While at low fluence the B_{1g} and B_{2g} dynamics are similar, in a strong perturbation regime the two symmetries exhibit a different behaviour: the B_{2g} symmetry remains positive, the B_{1g} mode displays instead a negative dip in the first hundreds of fs after the photo-excitation.

8.1.4 *Probe polarization dependence*

In order to experimentally verify the validity of Equation 8.6, we have performed a set of measurements by keeping fixed the polarization of the pump (aligned parallel to the CuCu axis of the CuO_2 plaquette, φ=45°) and rotating the polarization of the probe. The time- and spectral-resolved maps are summarized in Figure 8.4a.

We plot in Figure 8.4b the results of the measurements by averaging the birefringence signal in the first 2.5 ps and in the wavelength region ranging from 760 to 780 nm. In agreement with the third-order tensor predictions, the signal is maximum when the probe is parallel to the CuO axis (α=nπ/2) and is null when the probe is instead oriented along the CuCu axis (α=nπ/4). The wavelength-averaged time-traces plotted in Figure 8.4b for different α indicate that the dynamics of the non-zero birefringence is similar for the choice of probe polarizations resulting in a positive (α=0,180) and a negative (α=90,270) signal.

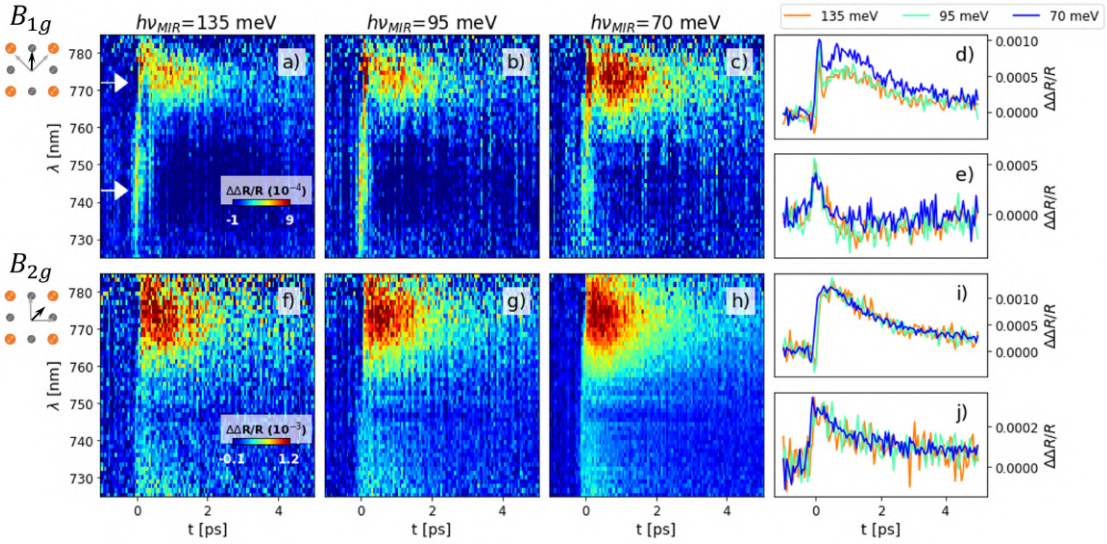

Figure 8.5: **Pump photon energy dependence in B_{1g} and B_{2g} symmetry. a-c)** Color-coded maps of the B_{1g} mode for different photon energy of the MIR pump (135, 95 and 70 meV, respectively). **d-e)** Temporal traces of the B_{1g} maps at two different probe wavelength (∼770 and ∼745 nm, respectively). **f-j)** Same as a-e) but for the B_{2g} symmetry.

According to Equation 8.6, the non-null birefringence signal in this configuration is related to the B_{2g} symmetry. The extinction of the signal at α=n$\pi/4$ confirms that the polarization of the pump is a crucial parameter and a third-order Raman tensor is required to correctly describe the selection rules in a pump-probe experiment.

8.1.5 *Pump photon energy dependence*

In Chapter 3 we have showed that the photon energy of the pump excitation can have a strong impact on the dynamical response in cuprates. In particular, we have showed that the response to sub-gap and above-gap pump pulses is different, both spectrally and as function of the sample temperature.

We examine here the behaviour of the B_{1g} and B_{2g} signals as function of the photon energy of the MIR pump. We consider a sub-gap pump (70 meV) and two pump energies larger than the SC gap (95 and 135 meV). The results of the measurements are plotted in Figure 8.5.

We observe that, while the B_{2g} signal is not affected by the photon energy of the pumps (neither spectrally nor temporally), the B_{1g} signal exhibits a mild dependence on the pump energy. In particular, the signal is identical when the sample is photo-excited by the above-gap pumps, but it is enhanced by the 70 meV pump. We stress that the pump fluence has been kept fixed (0.2 mJ cm^{-2}) in all the measurements.

This different behaviour of the two Raman modes could be directly ascribed to the *d*-wave symmetry of the SC gap. In fact, being the B_{2g} mode sensitive to the excitations in the nodal directions of the Brillouin zone, it is expected not to be

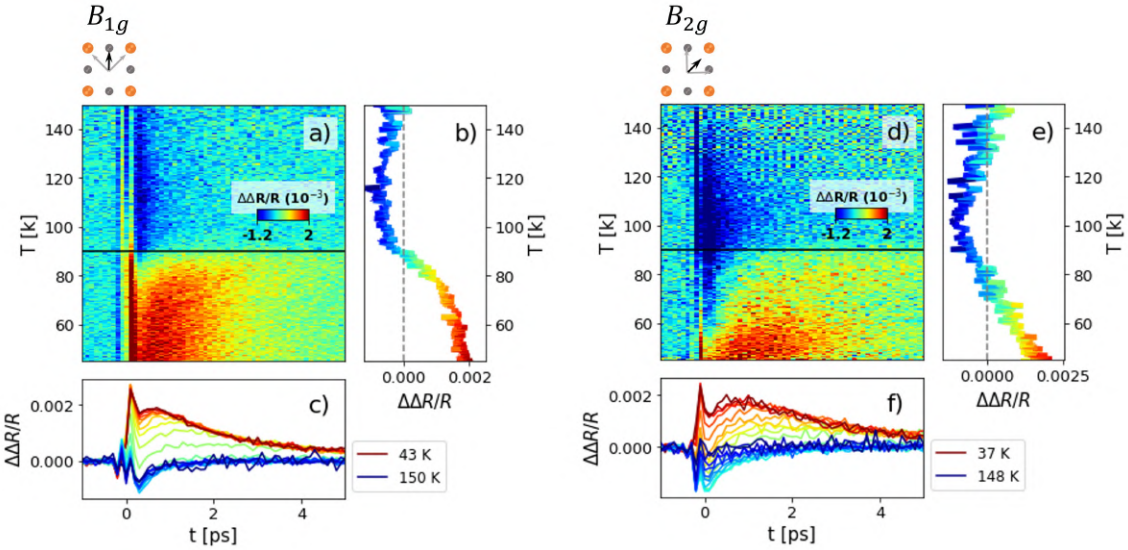

Figure 8.6: **Temperature scans in B_{1g} and B_{2g} symmetry. a)** Time- and temperature-dependent B_{1g} signal at a fixed probe wavelength ∼770 nm, $h\nu_{MIR}$=70 meV and ϕ_{MIR}=0.3 mJ cm^{-2}. **b)** B_{1g} response as function of temperature at a 1 ps pump-probe delay. **c)** Time-traces of the map at different temperatures. **d-f)** Same as a-c) but for the B_{2g} symmetry with identical pumping conditions.

affected by the photon energy of the pump because the SC order parameter is gapless. On the contrary, the B_{1g} symmetry probes the antinodal regions, where the gap has a finite value. In this condition, a pump photon energy smaller or larger is likely to give rise to different dynamics.

8.1.6 *Temperature-dependence*

Finally, we have performed continuous temperature scans of the birefringent signals in the two symmetries across the SC transition. The results of the measurements are displayed in Figure 8.6a,d, where the signals are plotted as function of the pump-probe delay and the sample temperature. The black horizontal line denotes the critical temperature T_C of the sample.

In both symmetries, the signal changes sign when the pseudogap (PG) phase is approached. However, the temperature dependence of the two modes is different, as showed in Figure 8.6b,e. While in the antinodal symmetry the sign change occurs at T_C, in the nodal one the PG-like contribution dominates the response at temperatures well below the SC transition one.

This finding is consistent with our recent report [1], where we used a *d*-wave BCS model to describe the effect in terms of a MIR-induced enhancement of the pair coherence in the antinodal region.

Summary

The transient broadband measurements carried out in the B_{1g} and B_{2g} symmetries have clarified two important points:

- The birefringent signal in both symmetries vanishes in the normal phase, so its presence is linked to the emergence of the SC order parameter. Similarly to what discussed in Chapter 3, the opening of a SC gap on the meV energy scale impacts on the high-energy electrodynamics of the system.

- The signal associated to the nodal and antinodal regions in the superconducting phase has a strong spectral dependence and it is visible only above $\sim$750 nm. This suggests that the link between the low- and high-energy scales may affect a specific optical resonance.

These two points will help us to rationalize the results obtained with the stochastic approach.

8.2 RANDOMIZED TIME-RESOLVED MEASUREMENTS

The stochastic measurements were performed using the same setup employed in the coherent ones, with the difference that the SLM was programmed to introduce spectrally uncorrelated fluctuations across the pulse, as described in Section 7.4.2.

The initial idea of the experiment was to work in a birefringence geometry ($\theta = \alpha \pm 45^{\circ}$) to isolate the B_{1g} and the B_{2g} contributions. As the scattering from these two Raman modes is expected to rotate the polarization of the incoming photons, we were initially determined to reveal the correlations established by the Raman process between spectral components having orthogonal polarizations. This idea led us to the implementation of the polarization pulse shaper, a tool to introduce stochastic and independent fluctuations in both the orthogonal polarization components. This approach would have guaranteed a null correlation between the two polarizations of the impinging probe pulse and thus enabling the potential observation of photon correlations upon the interaction with the sample.

Although the commissioning of the pulse shaper was successful and we achieved an independent stochastic shaping of the two polarization components, the approach discussed above was not feasible due to the presence of the polycrystalline diamond window at the optical entrance of the cryostat (chosen to guarantee a good transmission of the mid-infrared pump pulse) which was found to mix the two components. Even if this mixing was negligible in the coherent measurements, in the stochastic ones it was significantly amplified by the computation of the covariance, which is highly sensitive to very weak signals. The mixing resulted in the presence of strong instabilities due to the interference between the two mixed components, leading to correlations that would have obscured those introduced by the interaction with the sample.

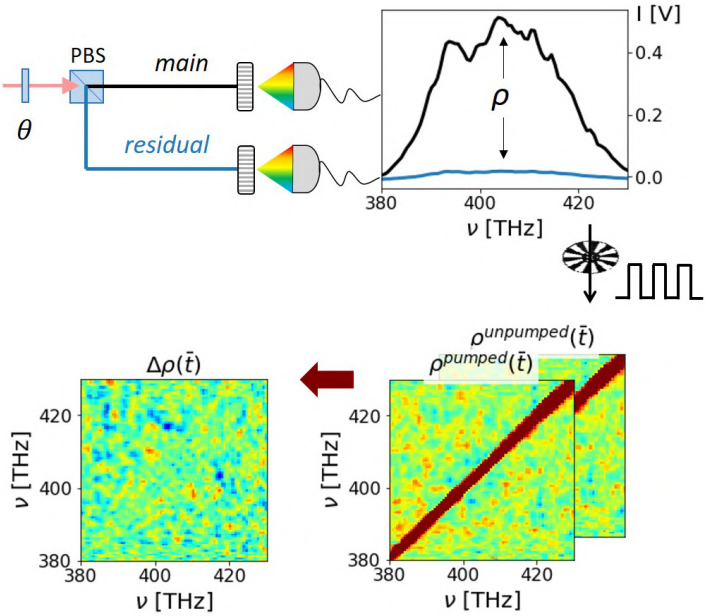

Figure 8.7: **Time-dependent randomized measurements.** The randomized probe reflected by the sample goes through a polarizing beam splitter cube which separates the polarization component parallel (main) and orthogonal (residual) to the beam, that are separately dispersed and detected using a pair of photodiode arrays. The probe pulses are sorted into pumped/unpumped spectra based on the status of the optical chopper (1 Hz) of the pump and the Pearson cross-correlation coefficient maps are calculated independently on the two subsets. The signal $\Delta\rho(\bar{t})$ is obtained by direct subtraction of the two maps at each pump-probe delay.

We then decided to block one arm of the pulse shaper and work with only one polarization component (the vertical one). In order to track the correlations between the photons changing their polarization after the interaction with the sample, we rotated the angle θ of the halfwave plate after the sample to split the main and the residual components of the reflected probe by means of the PBS (Figure 8.7). The angle θ is adjusted before each measurement to optimize the extinction of the residual component at equilibrium.

8.2.1 *Cross-correlation measurements*

As illustrated in Figure 8.7, at each pump-probe delay, a set of tens of thousand randomized pulses is acquired and sorted into pumped/unpumped spectra according to the status of the optical chopper placed along the path of the pump. The Pearson correlation coefficient ρ is computed between the main and the residual channels for the two subsets to get the two corresponding 2D maps.

The final observable of the experiment is the difference between the "pumped" and the "unpumped" covariance maps at each time delay, denoted as $\Delta\rho(\bar{t})$.

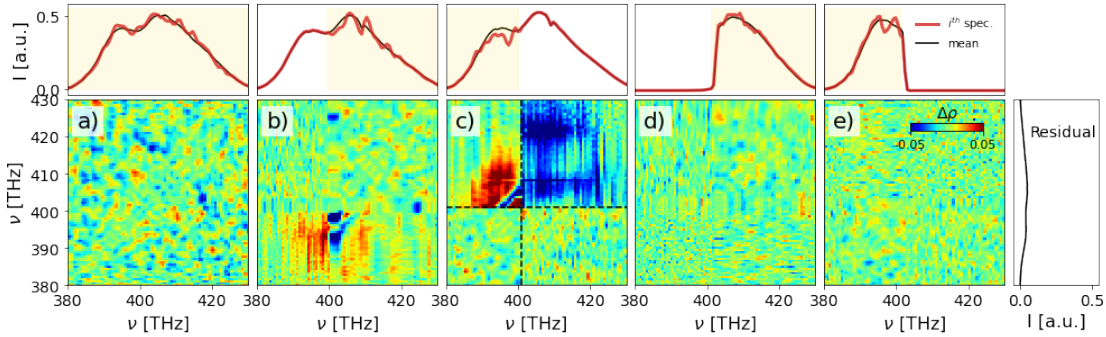

Figure 8.8: **Covariance dependence on the noise configuration.** Cross-correlation coefficient $\Delta\rho$ obtained at the pump-probe overlap (t=0 fs) at T=40 K for different noise configurations of the randomized probe pulses: spectral fluctuations introduced across the whole bandwidth (**a**), fluctuations introduced only on the high-energy side of the pulse while the opposite side is kept unmodulated (**b**) or viceversa (**c**), fluctuations present only on the high-energy side of the pulse while the intensity of the opposite side is suppressed to zero (**d**) or viceversa (**e**). The pump photon energy was set to $h\nu_{MIR}$=125 meV.

8.2.2 *Noise configurations*

The programmable nature of the pulse shaper enables a high flexibility in the introduction of the fluctuations, which affects the visibility of the pump-induced signal. In Figure 8.8 we explore five different noise configurations and compute the corresponding covariance map at the pump-probe overlap (t=0 fs).

In Figure 8.8a we consider a full modulation of the probe pulse, in which stochastic fluctuations are introduced across its whole bandwidth, as plotted in the top panel. The corresponding covariance map averages to zero, indicating that the spectral correlations are the same in the presence or in the absence of the pump.

Similarly to the approach adopted for the measurements in α-quartz, we consider a partial modulation of the pulses in which fluctuations are introduced either only on the high- (Figure 8.8b) or only on the low- (Figure 8.8c) energy side of the pulse. In these two cases, the covariance map has a chequered structure. Taking as an example Figure 8.8c, the map can be divided into four quadrants, as indicated by the dashed lines: the upper right (lower left) quadrant is related to the correlations computed between the unmodulated (modulated) part of the spectrum, while the remaining ones are the mixed blocks in which the covariance is computed between the coherent and the stochastic parts.

Finally, in Figure 8.8d,e we consider instead a mean value shaping in which the unmodulated part of the spectrum is suppressed to zero.

The picture emerging from these measurements is that pump-induced spectral correlations arise only when the probe pulses are partially modulated. In particular, a non-null covariance in the mixed blocks is found only when the low-energy side of the spectrum is stochastically modulated (Figure 8.8c). This result is consistent with the coherent measurements carried out in the previous section, where in the

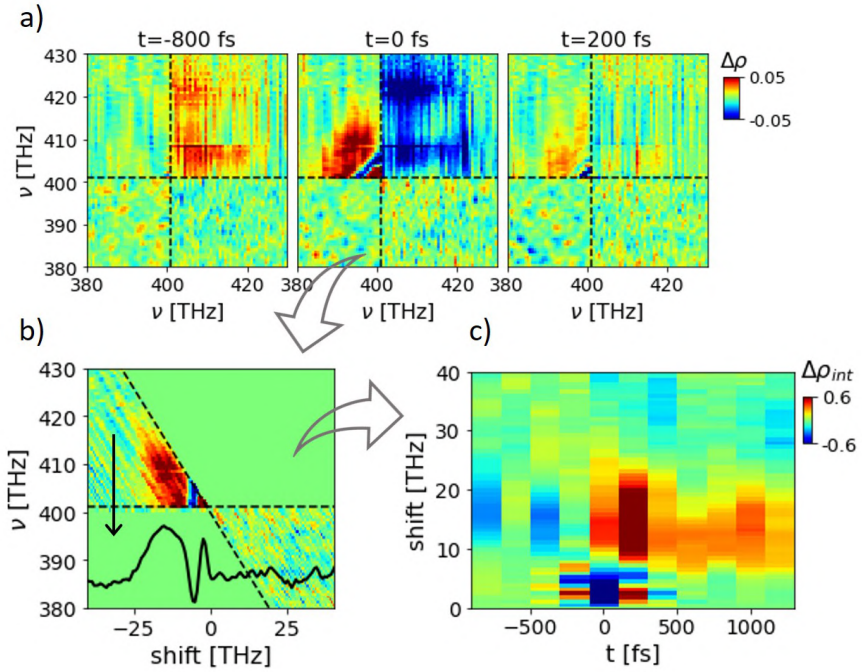

Figure 8.9: **Data analysis scheme for a time-dependent stochastic experiment. a)** Cross-correlation $\Delta\rho$ coefficients at different pump-probe delays. **b)** Rotation of one selected map and vertical integration of the mixed blocks to obtain the black curve. **c)** Collection of the curves for all the time delays to build a correlation map as function of the pump-probe delay (horizontal axis) and the shift from the diagonal (vertical axis).

superconducting phase a birefringence signal associated to the B Raman modes is present only above ∼750 nm (below 400 THz).

Interestingly, the map is not symmetric: correlations are imprinted in the pulses only when photons on the low-energy side of the main polarization component are scattered to the high-energy side of the residual one, and not viceversa. The fact that in the corresponding mean value shaping configuration (Figure 8.8e) the correlations are suppressed, suggests that the presence of a heterodyning field at the emission energy is a requirement for the detection of the signal. Moreover, the coherence of the heterodyning field in the partial modulation configuration seems to improve the visibility of the signal, that is instead washed out when the heterodyning components are also noisy, as in Figure 8.8a.

In the following, we will use only a partial noise modulation as in Figure 8.8c and address the dynamics of the signal.

8.2.3 *Temporal evolution of the correlations*

In Figure 8.9a we plot the cross-correlation Pearson coefficient computed at different pump-probe delays. At negative time delays, no pump-induced correlations are

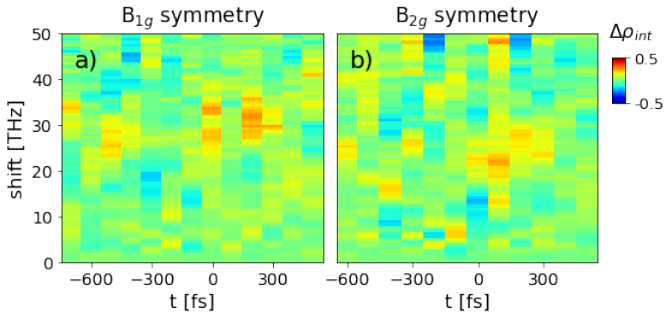

Figure 8.10: **Time-resolved covariance maps in the normal phase.** Maps measured at T=300 K in a B_{1g} (**a**) and B_{2g} (**b**) geometry.

present in the mixed blocks of the maps, which arise instead at the overlap and evolve at positive pump-probe delays.

In order to evaluate the frequency difference among the spectral components entangled by the interaction with the sample, we perform a rotation of the maps and re-define the horizontal axis to quantify the frequency shift from the diagonal (Figure 8.9b). As the only relevant information is contained in the mixed blocks, we cut the upper right and lower left quadrants and perform the integration of the remaining blocks along the vertical direction. In this way, one single curve is descriptive of the 2D correlation map at a fixed time delay.

By repeating the procedure for every pump-probe delay and stacking horizontally the curves, we build a color-coded 2D map as function of the time delay (horizontal axis) and the frequency shift from the diagonal (vertical axis) that compactly illustrates the result of a full time-resolved stochastic measurement (Figure 8.9). We will use in the following this map to discuss the results of the experiments conducted on Bi2212.

8.2.4 *Onset of correlations in different phases*

We performed time-resolved stochastic measurements on Bi2212 (T_C=90 K) in the B_{1g} and B_{2g} scattering geometries at different temperatures. The photon energy of the MIR pump was set to $h\nu_{MIR}$=125 meV and the pumping fluence to ϕ_{MIR}=1.5 mJ cm^{-2}. At each pump-probe delay, we acquired 60,000 different noise realizations, including "pumped" and "unpumped" spectra.

NORMAL PHASE We plot in Figure 8.10 the time-dependent correlation maps measured at T=300 K in both the B_{1g} and B_{2g} symmetries. We observe no distinctive features in the maps, meaning that no correlations are established within the pulses upon the photo-excitation with the pump. We stress that even increasing the pump fluence does not modify the result of the measurements.

SUPERCONDUCTING PHASE When the sample is cooled down to T=40 K, a positively-correlated signal arises in both the scattering geometries at the pump-probe overlap and endures for a few hundreds of femtoseconds after the photo-excitation

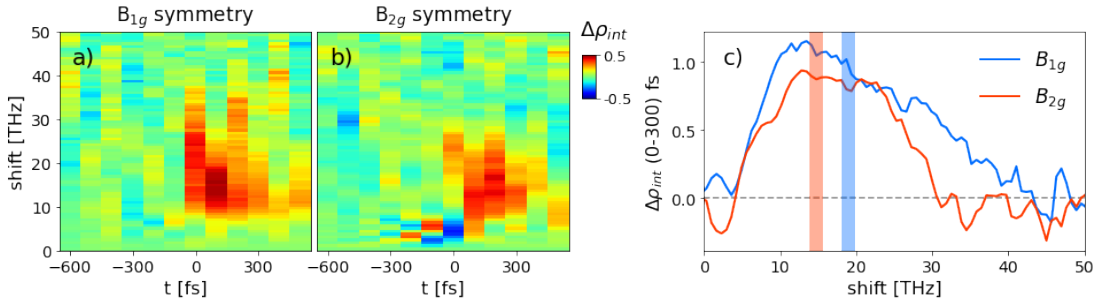

Figure 8.11: **Time-resolved covariance maps in the superconducting phase.** Maps measured at T=40 K in a B_{1g} (**a**) and B_{2g} (**b**) geometry. **c)** Integration of the maps in the first 300 fs. The vertical lines indicate the estimated first momentum of the two distributions.

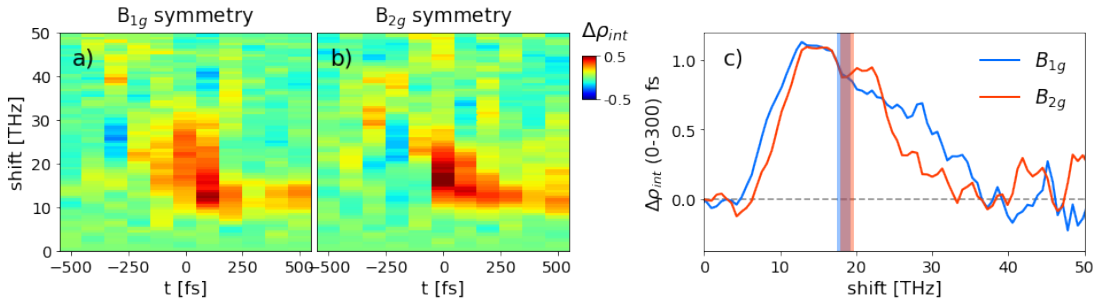

Figure 8.12: **Time-resolved covariance maps in the pseudogap phase.** Maps measured at T=110 K in a B_{1g} (**a**) and B_{2g} (**b**) geometry. **c)** Integration of the maps in the first 300 fs. The vertical lines indicate the estimated first momentum of the two distributions.

(Figure 8.11a,b). To study the spectral dependence of the correlations established, we integrate $\Delta\rho$ in the first 300 fs of the dynamics and plot the result in Figure 8.11c for both the B modes. If we compare the correlation spectra with the B_{1g} and B_{2g} responses in Figure 6.4, it is clear that the correlations imparted by the photo-excited sample have a spectral dependence consistent with the modes measured by spontaneous electronic Raman scattering. The estimation of the first-momentum of the two distributions computed in the range (0-50) THz indicates that the B_{2g} mode lies at lower energy with respect to the B_{1g} one, in agreement with the scattering from electronic excitation discussed in literature (ref. [5] and references therein).

PSEUDOGAP PHASE Interestingly, we observe in the PG phase (T=110 K, Figure 8.12) a time-resolved correlation signal that is qualitatively similar to the one measured at T=40 K. Analogously to the SC phase, only the spectral components whose frequency difference is less than ∼30 THz are correlated. The signal integrated in the first 300 fs after the photo-excitation is plotted in Figure 8.12c for the two electronic symmetries. In the PG phase, the estimation of the first momenta of the two distributions seems to indicate that the two modes lie at similar energies, that would possibly suggest a modified symmetry of the pairing in the PG phase. It should be stressed,

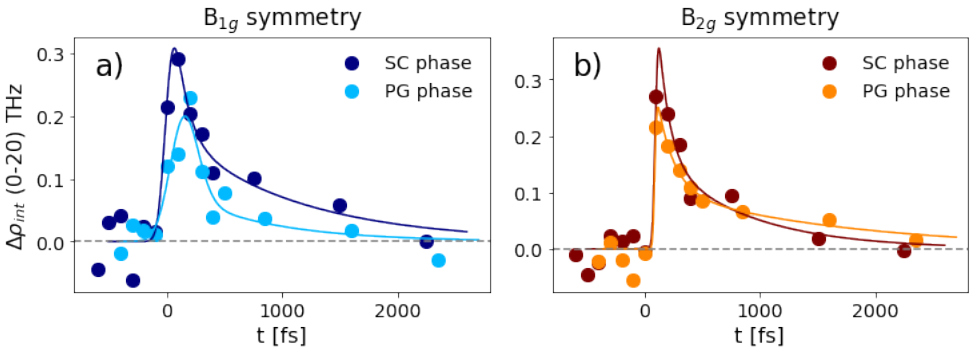

Figure 8.13: **Correlation dynamics.** Correlations integrated between 0 and 20 THz plotted as function of the pump-probe delay in the superconducting and pseudogap phase for the B_{1g} (**a**) and B_{2g} (**b**) mode.

however, that this is only a preliminary analysis and, although reproducible in this particular sample, this result should be confirmed in a more systematic campaign involving various samples with different dopings. The fact that a SC-like covariance signal is present also in the PG phase represents by itself the major outcome of our work, regardless of the details of its spectral dependence that will be neglected in the present discussion.

8.2.5 *Dynamics of the correlations*

In Figure 8.13 we compare the dynamics of the covariance signal measured in the two scattering geometries both in the SC and in the PG phase. Each point in the plot is the result of the integration of the time-resolved correlation maps over a frequency window from 0 up to 20 THz. In both symmetries and phases, the correlations are completely suppressed within the first 2-3 ps.

The decays of both the B modes cannot be represented by a single decaying exponential. The solid lines in the panels are fits to the data using a double-exponential function, characterized by two timescales τ_1 and τ_2, convoluted with a Gaussian to account for the finite duration of the pump and probe pulses. While the dynamics in the SC phase shows only a mild dependence on the symmetry of the modes, in the PG phase we observe a faster dynamics in the antinodal excitation with respect to the nodal one, whose lifetime is comparable instead with that measured below the SC critical temperature.

8.3 DISCUSSION AND CONCLUSIONS

The finding of a SC-like covariance signal in the PG phase represents the major outcome of our work. This evidence signals the presence of short-lived superconducting fluctuations throughout the PG phase.

On the other hand, the observation of a clear and reproducible signal in the PG phase has remained elusive in standard electronic Raman scattering measurements.

Some indications of a depletion of spectral weight at low energies (<700 cm^{-1}) at temperatures above T_C have been reported [6, 7, 8, 9, 10, 11], evidencing a strong dependence on the doping of the samples [12]. However, the study of the temperature dependence in the B_{1g} and B_{2g} electronic symmetries is still ambiguous and no consensus has been reached yet about the role of the two excitations in the onset of superconductivity.

In this regard, it is important to note that the interpretation of the covariance maps in our experiment is fundamentally different from the more familiar electronic Raman spectra. Our technique is sensitive to the presence of correlations, regardless of how they have been established. This means that we are not able to discriminate between an intensity depletion or gain, but we are only able to *quantify the energy scale in which a re-arrangement of the electronic continuum imparts correlations among the Fourier components of the probe pulse*. We stress that this important aspect prevents a direct comparison between our results and the literature.

More importantly, the Raman process itself revealed by our covariance-based method is different from the more common electronic Raman scattering in a number of ways. Firstly, in our experiment the excitation is *impulsive*, and not integrated in time as in a standard Raman measurement; this means that we are able not only to track the sub-ps evolution upon the pump photo-excitation, but also to heterodyne the detection of the signal fields thanks to the broad spectral content of the pulses. Secondly, in a standard Raman experiment the photon scattering process is spontaneous, in the sense that the Raman resonance is established by only one, off-resonance input field. In our framework, the Raman scattering has instead a *stimulated* character, arising from the simultaneous and resonant excitation by two incident fields, whose phase difference locks the initial phase of the excitation. This last aspect leads us in turn to the third point, that is the *coherent* nature of the signal that we detect, in contrast to the incoherent signal detected by the spontaneous electronic Raman scattering. Due to the fixed phase relationship among all the excited emitters, the photons are scattered coherently from the sample in our experiment.

The coherent character of the signal, in combination with the pump-probe scheme we implemented, allows to access not only the energy of the excitation, but also its coherence time, a piece of information that is lost in standard static experiments. The mean-value measurements discussed in Section 8.1.4 indicate that a third-order Raman tensor description based on the D_{4h} space group is required to formally describe the pump-probe experiment. Therefore, the signal dependence on the pump polarization implies that the pump pulse injects a coherent excitation in the system, that lasts at least for a few picoseconds.

In view of these considerations, the observation of a covariance signal in the PG phase that is spectrally consistent with the presence of a SC gap may be interpreted as a signature of a local pairing. There are several indications that superconducting fluctuations persist in cuprates at temperatures well above the critical one, despite the melting of the macroscopic SC state [13, 14, 15, 16, 17]. This opened to the possibility that the gap formation and the phase coherence are distinct and independent processes in cuprates, and the fragility of the SC phase arises from a loss

of phase coherence above T_C where, however, a local pair formation endures. In this perspective, due to its incoherent detection, spontaneous Raman scattering is not an adequate probe as the signal field would be averaged over a large portion of phase-disordered pairs. On the other hand, the intrinsic coherent nature of our covariance-based approach may provide the means to locally probe the scattering from preformed Cooper pairs and its dynamics.

The measurements currently at hand do not conclusively elucidate the origin of the gap in the PG phase nor its symmetry. A more systematic study involving samples with different dopings would be needed to build a more comprehensive picture. Furthermore, so far we have measured the dynamics at three fixed temperatures; nonetheless, a denser temperature scan is essential to draw a covariance-based phase diagram of the effect. Both these campaigns of measurements will be at the core of our future investigations. Their feasibility, however, relies on a structural improvement of the technique that, in the current form, is limited by the refresh rate of the SLM and requires acquisition times that are too long to make the measurements efficient in a large set of samples. We are currently envisioning diverse strategies based on different devices to manipulate the probe pulses and introduce the randomized fluctuations. The most promising one is a solution based on an acousto-optic programmable dispersive filter, in which the pulse shaping is the result of an acousto-optic interaction between a controllable acoustic wave in a nonlinear crystal and the light pulse propagating into it, that would allow to increase the speed of the experiment by at least two orders of magnitude. The implementation of such device would make the technique feasible to explore different doping and temperature regimes and establish it as a powerful tool to study transient nonlinear processes using higher modes beyond the mean-value.

REFERENCES

[1] Francesca Giusti, Angela Montanaro, Alexandre Marciniak, Francesco Randi, Fabio Boschini, Filippo Glerean, Giacomo Jarc, Hiroshi Eisaki, Martin Greven, Andrea Damascelli, et al. Anisotropic time-domain electronic response in cuprates driven by midinfrared pulses. *Physical Review B*, 104(12):125121, 2021.

[2] Francesca Giusti. *Intensity and fluctutaion dynamics in pump-probe experiments in complex materials*. PhD thesis, Università degli Studi di Trieste, 2018.

[3] Y Toda, F Kawanokami, T Kurosawa, M Oda, I Madan, T Mertelj, VV Kabanov, and D Mihailovic. Rotational symmetry breaking in $Bi_2Sr_2CaCu_2O_{8+\delta}$ probed by polarized femtosecond spectroscopy. *Physical Review B*, 90(9):094513, 2014.

[4] I Madan, VV Baranov, Y Toda, M Oda, T Kurosawa, VV Kabanov, T Mertelj, and D Mihailovic. Dynamics of superconducting order parameter through ultrafast normal-to-superconducting phase transition in $Bi_2Sr_2CaCu_2O_{8+\delta}$ from multipulse polarization-resolved transient optical reflectivity. *Physical Review B*, 96(18):184522, 2017.

[5] Thomas P Devereaux and Rudi Hackl. Inelastic light scattering from correlated electrons. *Reviews of modern physics*, 79(1):175, 2007.

[6] G Blumberg, Moonsoo Kang, MV Klein, K Kadowaki, and C Kendziora. Evolution of magnetic and superconducting fluctuations with doping of high-T_C superconductors. *Science*, 278(5342):1427–1432, 1997.

[7] Ralf Nemetschek, M Opel, C Hoffmann, PF Müller, R Hackl, H Berger, L Forró, A Erb, and E Walker. Pseudogap and superconducting gap in the electronic Raman spectra of underdoped cuprates. *Physical review letters*, 78(25):4837, 1997.

[8] JW Quilty, HJ Trodahl, and DM Pooke. Electronic Raman scattering from $Bi_2Sr_2CaCu_2O_{8+\delta}$: Doping dependence of the pseudogap and anomalous 600 cm^{-1} peak. *Physical Review B*, 57(18):R11097, 1998.

[9] M Opel, R Nemetschek, C Hoffmann, R Philipp, PF Müller, R Hackl, I Tüttő, A Erb, B Revaz, E Walker, et al. Carrier relaxation, pseudogap, and superconducting gap in high-T_C cuprates: A Raman scattering study. *Physical Review B*, 61(14):9752, 2000.

[10] Y Gallais, A Sacuto, TP Devereaux, and D Colson. Interplay between the pseudogap and superconductivity in underdoped $HgBa_2CuO_{4+\delta}$ single crystals. *Physical Review B*, 71(1):012506, 2005.

[11] Alain Sacuto, Siham Benhabib, Yann Gallais, Sébastien Blanc, Maximilien Cazayous, Marie-Aude Méasson, Jin Sheng Wen, Zhi Jun Xu, and GD Gu. Pseusogap

in cuprates by electronic Raman scattering. In *Journal of Physics: Conference Series*, volume 449, page 012011. IOP Publishing, 2013.

[12] Alain Sacuto, Y Gallais, M Cazayous, Marie-Aude Measson, GD Gu, and D Colson. New insights into the phase diagram of the copper oxide superconductors from electronic Raman scattering. *Reports on Progress in Physics*, 76(2):022502, 2013.

[13] John Corson, R Mallozzi, J Orenstein, JN Eckstein, and I Bozovic. Vanishing of phase coherence in underdoped $Bi_2Sr_2CaCu_2O_{8+\delta}$. *Nature*, 398(6724):221–223, 1999.

[14] Jhinhwan Lee, K Fujita, AR Schmidt, Chung Koo Kim, H Eisaki, S Uchida, and JC Davis. Spectroscopic fingerprint of phase-incoherent superconductivity in the underdoped $Bi_2Sr_2CaCu_2O_{8+\delta}$. *Science*, 325(5944):1099–1103, 2009.

[15] LS Bilbro, R Valdés Aguilar, G Logvenov, O Pelleg, I Bozović, and NP Armitage. Temporal correlations of superconductivity above the transition temperature in $La_{2-x}Sr_xCuO_4$ probed by terahertz spectroscopy. *Nature Physics*, 7(4):298–302, 2011.

[16] Ivan Madan, Toru Kurosawa, Yasunori Toda, Migaku Oda, Tomaz Mertelj, Primoz Kusar, and Dragan Mihailovic. Separating pairing from quantum phase coherence dynamics above the superconducting transition by femtosecond spectroscopy. *Scientific reports*, 4(1):1–5, 2014.

[17] F Boschini, EH da Silva Neto, E Razzoli, M Zonno, S Peli, RP Day, M Michiardi, M Schneider, B Zwartsenberg, P Nigge, et al. Collapse of superconductivity in cuprates via ultrafast quenching of phase coherence. *Nature materials*, 17(5):416–420, 2018.

9

CONCLUDING REMARKS

The phase diagram of quantum materials is ruled by competing interactions that, in response to even weak external stimuli, can lead to dramatic changes in their macroscopic properties. This complexity, which challenges our understanding of the properties of matter, makes these systems highly appealing from both a fundamental and a technological point of view.

The advent of sub-picosecond pulsed laser sources marked a turning point in the field, enabling to resolve the relaxation dynamics of the coupled degrees of freedom at their fundamental timescales. Moreover, many recent experiments in quantum materials opened the way to the ultrafast manipulation of their functional properties via the impulsive interaction with suitable light pulses.

In this work, we adopted a twofold strategy to investigate the non-equilibrium states in these systems.

- In the first part of the thesis, we designed and characterized a three-pulse setup combining a visible pump, a mid-infrared pump and a white-light visible probe. The uniqueness of this approach lies in the broad tunability of the sources that, ranging from tens of meV to a few eV, makes the setup ideally suited for the investigation of quantum materials, where the manifestation of several low-energy many-body states is pushed to higher energies by the strong correlations.

- In the second part of the thesis, we explored how the study of higher-order observables beyond the mean-value can provide information on nonlinear optical processes that is prevented in more standard integrated protocols. In particular, we developed a covariance-based approach to study the electronic Raman scattering from a cuprate superconductor in out-of-equilibrium conditions.

The measurements performed employing the three-pulse setup emphasized how the energy-selectivity of the photo-excitation is indeed a crucial parameter in determining the non-equilibrium properties of different classes of materials.

In cuprates, for example, above- and below-gap pulses were found to affect differently the electrodynamics at high energies, where an interband oscillator at 2 eV was identified to be involved in the onset of superconductivity (Chapter 3).

In the 1D antiferromagnet TiOCl, the selective stimulation of two *dd* transitions was found to induce a non-thermal renormalization of the Mott gap energy, whose dependence on the orbital symmetry (in addition to the different relaxation dynamics measured) could be an indication of a magnon-orbiton coupling in the spin-Peierls phase (Chapter 4).

In bulk black phosphorus, a layered van der Waals semiconductor, the photo-excitation with sub-gap mid-infrared pulses was found to possibly undress the monolayer exciton resonance through the non-adiabatic modification of the screening environment (Chapter 5).

The remarkable variety of materials and phenomena that we have studied in this work demonstrates the high versatility of the three-pulse technique developed. We stress, however, that the considerable size of the parameter space that can be explored by our setup paves the way to even more diverse applications, ranging from excited state absorption studies to the optical tuning of charge transfer rates in organic photovoltaic materials. The two above-mentioned examples, although not included in this dissertation, have also been investigated during my PhD project in collaboration with the Cerullo lab[1] and the Scholes group[2], respectively.

The second important aspect that emerged from this work is the hidden potential of noise-assisted techniques. By implementing a covariance-based Raman scattering, we showed how, without compromising the spectral resolution, this approach allows to track the pump-induced Cooper pair breaking in cuprates with a sub-picosecond resolution, not otherwise attainable in standard time-resolved Raman scattering experiments.

We observed that, upon the pump excitation, the electronic continuum re-arranges on an energy scale comparable with the superconducting gap and imparts distinguishable correlations among the spectral components of the randomized probe pulses (Chapter 8). In this regard, the experimental observation of gap-size correlations well above the critical temperature has been interpreted as an evidence of gap formation in the pseudogap phase, where, in spite of the phase-incoherence of the order parameter, a local pairing may endure. Additional measurements on samples with different doping contents, however, are required to improve our understanding of the effect.

Altogether, the body of evidence emerged from our investigation on copper-oxide superconductors, both via three-pulse spectroscopy and covariance-based Raman scattering, points to the following elements: i) a high-energy excitation at 2 eV (having either orbital or charge transfer character) is predominantly involved in the pairing; ii) signatures of superconducting fluctuations above the transition temperature suggest that the pairing and the phase coherence are separate processes in cuprates and, as such, may be independently manipulated.

1 *Dipartimento di Fisica, Politecnico di Milano, Milano, Italy*
2 *Department of Chemistry, Princeton University, Princeton, New Jersey 08544, United States*

In our opinion, these two aspects should be deemed central in any attempt to favour the pairing in these systems, equally in equilibrium and out-of-equilibrium approaches.

Finally, we highlight that a recently emerging possibility in the field of quantum materials is the control of their properties with quantized photon modes in cavities.[3] Although still mostly limited to theoretical works, the investigation of strong light-matter coupling regime in these materials is yielding promising results, such as the enhancement of magnetic interactions in electron correlated systems and the manipulation of the superconducting order-parameter phase coherence in cuprates embedded in THz cavities.

On the basis of our results, we suggest that the hybridization of high-energy electronic excitations (rather than low-energy vibrational modes or Josephson plasma resonances) via resonant optical cavities should also be explored. Given the central role played by high-energy excitations in the pairing mechanism, the tailored engineering of their electromagnetic environment may provide the holy grail of controlling and enhancing the superconducting phase in copper oxide-based compounds.

3 Schlawin, F., Kennes, D. M., and Sentef, M. A. (2022). Cavity quantum materials. *Applied Physics Reviews*, **9**(1), 011312. and references therein

AUTHOR CONTRIBUTIONS

I summarize here my contributions to the experiments presented in this thesis and mention the co-workers directly involved in the work.

CHAPTER 2 The three-pulse optical setup has been designed by me in collaboration with Alexandre Marciniak and Francesca Giusti. I especially want to thank Daniele Fausti and Federico Cilento for useful discussions and suggestions. The broadband detection system has been developed by Matija Colja, Gabriele Brajnik, Rudi Sergo and Giuseppe Cautero (Detectors and Instrumentation Laboratory of Elettra Sincrotrone Trieste). The Y-Bi2212 sample on which preliminary measurements have been performed was provided by Andrea Damascelli and Fabio Boschini.

CHAPTER 3 The introductory section on cuprates is the result of discussions with all colleagues in my group. The three-pulse measurements on Y-Bi2212 have been performed by me and Francesca Giusti. Andrea Damascelli and Fabio Boschini provided the samples. Luisa Barba and Giuseppe Chita oriented the sample through X-ray diffraction measurements. I have analysed the data and interpreted the results in collaboration with Daniele Fausti and Francesca Giusti. I acknowledge stimulating discussions with Claudio Giannetti and Dragan Mihailovic.

CHAPTER 4 The measurements on TiOCl have been carried out by me, Enrico Maria Rigoni and Filippo Glerean. The samples were provided by Sander van Smaalen and exfoliated in our laboratory to perform transmission measurements. I have analysed the data. I want to thank Daniele Fausti, Martin Eckstein and Philipp Hansmann for stimulating discussions.

CHAPTER 5 The pump-probe measurements on black phosphorus have been performed by me and Francesca Giusti. The samples were provided by Andrea Perucchi and Paola Di Pietro, who also performed the static FTIR measurements. Matteo Zanfrognini carried out the DFT calculations in collaboration with Daniele Varsano, Massimo Rontani and Elisa Molinari. I have analysed the experimental data. The interpretation of the results has been discussed with all the members of my group.

CHAPTER 6 The description of the Electronic Raman scattering is mainly the result of the study of the literature. The third-order Raman tensor treatment has been discussed with Daniele Fausti, Francesca Giusti and Enrico Maria Rigoni.

CHAPTER 7 The Femtosecond Covariance Spectroscopy has been developed by me, Giorgia Sparapassi, Jonathan O. Tollerud, Filippo Glerean and Daniele Fausti. The measurements on α-quartz were performed by me, Giorgia Sparapassi and Jonathan O. Tollerud. I want to thank Georgios Kourousias ans Fulvio Billè for helping us write the codes for the covariance analysis. Shahaf Asban and Shaul Mukamel derived the theory for the Raman description of the covariance measurements (not fully included in the present thesis). The polarization pulse shaper has been designed and set up by me. I characterized the pulse shaper in collaboration with Francesca Giusti and Enrico Maria Rigoni.

CHAPTER 8 The birefringence measurements on Bi2212 were performed by me and Enrico Maria Rigoni, on the basis of a previous work conducted by Francesca Giusti. Fabio Boschini provided the Bi2212 samples. The acquisition programs for the covariance measurements have been developed by me and Enrico Maria Rigoni, with the valuable support of Matija Colja and Marco Cautero. The randomized measurements were carried out and analysed by me and Enrico Maria Rigoni. I acknowledge fruitful discussions with Daniele Fausti and Francesca Giusti for the interpretation of the results.

LIST OF PUBLICATIONS

- **A. Montanaro**, F. Giusti, M. Zanfrognini, P. Di Pietro, F. Glerean, G. Jarc, E.M. Rigoni, S.Y. Mathengattil, D. Varsano, M. Rontani, A. Perucchi, E. Molinari, and D. Fausti. "Anomalous non-equilibrium response in black phosphorus to sub-gap mid-infrared excitation". *Nature Communications*, **13**, 2667, 2022.

- **A. Montanaro**, F. Giusti, M. Colja, G. Brajnik, A. Marciniak, R. Sergo, D. De Angelis, F. Glerean, G. Sparapassi, G. Jarc, S. Carrato, G. Cautero, and D. Fausti. "Visible pump–mid infrared pump–broadband probe: Development and characterization of a three-pulse setup for single-shot ultrafast spectroscopy at 50 kHz". *Review of Scientific Instruments*, **91**, 073106, 2020.

- **A. Montanaro**, F. Giusti, E.M. Rigoni, F. Glerean, G. Jarc, S.Y. Mathengattil, C. Giannetti, and D. Fausti. "Nodal and antinodal electronic excitations in optimally doped $Bi_2Sr_2Ca_{0.92}Y_{0.08}Cu_2O_{8+\delta}$ revealed by mid-infrared three-pulse spectroscopy"

  In preparation

- F. Giusti, **A. Montanaro**, A. Marciniak, F. Randi, F. Boschini, F. Glerean, G. Jarc, H. Eisaki, M. Greven, A. Damascelli, A. Avella, and D. Fausti. "Anisotropic time-domain electronic response in cuprates driven by midinfrared pulses". *Physical Review B*, **104**(12), 125121, 2021.

- G. Sparapassi, S.M. Cavaletto, J.O. Tollerud, **A. Montanaro**, F. Glerean, A. Marciniak, F. Giusti, S. Mukamel, and D. Fausti. "Transient measurement of phononic states with covariance-based stochastic spectroscopy". *Light: Science & Applications*, **11**(1), 1-8, 2022.

- J.O. Tollerud, G. Sparapassi, **A. Montanaro**, S. Asban, F. Glerean, F. Giusti, A. Marciniak, G. Kourousias, F. Billè, F. Cilento, S. Mukamel, and D. Fausti. "Femtosecond covariance spectroscopy". *Proceedings of the National Academy of Sciences*, **116**(12):5383–5386, 2019.

- K.H. Park, **A. Montanaro**, F. Giusti, F. Fassioli, D. Fausti, and G.D. Scholes. "Manipulation of Charge Delocalization in a Bulk Heterojunction Material Using Mid-Infrared Push Pulse".

  Submitted to *Journal of the American Chemical Society*.

- R.J. Kirby, **A. Montanaro**, F. Giusti, A. Koch-Liston, S. Lei, K.S. Burch, D. Fausti, G.D. Scholes, and L.M. Schoop. "Ultrafast dynamics of the ungapped and charge density wave phases of the topological semimetal $GdSb_xTe_{2-x-\delta}$".

In preparation

- G. Jarc, S.Y. Mathengattil, F. Giusti, M. Barnaba, A. Singh, **A. Montanaro**, F. Glerean, E.M. Rigoni, S. Dal Zilio, S. Winnerl, and D. Fausti. "Tunable cryogenic terahertz cavity for strong light–matter coupling in complex materials". *Review of Scientific Instruments*, **93**(3), 033102, 2022.
- F. Glerean, G. Jarc, A. Marciniak, F. Giusti, G. Sparapassi, **A. Montanaro**, E.M. Rigoni,J.O. Tollerud, and D. Fausti. "Time-resolved multimode heterodyne detection for dissecting coherent states of matter". *Optics Letters*, **45**(13), 3498-3501, 2020.

RICORDI E RINGRAZIAMENTI

È prassi nella nostra scuola di dottorato che i nuovi studenti inviino, entro il primo mese dall'inizio delle attività, una descrizione dettagliata del loro progetto di ricerca, indicando obiettivi da raggiungere e domande alle quali si vorrebbe rispondere. Ricordo la meticolosità con cui ho compilato questo documento allora, convinta, un po' come Zerocalcare, che sarebbe bastato "*tearing it along the dotted lines*", punto dopo punto, workpackage dopo workpackage, per giungere alla fine di questo percorso.

È anche prassi, però, che questo documento cada nel dimenticatoio e che nuove domande (sempre di più!) arrivino prepotenti. È quindi con stupore che, riaprendo ora quel progetto, mi accorgo che l'ultimo punto "*Study of superconducting gaps in Bi2212 via FCS*" è anche incredibilmente l'ultimo capitolo di questa tesi. E quindi, anche se il mio supervisor aveva suggerito di intitolare la mia dissertazione "*Whatever I did in the past four years*", ritengo dopotutto che "*My journey along the dotted lines, with some unexpected yet beautiful twists and turns*" sia più appropriato.

Per essere stato guida e compagno in questa avventura ringrazio Daniele, la cui curiosità verso il mondo è costante fonte di ispirazione. Lo ringrazio per gli stimoli continui, la fiducia, le mille pause caffè che diventano puntualmente, a seconda dell'umore, profonde disquisizioni filosofiche o invettive politiche (e, a volte, anche discussioni scientifiche). Senza il suo entusiasmo e inguaribile ottimismo questo progetto non sarebbe stato possibile.

Un ringraziamento speciale va a Francesca, compagna di avventure, ma soprattutto di innumerevoli disavventure. Una stima delle ore passate insieme in laboratorio è incalcolabile, ma sono certa che il trasloco del lab (vedi Figura I) e l'impacchettamento del laser per le tre (!) spedizioni in Lituania sono pietre miliari del mio dottorato e momenti che difficilmente dimenticherò. Non so se si renda effettivamente conto di quanto abbia imparato da lei negli ultimi anni; mi sembra perciò opportuno cogliere l'occasione per metterla di fronte a questa evidenza e per ringraziarla per l'ordine e la gentilezza che ha sempre portato in laboratorio.

Un ringraziamento anche ad Alexandre, la prima persona ad avermi insegnato come allineare due specchi e due iridi. Le sue soluzioni creative ma funzionali ai problemi pratici del laboratorio, di cui conserviamo ancora traccia nella forma di montaggi impossibili da smembrare e programmi Labview impossibili da decifrare, sono state una mancanza tangibile negli ultimi anni.

Ringrazio anche Jonathan e Giorgia, con cui l'avventura della stocasticità ha avuto inizio anni fa.

Grazie ad Enrico, che ha pazientemente condiviso con me le pene del lab negli ultimi mesi. Forse è una delle poche persone al mondo che, come me, reagirebbe con

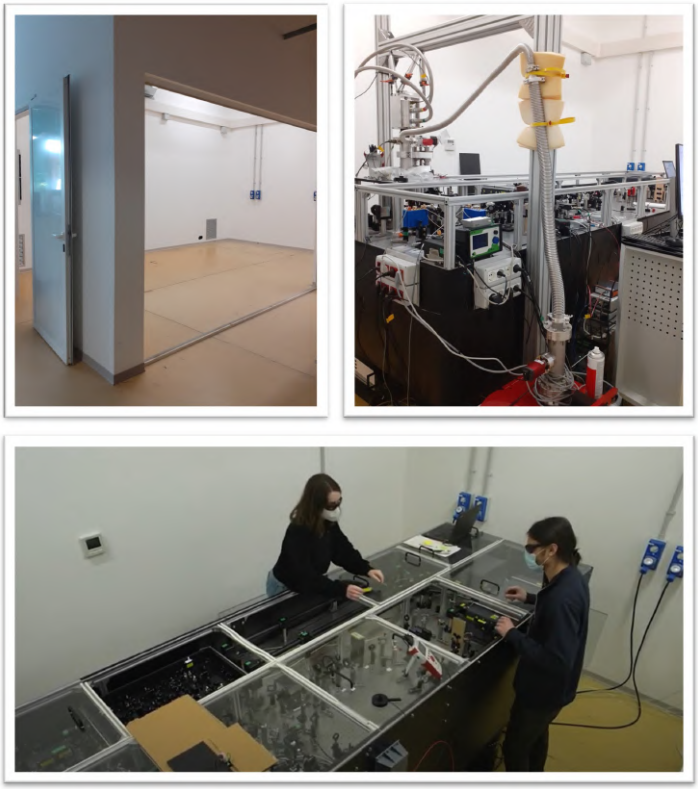

Figure I: **8 luglio 2020.** Il trasloco del lab in un hutch vuoto con un sistema di condizionamento vagamente funzionante.

inusitato terrore alla scritta "*armed, wait trigger*". A Giacomo, lo speleologo pioniere del gruppo, grazie per le barzellette del mercoledì e grazie soprattutto per la pronta traduzione friulano-italiano. Siamo sempre in attesa di un concerto dei *Biei watch*. Grazie anche a Shahla, speleologa cadetta, per aver fin da subito condiviso cene e ricette indiane.

Un pensiero anche a Filippo, che vive ora oltreoceano. La mancanza del suo spirito critico, pungente verso gli altri come verso se stesso, mi ha fatto apprezzare solo ora come fosse una risorsa per tutto il gruppo. Nonostante ciò, a mancarmi di più sono le serate passate insieme giù in città, quando anche un cappellino con la scritta "open day" poteva essere fonte di interminabili risate.

A tutte le persone appena menzionate va inoltre un ulteriore ringraziamento per essere state come una famiglia nei momenti bui di lockdown, quando le ore passate in ufficio rappresentavano l'unico effettivo momento di spensieratezza della giornata.

Non potrò mai ringraziare abbastanza Gabriele, Matija, Rudi, Bepo e tutto il gruppo degli elettronici per il costante supporto tecnico, ma anche psicologico. Sono stati in grado di aiutarci a realizzare tutti i nostri progetti, anche quelli più strampalati, sempre con professionalità e buonumore. Un grazie anche a Gianluca che, nonostante dicesse di avere sempre tanto lavoro da fare, trovava poi alla fine il tempo per portare a termine le nostre richieste. Grazie anche a tutta la "macchina" che ha reso possibile

il trasloco del nostro lab: a Walter, perché era l'unica persona davvero interessata ai nostri problemi con il maledetto sistema di condizionamento, a Marco, che ha speso un fine settimana a cercare un adattatore metrico per tubi imperiali e ci è incredibilmente riuscito, a Moreno, il cui numero aziendale conosco ormai a memoria a testimonianza della frequenza con cui ho cercato di chiamarlo in questi anni.

Un grazie anche alle tantissime persone che ho certamente importunato ad Elettra e che non ho qui menzionato. Grazie anche a tutti quelli (troppi, mio malgrado) che mi hanno gentilmente dato in prestito qualcosa che io poi non ho mai più restituito.

Desidero ringraziare anche lo European Research Council che attraverso il progetto INCEPT ERC-2015-STG (Grant No. 677488) ha co-finanziato la mia borsa di dottorato.

Un ringraziamento anche a Greg Scholes e a tutto il suo gruppo per avermi accolta durante il mio (purtroppo breve) periodo a Princeton. Robert, è stato bello poter ricambiare almeno un po' della gentilezza durante la tua visita a Trieste.

Perché sì, Princeton e New York saranno anche belle, però mai mi sono riconosciuta "*docile fibra dell'universo*" come sorseggiando uno spritz a Barcola. A Trieste - al suo mare, al suo vento - va un ringraziamento profondo. Nonostante l'idea di lasciare questa città mi atterrisca, il riviverla costantemente attraverso gli amici che qui ho incontrato e che continuano, seppur a distanza, a camminare ancora con me rende tutto più sopportabile.

Ci tengo però a precisare che, benché triestina d'adozione, le mie radici sono ben salde nella mia bella Noci e in tutta la mia famiglia che rende sempre nostalgico ogni rientro a casa (anche se, fortunatamente, le marmellate di zia Marina arrivano anche qui).

Ringrazio nonna Lina, esempio unico di libertà e amore per la cultura. Da lei ho malauguratamente ereditato il vizio della lettura notturna; spero anche una buona dose dei suoi geni.

Un grazie speciale alla mia "sorellina" Elena per riempire le mie giornate della leggerezza che per natura mi manca.

E, anche questa volta, almeno mila volte grazie a Nicola per continuare, con infinita pazienza e immutato amore, a prepararmi i pancakes la mattina.

Infine, il grazie più grande va ai miei genitori, che hanno permesso a me e a mia sorella di girare il mondo senza mai sentirci lontane da casa. Grazie al loro incondizionato supporto, sono cresciuta nella convinzione di poter diventare chiunque volessi da grande. Se sono qui oggi, a scrivere le ultime parole di questa tesi, è anche merito loro.

Con affetto,
Angela